



UNIL | Université de Lausanne

Unicentre

CH-1015 Lausanne

<http://serval.unil.ch>

Year : 2022

A study of the role of nonsense-mediated mRNA decay in circadian timekeeping using a novel mouse model

Katsioudi Georgia

Katsioudi Georgia, 2022, A study of the role of nonsense-mediated mRNA decay in circadian timekeeping using a novel mouse model

Originally published at : Thesis, University of Lausanne

Posted at the University of Lausanne Open Archive <http://serval.unil.ch>

Document URN : urn:nbn:ch:serval-BIB_A3D5242634BC4

Droits d'auteur

L'Université de Lausanne attire expressément l'attention des utilisateurs sur le fait que tous les documents publiés dans l'Archive SERVAL sont protégés par le droit d'auteur, conformément à la loi fédérale sur le droit d'auteur et les droits voisins (LDA). A ce titre, il est indispensable d'obtenir le consentement préalable de l'auteur et/ou de l'éditeur avant toute utilisation d'une oeuvre ou d'une partie d'une oeuvre ne relevant pas d'une utilisation à des fins personnelles au sens de la LDA (art. 19, al. 1 lettre a). A défaut, tout contrevenant s'expose aux sanctions prévues par cette loi. Nous déclinons toute responsabilité en la matière.

Copyright

The University of Lausanne expressly draws the attention of users to the fact that all documents published in the SERVAL Archive are protected by copyright in accordance with federal law on copyright and similar rights (LDA). Accordingly it is indispensable to obtain prior consent from the author and/or publisher before any use of a work or part of a work for purposes other than personal use within the meaning of LDA (art. 19, para. 1 letter a). Failure to do so will expose offenders to the sanctions laid down by this law. We accept no liability in this respect.



UNIL | Université de Lausanne

Faculté de biologie
et de médecine

Center for Integrative Genomics

A study of the role of nonsense-mediated mRNA decay in circadian timekeeping using a novel mouse model

Thèse de doctorat en Neurosciences

présentée à la

Faculté de biologie et de médecine
de l'Université de Lausanne

par

Georgia KATSIUDI

Research Master in Cognitive and Clinical Neuroscience
University of Maastricht, the Netherlands

Jury

Prof. Anita Lüthi, Présidente
Prof. David Gatfield, Directeur de thèse
Prof. Charna Dibner, Experte
Prof. Oliver Mühlemann, Expert

Thèse n° 335

Lausanne
2022

Programme doctoral interuniversitaire en Neurosciences
des Universités de Lausanne et Genève



UNIL | Université de Lausanne



**UNIVERSITÉ
DE GENÈVE**

Imprimatur

Vu le rapport présenté par le jury d'examen, composé de

Président·e	Madame	Prof.	Anita	Lüthi
Directeur·trice de thèse	Monsieur	Prof.	David	Gatfield
Expert·e-s	Madame	Prof.	Charna	Dibner
	Monsieur	Prof.	Olivier	Mühlemann

le Conseil de Faculté autorise l'impression de la thèse de

Madame Georgia Katsioudi

Research Master in Cognitive and Clinical Neuroscience,
Université de Maastricht, Pays-Bas (NL)

intitulée

**A study of the role of nonsense-mediated mRNA decay
in circadian timekeeping using a novel mouse model**

Lausanne, le 7 juillet 2022

pour Le Doyen
de la Faculté de Biologie et de Médecine

Prof. Anita Lüthi



Contents

Acknowledgements	6
Preface.....	8
Abstract.....	10
Résumé	12
Introduction	14
1. The mammalian circadian system	14
1.1 History and basic concepts of chronobiology	14
1.2 Clinical relevance of chronobiology	15
1.3 Organisation of the mammalian circadian system.....	17
<i>The Suprachiasmatic nucleus (SCN), as the master pacemaker</i>	<i>17</i>
<i>Peripheral clocks; as subsidiary clocks</i>	<i>18</i>
1.4 Molecular composition of circadian oscillators	19
1.5 Post-transcriptional regulation of circadian gene expression	22
2. Nonsense-mediated mRNA decay (NMD)	26
2.1 History and basic concepts of NMD	26
2.2 Key NMD factors	27
2.3 Current working model of NMD.....	29
2.4 NMD-inducing features	32
<i>Exon junction complex (EJC)</i>	<i>32</i>
<i>Translated upstream open reading frames (uORFs) in the 5' UTR.....</i>	<i>33</i>
<i>Long 3' UTR.....</i>	<i>33</i>
2.5 Tissue- and gene-specific NMD activity	34
2.6 Physiological roles of NMD.....	35
<i>Stress Adaptation.....</i>	<i>35</i>

<i>Development and cell differentiation</i>	36
<i>Circadian clock</i>	37
2.7 Clinical relevance of NMD	37
<i>B⁰ Thalassemia</i>	38
<i>Cancer</i>	38
<i>X-linked mental retardation</i>	40
Study objectives.....	41
Brief summary of the results	44
1. A novel <i>Smg6</i> mouse model reveals regulation of circadian period and daily CRY2 accumulation through the nonsense mediated mRNA decay	44
<i>Summary</i>	44
<i>Study contributions</i>	48
2. Recording of diurnal gene expression in peripheral organs of mice using the RT-Biolumicorder	51
<i>Summary</i>	51
<i>Study contributions</i>	52
3. The sleep-wake distribution contributes to the peripheral rhythms in PERIOD-2	54
<i>Summary</i>	54
<i>Study contributions</i>	54
Discussion	56
High levels of CRY2 slow down circadian oscillations	61
The SCN paradox: no detected differences in circadian rhythmicity in NMD-inactive SCN	64
No difference in liver oscillators in hepatocyte-specific NMD mutant mice <i>in vivo</i>	68
NMD-driven liver toxicity	71
Difference in locomotor activity in freely moving mice with hepatocyte-specific <i>Smg6</i> mutation	72
Future perspectives and ongoing work	74

<i>Sirtuins (SIRT)</i>	75
<i>The DBHS proteins</i>	77
Closing remarks: study validity and ethical considerations	79
References	80
A novel <i>Smg6</i> mouse model reveals regulation of circadian period and daily CRY2 accumulation through the nonsense mediated mRNA decay	96
Recording of diurnal gene expression in peripheral organs of mice using the RT-Biolumicorder	130
The sleep-wake distribution contributes to the peripheral rhythms in PERIOD-2...	153

Acknowledgements

I would like to express my warmest gratitude to all the people who supported me in several ways during the journey of my PhD.

Foremost I would like to thank my supervisor David Gatfield for all his support and availability, all the challenges and the long discussions and for trusting me with his genius project (for yet undiscovered reasons). Our different perspectives created multiple learning opportunities for me and helped the project to beautifully evolve in an holistic and multifaceted study with great results.

Special thanks go to Rene Dreos for the endless analysis of the RNA-seq data, always happy to help and never complaining, and for his constant willingness to eat all the chocolate at the office. I would also like to extend my gratitude to Angelica Liechti who prepared the RNA libraries of the project and she was always jumping to help when she had a minute to spare. I would also like to thank Enes Arpa, who helped these last months by doing several Western Blots and Yevheniia Kyriachenko, who was my first student during my PhD and gave the opportunity to gain insights into the supervising process.

Special thanks go to all the members of the Gatfield Lab, present and former for the collaborative and friendly atmosphere. Mara for always knowing where is what and her mini protocols for everything, Nikolay for the scientific discussions about clocks, Hima for bringing me oranges during the writing process, Sebastien for helping me with the translations in French and Romane for swimming at the lake with me (almost) every week over the past year, it's been a blast! I would also like to thank all the members of the CIG for the collaborative and friendly atmosphere.

Multiple people worked on the realisation of this project, to whose help I am immensely grateful. Special thanks go to Yann Emmenegger, the resident of the sleep lab, who helped me to fix every burnt lamp, blocked cable, broken sensor and many other mysterious

problems during my *in vivo* experiments. Sevasti Gaspari for the SCN injections, even on a sunny Sunday, and the extra glucose measurements to our extra fat mice. Miho Sato for the SCN explant cultures and her analysis, which she completed even during her maternity leave. Special thanks go Alejandro Osorio-Forero for designing with me Osiris, the MatLab based software we created for analysis of the RT-Lumicorder data and for always sharing his enthusiasm about science. I would also like to thank Evan Karousis for always conveying to me his love and knowledge on NMD. Here, together with my colleagues I would like to express my gratitude to the inconspicuous heroes of my PhD, namely the numerous experimental mice I used over the past years.

I would also like to express my deepest gratitude to my PhD mentor Paul Franken, who is always available (though he tries to hide behind the closed door of his office) to discuss science and other matters with me. He is always trying his best to support me.

I would also like to thank my initial PhD committee members: Steven Brown and Martine Collart, and the current members: Charna Dibner and Oliver Muehlemann for their availability, support and interest in our work. Special thanks go to the president of my PhD committee, Anita Lüthi, who initially brought me to Switzerland and she is a constant inspiration for me.

Closing I would like to thank all the people who stand by me in life, family, friends and my four-legged flatmates for their presence and support (obviously my cats have no other option).

I fear that over the past five years I learnt more about life and myself than about the RNA and the clock. But after all, *"Only time is ours, the rest we'll just wait and see!"**

*Lyrics from the song "I forget where we were", Ben Howard.

Preface

The aim of my PhD work was to study and characterize post-transcriptional mechanisms that regulate rhythmic gene expression in mammals.

In the current thesis I present my work focusing on the characterisation on a new mouse model of NMD and the newly discovered role of the pathway in regulating circadian rhythmicity. The vast majority of the *in vivo* and *in vitro* experiments done in this project are included in our publication Katsioudi *et al.*, 2022, which is currently in the process of submission. Data that are not included in the research paper manuscript, but still important for this thesis, are presented and discussed in the “Discussion” section. Additional analyses are currently ongoing on our RNA-seq and the metabolomic data of the *Smg6^{mut}* liver tissue around-the-clock that we plan to incorporate in the revised manuscript or a follow-up publication. Lastly, we have just received lipidomic data from NMD-deficient liver tissue around-the-clock, for which I did not have the opportunity of carrying out any analyses before the submission of this thesis.

As a global overview, I would like to point out that during the first two years in the lab, my work focused on the regulatory mechanisms of rhythmic protein levels in genes involved in iron metabolism and the potential impact of iron to core clock regulation. Previous work in the lab using ribosome profiling in mouse liver around-the-clock revealed that for a group of iron metabolism-related genes, the mRNAs are constantly abundant, yet rhythmically translated [2]. The common feature among these genes is an RNA hairpin loop termed Iron Responsive Element (IRE). The binding of IREs by Iron Regulatory Proteins IRP1 and IRP2 regulates mRNA translation or stability in response to intracellular iron levels. This study, part of which was presented in my midterm evaluation in 2019, involved a series of *in vitro* luciferase experiments in cell lines, circadian phenotyping of the locomotor activity of IRP (1 and 2) KO mice and setting up an *in vivo* system where translation in the liver can be monitored real-time in freely

moving mice (RT-Biolumicorder) using adenoviral luciferase reporters administered by tail vein injections [3].

The results of this study, even though often promising, were inconsistent and we decided to no longer proceed with this project, especially also when the pandemic forced us to take some strategic decision on the most promising projects. No data regarding this project will be presented in the current thesis for coherence reasons. However, the several months I invested in setting up the technique in the lab gave rise to a methods publication that has been included as a chapter in the “Circadian Regulation; Methods and Protocols” book (Methods in Molecular Biology by Humana press, Springer). Our chapter elaborately describes the protocol for using the RT-Biolumicorder, including a detailed guide for troubleshooting. In addition, in the same manuscript we reported a MatLab based software that was designed for the analysis of the RT-Lumicorder data, which is deposited online for open access (Katsioudi *et al.*, 2021). The book is currently available for ordering (<https://link.springer.com/book/9781071622483>) and our chapter just became visible at PubMed.gov [4].

My training with the RT-Lumicorder further allowed me to collaborate with the group of Prof. Paul Franken and contribute to their work (Hoekstra, Jan *et al.*, 2021), by performing some of the experiments that were requested during the revision process of their manuscript. Lastly, selected data of the *in vivo* experiments, mostly the RT-Biolumicorder experiments on the effect of feeding on the expression of ribosomal protein-encoding mRNA (luciferase reporter of RPL30) and running wheel assays of the IRP KO mice are planned to be included in future projects in the lab.



UNIL | Université de Lausanne

Unicentre

CH-1015 Lausanne

<http://serval.unil.ch>

Year : 2022

A study of the role of nonsense-mediated mRNA decay in circadian timekeeping using a novel mouse model

Katsioudi Georgia

Katsioudi Georgia, 2022, A study of the role of nonsense-mediated mRNA decay in circadian timekeeping using a novel mouse model

Originally published at : Thesis, University of Lausanne

Posted at the University of Lausanne Open Archive <http://serval.unil.ch>

Document URN : urn:nbn:ch:serval-BIB_A3D5242634BC4

Droits d'auteur

L'Université de Lausanne attire expressément l'attention des utilisateurs sur le fait que tous les documents publiés dans l'Archive SERVAL sont protégés par le droit d'auteur, conformément à la loi fédérale sur le droit d'auteur et les droits voisins (LDA). A ce titre, il est indispensable d'obtenir le consentement préalable de l'auteur et/ou de l'éditeur avant toute utilisation d'une oeuvre ou d'une partie d'une oeuvre ne relevant pas d'une utilisation à des fins personnelles au sens de la LDA (art. 19, al. 1 lettre a). A défaut, tout contrevenant s'expose aux sanctions prévues par cette loi. Nous déclinons toute responsabilité en la matière.

Copyright

The University of Lausanne expressly draws the attention of users to the fact that all documents published in the SERVAL Archive are protected by copyright in accordance with federal law on copyright and similar rights (LDA). Accordingly it is indispensable to obtain prior consent from the author and/or publisher before any use of a work or part of a work for purposes other than personal use within the meaning of LDA (art. 19, para. 1 letter a). Failure to do so will expose offenders to the sanctions laid down by this law. We accept no liability in this respect.

Abstract

Circadian rhythms regulate animal physiology and behaviour according to the solar day. The molecular clock, which shares a similar architecture in most cell types throughout the mammalian body, is driven by a network of negative transcriptional feedback loops that further drive the rhythmic expression of many output genes. In the core loop the heterodimer BMAL1:CLOCK activates the transcription of the *Per* and *Cry* genes which subsequently inhibit the expression of *Bmal1* and *Clock*, closing the loop. While the majority of the regulatory steps take place at transcriptional and post-translational levels, emerging literature suggests that several post-transcriptional modifications also regulate the rhythmicity of the clock.

A post-transcriptional mechanism of great importance is the nonsense-mediated mRNA decay (NMD) pathway, which facilitates quality and quantity control in gene expression via mRNA degradation. A handful of studies in non-mammalian model organisms have identified possible links between NMD and the clock, however, there is no existing evidence linking the two processes in mammalian organisms. We designed a new mouse model that inactivates NMD based on the pathway's endonuclease SMG6, and we further performed *in vivo* and *in vitro* circadian assays on the peripheral clocks of the liver and of fibroblasts, as well as the master clock in the brain's suprachiasmatic nucleus (SCN).

A period lengthening was observed in NMD-deficient peripheral tissues. Transcriptome-wide analyses of liver tissue gene expression around-the-clock revealed increased transcript stability of the core clock gene *Cry2* during the dark phase, accompanied by delayed high protein levels of CRY2 at the end of the dark phase. We propose a revised model of the core clock in which circadian period length is partly regulated by the NMD-targeting of the 3' UTR of *Cry2*.

Overall, my work uncovered new, previously unidentified, NMD substrates unravelling the pathway's important physiological role in circadian timekeeping. In addition to these

advances related to mammalian physiology and chronobiology, we anticipate that our new mouse model could be transposed to the study of the potential links between the NMD pathway and various human pathologies, such as cancer and neurological disorders and in designing novel therapeutic approaches.

Résumé

Les rythmes circadiens régulent la physiologie et le comportement des animaux en fonction du jour solaire. L'horloge moléculaire, qui partage une architecture similaire dans la plupart des cellules de mammifères, est pilotée par un réseau de boucles de rétroaction transcriptionnelles négatives qui stimulent l'expression rythmique de nombreux gènes. Dans la boucle centrale, l'hétérodimère BMAL1:CLOCK active la transcription des gènes *Per* et *Cry* qui inhibent ensuite l'expression de *Bmal1* et *Clock*, fermant la boucle. Alors que la majorité des étapes de régulation a lieu aux niveaux transcriptionnel et post-traductionnel, la littérature émergente suggère que plusieurs modifications post-transcriptionnelles régulent également la rythmicité de l'horloge.

Un mécanisme post-transcriptionnel important est la voie du nonsense-mediated mRNA decay (NMD). Il assure la surveillance de la qualité et de la quantité de certains ARNm au cours de l'expression des gènes. Certaines études menées sur des organismes modèles non-mammifères ont identifié de possibles liens entre le NMD et l'horloge interne. Néanmoins, il n'existe actuellement aucune preuve permettant de relier ces deux processus entre eux chez les mammifères. Nous avons donc conçu un nouveau modèle murin pour lequel SMG6, l'endonucléase centrale du NMD, est inactivable puis avons étudié, *in vivo* et *in vitro*, les horloges périphériques du foie et des fibroblastes, ainsi que l'horloge maitresse du noyau suprachiasmatique présent dans le cerveau (SCN).

Un allongement de la période a été observé dans les tissus périphériques déficients en NMD. Des analyses transcriptomiques de l'expression génique du tissu hépatique sur 24h ont révélé une stabilité accrue des transcrits *Cry2* pendant la phase d'obscurité. En plus de cet effet, l'inactivation de SMG6 était accompagnée d'une quantité élevée de protéine CRY2 présentant un retard temporel important à la fin de cette phase. Basé sur nos résultats, nous proposons un nouveau modèle adapté de l'horloge centrale selon lequel la

durée de la période circadienne serait en partie régulée par le ciblage du 3' UTR de CRY2 par le NMD.

Ainsi, mon travail a permis d'identifier de nouveaux substrats du NMD, renforçant ainsi l'importance physiologique de cette voie chez les mammifères. Enfin, en plus de ces avancées liées au rythme circadien, nous anticipons que notre nouveau modèle murin pourrait être transposée à d'autres études s'intéressant notamment à l'importance du rôle du NMD dans le cadre de diverses pathologies humaines telles que le cancer et les maladies neurologiques.

Introduction

1. The mammalian circadian system

1.1 History and basic concepts of chronobiology

Biological clocks are hereditary intrinsic rhythmic patterns in behaviour and physiology present in almost all living organisms. These biological oscillations are characterized as circadian when they have a period length between 20-30 hours, as ultradian for a period shorter of 20 hours or infradian with a > 30 hours period length [5]. In order for a biological rhythm to be characterized as circadian the following criteria must be met; (1) a period length of approximately 24 hours under free-running (constant) conditions, (2) temperature compensation (the free-running period remains largely unaltered across the physiological temperature range), (3) the rhythm adapts (entrains) to external time giving cues (*Zeitgebers*) such as light and feeding [6]. Circadian clocks pervade almost all living organisms, allowing them to anticipate environmental daily changes by regulating cellular processes, physiology and behaviour according to the 24h solar day with a great impact on fitness and survival [6].

Historically, the origins of the chronobiology field go back to antiquity and to observations of plant movements, which planted the idea of endogenous rhythmic processes in living organisms. In the 4th century BC Androstenes first described the closing of tree leaves at the dawn [7]. Centuries later Linnaeus and de Mairan further studied leaf movement and rhythmic flowering [7, 8]. Later, Zinn and Duhamel de Monceau proven that the accurate-in-time-of-the-day leaf movement in mimosa plants was independent to light-dark cycles and the ambient temperature [7]. In the 19th century AC de Candolle showed that this plant rhythmic movement corresponds to a cycle of approximately 24 hours [9]. The term circadian was at last introduced by Halberg in 1959, in order to describe biological processes with a periodicity of approximately 24h from the Latin words *circa* (= approximately) and *diem* (= day) [10, 11].

As the chronobiology field largely developed over the 20th century, animal research provided new insights and discoveries. The first genetic studies in clock mutants were performed in *Drosophila melanogaster* in the early 70s by Konopka and Benzer [12], which later led to the identification and characterisation of the first clock gene *Period* [13-17]. Michael Rosbach, Jeffrey Hall, and Michael Young, the pioneers who first studied *Period* were awarded with the Nobel Prize in Physiology or Medicine in 2017. The first mammalian mutant with altered circadian period was the short-period *tau* hamster, discovered by Menaker and Ralph in 1988 [18] and the first mammalian core clock gene, *Clock*, was identified in 1994 by Takahashi *et al.* [19]. Following these initial gene discoveries more and more clock genes have been identified, building gradually the molecular architecture of the clock.

Modern chronobiological research utilises a large variety of model organisms, spanning from cyanobacteria to fungi and plants all the way to mammalian models and human biology. Technology development has also largely impacted the development of the field allowing for high resolution images and longitudinal recordings in freely moving organisms. A critical point in mammalian chronobiology was the identification of the suprachiasmatic nucleus as the central clock in the brain [20, 21], followed by the discovery of the projections from the intrinsically photosensitive retinal ganglion cells (RGCs) to the SCN [22, 23] and the photopigment melanopsin in 2002 [24-26]. The identification and characterisation of peripheral clocks in mammals was mostly done by tissue culture experiments [27-29]. Today circadian research extends from gaining new insights at the basic circadian mechanisms to clinical research and therapeutics.

1.2 Clinical relevance of chronobiology

In this chapter the direct impact of chronobiology on human health and quality of life will be discussed. Several genes of the core clock machinery will be mentioned in terms of their clinical relevance, however the details of the molecular oscillator will be discussed later (section 1.4). Genetic polymorphisms within the core clock genes can affect the

circadian cycle, for example the preference for early morning or late evening activity, the so called diurnal preference [30]. For example, a single nucleotide polymorphism (SNP) of the *Clock* gene is associated to the owl or late chronotypes (people who typically feel most active in the late evening) [31, 32], though some studies failed to replicate this finding [33, 34].

Genetic mutations in the core clock genes can also lead to pathological conditions. Two of the officially characterized circadian rhythm and sleep disorders (CRSD) in humans, delayed sleep-wake phase syndrome and advanced sleep-wake phase syndrome, are strongly hereditary. A point mutation at a phosphorylation site of PER2 is associated with familial advanced sleep-wake phase syndrome [35]. On the other hand, length and structural polymorphisms in *hPer3* [36, 37] and a mutation in *Cry1* [38] have been identified in individuals with delayed sleep-wake phase syndrome.

Genetic polymorphisms in core clock genes have also been identified in other pathologies. As an example of such pathologies, there is a clear connection between circadian disruption and developmental diseases. Numerous mutations in core clock genes (*Rev-Erba*, *Bmal1*, *Clock*, *Per1* and *Npas2*) have been identified in children with autism [39, 40]. Similarly, animal and *in vitro* models of tuberous sclerosis complex (TSC), a neurodevelopmental disorder characterized by seizures, autistic behaviours and sleep disruptions, show circadian abnormalities, such as period shortening and impaired core body temperature regulation in constant darkness [41]. These phenotypes are caused by increased levels and abnormal subcellular localization of BMAL1 protein [41]. Changes in circadian behaviour have also been identified in patients with neurodegenerative disorders; particularly interesting is the fact that the circadian symptoms proceed the ones of the neurodegeneration and the disease diagnosis [42, 43]. Lastly, genetic polymorphisms of the core clock genes have also been linked with psychiatric diseases [44], for example genetic variants of *Cry2* are associated with bipolar disorder, depression and dysthymia [45].

In the other direction, living in harmony with the internal circadian clock is crucial for human health. Initially, the vast majority of data that indicate circadian desynchrony and health risks came from populations working in rotating shifts. The health impact is actually so profound that today there is a distinct disorder identified, namely “shift work sleep disorder” [46]. Circadian dysfunction can lead to a wide range of pathologies from cardiometabolic diseases (reviewed in [47]), to cognitive and mood problems [48]. Sleeping and eating at abnormal circadian times has been proven to lead to increased risk of hypertension [49], obesity (reviewed in [50]), cancer [51, 52] and gastrointestinal problems [53]. Extensive animal research aims to shed a light to the driving mechanisms of these correlations between the clock and diseases [54]. As an example, conditional ablation of the pancreatic clock causes diabetes mellitus in mice [55]. Closing this part from a more social perspective, circadian disruption negatively impacts social and emotional interactions, as shown from the increased rates of errors [56], accidents [57] and it even affects family stability and marital satisfaction [58].

1.3 Organisation of the mammalian circadian system

Circadian clocks are located in almost all cell types in the mammalian body. These clocks are organised in an hierarchical network of self-sustained cell-autonomous clocks that are capable of measuring time in the absence of external timing cues (reviewed in [59]). Mammalian oscillators orchestrate a large variety of cellular, physiological and behavioural processes according to the 24h solar day.

The Suprachiasmatic nucleus (SCN), as the master pacemaker

The SCN, located at the brain’s hypothalamus, is viewed as the “master clock”, lying at the top of the clock hierarchy in the mammalian body [20, 60]. The SCN is located in the anteroventral part of the hypothalamus, organized in two main nuclei that are bilaterally adjacent to the third ventricle (reviewed in [61]). Each of the nuclei is further separated into two anatomical subnuclei with distinct functions and neuronal profiles; the ventral “core” which receives light inputs directly from the retina, and the dorsal “shell” which mostly processes inputs from the core [62]. Within the ~20,000 neurons in the murine SCN

the most prominent neuropeptides are the arginine vasopressin (AVP, ~20% of all SCN cells) and the vasoactive intestinal polypeptide (VIP, ~10% of all SCN cells) [62]. These neuropeptides are colocalized in most of the SCN neurons with GABA and the majority of the synapses are indeed GABAergic [63, 64]. The glial cells of the SCN also exhibit rhythmic clock gene expression and recent studies indicate that the pacemaker function of the SCN is also (at least partially) regulated by astrocytes [65-67].

The view of the SCN as the dominant circadian pacemaker in mammals was established by lesion and transplant studies in animal models. Complete SCN lesion or genetic ablation of essential core clock genes leads to arrhythmic behaviour and physiology and this rhythm loss is restored by implantation of fetal SCN tissue [20, 60, 68, 69]. The strong neuronal coupling in the SCN and the direct connection to the retina ensures accurate synchronization with the external solar cycle, while peripheral clocks are entrained by circulating hormones, metabolic changes and other physiological signals, adapting this way to the local metabolic status according to the tissue function [16]. Thus, the SCN sets the rhythmic pace (phase coherence) for all the clocks within the mammalian body. Recent data challenge the traditional view in the circadian organization suggesting that peripheral clocks might be entrained independently to the SCN [70] and that they might even interact between them [71-73]. Shifting this way the paradigm of a top-down hierarchical network towards to a web network of body clocks oscillating in synchrony [74].

Peripheral clocks; as subsidiary clocks

Circadian oscillators are located in almost all cell types in the mammalian body, playing an important role in organ physiology and pathophysiology. Cultured cells from peripheral tissues like fibroblasts, hepatocytes [27] and pancreatic cells [75] exhibit robust rhythms in gene expression. Similarly, tissue explants from liver, lung, skeletal muscle, heart, stomach, spleen, kidney, cornea, pituitary gland and tail (skin) remain rhythmic in a culture dish for several days [28, 76, 77]. From the murine peripheral tissues that have been studied, testis and thymus seem to lack robust circadian oscillators [78], however

these results remain controversial [79]. Transcriptomic analysis on peripheral tissues indicate that numerous cellular functions are under circadian regulation [80]. The percentage of the reported rhythmic genes is estimated between 2-20% of all expressed genes, depending on the study and the tissue type [81-83]. Interestingly, only a small percentage of rhythmic genes seems to overlap between organs, suggesting that important physiological functions have to be finely tuned in time for the organ to accurately perform its biological role [84, 85].

Despite the autonomous oscillations of peripheral clocks in the absence of the SCN, the role of the SCN seems to be vital for keeping them aligned in phase, so that the whole system oscillates in synchrony to the external light-dark cycle [76]. There are several, partially redundant, indirect and direct ways, by which the SCN synchronises the peripheral clocks. Feeding and body temperature rhythms, strong time cues for several tissues, are driven by rest-activity rhythms that are regulated by the SCN. The SCN synchronises the peripheral clocks directly by hormones, such as plasma glucocorticoid hormone and by direct neuronal signals such as the projections from the SCN to the adrenal gland and the autonomic nervous system that are connected to the liver (reviewed in [74]). The peripheral clocks also respond directly to other environmental *Zeitgebers*, such as food [86] and body temperature fluctuations (although at least partially regulated by the SCN-driven rest-activity cycles) [87]. These non-photic synchronisation mechanisms of the peripheral clocks, which vary between the different tissues, are in contrast to the SCN synchronisation which only responds to light signals (reviewed in [88]). Lastly, an emerging body of literature suggests the existence of organ-to-organ crosstalk between the peripheral clocks [71-73].

1.4 Molecular composition of circadian oscillators

At the molecular level the intracellular clock consists of an extended network of interconnected transcription/translation negative feedback loops (TTFL) regulating rhythmic expression of core clock genes (Figure 1) and clock output genes [89]. The core clock architecture is similar across organisms [90] and genetic animal models lacking core

clock genes are arrhythmic or have profound differences in period length, highlighting their essential role in accurate timekeeping [91].

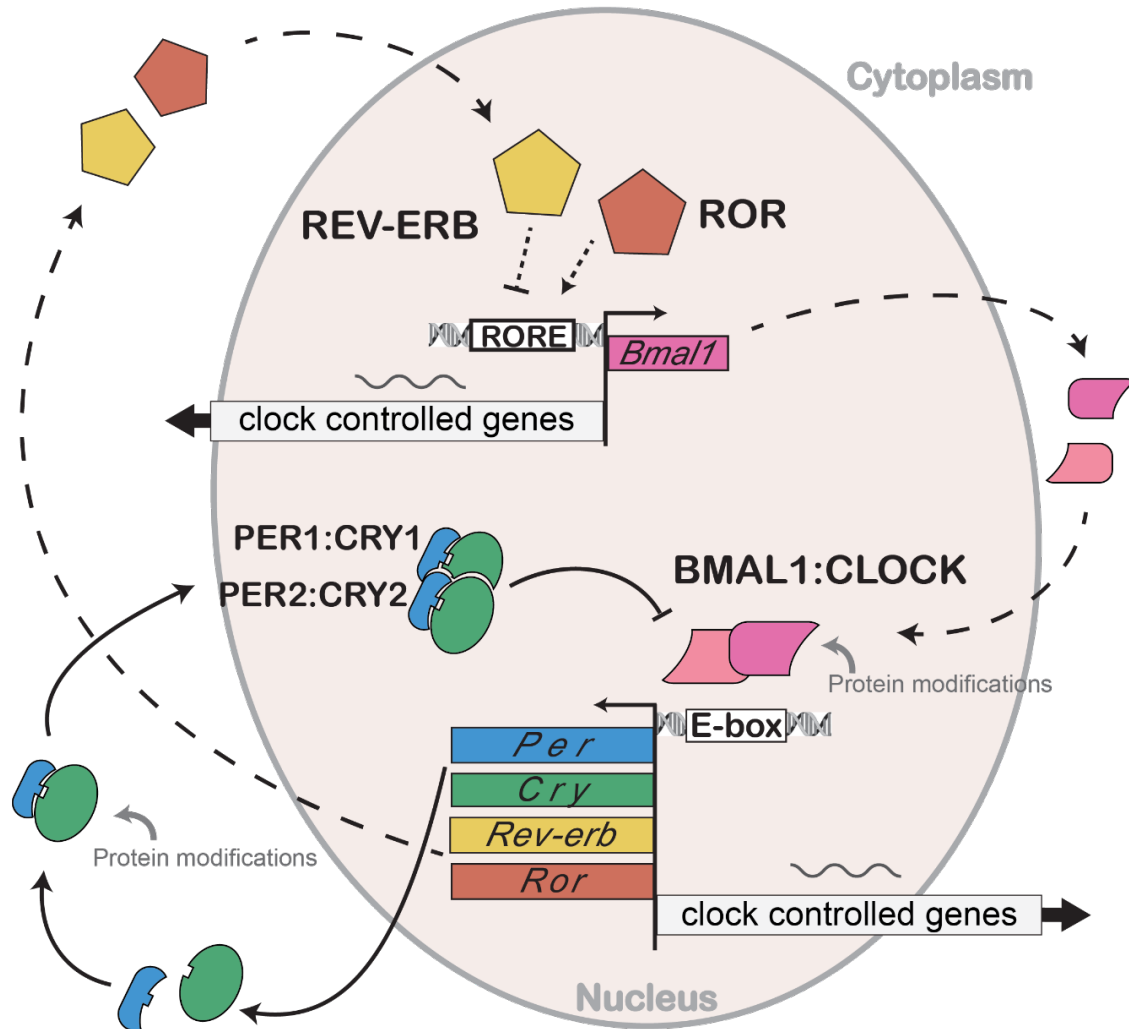


Figure 1: The mammalian core clock consists of a network of negative transcriptional feedback loops. Interconnected transcriptional feedback loops drive rhythmic expression of clock-controlled genes. In the primary loop (solid lines), BMAL1:CLOCK heterodimers activate transcription of *Per* and *Cry* genes. PER:CRY heterodimers translocate to the nucleus (beige ellipse), where they inhibit their own expression. In the secondary loop (dashed lines) *Rev-erb* and *Ror* regulate the expression levels of *Bmal1*, which activates their own transcription.

At the main loop of the mammalian clock, the transcription activators BMAL1 (Brain and Muscle ARNT-Like 1) and CLOCK (Circadian Locomotor Output Cycles Kaput) heterodimerize and bind to E-box *cis*-regulatory enhancing elements that allow transcription of the target genes, such as *Period* (*Per1*, *Per2*, *Per3*) and *Cryptochrome* (*Cry1*,

Cry2, *Cry3*) genes. The negative feedback loop is complete when PERs and CRYs form heterodimers and translocate back to the nucleus, where they inhibit CLOCK:BMAL1 activity, inhibiting this way their own expression. PER and CRY protein degradation allows again the expression of *Per* and *Cry* genes at the beginning of a new circadian cycle. In a secondary transcriptional loop, BMAL1:CLOCK heterodimers activate the transcription of the retinoic acid-related orphan nuclear receptors *Rev-erb* (α and β) and *Ror* (α , β and γ). REV-ERB and ROR translocate to the nucleus, where they compete to bind to the orphan receptor response element (RORE) on the *Bmal1* promoter. REV-ERBs inhibit *Bmal1* transcription, while RORs activate it. This autoregulatory cycle takes around 24h to complete and includes a plethora of additional transcriptional and post-translational regulatory steps (see [59] for an extensive review in the mammalian molecular clock).

Post-translational modifications further play an important role at the accurate timing of the oscillator by regulating stability of the clock proteins, protein-protein interactions and cellular localization. Phosphorylation of CLOCK is rhythmic and it inhibits its DNA binding activity [92], resulting this way in rhythmic DNA binding and thus rhythmic transcription activation [93]. Phosphorylation of PERs by Casein Kinase 1 (ϵ and δ) plays an important role in setting the clock phase by regulating the rate of protein degradation or nuclear translocation of the PER:CRY heterodimer [94, 95]. Other protein modifications that affect the speed of the clock are ubiquitination of PERs and CRYs [96, 97], acetylation and deacetylation of PER2 and BMAL1 [98, 99] and SUMOylation of BMAL1 [100]. Data from circadian studies in flies [101] and in mice [102] also report O-GlcNAcylation, a nutrient sensitive posttranslational modification, of PER proteins, BMAL1 and CLOCK. Lastly, in mammals Poly(ADP-Ribosyl)ation of CLOCK at the beginning of the light phase reduces the DNA binding activity of the heterodimer PER:CLOCK in a feeding-dependent manner [103].

The rhythmic expression of the core clock genes further drives the rhythmic transcription of hundreds of clock-controlled genes. As it was mentioned before, the expression of

rhythmic genes is different in each tissue type and its linked to the organ function. In the liver for example, the best studied peripheral clock, approximately 15% of all the expressed transcripts are expressed in a circadian manner [2, 104].

1.5 Post-transcriptional regulation of circadian gene expression

Data obtained in the past two decades indicate that a large proportion of rhythmically accumulating transcripts derive from constant transcription, pointing towards additional regulatory mechanisms at the post-transcriptional level [105, 106]. In a genome-wide study of the liver transcriptome, Koike *et al.* discovered that only 22% of the rhythmic transcripts are driven by *de novo* transcription [105]. Alternative splicing and changes in the splicing efficiency, transcript processing and degradation and translation efficiency are some of the post-transcriptional processes that contribute to circadian gene expression.

Alternative splicing

Initial data indicating that alternative splicing regulates the circadian clock came from studies in *Drosophila melanogaster*, that discovered light- and temperature-dependent alternative splice variants of *Period* [107, 108]. These transcript variations allow the fly to adjust its activity according to the seasonal variations in day length and temperature [107, 108]. Regarding the mammalian core clock genes, novel splice variants have been identified for *Cry1* in the murine SCN [109], and *Per2* in human keratinocytes [110]. However, the functions of these new isoforms remain elusive. In the mouse liver only a few rhythmic genes (~0.4 % of the detected genes) are regulated by alternative splicing in a circadian and tissue-specific manner [111]. In addition to alternative splicing a recent study proposes changes in splicing efficiency, as a mechanism that contributes to rhythmic gene expression [112]. The rhythmic expression of the Cold-inducible RNA-binding protein (CIRBP), a factor involved in phase and amplitude regulation of circadian clocks in the periphery via targeting core clock components such as *Clock* and *Rora* [113], is mediated by temperature-dependent splicing efficiency [112, 114].

Polyadenylation

Polyadenylation and deadenylation of the mRNA 3' end have important regulatory roles in transcript stability and translation efficiency. Circadian control of 3'- poly(A) tail dynamics regulates rhythmic protein expression. Kojima *et al.* at a transcriptome-wide study in the mouse liver identified hundreds of transcripts that exhibit robust circadian rhythms in the length of their poly(A) tails [115]. Rhythmicity in poly(A) tail length closely correlates with rhythmic protein expression, which indicates that circadian mRNA polyadenylation can mediate rhythmic protein expression from constant levels of mRNA [115]. The mammalian deadenylase Nocturnin (NOCT/CCRN4L) is expressed rhythmically [116] and it is proposed to be a molecular facilitator of the link between circadian clock and metabolism by targeting the metabolites NADP⁺ and NADPH [117]. However, recent data suggest that NOCT lacks the deadenylase activity [117]. Another example that highlights the role of polyadenylation in circadian timekeeping is the RNA-binding protein CIRBP that was mentioned above. CIRBP regulates translation of *Clock* [113] in response to core body temperature by controlling the alternative polyadenylation of its transcript [118].

MicroRNAs (miRNAs)

MiRNAs, small (~22nt) non-coding RNAs, regulate expression levels of 60% of all the protein-coding transcripts by modulating translation repression and transcript degradation [119]. Numerous reports prove the contribution of miRNAs in rhythmic gene expression [120]. Du *et al.* inhibited miRNA biogenesis in the liver by designing a hepatocyte-specific *Dicer* knockout mouse [121]. Whole transcriptome sequencing in the liver showed that miRNAs affect the phase and the amplitude of 30% of the detected cyclic transcripts [121]. In the same direction *Dicer*-deficient cells and mice exhibit a shortened circadian period that is regulated by augmented translation speed of PER1 and PER2 [122]. A genome-wide microRNA screening of almost a thousand of miRNAs using luciferase reporters revealed the approximately 130 miRNAs regulate circadian period in a human cell line [123]. Several miRNAs have been characterised and further studied as modulators of circadian rhythmicity in the master and peripheral clocks. For example, the

brain specific miR-219 is rhythmic in the SCN and it has been linked to the expression regulation of the BMAL1:CLOCK complex [124]. Downregulation of miR-219 in the SCN lengthens the period of locomotor activity in mice [124]. The same study has identified miR-132 as an additional regulator in photic entrainment at the murine SCN [124]. Lastly, the *Period* genes have been identified as targets of several miRNAs such as miR-24, miR-192 and miR-194 [125, 126].

mRNA decay

Time-dependent mRNA stability can potentially explain rhythmic levels in transcripts that originate from constant transcription. A study of the cyclic accumulations of pre-mRNA and mRNA in the mouse liver estimated that 20% of mRNA rhythms are driven by rhythmic mRNA degradation, and an additional 15% of rhythmic transcripts are regulated by both rhythmic transcription and rhythmic degradation [127]. Evidence of circadian regulation of mRNA decay in the mammalian clock come from the core clock genes *Per2*, *Per3* and *Cry1*. During the declining phase of the *Per2* rhythm expression, the transcript degradation is faster compared to the rising phase [128]. *Per2* transcript degradation is mediated by its 3' UTR and mediated by the heterogeneous nuclear ribonucleoprotein 1 (hnRNP I or PTB) [128]. RNAi depletion of hnRNP I in fibroblasts stabilizes *mPer2* levels [128]. Similarly, transcript stability of *mPer3* is also regulated by hnRNP proteins, K and D, through its 3' UTR [129]. The hnRNP D protein also interacts with the *mCry1* 3' UTR and mediates rhythmic transcript stability via cytoplasmic hnRNP D oscillations [130]. A role of nonsense-mediated mRNA decay (NMD) in circadian timekeeping has been proposed by studies in *Neurospora crassa* [131], *Arabidopsis thaliana* [132] and in *Drosophila melanogaster* [133]. As this thesis work focuses on the role of NMD in the mammalian clock, the links between NMD and clock genes will be described elaborately in second part of the introduction of this thesis, after explaining the key factors of the NMD pathway.

Translation efficiency

Data from whole proteome and transcriptome analysis in mammalian tissues provide evidence of rhythmic proteins arising from constant mRNA levels. A systematic analysis of the mammalian “circadian proteome” in the mouse liver revealed that approximately 20% of the studied soluble proteins are rhythmic, but only half of them come from rhythmic transcripts [134]. Further studying the liver proteome, using mass spectrometry in combination with *in vivo* Stable Isotope Labelling by Amino acids in Cell culture (SILAC), Robles *et al.* estimated that 6% of the total of 3000 detected proteins oscillate diurnally and the only 20% of these originate from rhythmic transcripts [135]. Similarly, Wang, Mauvoisin *et al.* estimated that approximately 3.4% of all detected proteins (~6000 proteins) in the mouse liver are rhythmic, the rhythmicity of about 50% of them was driven by rhythmic transcripts [136]. The differences between the two liver studies might have arisen from technical and analytical differences. In the same direction, analysis of the SCN proteome identified time-of-day-dependent protein levels in ~11% of the detected proteins [137]. Out of the 48 proteins with a circadian expression profile (~24 h period), only 9 (~18.8%) had rhythmic levels in corresponding mRNAs [137].

Studying ribosomal position with ribosome profiling (RPF-seq) together with RNA-seq around-the-clock in mouse liver, Janich *et al.* investigated the contribution of translation efficiency in protein rhythms that arise from constant transcript levels [2]. Approximately 150 genes displayed daytime-dependent translation from non-rhythmic transcripts, with a high enrichment for proteins of the translation machinery [2]. Transcription factors and genes containing Iron Regulatory Elements (IREs) and were also detected among the genes whose rhythmicity is generated at the level of protein synthesis [2]. In addition, the study identified translation of upstream Open Reading Frames (uORFs), present in several core clock genes such as *Reverba*, *Bmal1* and *Clock*, as an additional regulatory element in rhythmic gene expression [2]. Diurnal accumulation of ribosomes in mouse liver suggests diurnal changes in translation efficiency [138]. More specifically a study identified an increased proportion of ribosomes associated with large polysomes at the activity/feeding phase (~ZT16) in mouse liver which is associated with a general increase in liver mass and hepatocyte size [138].

2. Nonsense-mediated mRNA decay (NMD)

2.1 History and basic concepts of NMD

Accurate gene expression in eukaryotic cells requires multiple steps of quality control from transcription initiation to post-translational modifications. Numerous mechanisms ensure degradation of RNAs that carrying “faulty” information; such as the no-go decay pathway (transcript with “blocked” ribosomes, when translation cannot proceed), the nonstop decay pathway (transcripts without stop codons), deadenylation and decapping of mRNA followed by exonucleases and more (reviewed in [139]). Across the fidelity mechanisms our interest focuses on the nonsense-mediated mRNA decay (NMD), a well-conserved translation-dependent decay pathway that degrades transcripts containing (mostly) a premature termination codon within their open reading frames (ORFs). Besides the surveillance function of NMD, a plethora of studies reveals the pathway’s housekeeping functions in physiology and pathophysiology (see reviews [140-142]).

The first observations on NMD came almost 40 years ago from two independent studies that observed significant differences in half-life between mutated and normal transcripts [143, 144]. Specifically, Lousson and Lacroute introduced nonsense mutations (point mutations that introduce a stop codon) in different locations of the *URA3* gene in yeast and observed a reduction in transcript levels that was dependent on the mutation position, without affecting transcription rates [143]. A couple of years later, Maquat *et al.* while studying the molecular defect in patients with β^0 thalassemia, observed that the thalassemic β globin mRNA is rapidly degraded compared to the non-thalassemic that is highly stable [144]. Their findings indicated the existence of a potential mutation that activates an mRNA degradation mechanism. In 1989 Hodgkin *et al.* identified six genes with a gene expression suppressive role, mutations in which cause severe defects in the genitalia of the nematode *Caenorhabditis elegans* [145]. The authors named these loci “suppressor with morphogenetic effect on genitalia” (*Smg-1* to *-6*) and commented that “the smg suppressors affect a process other than translation, for example mRNA

processing, transport, or stability” [145]. In 1991 the first NMD factor, UPF1 was identified in yeast [146] and in 1993 the term nonsense mediated mRNA decay was introduced by Pelz *et al.* [147]. Since then, our understanding of the NMD machinery and its functions has largely improved, however numerous aspects of the pathway remain yet undiscovered.

2.2 Key NMD factors

The key factors of the mammalian NMD pathway are 3 members of the UPF (up-frameshift) protein family conserved from yeast to human, UPF1, UPF2 and UPF3, and 4 metazoan-specific members of the SMG protein family, initially identified in the nematode *Caenorhabditis elegans* [145], SMG1, SMG5, SMG6 and SMG7 (reviewed in [148]).

UPF1 is a well-conserved monomeric ATP-dependent RNA helicase essential for NMD in all eukaryotic cells, that binds single stranded RNA and DNA. UPF1 has the ability to slowly and progressively translocate on nucleic acids and to unwind extensive double-stranded structures and play an important role in NMD target selection [148, 149]. The ATPase activity of UPF1 seems to mediate the disassembly of the NMD complex from the soon-to-be-degraded transcripts [150]. Recent transcriptome-wide data revealed that UPF1 is present on both NMD-targeted and -non-targeted transcripts [151, 152], however, phosphorylated UPF1 is enriched on the 3' UTRs of NMD targets [153].

UPF2 is a ring-like protein that provides the scaffold for UPF1 and UPF3B interactions [154]. UPF2 binding to UPF1 induces large conformational changes in the later, which promotes its helicase activity [155]. UPF2 additionally interacts with SMG1, eRF3 (eukaryotic release factor 3) and ribosomal proteins, which suggests that it has an orchestrating role in NMD activation [148]. A group of NMD targets, whose degradation is independent of UPF2, was identified by Gehring *et al.* [156].

UPF3 is the least conserved member of the UPF family. In mammals there are two identified UPF3 paralogs, UPF3A and UPF3B (or UPF3X). UPF3 proteins interact with the

proteins of the exon junction complex (EJC), eIF4A3 (Eukaryotic Translation Initiation Factor 4A3), MAGOH and Y14 via a short motif in their C-terminal domain and with UPF2 via their N-terminal part, providing the molecular link between NMD and the EJC [157]. Recent data suggest that UPF3B directly interacts with eukaryotic release factors and potentially with UPF1 and the terminating ribosome [158].

The phosphatidylinositol 3-kinase related kinase **SMG1** catalyzes the phosphorylation of several positions at the N- and C-termini in UPF1 [159]. In mammals, UPF1 phosphorylation by SMG1 is an essential NMD step [160]. The UPF1-SMG1 complex is further associated with the translation termination factors eRF1 and eRF3, and together they build the so-called SURF complex [153, 161]. The interactions of the SURF complex with the EJC near to the terminating ribosome are required for the UPF1 phosphorylation by SMG1 [161]. In addition, the RNA helicase DHX34 is recruited to the SURF complex and triggers a series of molecular events that promote UPF1 phosphorylation and NMD activation [162].

SMG1 forms a complex with **SMG8** and **SMG9**, which often is collectively named as SMG1 complex [149]. The N-terminus of SMG1 serves as a scaffold for the metazoan-conserved SMG8 and SMG9 to bind to the SURF complex (UPF1-SMG1-eRF1- eRF3) [163]. Based on the current model SMG9 recruits SMG8 to the SMG1-SMG9 complex, which downregulates the kinase activity of SMG1 [163-165]. However, the event sequence [166] and the role of the SMG9-SMG8 binding to UPF1 is still unclear [167].

The proteins **SMG5** and **SMG7** form a heterodimer [168] that interacts with phosphorylated UPF1 [169], functionally required for NMD activity [170]. The SMG5-SMG7 complex directly recruits the CCR4-NOT deadenylase complex, through the interaction of SMG7 with CNOT8 [171]. SMG7 further induces DCP2-mediated decapping and mediated XRN1-exonucleolytic degradation [172]. SMG5 seems to be an important not only for the SMG5/SMG7-mediated decay branch, but also for the endonucleolysis

branch, mediated by SMG6 [173]. Recent data suggest that SMG5 have also important functions independent to SMG7 [173, 174].

SMG6 is a metazoan-specific endonuclease that acts as a monomer and seems to degrade the majority of NMD targets [175, 176]. SMG6 has a C-terminal PIN domain that contains 3 aspartic acid residues [177] that form the active nuclease domain [178, 179]. SMG6 degrades transcripts at the vicinity of the PTC [178] with a preference to a pentameric sequence motif [180]. Notably, *in vitro* assays suggest that the endonuclease activity of SMG6 requires the interaction with the phosphorylated UPF1 [169, 181].

2.3 Current working model of NMD

According to the predominant view today, UPF1 binds non-specifically to mRNA, but it is quickly removed by the translating ribosome of non-NMD targeted transcripts [148]. However, aberrant translation termination leads to phosphorylation of UPF1 by the kinase SMG1, which is currently considered as the NMD-activating step [149]. Co-precipitation analysis identified a formatted complex of hypophosphorylated UPF1, with SMG1 and the canonical translation termination factors eRF1 and eRF3 (SURF complex), which indicates that UPF1-SMG1 interaction takes place adjacent to the terminating ribosome (figure 2) [182]. The canonical ribosome recycling factor ABCE1 was also recently identified as an NMD factor [183]. The kinase activity of SMG1 is regulated by the complex of the newly identified NMD factors SMG8:SMG9, whose function is not fully understood yet [166, 184]. The predominant scenario is that SMG9 binds to the SMG1 and consequently recruits SMG8, which regulates the kinase activity of SMG1 by inducing conformational changes [164, 165]. *In vitro* studies show that SMG8 downregulates the SMG1 kinase activity [164], however, SMG8 depletion in fibroblasts reduced NMD activity and UPF1 phosphorylation [167].

Activated UPF1 forms a complex with UPF2 and UPF3, which activates the UPF1 ATPase and helicase activities [155, 157]. The interactions of UPF3B with the members of EJC, eIF4A3, MAGOH and Y14, directly link the NMD pathway with the EJC [157]. The

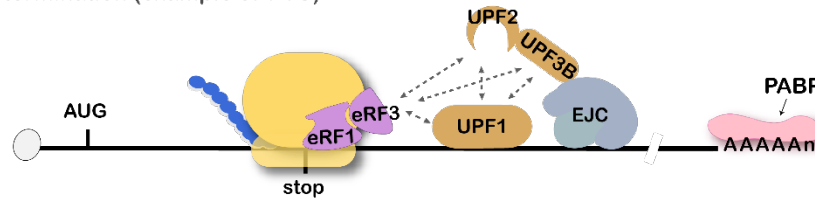
formation of the decay-inducing complex (DECID) between UPF2, UPF3B and the EJC, is induced by the RNA helicase DHX34, which promotes the recruitment of UPF2, the increase of UPF1 phosphorylation and the release of the eRF3-UPF1 interaction [162]. Of the two mammalian UPF3 paralogs, UPF3B is an important NMD activator, while UPF3A has been traditionally viewed as either a weak NMD activator through UPF2 or a weak suppressor through negative interactions with UPF3B [185-187]. However, very recent data indicate that both UPF3A and UPF3B are important and functionally redundant NMD activators in human cells [188, 189]. Of note, in mammalian cells UPF3 [190] and perhaps UPF2 [156] are not required for the degradation of all NMD substrates.

Following NMD activation the pathway employs two different, but probably intertwined, decay pathways. One is mediated by the NMD-specific endonuclease SMG6 and the other by the heterodimer SMG5-SMG7 (figure 2) that further attracts non-specific exonucleolytic mRNA decay factors [43-45]. SMG6 directly cleaves the targeted transcript at the PTC, or immediately downstream of it, via its nuclease activity in its PIN domain [178, 179]. The two generated mRNA fragments are further subjected to exonucleolytic degradation of the uncapped 3' fragment by the 5' – 3' exonuclease XRN1, and the 5' fragment by 3' – 5' decay through the exosome [191]. The alternative degradation branch is mediated by the highly stable heterodimer SMG5-SMG7 [168], which recruits the deadenylase CNOT8, member of the CCR4-NOT complex, that further triggers deadenylation-dependent decapping and XRN1-mediated decay [171, 172].

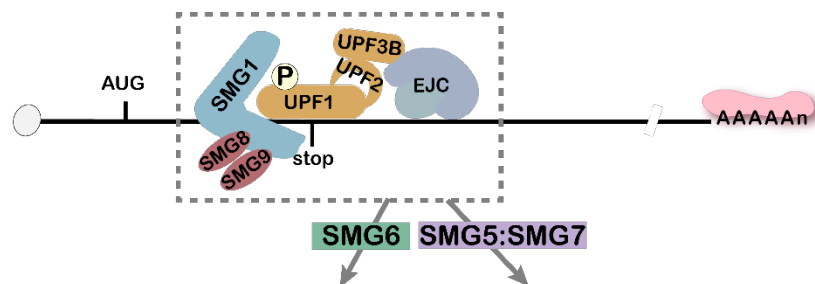
The SMG6 and SMG5-SMG7 decay branches seem to act, at least partially, redundantly, as depletion of all three decay factors inhibits NMD in a more potent way compared to each of the factors alone [192, 193]. In addition, transcriptome-wide analyses suggest that both branches target the same sets of transcripts [192]. The view of two independent NMD decay pathways, that was the traditional theory, was recently challenged by Boehm *et al.*, who reported that SMG6 activity requires the presence of the SMG5:SMG7 complex [173], indicating the existence of additional interactions between the decay branches at the last steps of the NMD reaction. In the same direction a recent study on the effect of SMG5,

SMG6 or SMG7 deficiency in embryonic stem cells suggests that SMG5 is an important regulator of both the exonucleolytic and the endonucleolytic decay branches [174].

Aberrant translation termination (example of PTC)



Activation of NMD



SMG6-mediated endonucleolytic mRNA decay



Exonucleolytic mRNA decay

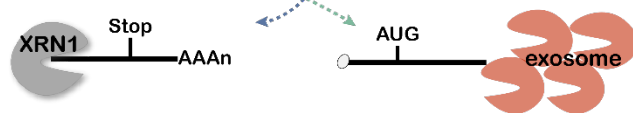


Figure 2: Representation of the main factors involved in NMD activation and target degradation.

Hypophosphorylated UPF1 residing at the mRNA is not removed by the translating ribosome due to aberrant translation termination, which activates the NMD pathway. At the initial steps of NMD activation, UPF1 interacts with UPF2 and UPF3 (UPFs shown in dark yellow), DHX34 (in grey) and the eukaryotic termination factors eRFs (in magenta). NMD activation results to the phosphorylation of UPF1 by the SMG1 (in light blue) - SMG8 - SMG9 (in red) complex. UPF1 phosphorylation promotes mRNA degradation, either directly, as in the case of endonucleolytic decay by SMG6 (in green), or indirectly, as in the case of exonucleolytic decay through the SMG5-SMG7 (in light purple) heterodimer. The SMG5-SMG7 complex recruits the CCR4-NOT (shown in beige) complex that deadenylates the transcript and further promotes DCP2-decapping. Deadenylated and decapped transcripts, as well as the fragmented transcripts that occur after the SMG6-mediated endocleavage, are further subjected to 5'-3' digestion by XRN1 (in grey) and 3'-5' digestion by the exosome (in orange). For reasons of simplicity, only the example of PTC is shown here and the proteins of EJC are not depicted.

2.4 NMD-inducing features

During quality control NMD is activated upon inefficient translation termination. Such abnormal termination can occur when there is a premature termination codon. Premature termination codons are caused by (1) point mutations in gene coding regions, (2) mutations in splice sites, (3) nucleotide deletions or insertions that cause a frameshift that creates a downstream stop codon [194] or processing errors i.e. during transcription or splicing. Several transcriptome-wide studies on NMD targets identified that the majority of targeted mRNAs encode for normal full-length proteins [192, 195], revealing the house-keeping role of NMD in eukaryotic gene expression regulation. Our ability to distinguish between direct NMD and indirect targets in such studies is somewhat limited, however they have provided new insights on predicting NMD-triggering features of normal transcripts. The composition and localization of the mRNA binding proteins at the transcript (mRNP complex) and its 3D structure further regulate the fate of an NMD-sensitive transcript [196].

Exon junction complex (EJC)

In mammalian cells the presence of a 3' exon-exon junction further than 50nt downstream of the TC, is the dominant NMD eliciting signal [148]. During splicing, large protein complexes known as EJCs are deposited at the mRNA close to the splice sites upon intron removal. EJCs are normally removed by the first translating ribosome, however, EJCs downstream of the stop codon will remain on the transcript triggering NMD [197-199]. Transcripts bearing a PTC within their ORF or an intron in their 3' UTR also belong in this category of NMD targets [148]. It is estimated that approximately 80% of the NMD-sensitive transcripts in human cells have an exon junction in their 3' UTR, and most likely a remaining EJC [196].

Despite the presence of an NMD-eliciting feature, in certain cases, a transcript might escape decay. PTCs in the last exon, as there are usually not followed by a downstream EJC, are more likely to pass by undetected and escape NMD. This phenomenon is characterized as the "last-exon rule of NMD evasion" [194]. Similarly, transcripts carrying

a PTC in the last ~50 nucleotides of the second last exon escape NMD, as the deposited EJC will be removed from the transcript due to size of the translating ribosome. To explain it simpler, if the EJC is located close to the PTC in the penultimate exon the translating ribosome will “push” the EJC and remove it from the transcript, without eliciting NMD [200]. This phenomenon is called “50nt rule of NMD evasion” [194]. Approximately 31% of the non-NMD-targeted transcripts have an exon junction at their 3' UTR [196].

Translated upstream open reading frames (uORFs) in the 5' UTR

The presence of an active uORF can potentially also trigger NMD [201], inhibiting this way the expression of the main ORF. Notably, it is estimated that approximately 35% - 50% of human and mice transcripts have a uORF [202, 203]. When a ribosome terminates translation at the uORF TC, several EJCs that remain downstream at the main ORF should in principle elicit NMD and the decay of the transcript [148]. A recent study suggests that the presence of an active uORF elicits NMD selectively in transcripts that contain no exon-exon junction in their 3' UTR [196]. Translation of a uORF is not always triggering NMD, as several transcripts with an active uORF are reported to escape NMD [201]. Another major caveat for deciphering the relationship between uORF and NMD is that not all computationally predicted uORFs are being translated and therefore do not elicit NMD [201]. Thus, it is challenging to confidently estimate the strength of an active uORF as an NMD eliciting feature [196]. Today there are no clear rules known to distinguish the NMD-targeted transcripts from all the transcripts with an actively translated uORF [148].

Long 3' UTR

Transcripts with long 3' UTRs, longer than 1kb [141], have been identified as NMD targets from several studies [175, 192, 201]. The NMD-eliciting ability of a long 3' UTR was further proven when the introduction of a 3' long UTR activates NMD in reporter assays [204, 205]. The current theory regarding the NMD sensitivity of transcripts with long 3' UTRs suggests that the poly(A) tail is physically too distant from the TC and the translating ribosome in order to properly terminate translation [148]. Eberle *et al.* showed that spatial

vicinity between the TC and the poly(A) binding protein PABPC1 determines transcript stability in reporter assays [206].

The presence of a long 3' UTR is a weak predictor of NMD degradation in human cells [207]. Accordingly, recent data suggest that the NMD sensitivity of transcripts with a long 3' UTR is due to the increased number of exon-exon junctions present and not to the increased length itself [196]. However, several studies have shown that reporter transcripts become NMD-sensitive by increasing the length of their 3' UTR [175, 208, 209]. Similarly to the NMD eliciting feature of the translating uORFs, long UTRs do not always elicit NMD [151, 201, 204]. A couple of studies have identified that the binding of the proteins hnRNP L [210] and PTB1 [211] renders protection to mRNAs with NMD-inducing features including long 3'UTRs. RNA binding proteins seem to protect NMD-sensitive transcripts via blocking the transcript accessibility to factors of the NMD machinery, however, our knowledge of how a long 3' UTR triggers or evades NMD is still fragmented.

2.5 Tissue- and gene-specific NMD activity

Theoretically, all PTC-bearing transcripts would always elicit NMD, however, genome analysis studies show that a large portion of them partially or even completely evades NMD [212]. The “ability” of a PTC-bearing transcript to escape NMD, which is called NMD evasion, results to the expression of a frameshifted and/or truncated protein with potentially deleterious effects for the cell [194]. The NMDetective model, a model that predicts genome-wide NMD efficiency in human cells, estimated that approximately 50% of all possible PTC-bearing transcript could potentially escape NMD to a certain extent [213]. This evasion ability is highly gene specific; a PTC in >75% of the coding area of certain genes (17% of the studied genes) would fully elicit NMD, while in another group of genes (36% of the studied genes) a PTC in <75% of their coding area would allow, at least partial NMD evasion [213]. NMD activity also seems to vary in a cell-type-specific manner. Tissue specificity in protein expression regulation couples NMD with alternative splicing, when a PTC-bearing exon is included in a tissue-specific transcript that results

in the silencing of this gene [214]. Lastly, cell-to-cell variability of NMD activity has been shown to correlate with SMG1 protein levels in a recent study using a dual-fluorescence NMD reporter quantified by flow cytometry in different cellular populations [215].

2.6 Physiological roles of NMD

Transcriptome-wide analyses identified several protein coding transcripts among the NMD targets, which are estimated to account for approximately 10% of the normal transcriptome [192, 216]. Several of these transcripts, the so-called natural NMD substrates, have been further identified and studied, revealing regulatory roles of NMD, beyond quality control. Some of these roles are briefly described below.

Stress Adaptation

Cellular stressors such as hypoxia, amino acid deprivation and reactive oxygen species (ROS) activate the integrated stress response (ISR), which results in a general reduction of NMD activity via phosphorylation of the eukaryotic initiation factor 2 (subunit eIF2 α). Three important ISR-regulated factors, ATF3 and ATF4 (activating transcription factor) and DDIT3 (DNA Damage Inducible Transcript 3) are NMD substrates (reviewed in [141]), elucidating the role of NMD in the ISR. Under normal conditions NMD keeps their expression levels low, however, upon cellular stress the activity of NMD is reduced and the levels of ATF3, ATF4 and DDIT3 are increased in order to regulate downstream stress response regulatory events [217].

During amino acid starvation reduction of NMD activity promotes the expression of genes that regulate amino acid homeostasis and autophagy [218, 219]. A similar mechanism has been described in response to endoplasmic reticulum stress, which is activated by increased protein folding demands [141]. Initiation of the unfolded protein response (UPR) leads to the eIF2 α -mediated reduction of NMD activity and the stabilization, among other regulatory genes, of the transcript of *Ire1a* through its long 3' UTR. IRE1a, a protein that regulates the abundance of chaperone proteins, together with

other NMD substrates of the UPR machinery, coordinates the stress response until the balance in protein folding demands is restored and NMD becomes active again [141]. Recent data based on a genome-wide CRISPR-Cas9 screening for NMD factors identified ABCE1 as an NMD factor and provided further evidence that oxidative stress, as well as iron deficiency, inhibit NMD [183].

Development and cell differentiation

Knockout of core NMD factors, UPF1 [220], UPF2 [221], SMG1 [222] or SMG6 [223] are embryonic lethal in mice, indicating the essential role of NMD in organism development. *Smg6* knockout embryonic stem cells are viable, but unable to differentiate *in vitro* and *in vivo* [223]. This differentiation inability seems to be mediated by the high levels of the NMD substrate *Myc*, which promotes stemness in embryonic stem cells [223]. These defects were also observed upon ablation of *Upf1*, *Upf2*, *Smg1* or *Smg5* [223], highlighting the role of NMD in mammalian development. In the same direction, NMD has a role in human stem cell differentiation. The differentiation of the endoderm layer is accompanied by a strong downregulation in NMD factors, and UPF1 overexpression induces endodermic defects [224]. NMD also regulates proper hematopoiesis in mice, as conditional loss of UPF2 in the hematopoietic compartment led to the cellular death of all stem and progenitor cells, an effect that was reduced in mature cells [221]. Lastly, NMD and specifically a noncanonical UPF2-mediated branch of NMD plays an important role in spermatogenesis by selective elimination of transcripts with long 3' UTRs in male germ cells [225].

Several studies have also identified the important role of NMD in developing and differentiated neurons. For example, in zebrafish embryos downregulation of any of UPF1, UPF2, SMG5 or SMG6 factors caused severe defects in the central nervous system, eye development and brain patterning [226]. In mammals, imaging of the prefrontal cortex of *Upf3b*-null mice revealed a reduction in mature dendritic spines which was accompanied by abnormal sensorimotor gating (defects in prepulse inhibition) and poor differentiation of *Upf3b*-null neural progenitors [227]. RNA-sequencing in the frontal

cortex of these mice revealed as novel NMD targets several genes involved in processes of neuronal differentiation and maturation, such as axon growth, synaptic formation, and retinal neural cell connectivity [227]. Neurophysiological and behavioural defects have also been reported in mice lacking *Upf2* in the forebrain [228]. Specifically, NMD disruption in the forebrain resulted in memory impairment, social and vocal deficits and abnormal long-term potentiation (LTP), accompanied by increased immune response and brain inflammation [228].

Circadian clock

It is well established that for the circadian core clock to function properly, its transcripts should have a short half-life that will allow the accurate turnover during the circadian day. Thus, it is potentially possible that core clock genes might be, yet unidentified, NMD targets. Studies from non-mammalian model organisms have provided some initial links between the NMD pathway and circadian regulation. Genetic studies in filamentous fungus *Neurospora crassa* reported that mutations in *Upf1* shorten the periodicity of the fungal growth rhythm [131]. NMD seems to play a regulatory role in the expression levels of the core clock gene *frequency*, the transcription inhibitor of the fungal molecular clock [131]. In *Arabidopsis thaliana* splice variants of core clock genes are regulated by NMD [132]. In addition, a recent study in *Drosophila melanogaster* reports that knocking down of NMD factors leads to behavioral arrhythmicity in flies, while overexpression disrupts rhythmicity [133]. Despite the potential regulatory connections between the clock and NMD, the evidence of the role of NMD in the mammalian clock still remains elusive.

2.7 Clinical relevance of NMD

NMD has an important role in development and physiology, which is further highlighted by the significant functions of several genes coding NMD substrates. As a pathway with multiple important biological roles, mutations in core NMD factors or other related proteins (such as mutations in EJC genes [140]) are implicated in human diseases. Of note, approximately ~11% of all known gene lesions causing hereditary human diseases are

estimated to originate from nonsense mutations [212]. Here, I list selected examples of human pathologies with genetic links to NMD.

B⁰ Thalassemia

A study on the stability of the human β -globin transcripts of thalassemic patients was one of the first studies that implied the existence of a quality control mRNA-decay pathway [144]. Since then, several studies have been conducted on β -globin mutant transcripts in order to decipher NMD mechanisms and gain further insights into the disease pathogenesis [199, 229]. Beta thalassemia is an inherited blood disorder characterised by abnormalities in protein synthesis of β -globin, a component of hemoglobin, in red blood cells [230]. In heterozygote carriers of a nonsense-mutated β -globin (or HBB) the NMD pathway eliminates the faulty transcripts and prevents the production of the deleterious truncated protein, which would lead to the development of symptomatic β -thalassemia [229]. However, nonsense mutations, in contrast to the expectations, often bypass NMD and the dominant-negative protein is expressed [231], resulting in severe forms of thalassemia. Surprisingly, most nonsense mutations that evade NMD in β -globin are located in the first exon [229], which is in contrast to the classical NMD activation theory [232]. Neu-Yilik *et al.* resolved this mystery by showing that translation reinitiation downstream to the PTC allows the transcript to escape NMD to be partially translated [229].

Cancer

Nonsense mutations are particularly common in cancerous cells, highlighting the importance of the NMD pathways at the disease development. A comprehensive analysis of the exome and transcriptome of thousands of human tumours estimated a mean of one nonsense mutation per patient, while there were patients with tumours carrying more than ten nonsense mutations [233]. NMD has a complex and yet not fully understood role in cancer development. The majority of data obtained from several cancer types indicate cancer-promoting NMD activity, as tumors utilise both functions of NMD, quality-control and abundance regulation of physiological transcripts [234]. Quality control selectively

eliminates the expression of mutated tumour suppressor genes, leading to a complete loss of truncated, but potentially partially active anti-cancer proteins (reviewed in [194]). In this case, NMD activity has a disease-promoting role, in contrast to the mechanism seen in β Thalassemia, which is protecting heterozygote carriers from a toxic truncated β -globin. Similarly, the multitude of mutations found in cancer cells would lead to the expression of cancer-specific neoantigens and the elimination of the tumour by the immune system, if NMD would not degrade these transcripts [235]. In addition, NMD is further utilized by tumours in order to selectively alter the expression levels of endogenous substrates that promote environmental adaptation [236]. At the antipode, NMD might have an anticancer role in certain cancers, as mutations in the NMD machinery, as reduced NMD activity is detected in certain types of pancreatic [237] and lung [238] cancer. Thus, when designing novel anticancer therapeutic approaches targeting NMD, it is important to first fully understand if the pathway exacerbates or ameliorates each cancer type.

Amyotrophic lateral sclerosis (ALS)

Given the important role of NMD in neuronal maturation and proper functioning, it is not surprising that abnormal NMD activity may contribute to the pathogenesis of neurodegenerative diseases. The vast majority of studies on NMD and neurodegeneration focus on pathogenetic mechanisms of ALS, a progressive neurodegenerative disease that affects motor neurons [239] and is characterized by intracellular protein inclusions, for example aggregations of the RNA proteins TDP-43 [240] and FUS [241]. The potential link between neurotoxicity and NMD was first suggested in a yeast ALS model [241, 242]. While screening of known yeast genes for suppressing cellular toxicity the researchers noticed that the overexpression of EMC32, an RNA helicase related to human UPF1, reduced FUS-mediated cytotoxicity and cytoplasmic protein aggregations, both hallmarks of ALS [241, 242]. Reduction in toxicity was also observed with overexpression of the human NMD factors UPF1, UPF2 and UPF3B, in these cells [242]. Primary rodent neurons, at an *in vitro* ALS model based on the *Tdp-43* gene (or *Tardbp*), displayed improved survival upon overexpression of human UPF1 and/or UPF2, an effect which was reversed

by pharmacological inhibition of NMD [243]. These findings were further validated by an *in vivo* rodent model of ALS that is based on TDP-43-induced paralysis [244]. Expression of the human UPF1 using an adeno-associated virus (AAV) in affected rats improved motor impairments at several levels (motor coordination, grip strength and more) [244]. Closing, solid evidence exists regarding the beneficial results of UPF1 gene therapy in ALS models, however the exact mechanism that links NMD and the RNA-binding proteins FUS and TDP-43 remains unclear hitherto.

X-linked mental retardation

Systematic sequencing of approximately 700 genes in 250 families with X-linked mental retardation identified several mutations in the *Upf3b* gene [245]. Three mutations were detected that theoretically would lead to truncated protein product; two caused by a deletion of 2 or 4 nucleotides that causes translational frameshift and a nonsense point mutation [245]. However, no normal or truncated UPF3B was detected in lymphoblastoid cell lysates from affected individuals. As these three mutations introduce a termination codon prematurely to UPF3B mRNA, NMD is expected to act and degrade these transcripts. Despite the absence of a functional UPF3B protein, NMD remains active and targets PTC-bearing *Upf3b* transcripts without affecting the protein levels of UPF3A. Taken together Tarpey *et al.* highlighted that UPF3B is an important but not essential NMD factor and provided evidence for a causal relation between NMD abnormalities and human disease [245]. These findings are in accordance with observations coming from a *Upf3b*-mutant mouse model, which shows severe defects in animal behaviour and neurogenesis [227].

Study objectives

We aimed to design a new mouse model that selectively targets NMD functions without affecting the “collateral” roles that many of the NMD factors have been reported to play. Our novel mouse model – created according to our design idea by a commercial supplier, Taconic Biosciences – introduces two point mutations in the catalytic triad of the PIN domain of the endonuclease SMG6. Thus, we expect that NMD substrates will not be degraded anymore (or at least less efficiently, if 5’ or 3’ nuclease activities partially compensate), making them readily detectable. We opted for this particular design rather than a full knockout because a previous study on murine embryonic stem cells reported that deletion of the SMG6 PIN domain inactivates NMD without affecting the role of the protein in telomere maintenance [223]. Moreover, given the embryonic lethality observed in mice lacking NMD constitutively, and aiming to bypass potential developmental effects of NMD deficiency, we built our model based on the Cre/lox system that allows time- and tissue-specific NMD inactivation.

The main study objectives were:

- Establishment of a new *Smg6^{fllox}* mouse line and its further crossing with a tamoxifen-activatable hepatocyte-specific *Cre* and the circadian reporter *mPer2::Luc* (genotype according to official nomenclature: *Smg6^{tm5498(D1352A,D1391A)Tac}* ; *Alb^{tm1(Cre/ERT2)Mtz}* ; *Per2^{tm1Jt}*).
- Establishment of an NMD cellular model based on immortalized *Smg6^{fllox}* fibroblasts carrying a tamoxifen-activatable *Cre* for reporter assays. Initial validation of successful NMD deficiency with RNA-seq in *Smg6^{mut}* fibroblasts.
- Evaluation of the effect of NMD deficiency in mouse liver. My aim was to evaluate isolated (free-running) liver rhythms (tissue explants) and hepatic circadian rhythmicity in the living mouse (entrained liver) with an intact circadian network (*in vivo* RT-Biolumicorder experiments).
- Evaluation of the effect of NMD deficiency in the mouse master clock (SCN). For this set of experiments I decided to stereotactically inject a *Cre*-expressing adeno-

associated virus (AAV) directly into the SCN of *Smg6^{flox} mPer2::Luc^{ki}* mice and to evaluate (1) the isolated SCN rhythms (tissue explants) and (2) rhythms in voluntary locomotor activity *in vivo* (running wheel assays)

- Analysis of known and new NMD substrates and their features, and transcriptome-wide analysis of rhythmic gene expression in the *Smg6^{mut}* liver (liver RNA-seq around-the-clock); the time series of liver samples would further be used for metabolomics and lipidomics characterisation of *Smg6^{mut}* liver tissue around the clock.
- Investigation of potential core clock genes (or other genes that impact circadian rhythmicity) found within the newly identified NMD substrates and the characterisation of their NMD-eliciting features and potential mechanism(s) underlying a prospective circadian phenotype that I hoped to observe in the functional assays described above.

Given the suggested links between circadian rhythmicity and the NMD pathway that have been reported in fungi [132], plants [132] and flies [133], and based on the concept that transcripts encoding the components of the molecular oscillator need to be comparably unstable in order to show rhythmicity, it was my hypothesis that members of the core clock genes may indeed represent novel NMD substrates, previously overlooked. Moreover, previous observations from the lab indicated that several clock genes, like *Bmal1*, *Clock* and *Cry1*, have actively translated uORFs in the mouse liver [2], or unusually long 3' UTRs (e.g. *Clock*, *Per2* and *Cry2*); both are well-characterised NMD-eliciting features [141].

Out of my PhD work several months were invested in obtaining the desired genetic combination of our experimental mice (*Smg6^{flox} ; Alb^{Cre-ERT2} ; mPer2::Luc^{ki}*), and in the successful spontaneous immortalization of the *Smg6^{flox}* fibroblasts and their subsequent retroviral or lentiviral transduction with *Cre* and circadian reporters and selection of single cell clones. Briefly, an intriguing phenotype (period lengthening) was observed at the level of *Smg6^{mut}* fibroblasts and liver tissue *ex vivo*, yet the SCN

clock was resilient to NMD loss-of-function. *In vivo*, the liver period phenotype was largely masked due to the entrainment of the liver clock by the wild-type SCN clock. Still, various clock components showed phase differences in the transcriptional oscillations in liver *in vivo*. The potential reasons for these differences between tissues and *ex vivo* vs. *in vivo* are explained in the discussion of our submitted work, as well as in the discussion section of this thesis. Transcriptome-wide analysis of *Smg6^{mut}* liver tissue around-the-clock revealed several interesting findings that are described at the attached article and identified *Cry2*, a core clock gene, as a novel NMD target, which was validated by a panel of bioluminescence-based reporter experiments and western blot analyses.

Currently my final experiments focus on elucidating the exact mechanism that creates the observed period lengthening in the absence of NMD and to understand whether the absence of a circadian phenotype in the SCN is indeed attributable to a different molecular organisation of the master clock and/or the NMD pathway in the brain, or possibly to technical limitations regarding the efficient induction of recombination in SCN neurons. Lastly, several aspects of the computational analysis of our transcriptome-wide data, as well as the complete metabolic characterisation of the *Smg6^{mut}* liver, are still ongoing.

Brief summary of the results

1. A novel *Smg6* mouse model reveals regulation of circadian period and daily CRY2 accumulation through the nonsense mediated mRNA decay

G. Katsioudi, R. Dreos, E. S. Arpa, S. Gaspari, A. Liechti, M. Sato, C. H. Gabriel,
A. Kramer, S. A. Brown & D. Gatfield
(submitted)

The majority of the work carried out during my PhD is included as this manuscript (from now on Katsioudi *et al.*, 2022) that we are in the process of submitting, in parallel to this thesis submission. The project is highly collaborative and assesses the role of NMD in the mammalian circadian clock. Data from the peripheral oscillators of fibroblasts and the liver are presented as the main body of the article, while the data focusing on the central clock in the brain's SCN, where we detected no changes in gene expression or behavioral levels, are currently in the supplementary material of the article. Additional data coming from ongoing analyses and experiments are expected to be included in the final manuscript.

Summary

In Katsioudi *et al.*, 2022 we studied the potential role of NMD in circadian timekeeping in mammals. We based our hypothesis on findings showing that NMD, beyond its quality control function, regulates transcript stability (and, thus, abundance) of vital physiological processes that require rapid and well-controlled RNA turnover. Studies in fungi, plants and flies [131-133] have implicated NMD in the regulation of the circadian clock, an important functional system that regulates rhythms in physiology, metabolism and behaviour [80]. However, there are no data connecting these two important pathways in mammals.

To ablate NMD *in vivo* we designed a new conditional NMD loss-of-function mouse model. The *Smg6^{flox}* allele, that encodes a wild-type SMG6 protein, conditionally recombines to the *Smg6^{mut}* allele, which expresses a point-mutated allele in which two

aspartic acids of the catalytic triad of the SMG6 PIN nuclease domain are changed to alanines. The mutated SMG6 is expected to possess no active nuclease activity, thus silencing the effector step of NMD in the living animal. We chose this approach over a whole gene knockout in order to avoid affecting additional roles of NMD factors, including SMG6, in telomere maintenance and genome stability [223, 246]. In addition, NMD inactivation in adult tissues bypasses the effects of NMD deficiency during organism development [226, 239, 247], which would potentially confound a specific circadian phenotype.

The genetic model was first validated in isolated fibroblasts from *Smg6^{flox/flox}* and *Smg6^{wt/wt}* adult male littermate mice. Cultured fibroblasts were stably transduced with a retroviral vector expressing a tamoxifen-activatable CreERT2 and I validated that upon 4-hydroxytamoxifen (4-OHT) treatment *Smg6^{flox/flox}* cells could be recombined to *Smg6^{mut/mut}*. Subsequently, the cells were lentivirally transduced with a luciferase reporter carrying an intron located within its 3' UTR. As expected, based on the current model of NMD, the intronic reporter was significantly upregulated under *Smg6* mutant conditions compared to various controls (*Smg6^{flox/flox}* cells with vehicle, *Smg6^{wt/wt}* with vehicle or 4-OHT). In accordance, RNA-seq on vehicle- or 4-OHT-treated cells revealed an upregulation of genes with NMD-annotated mRNA isoforms and with retained introns; validating our NMD loss-of-function model. Hundreds of protein coding genes, without an NMD-annotated isoform, were also upregulated in the NMD-deficient cells, pointing towards to the identification of new *bona fide* NMD substrates.

Smg6 CreERT2 fibroblasts were further transduced with the circadian reporter gene *Dbp-Luciferase* [248]. Following synchronisation of the cellular oscillators with temperature cycles [249], real time bioluminescence signal was recorded for several days under constant conditions. NMD-deficient fibroblasts had significantly longer periods of approximately 1.5 hours, a very interesting phenotype that we moved on to study at the liver, which more closely resembles the *in vivo* situation. To do so, I crossed the *Smg6^{flox}*

mouse line with a hepatocyte-specific CreERT2 (driven from the *Albumin* locus [250]) and the knock-in allele of the circadian reporter *mPer2::Luc* [76].

Four weeks following intraperitoneal tamoxifen injection, allowing for CreERT2 activation and efficient recombination, *Smg6* mutant and wild-type littermate mice were sacrificed and liver tissue, as well as kidney tissue as control, were excised. Tissue explants were cultured for several days allowing for longitudinal recording of *mPer2::Luc* expression rhythms. Real-time bioluminescence recording revealed a significantly prolonged period length of approximately 3 hours in hepatocyte-specific *Smg6^{mut}* organotypic liver cultures compared to control. Importantly, no differences in circadian rhythmicity were detected between the kidney explants from the same mice, as expected given the hepatocyte-specific expression of CreERT2.

Next, to assess liver clock oscillations *in vivo*, we used the RT-Biolumicorder apparatus [3], that allows for real-time longitudinal bioluminescence recording in freely moving mice implanted with a mini osmotic pump for constant luciferin supply. The same *Smg6^{flox/flox}* or *Smg6^{wt/wt}* (both with *AlbCreERT2^{ki} mPer2::Luc^{ki}*) mice were used; thus, in this model the *Smg6* mutant mice had an NMD-deficient liver but a wild-type SCN. Given the strong period lengthening that was observed in the free-running *Smg6^{mut}* liver, a difference in phase angle was expected under the constant entrainment of the master clock [251, 252]. However, no differences in mPER2::LUC phase were detected in the liver oscillations of the living mouse under light entrainment (skeleton photoperiod resembling an LD12:12 cycle) and *ad libitum* feeding.

To assess in depth the change of rhythmic gene expression *in vivo*, we collected *Smg6* mutant and wild-type liver tissue of LD12:12 light-entrained mice with free access to food at 4h intervals for 24h hours. Three individual mice were sacrificed per genotype at *Zeitgeber* Time (ZT) 0 ("lights on"), ZT4, ZT8, ZT12 ("lights off"), ZT16 and ZT20. RNA-seq around-the-clock provided us with insights into the diurnal liver transcriptome under control conditions or in the absence of NMD. A quality control analysis, similar to the

evaluation done in the fibroblasts, was performed for the efficacy of the NMD silencing in the *Smg6* mutant livers. Upregulation of mRNA levels of known NMD targets, such as members of the NMD machinery [204], further validated the successful downregulation of the NMD pathway.

Complete analysis of the pre-mRNA and mRNA rhythms of the core clock genes revealed transcriptional (pre-mRNA) phase differences in several genes; however, only few of them had differences at the mRNA level. In line with the *in vivo* RT-Biolumicorder experiments *mPer2* showed no phase difference in the NMD-deficient livers. The mRNA of the transcriptional repressor *Cry2*, the core loop component that displayed the strongest phase difference in the absence of NMD, had a delay of approximately 2 hours. The mRNA levels of *Cry2* normally peak around ZT8 -ZT12 and then decrease gradually, however, in NMD-deficient tissue *Cry2* levels remained high until ZT20. This prolonged plateau of *Cry2* does not originate from changes in transcription, but at post-transcriptional level, plausibly from an increase in transcript stability, suggesting that *Cry2* could be a direct NMD target.

Accordingly CRY2 protein reaches its maximum expression approximately 4 hours later in NMD-deficient tissue compared to control. In addition, *Smg6* mutant fibroblasts have generally elevated levels of CRY2, suggesting the NMD might directly regulate *Cry2*. The *Cry2* transcript has a rather simple architecture; its 5' UTR is very short, excluding the presence of an NMD-eliciting uORF, but it has a very long 3' UTR of approximately 2.2 kb, which could indeed represent the NMD-eliciting feature. Dual luciferase assay of cells that were stably transduced with a luciferase reporter carrying the *Cry2* 3' UTR, revealed a strong upregulation of the *Cry2* reporter compared to the vector-UTR expressing reporter, suggesting that NMD acts on the *Cry2* 3' UTR.

Lastly, to independently validate our findings from the *Smg6* genetic model, I used a pharmacological NMD inhibitor, which targets the kinase SMG1 (hSMG1-inhibitor 11e [253]). I recorded bioluminescence rhythms in our circadian model cell line, murine

NIH/3t3 fibroblasts stably transduced with the circadian reporter *Dbp-Luciferase*, in the presence of the SMG1 inhibitor or of the vehicle. In line with the *Smg6* mutant fibroblast data, the period length of the cells cultured with the NMD inhibitor was almost 4 hours longer than the cells treated with vehicle. To assess whether the *Cry2* 3' UTR elicits NMD in a specific fashion, I lentivirally transduced luciferase reporters carrying the 3' UTR of *Cry2* or of other core clock genes (*Per1*, *Per2*) with similar 3' UTR lengths, to *Smg6* mutant or wild-type fibroblasts. The expression levels of the full length *Cry2* 3' UTR were selectively and rapidly upregulated upon the addition of the SMG1 inhibitor in contrast to the other clock genes. Finally, I assessed whether the NMD effect was based on the length of the 3' UTR or on specific *cis*-elements contained in the UTR, I assayed reporters carrying fragments of the *Cry2* 3' UTR. Only the full-length 3' UTR was regulated by NMD, indicating that length was the critical determinant.

Taken together, our findings suggest that the core clock gene *Cry2* is directly targeted by NMD via its long 3' UTR and that NMD inhibition prolongs circadian period in peripheral clocks. We provide correlative evidence that NMD-mediated degradation of *Cry2* potentially tunes temporal gene expression and maintains the circadian periodicity of mammalian tissues (figure 3) at approximately 24h. Using a novel genetic NMD model we discovered a new, previously unidentified NMD target and a regulatory role of the NMD pathway in the mammalian circadian clock.

Study contributions

The study was designed by David Gatfield and me. The design of the transgenic mouse was done prior to my arrival in the lab by David Gatfield, and its generation was carried out by the commercial supplier, Taconic Biosciences. I performed all the crossings for obtaining the *Smg6^{flox} AlbCreERT2^{ki} mPer2::Luc^{ki}* mice, including all the procedures for the maintenance of the line. I also wrote most of the animal licences for the experiments and was involved in communication with the cantonal authorities to get the experiments approved. I performed the dissection, culture, viral production and transduction, pharmacological treatments of all the experiments using fibroblasts, including all the

reporter recordings and the dual luciferase assays. For the selection, culture and screening of single cell clones I was helped by David Gatfield. I performed all the tamoxifen injections for the liver experiments, the tissue dissection for the organotypic cultures and all the RT-Bioluminescence experiments, including the pump implantations. Tissue harvesting around-the-clock was done with the help of Angelica Liechti, who also prepared the RNA libraries of the project. All the analyses of the RNA-seq data was carried out by René Dreos and all the western blots by Enes S. Arpa. Stereotactic injections at the SCN were performed by Sevasti Gaspari and myself, and the culture of the SCN slices was carried out by Miho Sato and myself, in the lab of Steven Brown, University of Zurich. Analysis of the SCN rhythms was also performed by Miho Sato. All bioluminescence experiments using the pharmacological NMD inhibitors were also conducted by me. Compilation of manuscript figures and redaction of the manuscript text was by myself and David Gatfield, with the contribution of the co-authors. The SMG1 inhibitor was kindly provided by the lab of Oliver Mühlemann, University of Bern; apart from the intron-containing reporter that I cloned myself, most 3' UTR reporters were constructed previously in the lab [121].

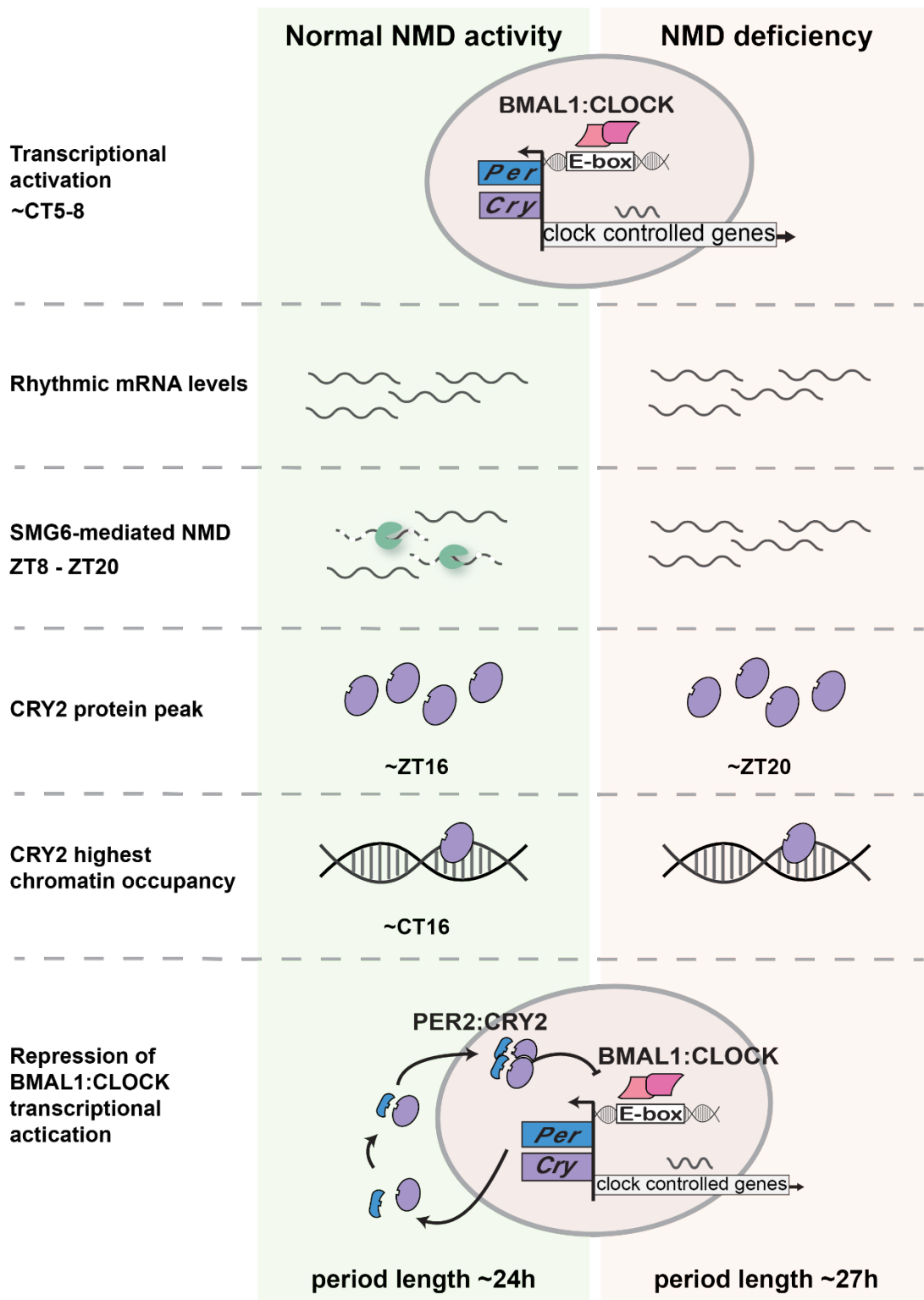


Figure 3: Proposed model. We propose that NMD actively mediates the mammalian circadian clock in peripheral tissues by regulating the mRNA levels of the transcription repressor *Cry2*. We speculate that the increased levels of *Cry2* during the dark phase and the delayed CRY2 peak (ZT20 instead of ZT16) in the absence of NMD, delay the CRY2 binding to its targets slowing down the oscillation rate (theory based on our data, previous animal studies [254] and chromatin occupancy analysis [105], see the “Discussion” for more details). The time estimates expressed in CT (circadian time) originate from [105], while the ones in ZT (zeitgeber time) originate from our *Smg6* mutant liver data.

2. Recording of diurnal gene expression in peripheral organs of mice using the RT-Biolumicorder

G. Katsioudi, A. Osorio-Forero, F. Sinturel, C. Hagedorn, F. Kreppel, U. Schibler
& D. Gatfield

Circadian Regulation; Methods and Protocols

Methods in Molecular Biology, Humana New York, Springer

This publication is a dedicated methods article that provides a detailed protocol for the *in vivo* recording of luciferase reporter rhythms in mice using the RT-Biolumicorder (a device originally developed by the group of Ueli Schibler at the University of Geneva [3]). Within this publication I also included example data from my work on the relationship between feeding and gene expression rhythms of ribosomal protein-encoding mRNAs, as well as a new software that we created for analysis and visualization of the RT-Biolumicorder data. Our publication, which is included as a chapter in the book “Circadian Regulation” from the “Methods in Molecular Biology” series, Springer publications, provides a detailed protocol for the use of the apparatus and all the relevant parameters, an extensive list of potential technical problems and their solutions. The preparation and submission of the manuscript was done at the beginning of 2021, therefore from now on I will refer to it as Katsioudi *et al.*, 2021. However, the book just recently became available for purchase and the chapter information can be found online [4].

Summary

The RT-Biolumicorder allows for real-time bioluminescence recording of peripheral circadian oscillations in freely moving mice. It is particularly used for the study of large organs such as the liver, or whole body oscillations. It provides information of reporter expression levels in number or photons per minute, as well as activity data per minute. The delivery of the circadian reporter gene can be done either genetically, like the

mPer2::Luc knock-in allele [76], or via adenoviral vectors. Luciferin, the substrate for the luciferase reporters, can be administered by drinking water or by implantation of a mini osmotic pump. One animal can be recorded in each RT-Biolumicorder apparatus and the recording can last from a few days to several weeks, according to the luciferin administration method (pumps have a maximum duration of 14 days), the legal animal experimentation framework, and the research question. During the recording the animals can be kept in constant darkness (free-running SCN) or in “skeleton photoperiod”, which describes short pulses of light exposure sufficient for light entrainment of the SCN; typically, a skeleton photoperiod consists of two 30 min light pulses applied at times corresponding to the beginning and to the end of the light phase in a 12h-light-12h-dark (LD12:12) cycle.

For the RT-Biolumicorder experiments, including for the *Smg6* project and also for another project on which I spent significant time of my thesis and that was dedicated to analyzing the rhythmic translation of mRNAs from iron-metabolic genes (project not presented in this thesis document, because the project was set aside during the pandemic and when the NMD project turned out more productive), we designed a custom-made MATLAB-based application, which allows for easy loading, analysis and visualization of the RT-Biolumicorder data from individual animals or experimental groups. Food availability and illumination are also available for display. The application, which we named “Osiris”, is publicly available at <https://github.com/aosorioforero>.

Study contributions

In the Gatfield lab, I set up the RT-Biolumicorder method, including many optimisation steps; this information I contributed to this methods manuscript. Regarding specific data presented in the manuscript, I performed the RT-Biolumicorder experiments with the altered feeding schedules presented in the chapter (Katsioudi *et al.*, 2021, figure 4), including the tail vein injections and the pump implantations. The main body of the text was written by me with the input of David

Gatfield. The design of the software used for the data analysis was done by Alejandro Osorio-Forero, who also wrote the relevant text and uploaded the scripts, and by myself. Claudia Hagedorn and Florian Kreppel wrote the part regarding the preparation of the adenoviral vectors, that were used for the example data. Flore Sinturel wrote about the luciferin delivery via drinking water and Ueli Schibler made general comments and corrections at the manuscript.

3. The sleep-wake distribution contributes to the peripheral rhythms in PERIOD-2

M.M.B. Hoekstra, M. Jan, G. Katsioudi, Y. Emmenegger & P. Franken

Elife, 2021

This publication was part of the PhD work of Marieke Hoekstra in the lab of Paul Franken, University of Lausanne. I contributed to this work by performing several experiments for which I had previously optimised the methodology within my own PhD project.

Summary

In brief, Hoekstra, Jan *et al.*, 2021 studied the influence of sleep-wake cycles on the expression levels of the core clock gene *Per2* in the SCN and in peripheral tissues. Using simultaneous recording of electroencephalogram (EEG), electromyogram (EMG), locomotor activity and PER2-dependent bioluminescence from the cortex and the kidneys in freely moving mice, we showed that *Per2* expression is increased during wakefulness and reduced during sleep, both in cortex and in kidneys. Interestingly, daily recurring sleep deprivations restored *mPer2::Luc* rhythms in behaviourally arrhythmic SCN-lesioned mice in constant darkness conditions. Mathematical modelling suggested that PER2 dynamics are driven by two forces: a sleep-wake-dependent force and an SCN-independent circadian force. Taken together, the main message of the article is that the clock circuitry in peripheral oscillators integrate sleep-wake information, potentially contributing to the physiological adaptation of the organ.

Study contributions

The study was designed and performed by the lab of Paul Franken. Marieke Hoekstra performed the experiments with the help of Yann Emmenegger. The data analysis was done by Marieke Hoekstra and Maxime Jan. I performed a small, but essential part of the experiments, which was requested during the revision of the article. Specifically, I carried out the experiment presented in the Supplementary Figure 5 (*Pgk1-Luc* reporter

recordings). I injected through tail vein the adenoviral vector pCV100, in which firefly luciferase is expressed from the constantly expressed *Pgk1* promoter. The adenoviral vector was generated by Claudia Hagedorn and Florian Kreppel, originally planned to be used in my study of the circadian regulation of iron metabolic transcripts. Pump implantation and RT-Lumicorder recording was done by me, while the data were analysed by Maxime Jan. Marieke Hoekstra, Maxime Jan and Paul Franken wrote the manuscript. I, together with David Gatfield, wrote the methods part of my experiment and I have contributed with general comments to the final version of the manuscript.

Discussion

In the following section the results of the *Smg6* study, which are described as the main publication of my PhD work Katsioudi *et al.*, 2022, will be discussed. At the end of the section I will comment on current ongoing work and future potential projects that arise from our findings.

In Katsioudi *et al.*, 2022 we reported on the creation of a novel mouse model to inactivate NMD that is based on the SMG6 endonuclease. Cre recombination of the *Smg6^{fllox}* allele in mice allows for time- and tissue-specific NMD inactivation. We evaluated the validity of the model initially in *Smg6^{mut}* fibroblasts, where we observed significant reduction of NMD activity in NMD-annotated exons and known NMD-targeted transcripts, as well as in an NMD-sensitive luciferase reporter. Successful NMD deficiency, similar to what we saw in fibroblasts, was observed in liver tissue of hepatocyte-specific *Smg6^{mut}* mice. Culture experiments of *Smg6^{mut}* fibroblasts and liver explants revealed a period lengthening in both tissues in the absence of NMD. *In vivo* recording of liver gene expression in freely moving mice showed no detectable circadian differences between hepatocyte-specific *Smg6^{mut}* mice and their control littermates in light-entrained and *ad libitum* fed conditions. In addition, no effect on the circadian rhythmicity of the SCN was observed upon NMD reduction, neither in locomotor activity *in vivo* nor in bioluminescence levels of SCN slices.

Our transcriptome-wide analysis in the hepatocyte-specific *Smg6^{mut}* liver tissue around the clock revealed that the mRNA stability of the core clock gene *Cry2* was increased during the dark phase. CRY2 protein levels in *Smg6* mutant tissue reached their highest levels at a later timepoint (ZT20) in comparison to the *Smg6* wild-type tissue (ZT16). We further evaluated the observation that *Cry2* is an NMD target by reporting elevated protein levels in NMD-deficient fibroblasts and increased expression of a luciferase exogenous reporter of the *Cry2* 3' UTR. Lastly, we showed that pharmacological inhibition of NMD

recapitulates the period lengthening we observed in *Smg6^{mut}* tissue, and that it rapidly and selectively increased the expression levels of the full length Cry2 3' UTR.

Mouse model validation : successful reduction of NMD activity

After designing and obtaining our new NMD mouse model our first aim was to evaluate its functionality via estimating NMD deficiency. Successful Cre-mediated recombination of the *Smg6^{flox}* allele in fibroblasts and in the liver was demonstrated by DNA genotyping (Katsioudi *et al.*, 2022, figure 1D & 2E). Furthermore, in order to evaluate NMD downregulation following the expression of mutant SMG6 in these two models we performed RNA-seq.

Transcriptome-wide analysis revealed an increased stability in NMD-annotated transcripts and in transcripts that contained retained introns. This difference was only present in *Smg6^{flox}* fibroblasts treated with tamoxifen and not in any of the control groups (Katsioudi *et al.*, 2022, figure 1F & G). Similarly, we observed a significant upregulation in a large portion of NMD annotated exons (n=595) and retained introns (n=474). A small portion of the detected transcripts, most of them constitutive exons, was downregulated in *Smg6^{mut}* fibroblasts; these likely represent genes that are indirectly regulated by NMD targets. A total of 2800 exons was detected to respond to the SMG6 nuclease inactivation in fibroblasts, 2543 of them were upregulated. An intriguingly similar number of a total of 2494 upregulated exons was detected upon SMG6 knockdown in human cells in Karousis *et al.* [196].

Subsequently, we evaluated alternative splicing pairs that have an NMD-annotated and a stable protein coding isoform, previously used by Li *et al.* for accessing NMD efficiency [255]. In figure 1H and 1I of our publication we show two representative examples of such loci, *Hnrnp1* and *Srsf11*, that clearly indicate upregulated expression of NMD-annotated exons in *Smg6^{mut}* cells (similarly see figure S2.A for NMD efficiency at the liver tissue). Taken together these findings suggest that we have successfully ablated NMD activity, or at least a large proportion of it. Of note, Karousis *et al.* reported that the majority of NMD

targets are degraded via SMG6, as less than 200 exons (out of a few thousands) seem to be uniquely sensitive to the SMG5-SMG7 decay branch [196]. This observation further enhances our confidence of the validity of our novel NMD model by targeting the SMG6 endonuclease.

To further validate NMD deficiency we evaluated transcript levels of known NMD targets, for example the transcripts of the three main factors that mediate cellular stress response *Atf3*, *Atf4*, and *Ddit3*. Two independent studies, by Mendell and colleagues [218] and later by Gardner [217] showed that NMD regulates the expression levels of the *Atf3*, *Atf4*, and *Ddit3* genes. In our data we observed elevated mRNA levels of all three genes in hepatocyte-specific *Smg6^{mut}* liver tissue (figure 4). Notably, there were no (or at least much smaller) differences in transcription levels (pre-mRNA), which indicates that the increase originated post-transcriptionally. The levels of phosphorylated eIF2 α , as shown in supplementary figure 2 of Katsioudi *et al.*, 2022 were not altered between NMD deficient and control liver tissue, indicating that the observed increase at the mRNA of the ISR-mediating genes is not an result of elevated intracellular stress.

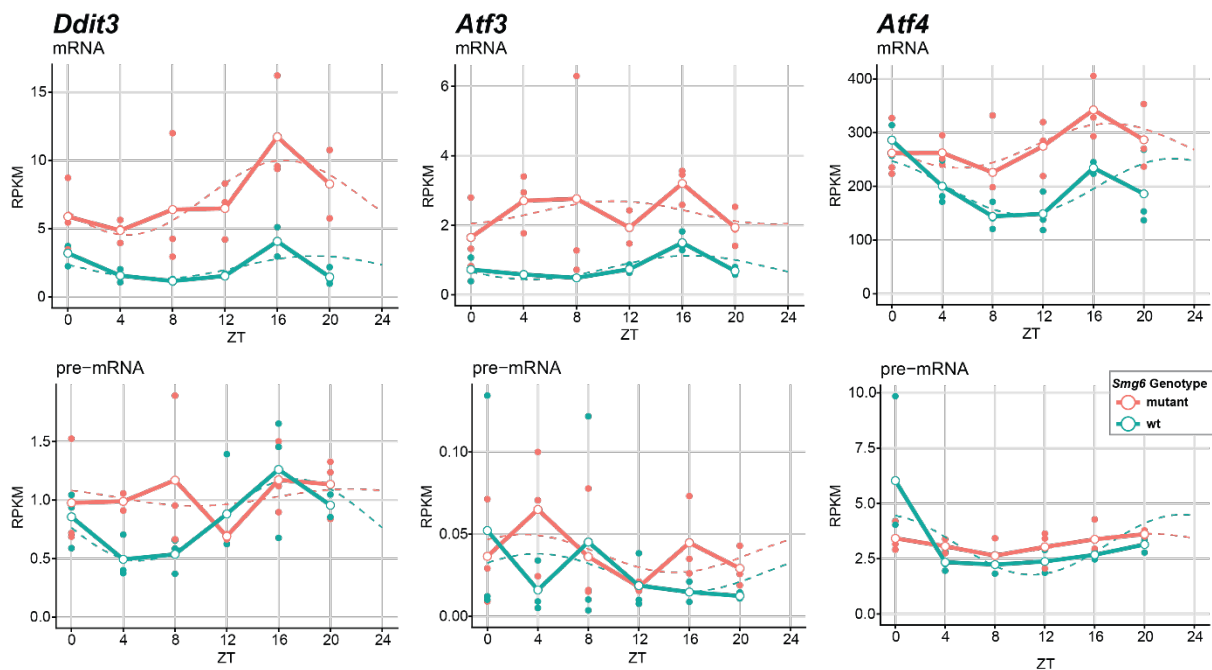


Figure 4: SMG6-mediated NMD ablation increases the mRNA levels of the three IRS-mediating genes, *Ddit3*, *Atf3* and *Atf4*. RNA-seq data is plotted for the indicated IRS-mediating genes for mRNA (upper panels; exonic reads) and pre-mRNA (lower panels; intronic reads) for *Smg6* mutant (pink) and control (green) liver tissue. RPK

values of individual animals are shown as dots with solid lines connecting the mean of each timepoint. The dashed line represents the rhythmic data fitting. NMD deficiency in hepatocyte-specific *Smg6^{mut}* liver tissue increased, as expected, the transcript levels of the three NMD-regulated genes. Only the mRNA levels were increased between the two genotypes, in comparison to the pre-mRNA levels that had similar levels, excluding indirect effects of changes in transcription and attributing this difference to post-transcriptional mechanisms, such as NMD activity. n=3 per group/4 hours.

Another set of genes that we examined in order to evaluate the validity of our model are the core members of the NMD machinery. Rehwinkel *et al.*, while studying the effects of RNA interference-mediated depletion of NMD components (UPF1, UPF2, UPF3, SMG1, SMG5, and SMG6) in *Drosophila* cells, had first suggested the potential existence of a feedback mechanism within the NMD machinery [256]. Specifically, they observed increased levels of the *Smg5* and *Smg6* transcripts, present upon downregulation of each of the tested NMD factors [256]. Yepiskoposyan *et al.* further observed this autoregulatory phenomenon in human cells, where they saw upregulation of the mRNA levels of *Upf2*, *Smg1*, *Smg5*, *Smg6* and *Smg7* following downregulation of *Upf1* [204]. In our liver transcriptome-wide analysis we observed significant upregulation in transcripts of almost all main NMD factors, *Upf1*, *Upf2*, *Smg1*, *Smg5*, *Smg6* and *Smg7*, upon inactivation of NMD (figure 5). No difference was observed in expression levels of *Upf3a* and only a mild upregulation in *Upf3b* levels, in accordance with data from UPF1 downregulation in HeLa cells [205]. Regarding the newly identified NMD factors SMG8 and SMG9, we observed no significant differences in mRNA levels between the two *Smg6* genotypes (data not shown). Significant upregulation was also observed at the mRNA levels of the translation initiation factor *Eif4a2* (data not shown) in NMD-deficient liver; in accordance to the newly identified feedback loop between NMD and translation initiation by Huth *et al.* [174].

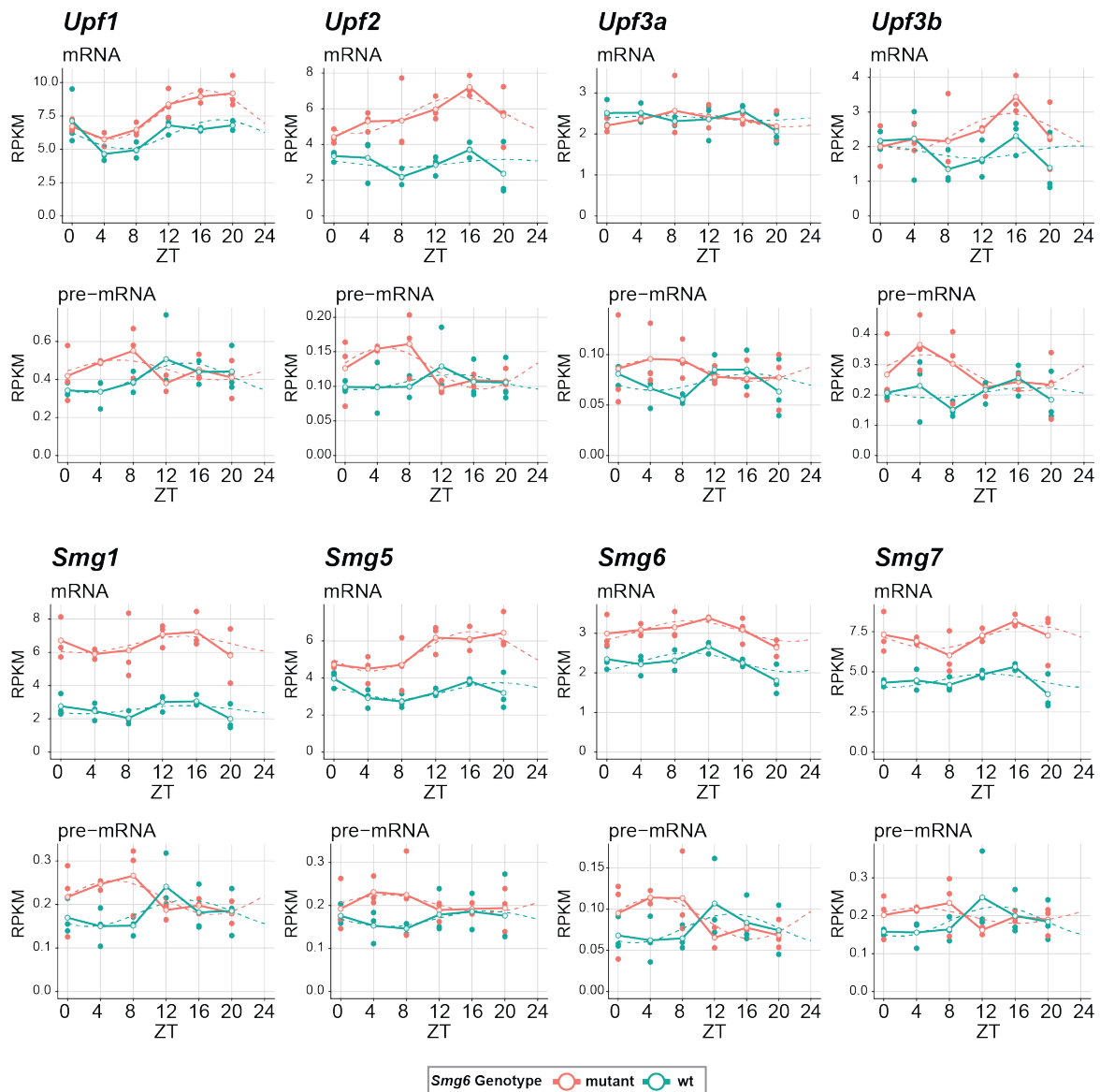


Figure 5: The nuclease-inactivation of SMG6 increases the mRNA levels of the main NMD factors in liver tissue around the clock. RNA-seq data is plotted for the indicated NMD genes for mRNA (upper panels; exonic reads) and pre-mRNA (lower panels; intronic reads) for *Smg6* mutant (pink) and control (green) liver tissue. RPK values of individual animals are shown as dots with solid lines connecting the mean of each timepoint. The dashed line represents the rhythmic data fitting. The mRNA levels of all NMD factors, except *Upf3a* and *Upf3b*, were upregulated in *Smg6^{mut}* liver. No significant differences were observed in global transcription levels. n=3 per group/4 hours.

There are two main points of concern regarding the validity of our *Smg6^{lox}* mouse, as an animal model that reliably inactivates NMD, namely the possible existence of several decay branches of the pathway (reviewed in [187]) and the redundancy between SMG6- and SMG5:SMG7-mediated degradation [192, 196]. Previous studies of NMD deficiency

in mammalian cells reported an upregulation of approximately 1.5% to 4.9% of the evaluated transcripts; the differences between the studies arise from different experimental and analytical approaches [204, 218, 257]. Our Transcriptome-wide analysis followed by SMG6-mediated NMD inactivation in liver detected an upregulation of approximately ~2.8% of the detected genes (447), which is within the range of previously reported data in mammalian cells [204, 218, 257] (here one should keep in mind the technical and analytical differences). Similarly, as mentioned above, the upregulation observed in known NMD targets in our dataset were in accordance with UPF1 knock down studies [205, 218]. Taken together our data suggest that we have successful ablation of NMD with our new *Smg6*-based mouse model.

High levels of CRY2 slow down circadian oscillations

The main finding of Katsioudi *et al.*, 2022 is that the transcript of the core clock gene *Cry2* is a *bona fide* NMD target, previously unidentified, and its impact on clock functionality. Increased levels of *Cry2* during the dark phase delayed the protein peak approximately 4 hours in the liver (Katsioudi *et al.*, 2022, figure 4B), in accordance with the period lengthening that we observed in circadian rhythmicity of liver explants (Katsioudi *et al.*, 2022, figure 2C). Period lengthening and increased levels of CRY2 were also observed in *Smg6^{mut}* fibroblasts (Katsioudi *et al.*, 2022, figure 2B, 4F & G). Lastly, pharmacological inhibition of NMD in fibroblasts increased potently the period length (Katsioudi *et al.*, 2022, figure 4K & L) and directly increased expression levels a *Cry2* luciferase reporter (Katsioudi *et al.*, 2022, figure 4J).

Animal studies in *Cry2* KO mice have reported a longer period in voluntary locomotor activity [258, 259] and in free-running rhythms in cultured tissue explants and dissociated cells [260]. Surprisingly, the increased transcript stability of *Cry2* in our NMD-deficient tissue, is also associated with increased period length. If the *Cry2* deregulation and the period lengthening in our model are causally connected (corresponding experiments are ongoing), then this is a paradoxical result because both the ablation and the overexpression of CRY2 would have a similar period lengthening phenotype. However,

this conundrum of the CRY2 effect on period length was also observed by Anand *et al.* in a genetic study of mice lacking *Cry1*, *Cry2* or both genes in combination with the *after hours* (Afh) mutation [261] of the *Fbxl3* gene [254]. FBXL3 is an ubiquitin ligase that regulates cryptochrome ubiquitination and degradation [262], inactivation of which delays the rate of CRY degradation [261]. The authors observed a period lengthening in locomotor activity of approximately an hour and a half upon CRY2 stabilisation in mice without *Cry1* [254]. Interestingly, the chemical compound TH301, a selective stabilizer of CRY2, also prolongs period in a variety of circadian luciferase reporters regardless of the cell type or the species [263]. This period lengthening followed by increased CRY2 stability is in accordance with our data that show a longer free-running period with corresponding elevated *Cry2* levels in NMD-deficient liver and fibroblasts. A potential hypothesis that causally links the prolonged circadian period with the delayed CRY2 levels, would be that CRY2, as an earlier transcription inhibitor (CT16 in wild type tissue) remains prolongedly bound to its targets, delaying the access of CRY1 [105] to them, which would eventually make the cycle slower. Of note, a publication from the Ueda lab [264] reported that the expression phase of *Cry1* and not the protein levels (within physiological margins) regulates circadian period, highlighting the importance of a well-regulated temporal orchestration between CRY1 and CRY2.

Kim *et al.* while studying the kinetics of the ascending and descending phase of the *Per3* transcript observed phase-dependent, translation-coupled mRNA decay [265]. Specifically, using the transcription inhibitor Actinomycin D, they revealed that *mPer3* was tremendously stable during the ascending phase, while it was quickly degraded during the declining phase [265]. Our transcriptome analysis around the clock detected differences in *Cry2* transcript stability between *Smg6^{mut}* and control liver tissue, but also hinted at temporal differences in transcript stability. In the absence of NMD we observed increased levels of *Cry2* mRNA specific to the dark phase, while the mRNA/pre-mRNA ratio – as a proxy for transcript stability – in control tissue was slightly reduced after ZT8 (figure 6 & Katsioudi *et al.*, 2022, figure 4A). Given that we define as “transcript stability”

the ratio of mRNA to pre-mRNA, the observed differences could reflect differences in various levels of gene expression, such as the kinetics of transcription, transcript editing or decay. Thus, the current data are not conclusive on time-specific NMD activity, but it still remains an open question.

Currently, in order to better understand the turnover rates of *Cry2*, in collaboration with the Charité University of Berlin and the research group of Prof. Achim Kramer, we are doing real-time-cell imaging of CRY2 protein dynamics. Specifically, we aim to dissect the CRY2 rhythms in presence of the SMG1 inhibitor [253] or in presence of a pharmacological stabiliser of CRY2 [263]. Our intention is to compare oscillation dynamics of CRY2 in the absence of NMD with the rhythms of another non-NMD-targeted core clock protein (CRY1). In addition, we aim to further prove that the observed period lengthening is indeed mediated, at least partially, by CRY2. To do so we are planning to pharmacologically inhibit NMD in a *Cry2* KO [266] cell line and subsequently evaluate period length. If CRY2 is the main mediator of the period phenotype, NMD inhibition should have no, or a reduced, effect on period lengthening in addition to the effect of *Cry2* ablation.

Genetic ablation of *Cry1* and *Cry2* in mice suggests that CRY2 is a less potent transcription inhibitor compared to CRY1 [267]. However similar in function, the two CRY proteins seem to antagonise for certain targets. Binding of CRY2 at the chromatin around circadian

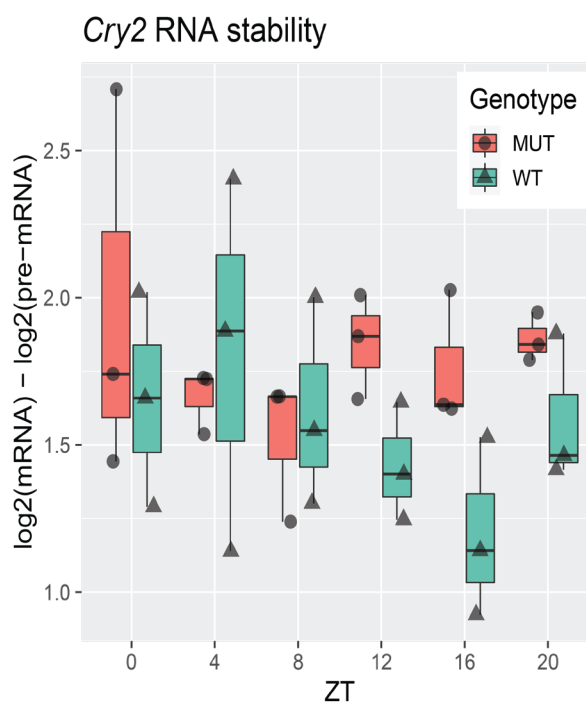


Figure 6: NMD deficiency increases *Cry2* mRNA stability during the dark phase (ZT12-ZT24). mRNA/pre-mRNA ratios across individual mice per timepoint. *Smg6* mutant liver samples (in pink) have showed increased mRNA/pre-mRNA ratios during the dark phase compared to their control littermates (in green).

time 16 (CT16) has been proposed to render unavailable the early targets of CRY1, which binds at the chromatin much later (~24 CT) [105]. Thus, the prolonged binding of the weak accelerator of the clock CRY2, potentially delays the binding of the potent accelerator CRY1, decelerating eventually the clock and resulting in a longer period [254].

The SCN paradox: no detected differences in circadian rhythmicity in NMD-inactive SCN

Smg6-mediated NMD inactivation prolonged the period length of both studied peripheral clocks *ex vivo*, the liver (tissue explants) and the skin (isolated fibroblasts). Following these promising results we wanted to study the role of NMD in the master clock. In order to promote Cre recombination of *Smg6^{flox}* in all the SCN cell types in the adult brain we decided to stereotactically inject an adeno-associated virus carrying a CMV-driven EGFP-Cre construct (Addgene, 105545-AAV). We evaluated the circadian rhythmicity of the SCN both *in vivo* using running wheel assays before and after the stereotactic injection, and *ex vivo* by recording expression rhythms of the genetic reporter *mPer2:luc* in SCN slices. The injection protocol, as well as the running wheel protocol (shown in Katsioudi *et al.*, 2022, Supplementary figure 1C) was adapted from Brancaccio *et al.* [65].

Both experimental approaches yielded no difference in circadian rhythmicity between the *Smg6^{mut}* and the wild-type SCN. However, based on our current data right now we cannot confidently conclude whether the phenotypic absence in the SCN originates from a different machinery of the clock and/or the NMD pathway, or from potential technical limitations. Accurate targeting of the SCN was validated by GFP imaging (Katsioudi *et al.*, 2022, Supplementary figure 1A & B) and DNA genotyping in micro-dissected SCN shows successful Cre recombination of the *Smg6* gene. However, we observed that this conversion was not 100% complete in all mice (Katsioudi *et al.*, 2022, Supplementary figure 1G).

Regarding the running wheel experiments, we observed a general reduction of the period length at the second constant darkness period (experimental τ) in both groups. This

reduction might be linked to the invasive procedure of the stereotactic injection itself and the administration of painkillers/anaesthetics [268], though it is unlikely that the pharmacological treatment would have such a long term effect, or age-related changes in circadian rhythmicity [269, 270] (Katsioudi *et al.*, 2022, Supplementary figure 1D). In addition, a severe reduction in activity levels of both experimental groups was apparent after stereotactic injection at the SCN (Katsioudi *et al.*, 2022, Supplementary figure 1C). This drastic decline in activity intensity, which might be partially explained by aging [271], may confound accurate estimation of the period length or other circadian features of the locomotor activity. We observed no signs of discomfort or pain in the animals, however most of them had increased body weight compared to non-injected C57BL/6J mice. The weight gain we observed has also been observed by other researchers (Miho Sato, Brown lab, personal communication) upon stereotactic injection and is most likely linked to tissue damage from the needle of adjacent brain areas to the SCN, that are involved in metabolism and appetitive behaviours [272].

However, the mice with *Smg6^{mut}* SCN were significantly more overweight compared to their control littermates (figure 7), even though no differences were observed in food consumption (data not shown). Interestingly, desynchrony between peripheral clocks and the SCN promotes weight gain in constant darkness, despite similar food consumption [273]. The authors suggest that this phenotype of the SCN-specific disrupted clock might be the effect of food intake randomly allocated across the circadian night, which is proven to contribute to weight gain [274]. In the same direction, it is possible that the increased weight we observed in the SCN-specific *Smg6^{mut}* mice is the outcome of a disrupted master clock following NMD inactivation. Follow-up experiments using metabolic cages that record precise time and levels of food intake, locomotor activity and energy expenditure would be required. Of note, Brancaccio *et al.*, i.e. the study on which we based our protocol reported no reduction in locomotor activity and they do not mention any weight differences before and after the stereotactic injections at the SCN.

Another possible explanation for not observing any differences in period length upon NMD inactivation would potentially be due to different efficacy of the NMD pathway in the brain and/or cellular variability of NMD activity [215]. The importance of NMD in brain development and health has been well studied [140, 228], however most of the details of the NMD machinery come from non-neuronal cell culture studies. Interestingly, *Smg6* deletion in different brain areas has different effects in neurogenesis [275], suggesting a cell type-specificity on its activity. Even though this study was focused on the developing brain and there are no data attributing different roles of SMG6 in the adult brain, it is still possible that the *Smg6* mutation we introduced has a more profound effect in ablating NMD activity in peripheral tissues compared to the brain or specifically to the SCN.



Figure 7: Weight differences between SCN-specific *Smg6^{mut}* mice and their littermate controls. At the left: Weight differences between the experimental (in pink) and control (in green) mice before the stereotactic injection of the Cre-carrying virus. At the right: Weight differences of the same mice after the stereotactic injection. The grey shaded area represents the average animal weight for male C57BL/6J mice according to the Jackson Laboratory® commercial provider. Each black dot represents an individual mouse (Mann–Whitney U test, $p=0,036$).

Similar to tissue-specific differences in NMD regulation and activity, differences in the architecture of the molecular clock between the SCN and the peripheral clocks might contribute to the observed insensitivity of the master clock to NMD deficiency. Several mammalian tissues oscillate with a different phase *in vivo* [276] and in culture [28, 76] and display different period lengths when free-running [277], indicating a tissue-specific variation not only in entrainment but also in cell-intrinsic clock mechanisms. Despite the common architecture of the clock, genetic ablation of some core clock genes results in different phenotypes in a tissue-specific manner. For example *Per3* knockout mice show only subtle behavioural changes [278]. Nevertheless, *Per3* ablation in peripheral clocks, such as the liver, the aorta and the lungs, causes a strong period lengthening [277]. In the same direction, genetic ablation of *Clock* leads to arrhythmic peripheral tissues in culture [279], but locomotor activity remains rhythmic [280], as NPAS2 and CLOCK have redundant roles in the SCN [281]. Interestingly, mRNA rhythms of *Cry2* in the SCN have a smaller amplitude in comparison to the liver rhythms of the same animals [282]. In line with this, a very recent publication suggests that CRY1 is the main negative regulator within the central clock [283]. Thus, it is potentially possible that the different effects we observe in period length between the SCN, the liver and fibroblasts are indeed attributed to cell-type variations of the clock machinery.

Lastly, as neurons differ dramatically from other cell types in metabolic and cellular processes [284] it is possible that the two weeks window that we allowed for the *Smg6* recombination to happen are not enough, and perhaps the wild-type NMD-active SMG6 remains longer in the neurons compared to the fibroblasts and the hepatocytes. Despite the successful recombination of *Smg6^{fllox}* in the SCN (Katsioudi *et al.*, 2022, Supplementary figure 1G), we have no data to prove the efficacious ablation of NMD activity. To get in-depth insights into NMD downregulation at the SCN upon *Smg6* recombination, RNA-seq or qPCR to evaluate transcript levels of known NMD substrates at the injected area are required. Another alternative option would be to add the SMG1 inhibitor in SCN slices of *mPer2:luc^{ki}* mice or directly to the SCN of the living mice, to observe whether NMD inhibition has any effect in the SCN rhythmicity. However, we have no information on

how the reagent is taken up by the tissue in culture or how it would act when injected directly to the SCN *in vivo*. Several pilot experiments would be required to optimize the protocol for using the pharmacological inhibitor to the SCN tissue. Given time restrictions and budget considerations, as well as the animal availability in relation to the animal experimentation license, we decided to not further explore the absence of a circadian phenotype at the SCN level, at least for now.

No difference in liver oscillators in hepatocyte-specific NMD mutant mice *in vivo*

Culture of liver explants, where the peripheral clock of the liver is free-running without the entraining signals of the SCN, revealed a strong period difference of almost 3 hours lengthening in the NMD-deficient tissue (Katsioudi *et al.*, 2022, figure 2C & D). To evaluate the rhythmicity of the entrained liver in the absence of NMD in the living animal, I performed *in vivo* real time recording of bioluminescence using the RT-Biolumicorder [3]. The RT-Biolumicorder allows evaluating in light-entrained conditions the circadian rhythmicity of the liver in hepatocyte-specific *Smg6^{mut}* mice and their control littermates, both carrying a *mPer2:luc^{ki}* [76] allele. The transgenic *mPer2:luc^{ki}* mouse model, which was already available at the lab, has been well-characterised and extensively studied in the field of chronobiology [76].

Given the profound period difference that was observed in the free-running liver explants, we expected to observe a phase difference between the two *Smg6* genotypes under the constant entrainment of the SCN [251, 252]. To our surprise we detected no phase difference or any other difference at the expression patterns of *mPer2:luc* *in vivo* (Katsioudi *et al.*, 2022, figure 2G & H). Temporal analysis on the mRNA levels of the core clock genes can also provide detailed insights on the phase angle of the entrained liver. RNA-seq data from tissue harvested around the clock, previously used to prove the validity of the NMD model, were used to estimate the peak phases of mRNA abundances in the entrained liver. Several genes displayed a robust phase shift at the *Smg6^{mut}* tissue compared to the wild-type. For example, *Cry2* and *Rev-erb β* (otherwise *Nr1d2*) have a phase shift of approximately two hours (Katsioudi *et al.*, 2022, figure 3K). However, *Per2*,

which we used as a reporter for our *in vivo* experiments, displayed a very subtle phase difference (~30 mins) in mRNA abundance upon NMD inactivation, consistent with the *in vivo* recording data. The likely explanation is that *Per2* rhythms in the liver are not only regulated by the local clock, but also by systemic cues from the SCN that do not require a functional hepatocyte clock [280, 285]. Lastly, *Per2* expression rhythms in peripheral oscillators are also directly regulated by sleep-wake [286] and feeding rhythms [287].

Beyond the possibly unfortunate selection of *Per2:luc* as our circadian reporter for the RT-Biolumicorder experiments, there are other potential technical limitations to our approach. One main aspect of debate is whether we record rhythms that predominantly originate from the liver or other peripheral tissues. In the original publication, where the RT-Biolumicorder is introduced, Saini *et al.* show that the majority, but not the total, of the bioluminescence signal of the *mPer2:luc^{ki}* mice [76] originates from the liver. The *mPer2:luc^{ki}* mice that we use have a C57BL/6J background, which have dark fur that largely absorbs bioluminescence. Hence by shaving the fur at the area of the liver, which is a large organ with a robust rhythmicity located closely under the skin at the back of the animal, the signal from the other tissues is eliminated [3]. In the same direction Sinturel *et al.* used *mPer2:luc^{ki}* hairless mice to address whole-body rhythms [70]. However, Hoekstra, Jan *et al.* have suggested that the majority of the bioluminescence signal in *mPer2:luc^{ki}* hairless mice derives from the kidneys [286].

In food shifting experiments with *Smg^{flox} ; mPer2:luc^{ki}*, when the mice have access to food only during the light phase in contrast to their nocturnal preference, we observed a typical double peak (data not shown), similar to Saini *et al.*, which indicates that the signal comes not only from the liver, but also from other peripheral tissue(s) [3] that respond with different speed to food entrainment [86]. Thus, it is possible that the signal from the NMD-deficient liver is getting “diluted” from the signal from other peripheral tissues with an active NMD pathway, masking a hepatic phase difference.

In future experiments, tail vein injection of adenovirus carrying a circadian reporter would be a valuable approach to ensure that the totality of the detected rhythms purely originate from the liver, as it has been used before [3]. Adenoviral particles injected through the tail vein in mice primarily transduce the animal's liver, this way we will ensure that the recorded signal comes from the liver (see [3] and references within). Currently, the two available adenoviruses we could use are based on *Bmal1* and *Rev-erba* [3, 288], however, both transcripts show no phase difference in the entrained liver in the absence of NMD based on our RNA-seq data. Another alternative option would be to use a clock-controlled gene, as a output reporter of the core clock function in the absence of NMD. For example we could use the luciferase reporter of the ribosomal protein RPL30, which is shown to be rhythmic in the liver [2] and it gives high-amplitude robust rhythms in the RT-Biolumicorder (tail vein injected adenovirus), as we showed in our publication Katsioudi *et al.*, 2021 (figure 3 & 4).

Another parameter that could be taken into account is the effect of light entrainment on the SCN. In order to circumvent the inter-animal differences in the SCN rhythmicity I used skeleton photoperiod (two light pulses of 30 minutes at 12-h intervals) to keep all the mice in synchrony [289]. Alternatively, the recording could be done in constant darkness, where the SCN would be free-running. We concluded that given the small group size of the RT-Biolumicorder experiments and as we are solely interested in the liver rhythms in the current experimental setup, the skeleton photoperiod would provide us with insights selectively on liver rhythmicity, removing the additional "noise" of the individual SCN rhythms.

Lastly, in contrast with a recent study [70] that used drinking water to provide luciferin, we used mini osmotic pumps, as Hoekstra, Jan *et al.* [286] detected significant bioluminescence rhythms coinciding with drinking rhythms using the same experimental facilities with my experiments. However, we must keep in mind that the implantation of an osmotic pump requires anesthesia and is a stressful procedure for the mice. In addition, hepatocyte-specific NMD deficiency is expected to cause some tissue abnormalities or

even damage selective to our *Smg6^{mut}* mice [247], which is not present to their control littermates, a toxicity that might be aggravated by the painkillers and anesthetics used during the surgery.

NMD-driven liver toxicity

To evaluate the metabolic status of the hepatocyte-specific *Smg6^{mut}* mice, we conducted blood chemistry analysis around the clock (3 mice/genotype, 4 hours window), where five main metabolites related to liver health and metabolism were measured (figure 8). In the serum of the hepatocyte-specific *Smg6^{mut}* mice, elevated levels of alanine aminotransferase and aspartate aminotransferase were detected compared to their *Smg6^{wt}* littermates, as well as high levels of triglycerides. In contrast, albumin levels were reduced and no differences were detected at the levels of glucose, non-esterified fatty acids and β -hydroxybutyrate.

Increased alanine aminotransferase and aspartate aminotransferase levels are markers of hepatocyte injury [290, 291]. Similarly, abnormal levels of triglycerides [292, 293] and albumin [294] indicate potential liver dysfunction. Taken together, the levels of the studied serum metabolites indicate an underlying liver damage in the NMD-deficient tissue, which however was not noticeable in animal behavior, weight and appearance or during visual inspection of the dissected liver. Our observation that NMD deficiency compromises the tissue function is not surprising given the important physiological roles of NMD [295] and it is in accordance with a previous mammalian NMD model, that reported hepatosteatosis, disrupted liver homeostasis and loss of regeneration following genetic ablation of the NMD factor UPF2 [247]. Liver tissue harvesting and culture, as well as *in vivo* experiments were all done four weeks after the Cre-activating tamoxifen injections. Thus, and given the healthy appearance and normal behaviour of the mice, we believe that the severity and the duration of the toxicity was not as extended as to confound our findings.

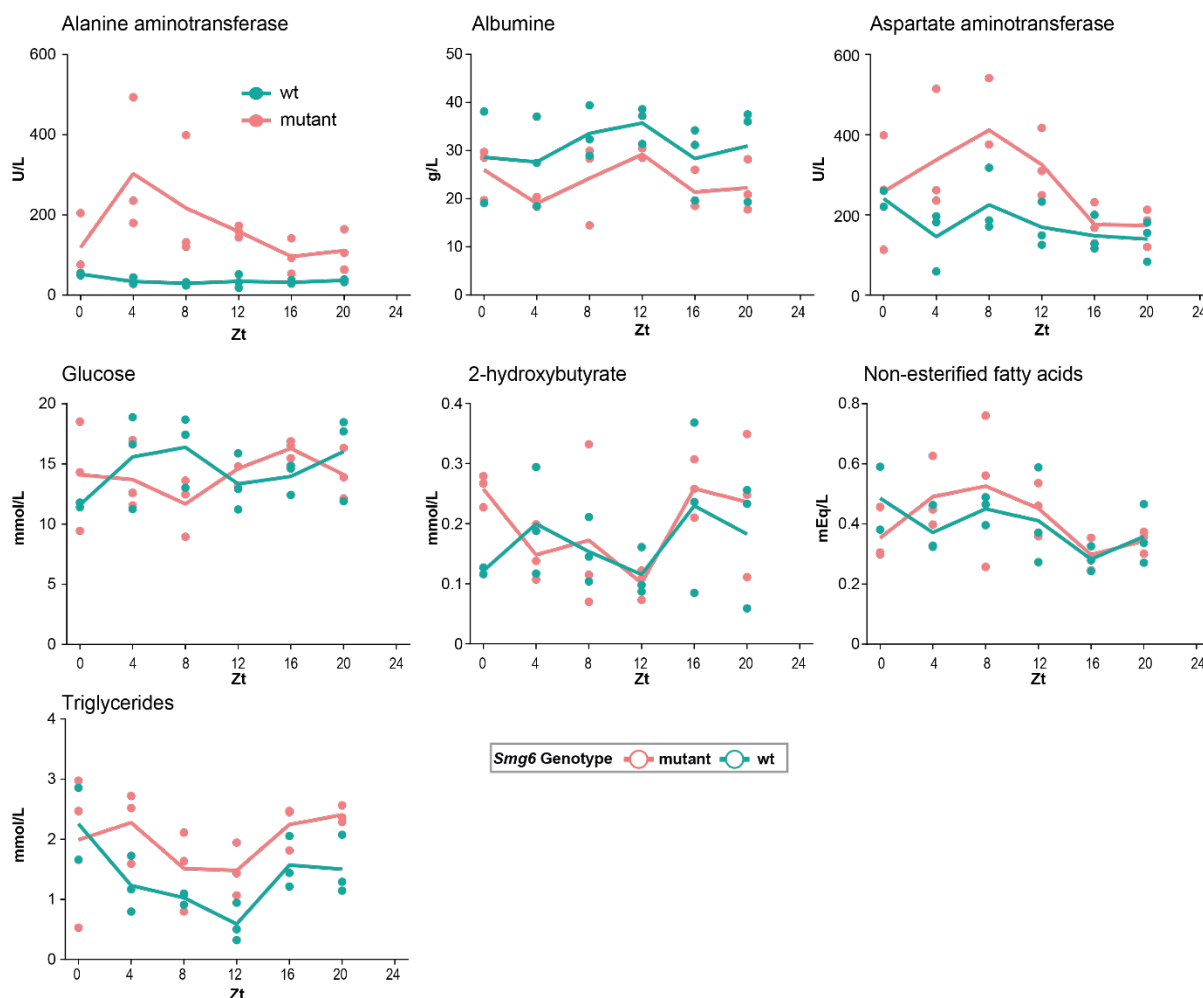


Figure 8: Analysis of basic blood chemistry around the clock. Hepatocyte-specific *Smg6^{mut}* animals (in pink) had increased serum levels of alanine and aspartate aminotransferase and triglycerides compared to their control littermates (in green). Albumin levels were reduced and no differences were detected at the levels of glucose, non-esterified fatty acids and β -hydroxybutyrate. Each dot represents an individual animal. Measurements were done using the Cobas C111 diagnostic robot. The measurement unit for each metabolite is shown at the left of the y axis. N= 3 mice/4 hours

Difference in locomotor activity in freely moving mice with hepatocyte-specific *Smg6* mutation

During the bioluminescence recording using the RT-Biolumicorder of the hepatocyte-specific *Smg6^{mut}* mice we observed a very reproducible difference in spontaneous locomotor activity (Katsioudi *et al.*, 2022, figure 2G). Specifically, the liver-specific NMD-deficient mice were becoming active right after the light pulse at ZT12, which corresponds to the “lights off” and the beginning of the circadian night. Mice, as nocturnal animals,

become active during the night and in fact they anticipate the dusk and become more active before the lights go off. This anticipatory behavior is partially driven by anticipation of feeding as rodents feed primarily during the dark phase [296, 297].

To our surprise, we observed that in contrast to the *Smg6^{wt}* mice that displayed this anticipatory behaviour, the liver-specific NMD deficient mice were becoming active later than ZT12 (figure 9). This finding suggested a potential crosstalk between the liver oscillator and the brain areas that regulate locomotor activity. Notably, daily rhythms in food-anticipatory behaviour do not necessarily require the known core clock machinery [80, 298] and are independent of the SCN [299]. The precise mechanisms of this independent food-entrainable oscillator remain elusive; however, studies suggest that feeding-dependent signals can alter neuronal activity of the SCN [300, 301].

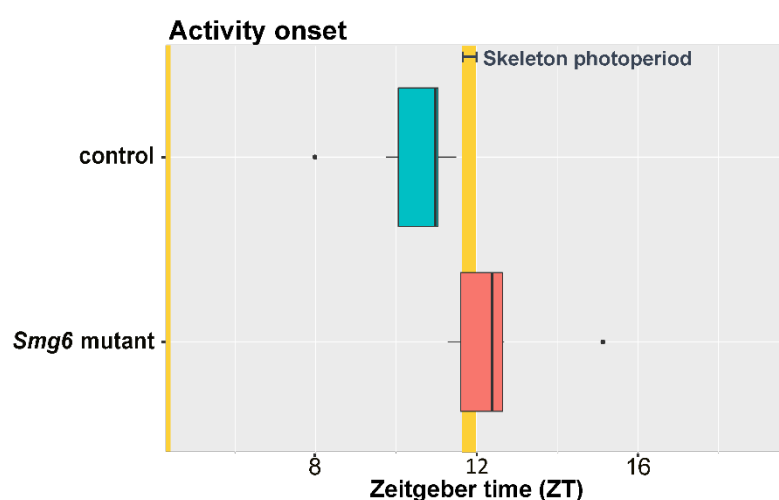


Figure 9: Mice with *Smg6^{mut}* liver have a slightly delayed activity onset compared to the control animals. In green the activity onset of the control mice (n= 6) and in pink the hepatocyte-specific *Smg6^{mut}* mice (n=6), activity onset was calculated with ClockLab analysis package according to [1].

In order to further validate and fully understand the difference in the activity onset between the hepatocyte-specific *Smg6* mutant and wild-type animals, we would have to design and perform a series of experiments. Firstly, we observed this difference in locomotor activity through the infrared detector (that is embedded in the RT-Lumicorder apparatus) in animals that are implanted with a mini osmotic pump. Thus, it would be appropriate to validate this phenotype in non-operated animals using cages connected to an infrared sensor or to running wheels. In addition, to elucidate whether this phenomenon is indeed linked to food-anticipatory behaviour, classic food entrainment

experiments are required, during which food is available only at specific time during the light phase [302]. Lastly, to identify the metabolic signals that drive this phenotype, metabolic analysis of the liver tissue around the clock is required.

Future perspectives and ongoing work

In the presented project I studied the efficacy of a novel mammalian NMD model and the pathway's role in circadian timekeeping. I chose to study fibroblasts and liver, as two examples of peripheral clocks, and the SCN as the master clock. We discovered that NMD has indeed a pivotal role in circadian timekeeping in peripheral clocks through transcript quantity regulation of the core clock gene *Cry2*. Nevertheless, as it often happens in biological research when a new model and/or a new mechanism is described, there are several new, downstream open questions that arise.

Our submitted work briefly touches upon known NMD substrates and the NMD-eliciting features, such as the positive correlation of the 3' UTR length with the effect on NMD inactivation (Katsioudi *et al.*, 2022, figure 1N), in the transcriptome-wide data coming from *Smg6^{mut}* fibroblasts. Similar analyses, but to a lesser extent, were performed in the transcriptome-wide data from the NMD deficient liver tissue, however we mostly focused on the expression patterns of the core clock and clock output genes. Complete characterisation of the detected NMD targets, known and novel, would provide valuable insights on NMD function and machinery. For example, one could search and quantify long noncoding RNAs, small nucleolar RNAs, miRNAs and pseudogenes among the detected NMD targets, similar to the analysis done by Colombo *et al.*, 2017 [192]. Lastly, in accordance with previously published work [204] we also detected autoregulation within the NMD pathway, however we have not yet attempted to compare the overlap of targets and the redundancy between the SMG6 and the SMG7-SMG5 decay branches with previously published data [192, 196]. Exhaustive analysis of our transcriptome-wide data from two different mammalian tissues could be a potential "spin off" project of my thesis.

Additional analysis of the physiological functions and the evolutionary conservation of the newly identified NMD targets would provide information for the physiological roles of NMD, similar to the identification of *Cry2* and the pathway's regulatory role in the circadian clock. Below, I list two examples of factors involved in important cellular processes, that were identified as potential NMD targets in our dataset, and further suggest a set of experimental approaches to elucidate the role of NMD in them.

Sirtuins (SIRT)

Sirtuins are nicotinamide adenine dinucleotide (NAD⁺)-dependent proteins, with different enzymatic activities, subcellular localisation, various targets and biological roles [303]. Among the seven mammalian SIRTs four of them, SIRT3, SIRT4, SIRT5 (located in the mitochondria [303]) and SIRT6 (located in the nucleus [303]) displayed increased transcript levels in the absence of NMD in liver (figure 10). The increased transcript levels of *Sirt5* and *Sirt6* seem to be generated mostly by increased levels of transcription, whereas the increase of *Sirt3*, and perhaps *Sirt4* as well, is generated post-transcriptionally. Thus, it is possible that NMD directly regulates certain sirtuin transcripts. This is an interesting finding, as with the exception in *Arabidopsis thaliana* that identified NMD-targeted splicing isoforms in the mitochondrial SIRT [304], no other data, to my knowledge suggest that members of the sirtuin family are under NMD regulation.

SIRTS have important physiological roles spanning from metabolism and aging to cancer and circadian regulation [303]. Focusing on their timekeeping function, SIRT6 interacts with CLOCK:BMAL1 regulating their chromatin recruitment to circadian gene promoters [305]. The deacetylase SIRT3 is involved in circadian regulation of mitochondrial function [306] and together with SIRT4 and SIRT5 are implicated in clock-dependent regulation of oxidative pathways [305]. Of note, no differences were detected in *Sirt1* mRNA levels, which is known to regulate both central [307] and peripheral oscillators [99, 308] in our liver *Smg6* dataset.

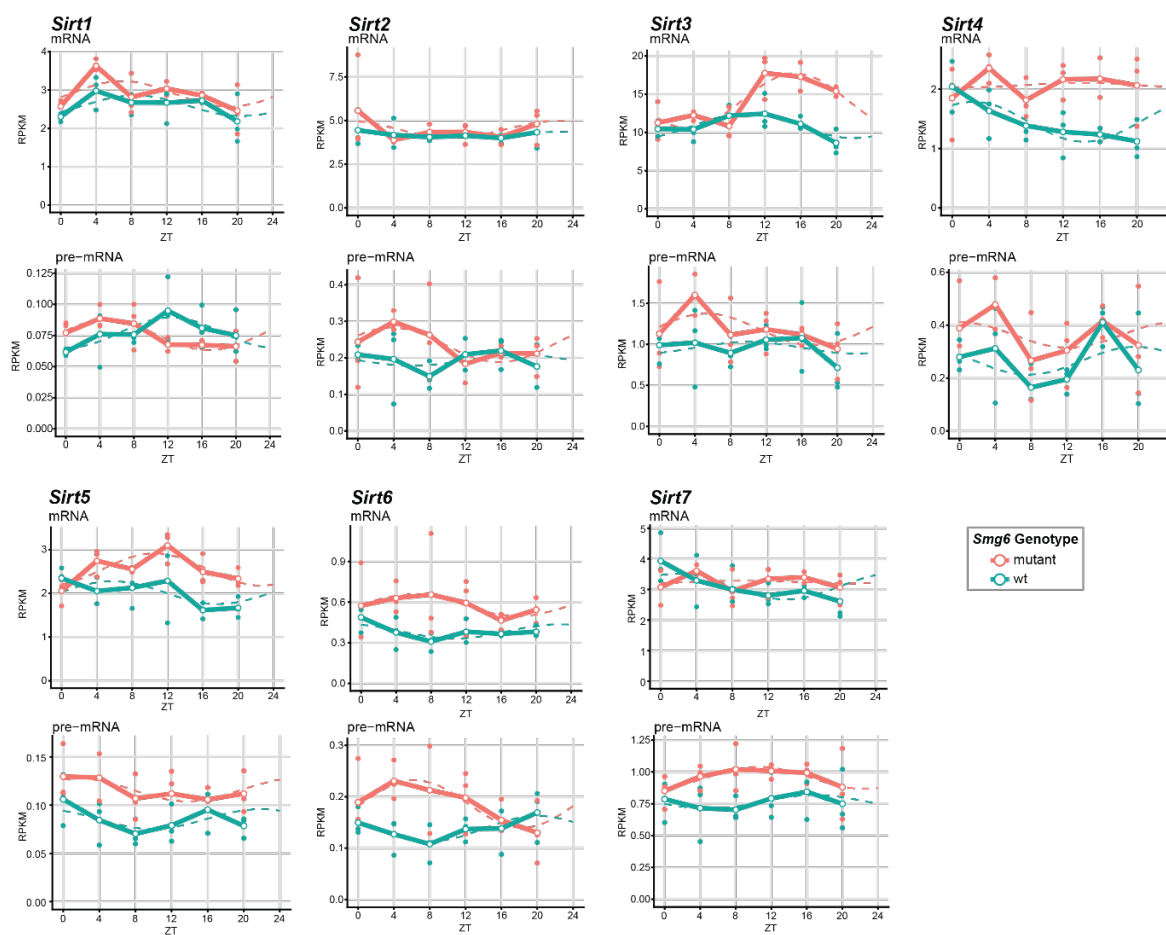


Figure 10: mRNA and pre-mRNA levels of the seven mammalian sirtuins in the liver tissue around the clock. RNA-seq data is plotted for the indicated *sirtuin* genes for mRNA (upper panels; exonic reads) and pre-mRNA (lower panels; intronic reads) for *Smg6* mutant (pink) and control (green) liver tissue. RPK values of individual animals are shown as dots with solid lines connecting the mean of each timepoint. The dashed line represents the rhythmic data fitting. $n=3$ per group/4 hours.

Beyond the chronobiological interest SIRTs have been implicated in cell metabolism, aging and cell death. SIRT4 for example regulates tumour suppression [309, 310] and is downregulated in human cancer [310]. SIRT3 levels reduce with age and has a protective role in aging [261] and neurodegeneration [262]. Without getting into details it becomes apparent that well-regulated levels of sirtuins are crucial for mammalian health and disease. Hence, investigating whether *Sirt3* and *Sirt4* transcripts are *bona fide* NMD substrates, and how NMD regulates directly or indirectly the mRNA levels of sirtuins would be an interesting project with possible human applications and therapeutic perspectives.

Lastly, preliminary analysis of our metabolic data of liver tissue around the clock identified significantly reduced levels of NAD⁺ in the NMD-deficient tissue. In addition, pathway analysis identified the “Nicotinate and nicotinamide metabolism” pathway as both significantly rhythmic, in accordance to previous studies [306], and significantly different between NMD-active and -inactive liver tissue, pointing towards a potential regulatory role of NMD in transcripts implicated in mitochondrial oxidative metabolism.

The DBHS proteins

Another group of proteins with important cellular roles and implicated in circadian rhythmicity are the DBHS proteins (*Drosophila* behavior human splicing), which consists of NONO and the paralogs SFPQ and PSPC1 [311]. These multifunctional RNA-binding proteins, that are core proteins of the nuclear paraspeckles, mediate gene expression in various ways, such as activation or inhibition of transcription, RNA splicing, localization and transportation [311]. Of the three members of the DBHS proteins, *Pspc1* displayed a significant transcript upregulation at post-transcriptional level in *Smg6^{mut}* liver. *Pfpq* displayed subtle changes in transcriptional, and possibly in post-transcriptional levels, while NMD-inactivation did not affect the mRNA levels of *Nono* (figure 11).

All three members of the DBHS protein family are implicated in post-transcriptional regulation of the circadian clock [312]. It is known that NONO interacts with PERIOD proteins and downregulation of it changes circadian rhythmicity in mammalian cells and flies [313] and it alters the period of locomotor activity in mice [312]. In addition NONO couples the circadian clock to the cell cycle [314] and it regulates the rhythmic expression of metabolic genes in the liver [315]. Less data are available about the other two members on circadian timekeeping in mammals. SFPQ also interacts with PERs [316] and abnormal protein levels lead to lost rhythmicity in mammalian cells, but do not affect periodicity on locomotor activity in (heterozygote) mice [316]. Similarly, low levels of PSPC1 prolong period in cultured cells, while no differences were detected in animal behavior patterns [312].

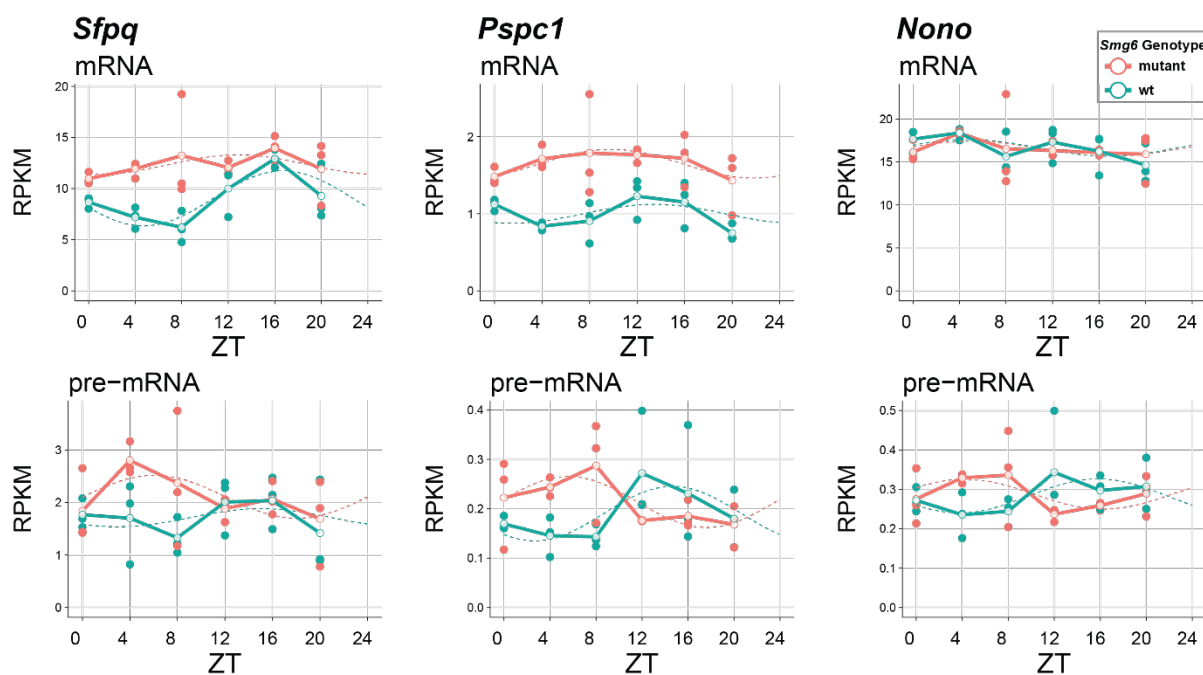


Figure 11: The mRNA and the pre-mRNA levels of DBHS proteins in the liver around the clock. RNA-seq data is plotted for the indicated NMD genes for mRNA (upper panels; exonic reads) and pre-mRNA (lower panels; intronic reads) for *Smg6* mutant (pink) and control (green) liver tissue. RPK values of individual animals are shown as dots with solid lines connecting the mean of each timepoint. The dashed line represents the rhythmic data fitting. The mRNA levels of *Sfpq* and *Pspc1* were upregulated in *Smg6^{mut}* liver. No significant differences were observed in transcript levels of *Nono*. n=3 per group/4 hours.

DBHS proteins have a regulatory role in almost every step of gene expression [311], so their importance for cell and organism health, beyond circadian timekeeping, is expected. DBHS are involved in neurodevelopment, innate immunity and cancer (see [311] for a review on the functions of DBHS proteins). DBHS proteins as splicing proteins are closely linked to the NMD machinery. SFPQ autoregulates its expression levels by binding its mRNA and promoting alternative splicing that switches to an alternative long 3' UTR that is targeted by NMD [317]. It is potentially possible that a similar mechanism is in action for regulating the expression levels of PSPC1. According to *Ensembl* [318] there are two annotated alternative splicing variants for *Ppspc1* with different 3' UTR lengths (~1200 nt and ~2400 nt) that give rise to proteins with slightly different sizes (466 aa and 523 aa respectively). Therefore, it would be of great interest to further evaluate whether NMD directly regulates any members of the DBHS family and further inspect the cellular and physiological consequences of this relationship. Initial evaluation of the increased

transcript levels would be validated by protein levels and reporter assays followed by mechanistic studies to inspect any potential phenotypes at cellular level.

Closing remarks: study validity and ethical considerations

This research work aimed to design a new animal model to study NMD in mammals and to study the role of the decay pathway in circadian rhythmicity. A mammalian model always has high translational validity as murine biology closely resembles the human one. However, our model introduces a tissue-specific mutation in adult animals, which is in contrast with the usual genetic diseases seen in humans. Following validation of the efficiency of the NMD model I used well-validated assays to assess circadian rhythmicity which provide high face (appropriate test) and construct (appropriate measurement) validity in our study.

During experimental procedures and analysis all possible measures to reduce potential bias were taken. For example, the analysis of the signal from the liver and kidney explants, in which some explants had to be removed due to low quality of signal, was performed blindly. Animal localization and handling were always the same between experimental groups and littermate mice were always used. In order to remove the effect of the menstrual cycle and the hormonal changes in female animals, only male mice were used. Given the fundamental mechanisms of both NMD and the circadian clock, we speculate that our findings extend to female biology as well. However, we have no data to prove this speculation. Lastly, all possible care was taken to ensure minimal animal suffering according, and beyond, to the official guidelines of the cantonal authorities.

References

1. Brown, L.A., et al., *Telling the time with a broken clock: quantifying circadian disruption in animal models*. *Biology*, 2019. **8**(1): p. 18.
2. Janich, P., et al., *Ribosome profiling reveals the rhythmic liver transcriptome and circadian clock regulation by upstream open reading frames*. *Genome research*, 2015. **25**(12): p. 1848-1859.
3. Saini, C., et al., *Real-time recording of circadian liver gene expression in freely moving mice reveals the phase-setting behavior of hepatocyte clocks*. *Genes & development*, 2013. **27**(13): p. 1526-1536.
4. Katsioudi, G., et al., *Recording of Diurnal Gene Expression in Peripheral Organs of Mice Using the RT-Bioluminescence Reporter*, in *Circadian Regulation*. 2022, Springer. p. 217-242.
5. Schibler, U., *The daily rhythms of genes, cells and organs: biological clocks and circadian timing in cells*. *EMBO reports*, 2005. **6**(S1): p. S9-S13.
6. Kuhlman, S.J., L.M. Craig, and J.F. Duffy, *Introduction to chronobiology*. Cold Spring Harbor Perspectives in Biology, 2018. **10**(9): p. a033613.
7. McClung, C.R., *The plant circadian oscillator*. *Biology*, 2019. **8**(1): p. 14.
8. De Mairan, J.-J., *Observation botanique*. *Hist. Acad. Roy. Sci.*, 1731(1729): p. 35–36.
9. De Candolle, A.P., *Physiologie Végétale*. Bechet Jeune: Paris, 1832. **Volume 2**.
10. Halberg, F., *Chronobiology*. *Annual review of physiology*, 1969. **31**(1): p. 675-726.
11. Lee, J.Y., et al., *A tribute to Franz Halberg, MD*. *Hypertension*, 2015. **66**(6): p. 1090-1092.
12. Konopka, R.J. and S. Benzer, *Clock mutants of Drosophila melanogaster*. *Proceedings of the National Academy of Sciences*, 1971. **68**(9): p. 2112-2116.
13. Baylies, M.K., et al., *Changes in abundance or structure of the per gene product can alter periodicity of the Drosophila clock*. *Nature*, 1987. **326**(6111): p. 390-392.
14. Bargiello, T.A., F.R. Jackson, and M.W. Young, *Restoration of circadian behavioural rhythms by gene transfer in Drosophila*. *Nature*, 1984. **312**(5996): p. 752-754.
15. Hardin, P.E., J.C. Hall, and M. Rosbash, *Feedback of the Drosophila period gene product on circadian cycling of its messenger RNA levels*. *Nature*, 1990. **343**(6258): p. 536-540.
16. Petersen, G., J.C. Hall, and M. Rosbash, *The period gene of Drosophila carries species-specific behavioral instructions*. *The EMBO journal*, 1988. **7**(12): p. 3939-3947.
17. Liu, X., et al., *Spatial and temporal expression of the period gene in Drosophila melanogaster*. *Genes & development*, 1988. **2**(2): p. 228-238.
18. Ralph, M.R. and M. Menaker, *A mutation of the circadian system in golden hamsters*. *Science*, 1988. **241**(4870): p. 1225-1227.
19. Vitaterna, M.H., et al., *Mutagenesis and mapping of a mouse gene, Clock, essential for circadian behavior*. *Science*, 1994. **264**(5159): p. 719-725.
20. Moore, R.Y. and V.B. Eichler, *Loss of a circadian adrenal corticosterone rhythm following suprachiasmatic lesions in the rat*. *Brain research*, 1972.
21. Richter, C.P., *Biological clocks in medicine and psychiatry*. 1965.
22. Moore, R.Y. and N.J. Lenn, *A retinohypothalamic projection in the rat*. *Journal of Comparative Neurology*, 1972. **146**(1): p. 1-14.
23. Berson, D.M., F.A. Dunn, and M. Takao, *Phototransduction by retinal ganglion cells that set the circadian clock*. *Science*, 2002. **295**(5557): p. 1070-1073.
24. Provencio, I., M.D. Rollag, and A.M. Castrucci, *Photoreceptive net in the mammalian retina*. *Nature*, 2002. **415**(6871): p. 493-493.

25. Provencio, I., et al., *A novel human opsin in the inner retina*. Journal of Neuroscience, 2000. **20**(2): p. 600-605.
26. Hannibal, J., et al., *The photopigment melanopsin is exclusively present in pituitary adenylate cyclase-activating polypeptide-containing retinal ganglion cells of the retinohypothalamic tract*. Journal of Neuroscience, 2002. **22**(1): p. RC191-RC191.
27. Balsalobre, A., F. Damiola, and U. Schibler, *A serum shock induces circadian gene expression in mammalian tissue culture cells*. Cell, 1998. **93**(6): p. 929-937.
28. Yamazaki, S., et al., *Resetting central and peripheral circadian oscillators in transgenic rats*. Science, 2000. **288**(5466): p. 682-685.
29. Yagita, K., et al., *Molecular mechanisms of the biological clock in cultured fibroblasts*. Science, 2001. **292**(5515): p. 278-281.
30. Hastings, M.H., A.B. Reddy, and E.S. Maywood, *A clockwork web: circadian timing in brain and periphery, in health and disease*. Nature Reviews Neuroscience, 2003. **4**(8): p. 649-661.
31. Mishima, K., et al., *The 3111T/C polymorphism of hClock is associated with evening preference and delayed sleep timing in a Japanese population sample*. American Journal of Medical Genetics Part B: Neuropsychiatric Genetics, 2005. **133**(1): p. 101-104.
32. Katzenberg, D., et al., *A CLOCK polymorphism associated with human diurnal preference*. Sleep, 1998. **21**(6): p. 569-576.
33. Robilliard, D.L., et al., *The 3111 Clock gene polymorphism is not associated with sleep and circadian rhythmicity in phenotypically characterized human subjects*. Journal of sleep research, 2002. **11**(4): p. 305-312.
34. Iwase, T., et al., *Mutation screening of the human Clock gene in circadian rhythm sleep disorders*. Psychiatry research, 2002. **109**(2): p. 121-128.
35. Toh, K.L., et al., *An h Per2 phosphorylation site mutation in familial advanced sleep phase syndrome*. Science, 2001. **291**(5506): p. 1040-1043.
36. Archer, S.N., et al., *A length polymorphism in the circadian clock gene Per3 is linked to delayed sleep phase syndrome and extreme diurnal preference*. Sleep, 2003. **26**(4): p. 413-415.
37. Ebisawa, T., et al., *Association of structural polymorphisms in the human period3 gene with delayed sleep phase syndrome*. EMBO reports, 2001. **2**(4): p. 342-346.
38. Patke, A., et al., *Mutation of the human circadian clock gene CRY1 in familial delayed sleep phase disorder*. Cell, 2017. **169**(2): p. 203-215. e13.
39. Nicholas, B., et al., *Association of Per1 and Npas2 with autistic disorder: support for the clock genes/social timing hypothesis*. Molecular psychiatry, 2007. **12**(6): p. 581.
40. Yang, Z., et al., *Circadian-relevant genes are highly polymorphic in autism spectrum disorder patients*. Brain and Development, 2016. **38**(1): p. 91-99.
41. Lipton, J.O., et al., *Aberrant proteostasis of BMAL1 underlies circadian abnormalities in a paradigmatic mTOR-opathy*. Cell reports, 2017. **20**(4): p. 868-880.
42. Videnovic, A., et al., *'The clocks that time us'—circadian rhythms in neurodegenerative disorders*. Nature Reviews Neurology, 2014. **10**(12): p. 683-693.
43. Musiek, E.S. and D.M. Holtzman, *Mechanisms linking circadian clocks, sleep, and neurodegeneration*. Science, 2016. **354**(6315): p. 1004-1008.
44. Partonen, T., *Circadian clock genes and mood disorders*, in *Melatonin, Neuroprotective Agents and Antidepressant Therapy*. 2016, Springer. p. 319-334.
45. Kovanen, L., et al., *CRY2 genetic variants associate with dysthymia*. PLoS One, 2013. **8**(8): p. e71450.
46. Edition, F., *Diagnostic and statistical manual of mental disorders*. Am Psychiatric Assoc, 2013. **21**: p. 591-643.

47. Masri, S. and P. Sassone-Corsi, *The emerging link between cancer, metabolism, and circadian rhythms*. *Nature medicine*, 2018. **24**(12): p. 1795-1803.
48. Lyall, L.M., et al., *Association of disrupted circadian rhythmicity with mood disorders, subjective wellbeing, and cognitive function: a cross-sectional study of 91 105 participants from the UK Biobank*. *The Lancet Psychiatry*, 2018. **5**(6): p. 507-514.
49. Manohar, S., et al., *Associations of rotational shift work and night shift status with hypertension: a systematic review and meta-analysis*. *Journal of hypertension*, 2017. **35**(10): p. 1929-1937.
50. Antunes, L.d.C., et al., *Obesity and shift work: chronobiological aspects*. *Nutrition research reviews*, 2010. **23**(1): p. 155-168.
51. Lie, J.-A.S., J. Roessink, and K. Kjaerheim, *Breast cancer and night work among Norwegian nurses*. *Cancer Causes & Control*, 2006. **17**(1): p. 39-44.
52. Papantoniou, K., et al., *Night shift work, chronotype and prostate cancer risk in the MCC-Spain case-control study*. *International journal of cancer*, 2015. **137**(5): p. 1147-1157.
53. Knutsson, A. and H. Bøggild, *Gastrointestinal disorders among shift workers*. *Scandinavian journal of work, environment & health*, 2010: p. 85-95.
54. Dibner, C. and U. Schibler, *Circadian timing of metabolism in animal models and humans*. *Journal of internal medicine*, 2015. **277**(5): p. 513-527.
55. Marcheiva, B., et al., *Disruption of the clock components CLOCK and BMAL1 leads to hypoinsulinaemia and diabetes*. *Nature*, 2010. **466**(7306): p. 627-631.
56. Smith-Coggins, R., et al., *Relationship of day versus night sleep to physician performance and mood*. *Annals of emergency medicine*, 1994. **24**(5): p. 928-934.
57. Härmä, M., et al., *The effect of an irregular shift system on sleepiness at work in train drivers and railway traffic controllers*. *Journal of sleep research*, 2002. **11**(2): p. 141-151.
58. Costa, G., *Shift work and health: current problems and preventive actions*. *Safety and health at Work*, 2010. **1**(2): p. 112-123.
59. Partch, C.L., C.B. Green, and J.S. Takahashi, *Molecular architecture of the mammalian circadian clock*. *Trends in cell biology*, 2014. **24**(2): p. 90-99.
60. Stephan, F.K. and I. Zucker, *Circadian rhythms in drinking behavior and locomotor activity of rats are eliminated by hypothalamic lesions*. *Proceedings of the National Academy of Sciences*, 1972. **69**(6): p. 1583-1586.
61. Welsh, D.K., J.S. Takahashi, and S.A. Kay, *Suprachiasmatic nucleus: cell autonomy and network properties*. *Annual review of physiology*, 2010. **72**: p. 551-577.
62. Abrahamson, E.E. and R.Y. Moore, *Suprachiasmatic nucleus in the mouse: retinal innervation, intrinsic organization and efferent projections*. *Brain research*, 2001. **916**(1-2): p. 172-191.
63. Moore, R.Y. and J.C. Speh, *GABA is the principal neurotransmitter of the circadian system*. *Neuroscience letters*, 1993. **150**(1): p. 112-116.
64. Strecker, G.J., J.-P. Wuarin, and F.E. Dudek, *GABAA-mediated local synaptic pathways connect neurons in the rat suprachiasmatic nucleus*. *Journal of neurophysiology*, 1997. **78**(4): p. 2217-2220.
65. Brancaccio, M., et al., *Cell-autonomous clock of astrocytes drives circadian behavior in mammals*. *Science*, 2019. **363**(6423): p. 187-192.
66. Prolo, L.M., J.S. Takahashi, and E.D. Herzog, *Circadian rhythm generation and entrainment in astrocytes*. *Journal of Neuroscience*, 2005. **25**(2): p. 404-408.

67. Brancaccio, M., et al., *Astrocytes control circadian timekeeping in the suprachiasmatic nucleus via glutamatergic signaling*. *Neuron*, 2017. **93**(6): p. 1420-1435. e5.
68. Lehman, M.N., et al., *Circadian rhythmicity restored by neural transplant. Immunocytochemical characterization of the graft and its integration with the host brain*. *Journal of Neuroscience*, 1987. **7**(6): p. 1626-1638.
69. Sujino, M., et al., *Suprachiasmatic nucleus grafts restore circadian behavioral rhythms of genetically arrhythmic mice*. *Current biology*, 2003. **13**(8): p. 664-668.
70. Sinturel, F., et al., *Circadian hepatocyte clocks keep synchrony in the absence of a master pacemaker in the suprachiasmatic nucleus or other extrahepatic clocks*. *Genes & development*, 2021. **35**(5-6): p. 329-334.
71. Leone, V., et al., *Effects of diurnal variation of gut microbes and high-fat feeding on host circadian clock function and metabolism*. *Cell host & microbe*, 2015. **17**(5): p. 681-689.
72. Koronowski, K.B., et al., *Defining the independence of the liver circadian clock*. *Cell*, 2019. **177**(6): p. 1448-1462. e14.
73. Koronowski, K.B. and P. Sassone-Corsi, *Communicating clocks shape circadian homeostasis*. *Science*, 2021. **371**(6530): p. eabd0951.
74. Schibler, U., et al. *Clock-talk: interactions between central and peripheral circadian oscillators in mammals*. in *Cold Spring Harbor symposia on quantitative biology*. 2015. Cold Spring Harbor Laboratory Press.
75. Petrenko, V., et al., *Pancreatic α - and β -cellular clocks have distinct molecular properties and impact on islet hormone secretion and gene expression*. *Genes & development*, 2017. **31**(4): p. 383-398.
76. Yoo, S.-H., et al., *PERIOD2::LUCIFERASE real-time reporting of circadian dynamics reveals persistent circadian oscillations in mouse peripheral tissues*. *Proceedings of the National Academy of Sciences*, 2004. **101**(15): p. 5339-5346.
77. Yamamoto, T., et al., *Transcriptional oscillation of canonical clock genes in mouse peripheral tissues*. *BMC molecular biology*, 2004. **5**(1): p. 1-9.
78. Alvarez, J. and A. Sehgal, *The thymus is similar to the testis in its pattern of circadian clock gene expression*. *Journal of biological rhythms*, 2005. **20**(2): p. 111-121.
79. Liu, S., et al., *Chronobiological analysis of circadian patterns in transcription of seven key clock genes in six peripheral tissues in mice*. *Chronobiology international*, 2007. **24**(5): p. 793-820.
80. Dibner, C., U. Schibler, and U. Albrecht, *The mammalian circadian timing system: organization and coordination of central and peripheral clocks*. *Annual review of physiology*, 2010. **72**: p. 517-549.
81. Zhang, R., et al., *A circadian gene expression atlas in mammals: implications for biology and medicine*. *Proceedings of the National Academy of Sciences*, 2014. **111**(45): p. 16219-16224.
82. Storch, K.-F., et al., *Extensive and divergent circadian gene expression in liver and heart*. *Nature*, 2002. **417**(6884): p. 78-83.
83. Akhtar, R.A., et al., *Circadian cycling of the mouse liver transcriptome, as revealed by cDNA microarray, is driven by the suprachiasmatic nucleus*. *Current biology*, 2002. **12**(7): p. 540-550.
84. Finger, A.M., C. Dibner, and A. Kramer, *Coupled network of the circadian clocks: A driving force of rhythmic physiology*. *FEBS letters*, 2020. **594**(17): p. 2734-2769.
85. Castelo-Szekely, V., et al., *Translational contributions to tissue specificity in rhythmic and constitutive gene expression*. *Genome biology*, 2017. **18**(1): p. 1-17.

86. Damiola, F., et al., *Restricted feeding uncouples circadian oscillators in peripheral tissues from the central pacemaker in the suprachiasmatic nucleus*. *Genes & development*, 2000. **14**(23): p. 2950-2961.
87. Saini, C., et al., *Simulated body temperature rhythms reveal the phase-shifting behavior and plasticity of mammalian circadian oscillators*. *Genes & development*, 2012. **26**(6): p. 567-580.
88. Zhang, S., et al., *Signalling entrains the peripheral circadian clock*. *Cellular Signalling*, 2020. **69**: p. 109433.
89. Ueda, H.R., et al., *System-level identification of transcriptional circuits underlying mammalian circadian clocks*. *Nature genetics*, 2005. **37**(2): p. 187-192.
90. Doherty, C.J. and S.A. Kay, *Circadian control of global gene expression patterns*. *Annual review of genetics*, 2010. **44**: p. 419-444.
91. Ko, C.H. and J.S. Takahashi, *Molecular components of the mammalian circadian clock*. *Human molecular genetics*, 2006. **15**(suppl_2): p. R271-R277.
92. Yoshitane, H., et al., *Roles of CLOCK phosphorylation in suppression of E-box-dependent transcription*. *Molecular and cellular biology*, 2009. **29**(13): p. 3675-3686.
93. Ripperger, J.A. and U. Schibler, *Rhythmic CLOCK-BMAL1 binding to multiple E-box motifs drives circadian Dbp transcription and chromatin transitions*. *Nature genetics*, 2006. **38**(3): p. 369-374.
94. Lee, H.-m., et al., *The period of the circadian oscillator is primarily determined by the balance between casein kinase 1 and protein phosphatase 1*. *Proceedings of the National Academy of Sciences*, 2011. **108**(39): p. 16451-16456.
95. Keesler, G.A., et al., *Phosphorylation and destabilization of human period 1 clock protein by human casein kinase 1 ϵ* . *Neuroreport*, 2000. **11**(5): p. 951-955.
96. Hirano, A., et al., *FBXL21 regulates oscillation of the circadian clock through ubiquitination and stabilization of cryptochromes*. *Cell*, 2013. **152**(5): p. 1106-1118.
97. Reischl, S., et al., *β -TrCP1-mediated degradation of PERIOD2 is essential for circadian dynamics*. *Journal of biological rhythms*, 2007. **22**(5): p. 375-386.
98. Hirayama, J., et al., *CLOCK-mediated acetylation of BMAL1 controls circadian function*. *Nature*, 2007. **450**(7172): p. 1086-1090.
99. Asher, G., et al., *SIRT1 regulates circadian clock gene expression through PER2 deacetylation*. *Cell*, 2008. **134**(2): p. 317-328.
100. Cardone, L., et al., *Circadian clock control by SUMOylation of BMAL1*. *science*, 2005. **309**(5739): p. 1390-1394.
101. Li, Y.H., et al., *O-GlcNAcylation of PERIOD regulates its interaction with CLOCK and timing of circadian transcriptional repression*. *PLoS genetics*, 2019. **15**(1): p. e1007953.
102. Li, M.-D., et al., *O-GlcNAc signaling entrains the circadian clock by inhibiting BMAL1/CLOCK ubiquitination*. *Cell metabolism*, 2013. **17**(2): p. 303-310.
103. Asher, G., et al., *Poly (ADP-ribose) polymerase 1 participates in the phase entrainment of circadian clocks to feeding*. *Cell*, 2010. **142**(6): p. 943-953.
104. Vollmers, C., et al., *Time of feeding and the intrinsic circadian clock drive rhythms in hepatic gene expression*. *Proceedings of the National Academy of Sciences*, 2009. **106**(50): p. 21453-21458.
105. Koike, N., et al., *Transcriptional architecture and chromatin landscape of the core circadian clock in mammals*. *science*, 2012. **338**(6105): p. 349-354.
106. Menet, J.S., et al., *Nascent-Seq reveals novel features of mouse circadian transcriptional regulation*. *elife*, 2012. **1**: p. e00011.

107. Majercak, J., W.-F. Chen, and I. Edery, *Splicing of the period gene 3'-terminal intron is regulated by light, circadian clock factors, and phospholipase C*. *Molecular and Cellular Biology*, 2004. **24**(8): p. 3359-3372.
108. Majercak, J., et al., *How a circadian clock adapts to seasonal decreases in temperature and day length*. *Neuron*, 1999. **24**(1): p. 219-230.
109. Pembroke, W.G., et al., *Temporal transcriptomics suggest that twin-peaking genes reset the clock*. *Elife*, 2015. **4**: p. e10518.
110. Avitabile, D., et al., *Nucleolar localization and circadian regulation of Per2S, a novel splicing variant of the Period 2 gene*. *Cellular and molecular life sciences*, 2014. **71**(13): p. 2547-2559.
111. McGlincy, N.J., et al., *Regulation of alternative splicing by the circadian clock and food related cues*. *Genome biology*, 2012. **13**(6): p. 1-17.
112. Gotic, I., et al., *Temperature regulates splicing efficiency of the cold-inducible RNA-binding protein gene Cirbp*. *Genes & development*, 2016. **30**(17): p. 2005-2017.
113. Morf, J., et al., *Cold-inducible RNA-binding protein modulates circadian gene expression posttranscriptionally*. *Science*, 2012. **338**(6105): p. 379-383.
114. Gotic, I. and U. Schibler, *Posttranscriptional mechanisms controlling diurnal gene expression cycles by body temperature rhythms*. *RNA biology*, 2017. **14**(10): p. 1294-1298.
115. Kojima, S., E.L. Sher-Chen, and C.B. Green, *Circadian control of mRNA polyadenylation dynamics regulates rhythmic protein expression*. *Genes & development*, 2012. **26**(24): p. 2724-2736.
116. Wang, Y., et al., *Rhythmic expression of Nocturnin mRNA in multiple tissues of the mouse*. *BMC Developmental Biology*, 2001. **1**(1): p. 1-15.
117. Estrella, M.A., et al., *The metabolites NADP⁺ and NADPH are the targets of the circadian protein Nocturnin (Curled)*. *Nature communications*, 2019. **10**(1): p. 1-10.
118. Liu, Y., et al., *Cold-induced RNA-binding proteins regulate circadian gene expression by controlling alternative polyadenylation*. *Scientific reports*, 2013. **3**(1): p. 1-11.
119. Lewis, B.P., C.B. Burge, and D.P. Bartel, *Conserved seed pairing, often flanked by adenosines, indicates that thousands of human genes are microRNA targets*. *cell*, 2005. **120**(1): p. 15-20.
120. Wang, X., et al., *The crosstalk between miRNA and mammalian circadian clock*. *Current Medicinal Chemistry*, 2015. **22**(13): p. 1582-1588.
121. Du, N.-H., et al., *MicroRNAs shape circadian hepatic gene expression on a transcriptome-wide scale*. *Elife*, 2014. **3**: p. e02510.
122. Chen, R., M. D'Alessandro, and C. Lee, *miRNAs are required for generating a time delay critical for the circadian oscillator*. *Current Biology*, 2013. **23**(20): p. 1959-1968.
123. Zhou, L., et al., *A genome-wide microRNA screen identifies the microRNA-183/96/182 cluster as a modulator of circadian rhythms*. *Proceedings of the National Academy of Sciences*, 2021. **118**(1): p. e2020454118.
124. Cheng, H.-Y.M., et al., *microRNA modulation of circadian-clock period and entrainment*. *Neuron*, 2007. **54**(5): p. 813-829.
125. Nagel, R., L. Clijsters, and R. Agami, *The miRNA-192/194 cluster regulates the Period gene family and the circadian clock*. *The FEBS journal*, 2009. **276**(19): p. 5447-5455.
126. Yoo, S.-H., et al., *Period2 3'-UTR and microRNA-24 regulate circadian rhythms by repressing PERIOD2 protein accumulation*. *Proceedings of the National Academy of Sciences*, 2017. **114**(42): p. E8855-E8864.

127. Wang, J., et al., *Circadian clock-dependent and-independent posttranscriptional regulation underlies temporal mRNA accumulation in mouse liver*. Proceedings of the National Academy of Sciences, 2018. **115**(8): p. E1916-E1925.
128. Woo, K.-C., et al., *Mouse period 2 mRNA circadian oscillation is modulated by PTB-mediated rhythmic mRNA degradation*. Nucleic acids research, 2009. **37**(1): p. 26-37.
129. Kim, S.H., et al., *Rhythmic control of mRNA stability modulates circadian amplitude of mouse Period3 mRNA*. Journal of Neurochemistry, 2015. **132**(6): p. 642-656.
130. Woo, K.-C., et al., *Circadian amplitude of cryptochrome 1 is modulated by mRNA stability regulation via cytoplasmic hnRNP D oscillation*. Molecular and cellular biology, 2010. **30**(1): p. 197-205.
131. Wu, Y., et al., *Up-frameshift protein UPF1 regulates neurospora crassa circadian and diurnal growth rhythms*. Genetics, 2017. **206**(4): p. 1881-1893.
132. Kwon, Y.-J., et al., *Alternative splicing and nonsense-mediated decay of circadian clock genes under environmental stress conditions in Arabidopsis*. BMC plant biology, 2014. **14**(1): p. 1-15.
133. Ri, H., et al., *Drosophila CrebB is a substrate of the Nonsense-Mediated mRNA decay pathway that sustains circadian behaviors*. Molecules and cells, 2019. **42**(4): p. 301.
134. Reddy, A.B., et al., *Circadian orchestration of the hepatic proteome*. Current Biology, 2006. **16**(11): p. 1107-1115.
135. Robles, M.S., J. Cox, and M. Mann, *In-vivo quantitative proteomics reveals a key contribution of post-transcriptional mechanisms to the circadian regulation of liver metabolism*. PLoS genetics, 2014. **10**(1): p. e1004047.
136. Wang, J., et al., *Nuclear proteomics uncovers diurnal regulatory landscapes in mouse liver*. Cell metabolism, 2017. **25**(1): p. 102-117.
137. Chiang, C.-K., et al., *The proteomic landscape of the suprachiasmatic nucleus clock reveals large-scale coordination of key biological processes*. PLoS genetics, 2014. **10**(10): p. e1004695.
138. Sinturel, F., et al., *Diurnal oscillations in liver mass and cell size accompany ribosome assembly cycles*. Cell, 2017. **169**(4): p. 651-663. e14.
139. Houseley, J. and D. Tollervey, *The many pathways of RNA degradation*. Cell, 2009. **136**(4): p. 763-776.
140. Jaffrey, S.R. and M.F. Wilkinson, *Nonsense-mediated RNA decay in the brain: emerging modulator of neural development and disease*. Nature Reviews Neuroscience, 2018. **19**(12): p. 715-728.
141. Kurosaki, T., M.W. Popp, and L.E. Maquat, *Quality and quantity control of gene expression by nonsense-mediated mRNA decay*. Nature reviews Molecular cell biology, 2019. **20**(7): p. 406-420.
142. Fatscher, T., V. Boehm, and N.H. Gehring, *Mechanism, factors, and physiological role of nonsense-mediated mRNA decay*. Cellular and Molecular Life Sciences, 2015. **72**(23): p. 4523-4544.
143. Losson, R. and F. Lacroute, *Interference of nonsense mutations with eukaryotic messenger RNA stability*. Proceedings of the National Academy of Sciences, 1979. **76**(10): p. 5134-5137.
144. Maquat, L.E., et al., *Unstable β -globin mRNA in mRNA-deficient β^0 thalassemia*. Cell, 1981. **27**(3): p. 543-553.
145. Hodgkin, J., et al., *A new kind of informational suppression in the nematode Caenorhabditis elegans*. Genetics, 1989. **123**(2): p. 301-313.
146. Leeds, P., et al., *The product of the yeast UPF1 gene is required for rapid turnover of mRNAs containing a premature translational termination codon*. Genes & development, 1991. **5**(12a): p. 2303-2314.

147. Peltz, S.W., A.H. Brown, and A. Jacobson, *mRNA destabilization triggered by premature translational termination depends on at least three cis-acting sequence elements and one trans-acting factor*. *Genes & development*, 1993. **7**(9): p. 1737-1754.
148. Karousis, E.D. and O. Mühlemann, *Nonsense-mediated mRNA decay begins where translation ends*. *Cold Spring Harbor Perspectives in Biology*, 2019. **11**(2): p. a032862.
149. Karousis, E.D., S. Nasif, and O. Mühlemann, *Nonsense-mediated mRNA decay: novel mechanistic insights and biological impact*. *Wiley Interdisciplinary Reviews: RNA*, 2016. **7**(5): p. 661-682.
150. Franks, T.M., G. Singh, and J. Lykke-Andersen, *Upf1 ATPase-dependent mRNP disassembly is required for completion of nonsense-mediated mRNA decay*. *Cell*, 2010. **143**(6): p. 938-950.
151. Hogg, J.R. and S.P. Goff, *Upf1 senses 3' UTR length to potentiate mRNA decay*. *Cell*, 2010. **143**(3): p. 379-389.
152. Zünd, D., et al., *Translation-dependent displacement of UPF1 from coding sequences causes its enrichment in 3' UTRs*. *Nature structural & molecular biology*, 2013. **20**(8): p. 936-943.
153. Kurosaki, T., et al., *A post-translational regulatory switch on UPF1 controls targeted mRNA degradation*. *Genes & development*, 2014. **28**(17): p. 1900-1916.
154. Serin, G., et al., *Identification and characterization of human orthologues to *Saccharomyces cerevisiae* Upf2 protein and Upf3 protein (*Caenorhabditis elegans* SMG-4)*. *Molecular and cellular biology*, 2001. **21**(1): p. 209-223.
155. Chakrabarti, S., et al., *Molecular mechanisms for the RNA-dependent ATPase activity of Upf1 and its regulation by Upf2*. *Molecular cell*, 2011. **41**(6): p. 693-703.
156. Gehring, N.H., et al., *Exon-junction complex components specify distinct routes of nonsense-mediated mRNA decay with differential cofactor requirements*. *Molecular cell*, 2005. **20**(1): p. 65-75.
157. Chamieh, H., et al., *NMD factors UPF2 and UPF3 bridge UPF1 to the exon junction complex and stimulate its RNA helicase activity*. *Nature structural & molecular biology*, 2008. **15**(1): p. 85-93.
158. Neu-Yilik, G., et al., *Deniaud, A.,... Kulozik, AE (2017). Dual function of UPF3B in early and late translation termination*. *EMBO Journal*, **36** (20), 2968-2986.
159. Yamashita, A., *Role of SMG-1-mediated Upf1 phosphorylation in mammalian nonsense-mediated mRNA decay*. *Genes to Cells*, 2013. **18**(3): p. 161-175.
160. Yamashita, A., et al., *Human SMG-1, a novel phosphatidylinositol 3-kinase-related protein kinase, associates with components of the mRNA surveillance complex and is involved in the regulation of nonsense-mediated mRNA decay*. *Genes & development*, 2001. **15**(17): p. 2215-2228.
161. Kashima, I., et al., *Binding of a novel SMG-1-Upf1-eRF1-eRF3 complex (SURF) to the exon junction complex triggers Upf1 phosphorylation and nonsense-mediated mRNA decay*. *Genes & development*, 2006. **20**(3): p. 355-367.
162. Hug, N. and J.F. Cáceres, *The RNA helicase DHX34 activates NMD by promoting a transition from the surveillance to the decay-inducing complex*. *Cell reports*, 2014. **8**(6): p. 1845-1856.
163. Yamashita, A., et al., *SMG-8 and SMG-9, two novel subunits of the SMG-1 complex, regulate remodeling of the mRNA surveillance complex during nonsense-mediated mRNA decay*. *Genes & development*, 2009. **23**(9): p. 1091-1105.

164. Arias-Palomo, E., et al., *The nonsense-mediated mRNA decay SMG-1 kinase is regulated by large-scale conformational changes controlled by SMG-8*. Genes & development, 2011. **25**(2): p. 153-164.
165. Deniaud, A., et al., *A network of SMG-8, SMG-9 and SMG-1 C-terminal insertion domain regulates UPF1 substrate recruitment and phosphorylation*. Nucleic acids research, 2015. **43**(15): p. 7600-7611.
166. Gat, Y., et al., *InsP6 binding to PIKK kinases revealed by the cryo-EM structure of an SMG1–SMG8–SMG9 complex*. Nature structural & molecular biology, 2019. **26**(12): p. 1089-1093.
167. Usuki, F., et al., *Inhibition of SMG-8, a subunit of SMG-1 kinase, ameliorates nonsense-mediated mRNA decay-exacerbated mutant phenotypes without cytotoxicity*. Proceedings of the National Academy of Sciences, 2013. **110**(37): p. 15037-15042.
168. Jonas, S., O. Weichenrieder, and E. Izaurralde, *An unusual arrangement of two 14-3-3-like domains in the SMG5–SMG7 heterodimer is required for efficient nonsense-mediated mRNA decay*. Genes & development, 2013. **27**(2): p. 211-225.
169. Okada-Katsuhata, Y., et al., *N-and C-terminal Upf1 phosphorylations create binding platforms for SMG-6 and SMG-5: SMG-7 during NMD*. Nucleic acids research, 2012. **40**(3): p. 1251-1266.
170. Nicholson, P., et al., *Dissecting the functions of SMG5, SMG7, and PNRC2 in nonsense-mediated mRNA decay of human cells*. Rna, 2018. **24**(4): p. 557-573.
171. Loh, B., S. Jonas, and E. Izaurralde, *The SMG5–SMG7 heterodimer directly recruits the CCR4–NOT deadenylase complex to mRNAs containing nonsense codons via interaction with POP2*. Genes & development, 2013. **27**(19): p. 2125-2138.
172. Unterholzner, L. and E. Izaurralde, *SMG7 acts as a molecular link between mRNA surveillance and mRNA decay*. Molecular cell, 2004. **16**(4): p. 587-596.
173. Boehm, V., et al., *SMG5-SMG7 authorize nonsense-mediated mRNA decay by enabling SMG6 endonucleolytic activity*. Nature communications, 2021. **12**(1): p. 1-19.
174. Huth, M., et al., *NMD is required for timely cell fate transitions by fine-tuning gene expression and regulating translation*. Genes & development, 2022. **36**(5-6): p. 348-367.
175. Boehm, V., et al., *3' UTR length and messenger ribonucleoprotein composition determine endocleavage efficiencies at termination codons*. Cell reports, 2014. **9**(2): p. 555-568.
176. Lykke-Andersen, S., et al., *Human nonsense-mediated RNA decay initiates widely by endonucleolysis and targets snoRNA host genes*. Genes & development, 2014. **28**(22): p. 2498-2517.
177. Glavan, F., et al., *Structures of the PIN domains of SMG6 and SMG5 reveal a nuclease within the mRNA surveillance complex*. The EMBO journal, 2006. **25**(21): p. 5117-5125.
178. Eberle, A.B., et al., *SMG6 promotes endonucleolytic cleavage of nonsense mRNA in human cells*. Nature structural & molecular biology, 2009. **16**(1): p. 49-55.
179. Huntzinger, E., et al., *SMG6 is the catalytic endonuclease that cleaves mRNAs containing nonsense codons in metazoan*. Rna, 2008. **14**(12): p. 2609-2617.
180. Schmidt, S.A., et al., *Identification of SMG6 cleavage sites and a preferred RNA cleavage motif by global analysis of endogenous NMD targets in human cells*. Nucleic acids research, 2015. **43**(1): p. 309-323.
181. Nicholson, P., et al., *A novel phosphorylation-independent interaction between SMG6 and UPF1 is essential for human NMD*. Nucleic acids research, 2014. **42**(14): p. 9217-9235.

182. Ivanov, I., et al., *Identifying candidate colon cancer tumor suppressor genes using inhibition of nonsense-mediated mRNA decay in colon cancer cells*. *Oncogene*, 2007. **26**(20): p. 2873-2884.
183. Zhu, X., H. Zhang, and J.T. Mendell, *Ribosome Recycling by ABCE1 Links Lysosomal Function and Iron Homeostasis to 3' UTR-Directed Regulation and Nonsense-Mediated Decay*. *Cell reports*, 2020. **32**(2): p. 107895.
184. Li, L., et al., *Structure of a SMG8–SMG9 complex identifies a G-domain heterodimer in the NMD effector proteins*. *RNA*, 2017. **23**(7): p. 1028-1034.
185. Kunz, J.B., et al., *Functions of hUpf3a and hUpf3b in nonsense-mediated mRNA decay and translation*. *Rna*, 2006. **12**(6): p. 1015-1022.
186. Shum, E.Y., et al., *The antagonistic gene paralogs Upf3a and Upf3b govern nonsense-mediated RNA decay*. *Cell*, 2016. **165**(2): p. 382-395.
187. Yi, Z., M. Sanjeev, and G. Singh, *The branched nature of the nonsense-mediated mRNA decay pathway*. *Trends in Genetics*, 2021. **37**(2): p. 143-159.
188. Wallmeroth, D., et al., *Human UPF3A and UPF3B enable fault-tolerant activation of nonsense-mediated mRNA decay*. *The EMBO Journal*, 2022. **41**(10): p. e109191.
189. Yi, Z., et al., *Mammalian UPF3A and UPF3B can activate nonsense-mediated mRNA decay independently of their exon junction complex binding*. *The EMBO journal*, 2022. **41**(10): p. e109202.
190. Chan, W.K., et al., *An alternative branch of the nonsense-mediated decay pathway*. *The EMBO journal*, 2007. **26**(7): p. 1820-1830.
191. Gatfield, D. and E. Izaurralde, *Nonsense-mediated messenger RNA decay is initiated by endonucleolytic cleavage in Drosophila*. *Nature*, 2004. **429**(6991): p. 575-578.
192. Colombo, M., et al., *Transcriptome-wide identification of NMD-targeted human mRNAs reveals extensive redundancy between SMG6-and SMG7-mediated degradation pathways*. *Rna*, 2017. **23**(2): p. 189-201.
193. Metzke, S., et al., *Comparison of EJC-enhanced and EJC-independent NMD in human cells reveals two partially redundant degradation pathways*. *Rna*, 2013. **19**(10): p. 1432-1448.
194. Supek, F., B. Lehner, and R.G. Lindeboom, *To NMD or Not To NMD: nonsense-mediated mRNA decay in cancer and other genetic diseases*. *Trends in Genetics*, 2021. **37**(7): p. 657-668.
195. Rehwinkel, J., J. Raes, and E. Izaurralde, *Nonsense-mediated mRNA decay: Target genes and functional diversification of effectors*. *Trends in biochemical sciences*, 2006. **31**(11): p. 639-646.
196. Karousis, E.D., et al., *Nanopore sequencing reveals endogenous NMD-targeted isoforms in human cells*. *Genome biology*, 2021. **22**(1): p. 1-23.
197. Zhang, J., et al., *At least one intron is required for the nonsense-mediated decay of triosephosphate isomerase mRNA: a possible link between nuclear splicing and cytoplasmic translation*. *Molecular and cellular biology*, 1998. **18**(9): p. 5272-5283.
198. Le Hir, H., et al., *The exon–exon junction complex provides a binding platform for factors involved in mRNA export and nonsense-mediated mRNA decay*. *The EMBO journal*, 2001. **20**(17): p. 4987-4997.
199. Thermann, R., et al., *Binary specification of nonsense codons by splicing and cytoplasmic translation*. *The EMBO journal*, 1998. **17**(12): p. 3484-3494.
200. Nagy, E. and L.E. Maquat, *A rule for termination-codon position within intron-containing genes: when nonsense affects RNA abundance*. *Trends in biochemical sciences*, 1998. **23**(6): p. 198-199.

201. Hurt, J.A., A.D. Robertson, and C.B. Burge, *Global analyses of UPF1 binding and function reveal expanded scope of nonsense-mediated mRNA decay*. Genome research, 2013. **23**(10): p. 1636-1650.
202. Iacono, M., F. Mignone, and G. Pesole, *uAUG and uORFs in human and rodent 5' untranslated mRNAs*. Gene, 2005. **349**: p. 97-105.
203. Matsui, M., et al., *Bioinformatic analysis of post-transcriptional regulation by uORF in human and mouse*. FEBS letters, 2007. **581**(22): p. 4184-4188.
204. Yepiskoposyan, H., et al., *Autoregulation of the nonsense-mediated mRNA decay pathway in human cells*. Rna, 2011. **17**(12): p. 2108-2118.
205. Huang, L., et al., *RNA homeostasis governed by cell type-specific and branched feedback loops acting on NMD*. Molecular cell, 2011. **43**(6): p. 950-961.
206. Eberle, A.B., et al., *Posttranscriptional gene regulation by spatial rearrangement of the 3' untranslated region*. PLoS biology, 2008. **6**(4): p. e92.
207. French, C.E., et al., *Transcriptome analysis of alternative splicing-coupled nonsense-mediated mRNA decay in human cells reveals broad regulatory potential*. bioRxiv, 2020.
208. Karousis, E.D., et al., *Human NMD ensues independently of stable ribosome stalling*. Nature communications, 2020. **11**(1): p. 1-12.
209. Bühler, M., et al., *EJC-independent degradation of nonsense immunoglobulin- μ mRNA depends on 3' UTR length*. Nature structural & molecular biology, 2006. **13**(5): p. 462-464.
210. Kishor, A., Z. Ge, and J.R. Hogg, *hnRNP L-dependent protection of normal mRNAs from NMD subverts quality control in B cell lymphoma*. The EMBO journal, 2019. **38**(3): p. e99128.
211. Ge, Z., et al., *Polypyrimidine tract binding protein 1 protects mRNAs from recognition by the nonsense-mediated mRNA decay pathway*. Elife, 2016. **5**: p. e11155.
212. Mort, M., et al., *A meta-analysis of nonsense mutations causing human genetic disease*. Human mutation, 2008. **29**(8): p. 1037-1047.
213. Lindeboom, R.G., et al., *The impact of nonsense-mediated mRNA decay on genetic disease, gene editing and cancer immunotherapy*. Nature genetics, 2019. **51**(11): p. 1645-1651.
214. Lewis, B.P., R.E. Green, and S.E. Brenner, *Evidence for the widespread coupling of alternative splicing and nonsense-mediated mRNA decay in humans*. Proceedings of the National Academy of Sciences, 2003. **100**(1): p. 189-192.
215. Sato, H. and R.H. Singer, *Cellular variability of nonsense-mediated mRNA decay*. Nature Communications, 2021. **12**(1): p. 1-12.
216. Tani, H., et al., *Identification of hundreds of novel UPF1 target transcripts by direct determination of whole transcriptome stability*. RNA biology, 2012. **9**(11): p. 1370-1379.
217. Gardner, L.B., *Hypoxic inhibition of nonsense-mediated RNA decay regulates gene expression and the integrated stress response*. Molecular and cellular biology, 2008. **28**(11): p. 3729-3741.
218. Mendell, J.T., et al., *Nonsense surveillance regulates expression of diverse classes of mammalian transcripts and mutes genomic noise*. Nature genetics, 2004. **36**(10): p. 1073-1078.
219. Wengrod, J., et al., *Inhibition of nonsense-mediated RNA decay activates autophagy*. Molecular and cellular biology, 2013. **33**(11): p. 2128-2135.

220. Medghalchi, S.M., et al., *Rent1, a trans-effector of nonsense-mediated mRNA decay, is essential for mammalian embryonic viability*. Human molecular genetics, 2001. **10**(2): p. 99-105.
221. Weischenfeldt, J., et al., *NMD is essential for hematopoietic stem and progenitor cells and for eliminating by-products of programmed DNA rearrangements*. Genes & development, 2008. **22**(10): p. 1381-1396.
222. McIlwain, D.R., et al., *Smg1 is required for embryogenesis and regulates diverse genes via alternative splicing coupled to nonsense-mediated mRNA decay*. Proceedings of the National Academy of Sciences, 2010. **107**(27): p. 12186-12191.
223. Li, T., et al., *Smg6/Est1 licenses embryonic stem cell differentiation via nonsense-mediated mRNA decay*. The EMBO journal, 2015. **34**(12): p. 1630-1647.
224. Lou, C.-H., et al., *Nonsense-mediated RNA decay influences human embryonic stem cell fate*. Stem cell reports, 2016. **6**(6): p. 844-857.
225. Bao, J., et al., *UPF2-dependent nonsense-mediated mRNA decay pathway is essential for spermatogenesis by selectively eliminating longer 3'UTR transcripts*. PLoS genetics, 2016. **12**(5): p. e1005863.
226. Wittkopp, N., et al., *Nonsense-mediated mRNA decay effectors are essential for zebrafish embryonic development and survival*. Molecular and Cellular Biology, 2009. **29**(13): p. 3517-3528.
227. Huang, L., et al., *A Upf3b-mutant mouse model with behavioral and neurogenesis defects*. Molecular psychiatry, 2018. **23**(8): p. 1773-1786.
228. Johnson, J.L., et al., *Inhibition of Upf2-dependent nonsense-mediated decay leads to behavioral and neurophysiological abnormalities by activating the immune response*. Neuron, 2019. **104**(4): p. 665-679. e8.
229. Neu-Yilik, G., et al., *Mechanism of escape from nonsense-mediated mRNA decay of human β -globin transcripts with nonsense mutations in the first exon*. Rna, 2011. **17**(5): p. 843-854.
230. Galanello, R. and R. Origa, *Beta-thalassemia*. Orphanet journal of rare diseases, 2010. **5**(1): p. 1-15.
231. Inácio, A., et al., *Nonsense mutations in close proximity to the initiation codon fail to trigger full nonsense-mediated mRNA decay*. Journal of Biological Chemistry, 2004. **279**(31): p. 32170-32180.
232. Rebbapragada, I. and J. Lykke-Andersen, *Execution of nonsense-mediated mRNA decay: what defines a substrate?* Current opinion in cell biology, 2009. **21**(3): p. 394-402.
233. Lindeboom, R.G., F. Supek, and B. Lehner, *The rules and impact of nonsense-mediated mRNA decay in human cancers*. Nature genetics, 2016. **48**(10): p. 1112-1118.
234. Popp, M.W. and L.E. Maquat, *Nonsense-mediated mRNA decay and cancer*. Current opinion in genetics & development, 2018. **48**: p. 44-50.
235. Litchfield, K., et al., *Escape from nonsense-mediated decay associates with anti-tumor immunogenicity*. Nature communications, 2020. **11**(1): p. 1-11.
236. Goetz, A.E. and M. Wilkinson, *Stress and the nonsense-mediated RNA decay pathway*. Cellular and Molecular Life Sciences, 2017. **74**(19): p. 3509-3531.
237. Liu, C., et al., *The UPF1 RNA surveillance gene is commonly mutated in pancreatic adenocarcinoma*. Nature medicine, 2014. **20**(6): p. 596-598.
238. Cao, L., et al., *Human nonsense-mediated RNA decay regulates EMT by targeting the TGF- β signaling pathway in lung adenocarcinoma*. Cancer Letters, 2017. **403**: p. 246-259.

239. Lee, P.J., et al., *Regulation of nonsense-mediated mRNA decay in neural development and disease*. Journal of Molecular Cell Biology, 2021. **13**(4): p. 269-281.
240. Neumann, M., et al., *TDP-43 proteinopathy in frontotemporal lobar degeneration and amyotrophic lateral sclerosis: protein misfolding diseases without amyloidosis*. Archives of neurology, 2007. **64**(10): p. 1388-1394.
241. Sun, Z., et al., *Molecular determinants and genetic modifiers of aggregation and toxicity for the ALS disease protein FUS/TLS*. PLoS biology, 2011. **9**(4): p. e1000614.
242. Ju, S., et al., *A yeast model of FUS/TLS-dependent cytotoxicity*. PLoS biology, 2011. **9**(4): p. e1001052.
243. Barmada, S.J., et al., *Amelioration of toxicity in neuronal models of amyotrophic lateral sclerosis by hUPF1*. Proceedings of the National Academy of Sciences, 2015. **112**(25): p. 7821-7826.
244. Jackson, K., et al., *Preservation of forelimb function by UPF1 gene therapy in a rat model of TDP-43-induced motor paralysis*. Gene therapy, 2015. **22**(1): p. 20-28.
245. Tarpey, P.S., et al., *Mutations in UPF3B, a member of the nonsense-mediated mRNA decay complex, cause syndromic and nonsyndromic mental retardation*. Nature genetics, 2007. **39**(9): p. 1127-1133.
246. Azzalin, C.M. and J. Lingner, *The double life of UPF1 in RNA and DNA stability pathways*. Cell cycle, 2006. **5**(14): p. 1496-1498.
247. Thoren, L.A., et al., *UPF2 is a critical regulator of liver development, function and regeneration*. PLoS One, 2010. **5**(7): p. e11650.
248. Stratmann, M., et al., *Circadian Dbp transcription relies on highly dynamic BMAL1-CLOCK interaction with E boxes and requires the proteasome*. Molecular cell, 2012. **48**(2): p. 277-287.
249. Brown, S.A., et al., *Rhythms of mammalian body temperature can sustain peripheral circadian clocks*. Current Biology, 2002. **12**(18): p. 1574-1583.
250. Schuler, M., et al., *Efficient temporally controlled targeted somatic mutagenesis in hepatocytes of the mouse*. genesis, 2004. **39**(3): p. 167-172.
251. Aschoff, J. and H. Pohl, *Phase relations between a circadian rhythm and its zeitgeber within the range of entrainment*. Naturwissenschaften, 1978. **65**(2): p. 80-84.
252. Granada, A.E., et al., *Human chronotypes from a theoretical perspective*. PLoS One, 2013. **8**(3): p. e59464.
253. Gopalsamy, A., et al., *Identification of pyrimidine derivatives as hSMG-1 inhibitors*. Bioorganic & medicinal chemistry letters, 2012. **22**(21): p. 6636-6641.
254. Anand, S.N., et al., *Distinct and separable roles for endogenous CRY1 and CRY2 within the circadian molecular clockwork of the suprachiasmatic nucleus, as revealed by the Fbxl3Afh mutation*. Journal of Neuroscience, 2013. **33**(17): p. 7145-7153.
255. Li, Z., et al., *Inhibition of nonsense-mediated RNA decay by ER stress*. Rna, 2017. **23**(3): p. 378-394.
256. Rehwinkel, J., et al., *Nonsense-mediated mRNA decay factors act in concert to regulate common mRNA targets*. Rna, 2005. **11**(10): p. 1530-1544.
257. Wittmann, J., E.M. Hol, and H.-M. Jäck, *hUPF2 silencing identifies physiologic substrates of mammalian nonsense-mediated mRNA decay*. Molecular and cellular biology, 2006. **26**(4): p. 1272-1287.
258. Van Der Horst, G.T., et al., *Mammalian Cry1 and Cry2 are essential for maintenance of circadian rhythms*. Nature, 1999. **398**(6728): p. 627-630.
259. Vitaterna, M.H., et al., *Differential regulation of mammalian period genes and circadian rhythmicity by cryptochromes 1 and 2*. Proceedings of the National Academy of Sciences, 1999. **96**(21): p. 12114-12119.

260. Liu, A.C., et al., *Intercellular coupling confers robustness against mutations in the SCN circadian clock network*. Cell, 2007. **129**(3): p. 605-616.
261. Godinho, S.I., et al., *The after-hours mutant reveals a role for Fbxl3 in determining mammalian circadian period*. Science, 2007. **316**(5826): p. 897-900.
262. Xing, W., et al., *SCFFBXL3 ubiquitin ligase targets cryptochromes at their cofactor pocket*. Nature, 2013. **496**(7443): p. 64-68.
263. Miller, S., et al., *Isoform-selective regulation of mammalian cryptochromes*. Nature chemical biology, 2020. **16**(6): p. 676-685.
264. Ukai-Tadenuma, M., et al., *Delay in feedback repression by cryptochrome 1 is required for circadian clock function*. Cell, 2011. **144**(2): p. 268-281.
265. Kim, D.-Y., et al., *hnRNP Q mediates a phase-dependent translation-coupled mRNA decay of mouse Period3*. Nucleic acids research, 2011. **39**(20): p. 8901-8914.
266. Börding, T., et al., *Generation of human CRY1 and CRY2 knockout cells using duplex CRISPR/Cas9 technology*. Frontiers in physiology, 2019. **10**: p. 577.
267. Miller, S. and T. Hirota, *Structural and Chemical Biology Approaches Reveal Isoform-Selective Mechanisms of Ligand Interactions in Mammalian Cryptochromes*. Frontiers in Physiology, 2022: p. 36.
268. Kärkelä, J., et al., *The influence of anaesthesia and surgery on the circadian rhythm of melatonin*. Acta anaesthesiologica scandinavica, 2002. **46**(1): p. 30-36.
269. Van Gool, W., W. Witting, and M. Mirmiran, *Age-related changes in circadian sleep-wakefulness rhythms in male rats isolated from time cues*. Brain research, 1987. **413**(2): p. 384-387.
270. Weinert, D., *Age-dependent changes of the circadian system*. Chronobiology international, 2000. **17**(3): p. 261-283.
271. Shoji, H. and T. Miyakawa, *Age-related behavioral changes from young to old age in male mice of a C57 BL/6J strain maintained under a genetic stability program*. Neuropsychopharmacology reports, 2019. **39**(2): p. 100-118.
272. Jennings, J.H., et al., *Visualizing hypothalamic network dynamics for appetitive and consummatory behaviors*. Cell, 2015. **160**(3): p. 516-527.
273. Kolbe, I., et al., *Circadian clock network desynchrony promotes weight gain and alters glucose homeostasis in mice*. Molecular metabolism, 2019. **30**: p. 140-151.
274. Arble, D.M., et al., *Circadian timing of food intake contributes to weight gain*. Obesity, 2009. **17**(11): p. 2100-2102.
275. Guerra, G.M., et al., *Cell Type-Specific Role of RNA Nuclease SMG6 in Neurogenesis*. Cells, 2021. **10**(12): p. 3365.
276. Harbour, V.L., et al., *Phase differences in expression of circadian clock genes in the central nucleus of the amygdala, dentate gyrus, and suprachiasmatic nucleus in the rat*. PloS one, 2014. **9**(7): p. e103309.
277. Pendergast, J.S., K.D. Niswender, and S. Yamazaki, *Tissue-specific function of Period3 in circadian rhythmicity*. PloS one, 2012. **7**(1): p. e30254.
278. Shearman, L.P., et al., *Targeted disruption of the mPer3 gene: subtle effects on circadian clock function*. Molecular and cellular biology, 2000. **20**(17): p. 6269-6275.
279. DeBruyne, J.P., D.R. Weaver, and S.M. Reppert, *Peripheral circadian oscillators require CLOCK*. Current Biology, 2007. **17**(14): p. R538-R539.
280. DeBruyne, J.P., et al., *A clock shock: mouse CLOCK is not required for circadian oscillator function*. Neuron, 2006. **50**(3): p. 465-477.
281. DeBruyne, J.P., D.R. Weaver, and S.M. Reppert, *CLOCK and NPAS2 have overlapping roles in the suprachiasmatic circadian clock*. Nature neuroscience, 2007. **10**(5): p. 543-545.

282. Peirson, S.N., et al., *Comparison of clock gene expression in SCN, retina, heart, and liver of mice*. Biochemical and biophysical research communications, 2006. **351**(4): p. 800-807.
283. McManus, D., et al., *Cryptochrome 1 as a state variable of the circadian clockwork of the suprachiasmatic nucleus: Evidence from translational switching*. Proceedings of the National Academy of Sciences, 2022. **119**(34): p. e2203563119.
284. Savage, V.M., et al., *Scaling of number, size, and metabolic rate of cells with body size in mammals*. Proceedings of the National Academy of Sciences, 2007. **104**(11): p. 4718-4723.
285. Kornmann, B., et al., *System-driven and oscillator-dependent circadian transcription in mice with a conditionally active liver clock*. PLoS biology, 2007. **5**(2): p. e34.
286. Hoekstra, M.M., et al., *The sleep-wake distribution contributes to the peripheral rhythms in PERIOD-2*. Elife, 2021. **10**: p. e69773.
287. Crosby, P., et al., *Insulin/IGF-1 drives PERIOD synthesis to entrain circadian rhythms with feeding time*. Cell, 2019. **177**(4): p. 896-909. e20.
288. Kreppel, F., et al., *A DNA-based method to assay total and infectious particle contents and helper virus contamination in high-capacity adenoviral vector preparations*. Human gene therapy, 2002. **13**(10): p. 1151-1156.
289. Oishi, K., et al., *Differential expressions of mPer1 and mPer2 mRNAs under a skeleton photoperiod and a complete light-dark cycle*. Molecular brain research, 2002. **109**(1-2): p. 11-17.
290. Kaplan, M.M., *Alanine aminotransferase levels: what's normal?* Annals of internal medicine, 2002. **137**(1): p. 49-51.
291. Lehmann-Werman, R., et al., *Monitoring liver damage using hepatocyte-specific methylation markers in cell-free circulating DNA*. JCI insight, 2018. **3**(12).
292. Vitaglione, P., et al., *Coffee reduces liver damage in a rat model of steatohepatitis: the underlying mechanisms and the role of polyphenols and melanoidins*. Hepatology, 2010. **52**(5): p. 1652-1661.
293. Ghadir, M.R., et al., *The relationship between lipid profile and severity of liver damage in cirrhotic patients*. Hepatitis monthly, 2010. **10**(4): p. 285.
294. Pugh, R., et al., *Transection of the oesophagus for bleeding oesophageal varices*. British journal of surgery, 1973. **60**(8): p. 646-649.
295. Bhuvanagiri, M., et al., *NMD: RNA biology meets human genetic medicine*. Biochemical Journal, 2010. **430**(3): p. 365-377.
296. Mistlberger, R.E., *Circadian food-anticipatory activity: formal models and physiological mechanisms*. Neuroscience & Biobehavioral Reviews, 1994. **18**(2): p. 171-195.
297. Mistlberger, R.E., *Neurobiology of food anticipatory circadian rhythms*. Physiology & behavior, 2011. **104**(4): p. 535-545.
298. Storch, K.-F. and C.J. Weitz, *Daily rhythms of food-anticipatory behavioral activity do not require the known circadian clock*. Proceedings of the National Academy of Sciences, 2009. **106**(16): p. 6808-6813.
299. Stephan, F.K., J.M. Swann, and C.L. Sisk, *Entrainment of circadian rhythms by feeding schedules in rats with suprachiasmatic lesions*. Behavioral and neural biology, 1979. **25**(4): p. 545-554.
300. Yi, C.-X., et al., *Ventromedial arcuate nucleus communicates peripheral metabolic information to the suprachiasmatic nucleus*. Endocrinology, 2006. **147**(1): p. 283-294.
301. Grosbellet, E., et al., *Leptin normalizes photic synchronization in male ob/ob mice, via indirect effects on the suprachiasmatic nucleus*. Endocrinology, 2015. **156**(3): p. 1080-1090.

302. Martini, T., J.A. Ripperger, and U. Albrecht, *Measuring food anticipation in mice*. *Clocks & sleep*, 2018. **1**(1): p. 65-74.
303. Masri, S. and P. Sassone-Corsi, *Sirtuins and the circadian clock: bridging chromatin and metabolism*. *Science signaling*, 2014. **7**(342): p. re6-re6.
304. König, A.-C., et al., *The Arabidopsis class II sirtuin is a lysine deacetylase and interacts with mitochondrial energy metabolism*. *Plant physiology*, 2014. **164**(3): p. 1401-1414.
305. Masri, S., et al., *Partitioning circadian transcription by SIRT6 leads to segregated control of cellular metabolism*. *Cell*, 2014. **158**(3): p. 659-672.
306. Peek, C.B., et al., *Circadian clock NAD⁺ cycle drives mitochondrial oxidative metabolism in mice*. *Science*, 2013. **342**(6158): p. 1243417.
307. Chang, H.-C. and L. Guarente, *SIRT1 mediates central circadian control in the SCN by a mechanism that decays with aging*. *Cell*, 2013. **153**(7): p. 1448-1460.
308. Nakahata, Y., et al., *The NAD⁺-dependent deacetylase SIRT1 modulates CLOCK-mediated chromatin remodeling and circadian control*. *Cell*, 2008. **134**(2): p. 329-340.
309. Jeong, S.M., et al., *SIRT4 has tumor-suppressive activity and regulates the cellular metabolic response to DNA damage by inhibiting mitochondrial glutamine metabolism*. *Cancer cell*, 2013. **23**(4): p. 450-463.
310. Hicklin, D.J., F.M. Marincola, and S. Ferrone, *HLA class I antigen downregulation in human cancers: T-cell immunotherapy revives an old story*. *Molecular medicine today*, 1999. **5**(4): p. 178-186.
311. Knott, G.J., C.S. Bond, and A.H. Fox, *The DBHS proteins SFPQ, NONO and PSPC1: a multipurpose molecular scaffold*. *Nucleic acids research*, 2016. **44**(9): p. 3989-4004.
312. Kowalska, E., et al., *Distinct roles of DBHS family members in the circadian transcriptional feedback loop*. *Molecular and cellular biology*, 2012. **32**(22): p. 4585-4594.
313. Brown, S.A., et al., *PERIOD1-associated proteins modulate the negative limb of the mammalian circadian oscillator*. *Science*, 2005. **308**(5722): p. 693-696.
314. Kowalska, E., et al., *NONO couples the circadian clock to the cell cycle*. *Proceedings of the National Academy of Sciences*, 2013. **110**(5): p. 1592-1599.
315. Benegiamo, G., et al., *The RNA-binding protein NONO coordinates hepatic adaptation to feeding*. *Cell metabolism*, 2018. **27**(2): p. 404-418. e7.
316. Duong, H.A., et al., *A molecular mechanism for circadian clock negative feedback*. *Science*, 2011. **332**(6036): p. 1436-1439.
317. Pervouchine, D., et al., *Integrative transcriptomic analysis suggests new autoregulatory splicing events coupled with nonsense-mediated mRNA decay*. *Nucleic acids research*, 2019. **47**(10): p. 5293-5306.
318. Cunningham, F., et al., *Ensembl 2022*. *Nucleic acids research*, 2022. **50**(D1): p. D988-D995.

A novel *Smg6* mouse model reveals regulation of circadian period and daily CRY2 accumulation through the nonsense mediated mRNA decay

G. Katsioudi, R. Dreos, E. S. Arpa, S. Gaspari, A. Liechti, M. Sato, C. H. Gabriel, A. Kramer, S. A. Brown & D. Gatfield

submitted

* for the reader's convenience the figures and their legends appear within the main body of the article

1 **A novel *Smg6* mouse model reveals regulation of circadian period and daily**
2 **CRY2 accumulation through the nonsense-mediated mRNA decay pathway**

3 Georgia Katsioudi¹, René Dreos¹, Enes S. Arpa¹, Sevasti Gaspari¹, Angelica Liechti¹, Miho
4 Sato², Christian H. Gabriel³, Achim Kramer³, Steven A. Brown², David Gatfield^{1*}

5 ¹ Center for Integrative Genomics, University of Lausanne, Lausanne, Switzerland

6 ² Chronobiology and Sleep Research Group, Institute of Pharmacology and Toxicology,
7 University of Zürich, Zürich, Switzerland

8 ³ Charité Universitätsmedizin Berlin, corporate member of Freie Universität Berlin, Humboldt-
9 Universität zu Berlin, and Berlin Institute of Health, Laboratory of Chronobiology, Berlin,
10 Germany

11 *lead contact: david.gatfield@unil.ch

12 **Abstract**

13 Nonsense-mediated mRNA decay (NMD) has been intensively studied as a surveillance
14 pathway that degrades erroneous transcripts arising from mutations or RNA processing errors.
15 While additional roles in controlling regular mRNA stability have emerged, possible functions
16 in mammalian physiology *in vivo* have remained unclear. Here, we report a novel conditional
17 mouse allele that allows converting the NMD effector nuclease SMG6 from wild-type to
18 nuclease domain-mutant protein. We analyzed how NMD downregulation affects the function
19 of the circadian clock, a system known to require rapid mRNA turnover. We uncover strong
20 lengthening of free-running circadian periods for liver and fibroblast clocks, and direct NMD
21 regulation of *Cry2* mRNA, encoding a key transcriptional repressor within the rhythm-
22 generating feedback loop. In the entrained livers of *Smg6* mutant animals we reveal
23 transcriptome-wide alterations in daily mRNA accumulation patterns, altogether expanding the
24 known scope of NMD regulation in mammalian gene expression and physiology.

25 **Introduction**

26 Nonsense-mediated mRNA decay (NMD) functions as an important surveillance pathway to
27 reduce gene expression errors that arise from mutations or mis-splicing and that are
28 recognized due to aberrant translation termination on “premature translation termination
29 codons” (PTCs) (reviewed in ^{1,2}). In mammals, PTCs are defined due to their position relative
30 to an exon-junction complex (EJC), a multiprotein assembly that is deposited on mRNAs
31 during splicing and removed from the transcript by the passage of translating ribosomes.
32 Termination upstream of an EJC identifies the stop codon as aberrant, promoting the
33 formation of an NMD factor complex comprising several UPF (up-frameshift) and SMG
34 (suppressor with morphogenetic effects on genitalia) proteins. Briefly, interactions between
35 UPF1, UPF2 and UPF3 proteins trigger UPF1 phosphorylation by the kinase SMG1.
36 Phosphorylated UPF1 further recruits SMG5, SMG6 and SMG7, which are involved in
37 executing the actual mRNA degradation step. Previous models suggested two distinct,
38 redundant branches for decay involving SMG5-SMG7 (that can recruit general, non-NMD-
39 specific exonucleases) or SMG6 (an NMD-specific endonuclease); recent evidence, however,
40 argues for mechanistic overlap ³, and a linear pathway involving decay “licensing” through
41 SMG5-SMG7 followed by SMG6-mediated endonucleolytic cleavage has been proposed as
42 the main mechanism of how mRNA decay is carried out ⁴.

43 Early transcriptome-wide analyses already noted that in addition to NMD activity on aberrant
44 transcripts, the pathway can be co-opted for the decay of regular, physiological mRNAs as
45 well ⁵. Most of the initially identified NMD-activating features on endogenous transcripts are in
46 line with the above rules for PTC definition - e.g.: introns in 3' untranslated regions (UTRs);
47 translated upstream open reading frames (uORFs) in 5' UTRs; selenocysteine codons that
48 are interpreted as stop codons - yet later studies showed that long 3' UTRs can activate NMD
49 *per se*, in the absence of a downstream splice junction ^{6,7}. The generality of a “3' UTR length
50 rule” has, however, been questioned recently in a nanopore sequencing-based study that
51 (after removing the transcripts from the analysis for which there was evidence for splicing in
52 the 3' UTR) found no predictive value of 3' UTR length for NMD regulation ⁸. Independently of
53 which mechanisms trigger NMD on non-classical NMD substrates, it has been proposed that
54 the expression of up to 20-40% of genes is directly or indirectly affected when NMD is
55 inactivated in mammalian cell lines ^{4,8}, and it is tempting to speculate that the pathway may
56 have extensive functions in regular gene expression control ². It is largely unknown whether
57 this regulatory potential of NMD extends to the intact organ and living organism *in vivo*, and if
58 so, which specific molecular and physiological pathways it controls.

59 Certain physiological processes are particularly reliant on rapid, well-controlled RNA turnover;
60 conceivably, co-opting NMD could thus be especially opportune. In this respect, the circadian

61 clock stands out as an important functional system that controls daily rhythms in transcription,
62 mRNA and protein abundances, affecting thousands of genes across the organism and
63 controlling daily changes in behavior, physiology and metabolism (reviewed in ⁹). In the
64 mammalian body, the circadian system is hierarchically organized with a master clock in the
65 brain's suprachiasmatic nucleus (SCN) that synchronizes peripheral clocks that operate in
66 most cell types and that are responsible for driving cellular rhythmic gene expression
67 programs. Across cell types, clocks have a similar molecular architecture, with a core clock
68 mechanism that generates gene expression oscillations through transcription factors that
69 interact in negative feedback loops. In the main loop, BMAL1:CLOCK (BMAL1:NPAS2 in
70 neurons) function as the main activators and bind to E-box enhancers in their target genes,
71 which include the *Period* (*Per1*, *2*, *3*) and *Cryptochrome* (*Cry1*, *2*) genes. Negative feedback
72 is achieved when PER:CRY complexes translocate to the nucleus and repress their own
73 transcription by inhibiting BMAL1:CLOCK. PER and CRY protein degradation temporally limits
74 the repressive activity, eventually allowing a new cycle to ensue. Conceivably, the rapid decay
75 of *Per* and *Cry* mRNAs is critical for this mechanism - as a means of restricting PER:CRY
76 biosynthesis and availability in time - yet the responsible decay pathways remain poorly
77 investigated. Additional feedback mechanisms (in particular involving nuclear receptors of the
78 REV-ERB/ROR families) interlock with the above main feedback loop and confer both
79 robustness and plasticity to this system (reviewed in ¹⁰). Through the numerous rhythmic
80 transcriptional activities that are generated through this clockwork, rhythmic mRNA production
81 is driven at hundreds to thousands of downstream, clock-controlled genes (CCGs). The
82 stability of CCG transcripts critically determines to what extent their initial transcriptional
83 rhythm is propagated to the mRNA and protein abundance levels. Mechanisms that have been
84 implicated in post-transcriptionally regulating rhythmic mRNAs in mammals include miRNA-
85 mediated mRNA decay ¹¹ and regulated deadenylation ¹². With regard to a possible
86 involvement of NMD, first evidence for roles in the circadian system has been reported from
87 fungi, plants and flies ¹³⁻¹⁵, but how NMD globally shapes rhythmic transcriptomes, let alone in
88 a mammalian organism *in vivo*, is still unknown.

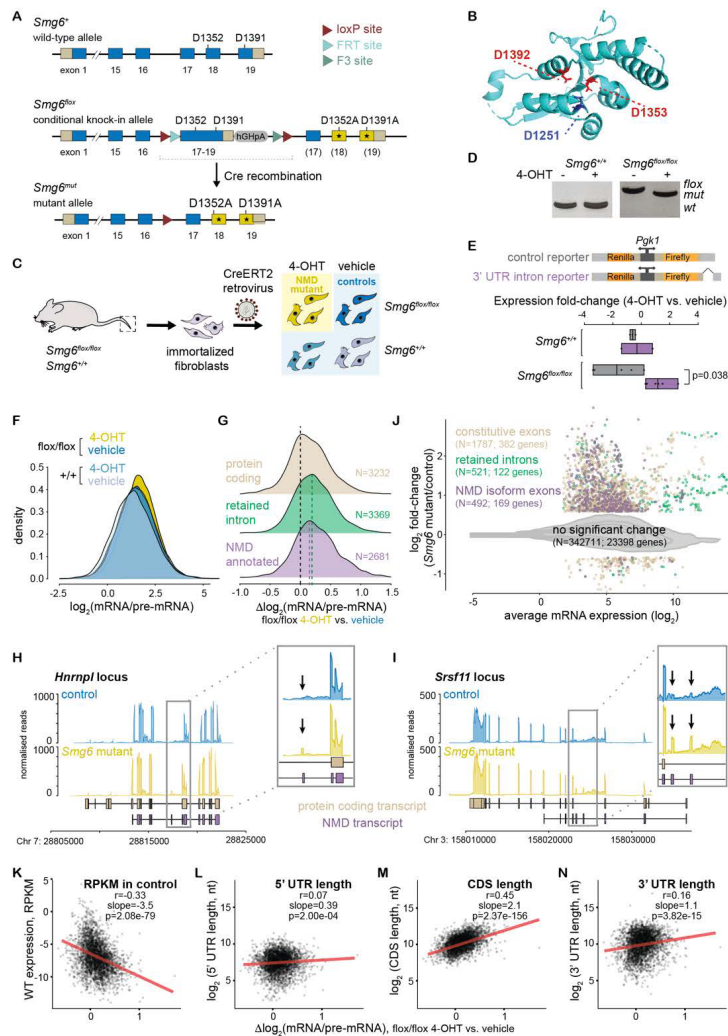
89 In this study, we have comprehensively investigated the role of NMD in the mammalian
90 circadian system *in vivo*. Using a novel conditional NMD loss-of-function mouse model, we
91 uncover that NMD is directly implicated in regulating the circadian period of peripheral clocks.
92 We identify *Cry2* as a direct NMD target and further determine how the hepatic diurnal
93 transcriptome is rewired in the absence of a functional NMD pathway. Our new mouse model
94 and findings on circadian regulation provide important conceptual advances on *in vivo*
95 functions of NMD and reveal a novel mechanism of post-transcriptional gene expression
96 regulation that acts in the mammalian core clock.

97 **Results**

98 **A novel conditional NMD loss-of-function allele based on SMG6 mutated in its nuclease**
 99 **domain**

100 To inactivate NMD *in vivo* we generated mice in which we could conditionally recombine
 101 *Smg6^{fllox}* to *Smg6^{mut}* (**Fig. 1A**), i.e. from an allele encoding wild-type SMG6 protein to a version
 102 specifically point-mutated at two of the three highly conserved aspartic acid (D) residues of
 103 the catalytic triade of the protein's PIN (PiIT N-terminus) nuclease domain¹⁶ (**Fig. 1B**). We
 104 chose this strategy over a full gene knockout because NMD factors, including SMG6, carry
 105 additional functions in telomere and genome stability¹⁷. These functions have been shown to
 106 be selectively maintained by expressing an NMD-inactive SMG6 protein lacking its nuclease
 107 domain¹⁸. We first validated our genetic model in primary tail fibroblasts from homozygous
 108 *Smg6^{fllox/fllox}* and *Smg6^{+/+}* littermate mice that we stably transduced with a retroviral vector
 109 expressing tamoxifen-activatable CreERT2 (**Fig. 1C**). *Smg6^{fllox/fllox}* cells specifically and
 110 efficiently recombined to *Smg6^{mut/mut}* by addition of 4-hydroxytamoxifen (4-OHT) to the culture
 111 medium (**Fig. 1D**). In these cells, a lentiviral luciferase reporter carrying an intron in its 3' UTR
 112 became upregulated, as expected for an inactive NMD pathway (**Fig. 1E**). We next used RNA-
 113 seq on 4-OHT-treated and -untreated cells of both genotypes to analyze gene expression
 114 changes transcriptome-wide. Our method, based on random priming of rRNA-depleted total
 115 RNA, allowed for the quantification of both mRNA (exon-mapping reads) and pre-mRNA
 116 abundances (intron-mapping reads), the latter serving as a proxy for gene transcription rates
 117^{11,19,20}. In analogy to previous studies^{11,19} we used mRNA/pre-mRNA ratios to estimate mRNA
 118 stability changes between NMD-inactive and control cells, and to distinguish them from
 119 secondary effects involving altered transcription rates. Our analyses revealed a shift to higher
 120 mRNA/pre-mRNA ratios (more stable mRNAs) specifically in NMD-inactive (*Smg6^{fllox/fllox}* + 4-
 121 OHT) cells (**Fig. 1F**). Two transcript groups that were particularly affected, as predicted, were
 122 genes with known, annotated NMD-sensitive mRNA isoforms (according to Ensembl
 123 annotations) and with retained introns (**Fig. 1G**). Visual inspection of individual examples
 124 further validated these findings, as shown for *Hnrnp1* and *Srsf11*, for which a specific up-
 125 regulation of NMD isoform-specific exons in the mutants was evident (**Fig. 1H-I**).
 126 Transcriptome-wide differential expression analysis at the exon level indicated that apart from
 127 NMD-annotated isoforms and retained introns, hundreds of constitutive exons from canonical
 128 mRNAs (i.e., without annotated NMD isoforms) increased in abundance under *Smg6* mutant
 129 conditions, pointing to widespread NMD regulation of the transcriptome (**Fig. 1J**). We next
 130 analyzed if specific transcript features correlated with *Smg6* mutation-dependent changes in
 131 mRNA/pre-mRNA ratios. As expected for potential NMD substrates, the transcripts that were
 132 most strongly affected were low expressed in control cells (**Fig. 1K**). 5' UTR length (which

133 correlates with uORF content²¹) was weakly, though significantly, associated with increased
 134 mRNA/pre-mRNA ratios (**Fig. 1L**), suggesting that translated uORFs may contribute as an
 135 NMD-activating feature to endogenous mRNA upregulation in *Smg6* mutants. Stronger
 136 correlations were observed with the lengths of the CDS (**Fig. 1M**) and 3' UTRs (**Fig. 1N**). The
 137 latter association is consistent with the ability of long 3' UTRs to function as NMD-activating
 138 features. Altogether these associations match those observed for other NMD loss-of-function
 139 models, e.g. in HeLa cells subjected to *Upf1* knockdown²². Taken together, we concluded that
 140 our genetic model based on mutant *Smg6* was suitable to analyze endogenous targets and
 141 functions of the NMD pathway.

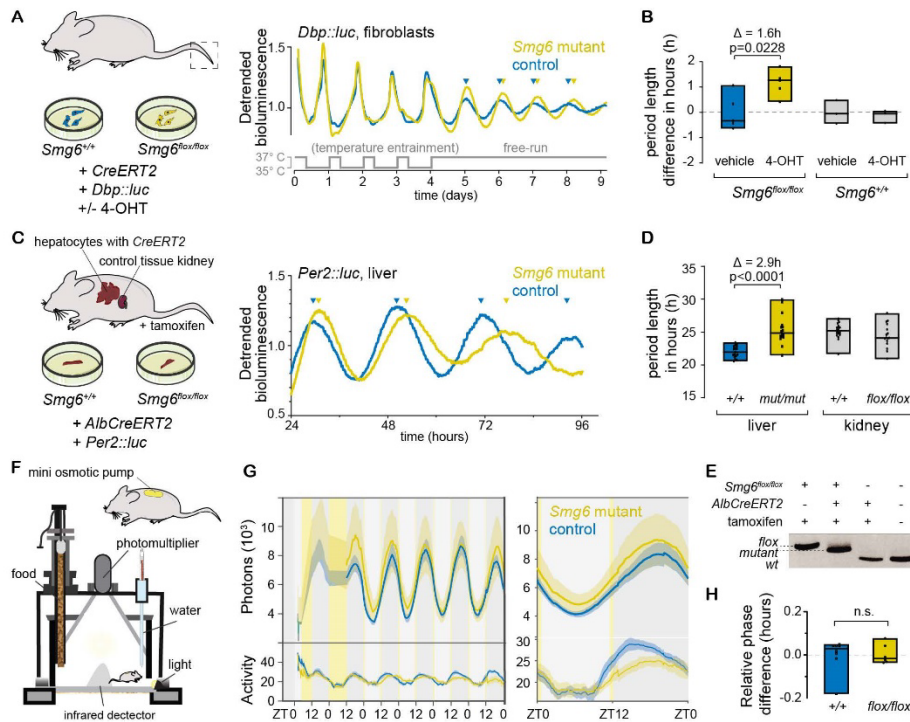


142

143 **Figure 1. A novel conditional NMD loss-of-function allele based on PIN nuclease domain mutant *Smg6*.** **A.** Schematic of the genetic
 144 model. *Smg6^{fllox}* expresses wild-type SMG6 protein encoded by the blue exons; after Cre-mediated recombination to *Smg6^{mut}*, point-mutated
 145 exons 18 and 19 (yellow) lead to expression of mutant SMG6 (D1352A, D1391A). **B.** The mutated aspartic acid residues are within the
 146 catalytic triade of the PIN nuclease domain, shown in the structure of the human protein (PDB accession 2HWW; ¹⁶). **C.** For cellular studies,
 147 tail fibroblasts from adult male mice (*Smg6^{fllox}* and wild-type littermates) were cultured until spontaneous immortalization, and tamoxifen-
 148 activatable CreERT2 expression was achieved by a retrovirus. Upon 4-hydroxytamoxifen (4-OHT) treatment, NMD mutants (yellow) were
 149 compared to different control cells (shades of blue). **D.** PCR-based genotyping of genomic DNA extracted from cells depicted in C. indicates
 150 efficient recombination upon 4-OHT treatment. **E.** A luciferase reporter containing an intron in the 3' UTR is upregulated in 4-OHT-treated
 151 *Smg6^{fllox/fllox}* cells, as expected under NMD-inactive conditions. N=2-6 plates/group, adjusted p=0.0038; multiple Student's t-test. **F.** Density
 152 plot showing transcriptome-wide mRNA/pre-mRNA ratio distributions calculated from RNA-seq, in NMD-inactive (yellow) vs. control cells.
 153 **G.** The difference in mRNA/pre-mRNA ratios between NMD-inactivated (*Smg6^{fllox/fllox}* + 4-OHT) and control cells (*Smg6^{fllox/fllox}* + vehicle) is
 154 consistent with higher stability of annotated NMD substrates (purple, N=2681) and transcripts with retained introns (green, N=3369).
 155 Moreover, the broad distribution and shift to positive values for non-NMD-annotated protein coding transcripts (beige, N=3232) is indicative
 156 of transcriptome-wide NMD regulation. **H.** Read coverage on the *Hmnp11* and *L. Srsf11* loci indicates the specific upregulation of transcript
 157 isoforms that are NMD-annotated (purple) and that can be identified via specific exons (marked by arrows in insets). **J.** Differential expression
 158 analysis at the exon level, comparing *Smg6^{fllox/fllox}* + 4-OHT vs. *Smg6^{fllox/fllox}* + vehicle conditions, reveals significant upregulation of NMD-
 159 annotated exons (purple; N=492; 169 genes), retained introns (green; N=521; 122 genes), and a sizeable number of constitutive exons
 160 (beige; N=1787, 382 genes), suggestive of NMD regulating many protein coding genes. **K.** Correlation analysis between mRNA/pre-mRNA
 161 ratio change upon NMD activation and expression levels in wild-type cells shows significant anticorrelation. The lengths of L. the 5' UTR,
 162 M. the CDS and N. the 3' UTR are all positively correlated with mRNA/pre-mRNA ratio change upon NMD inactivation. Pearson correlation
 163 coefficient (r), slope and p-values were calculated by a linear model.

164 **NMD inactivation lengthens free-running circadian periods in fibroblasts and in liver**

165 We next investigated how mutant *Smg6* affected the circadian clock. First, we stably
 166 transfected the above fibroblasts with a circadian reporter gene, *Dbp-Luciferase* ²³, and
 167 recorded their free-running circadian rhythms upon NMD inactivation with 4-OHT. Briefly, we
 168 synchronized the cellular oscillators using temperature cycles ²⁴, released them at 37°C, and
 169 continued real-time bioluminescence recordings for an additional 5 days under constant
 170 conditions (**Fig. 2A**). These experiments revealed a lengthening of the free-running circadian
 171 period in NMD-deficient cells by ca. 1.5 hours (**Fig. 2B**). We next wished to corroborate a
 172 potential period phenotype using an alternative peripheral clock model that was more relevant
 173 for circadian physiology and functions *in vivo*. We thus crossed into the *Smg6^{fllox}* mouse line a
 174 hepatocyte-specific *CreERT2* (driven from the *Albumin* locus ²⁵) and a circadian reporter,
 175 *mPer2::Luc* ²⁶. After intraperitoneal tamoxifen injections into young adult mice, animals were
 176 sacrificed 4 weeks later, a time at which highly efficient recombination to *Smg6^{mut}* had taken
 177 place (**Fig. 2E**). We then prepared organotypic slices (tissue explants) for real-time recording
 178 of luciferase rhythms *ex vivo* (**Fig. 2C**). In these experiments we observed a strong and
 179 specific period lengthening by almost 3 hours in liver explants from animals with inactivated
 180 NMD (tamoxifen-treated *Smg6^{fllox/fllox}* mice) as compared to livers from identically treated
 181 littermate animals of the control genotype (**Fig. 2D**). As an additional specificity control, we
 182 recorded kidney explant rhythms from the same animals. Free-running periods were generally
 183 longer in this organ, as reported previously ²⁶, yet we did not observe any differences between
 184 genotypes (**Fig. 2D**), in line with the hepatocyte-specificity of CreERT2 expression in our
 185 genetic model.



186

187 **Figure 2. NMD inactivation through *Smg6* mutation lengthens free-running circadian periods.** A. Real-time recording of
 188 bioluminescence rhythms in immortalized fibroblasts of genotypes *Smg6*^{flox/flox} and *Smg6*^{+/+} (both transduced with *CreERT2* retrovirus and
 189 circadian reporter *Dbp::Luc*); after temperature-entrainment (24-h periodic square wave, 35°C-37°C), cells were released into free-running
 190 conditions (37°C) from day 4. Representative traces show longer free-running period in *Smg6*^{mut} cells (yellow) as compared to control cells
 191 (blue). B. Quantification of several experiments as in A. *Smg6* mutants (yellow) showed significantly longer periods in comparison to controls
 192 (*Smg6*^{flox/flox} treated with vehicle in blue, or *Smg6*^{+/+} with/without 4-OHT in grey). N=5 for *Smg6*^{flox/flox} cells; N=3 for *Smg6*^{wt/wt} cells; period
 193 difference between 4-OHT and vehicle-treated *Smg6*^{flox/flox} cells is 1.6 hours, Bonferroni's multiple comparisons test adjusted $p=0.0228$. C.
 194 Adult *Smg6*^{flox/flox} male mice and their *Smg6*^{+/+} littermates (all carrying tamoxifen-activatable *AlbCreERT2* and the circadian reporter
 195 *Per2::Luc*) were sacrificed 4-5 weeks after tamoxifen injections. Liver and kidney explants were used for real-time recording of luciferase
 196 rhythms. Representative traces from livers show strong free-running period lengthening in the *Smg6* mutant (yellow) vs. control (blue). D.
 197 Quantification of several experiments as in C. Robustly increased periods, by almost 3 hours, were observed in NMD-deficient liver explants
 198 (yellow; mean = 25.36 ± 2.23 h) in comparison to control livers (blue; mean = 22.0 ± 0.90 h). No period length difference was observed for
 199 kidney explants from the same animals (grey; flox/flox mean \pm SD = 25.2 ± 1.19 h, control mean \pm SD = 24.4 ± 1.83 h). Liver tissue: N=16
 200 slices *Smg6*^{flox/flox}; N=17 slices for controls; Mann-Whitney test $p<0.0001$. Kidney tissue: N=16 for *Smg6*^{flox/flox}; N=20 for controls, Mann-
 201 Whitney test $p=0.0771$. 1-4 tissue slices were used per mouse; analyses performed blindly. E. Efficient recombination was validated by
 202 genotyping of livers (PCR analysis of genomic DNA). F. Cartoon depicting the *in vivo* recording setup (RT-Biolumicorder); *Smg6*^{flox/flox} or
 203 *Smg6*^{+/+} mice carrying *AlbCreERT2* and *mPer2::Luc* alleles were implanted with a luciferin-loaded mini osmotic pump 4 weeks after
 204 tamoxifen injections before placing in the recording device. G. Left panel: After 2 days under LD12:12, bioluminescence rhythms (photons)
 205 and activity (infrared signal) were recorded for 5 days under photoskeleton photoperiod conditions (indicated by yellow vertical lines at ZT12
 206 and before ZT0). The plot shows mean signal (solid trace) and SEM (shaded) over the whole course of the experiment in the left panel,
 207 and compiled data, averaged from all days and mice, in the right panel. H. Quantification of PER2::LUC bioluminescence signal showed no
 208 difference in phase between tamoxifen-injected *Smg6*^{flox/flox} (yellow) and *Smg6*^{+/+} (blue) control animals. N=6 per group; Mann-Whitney test
 209 $p=0.7251$.

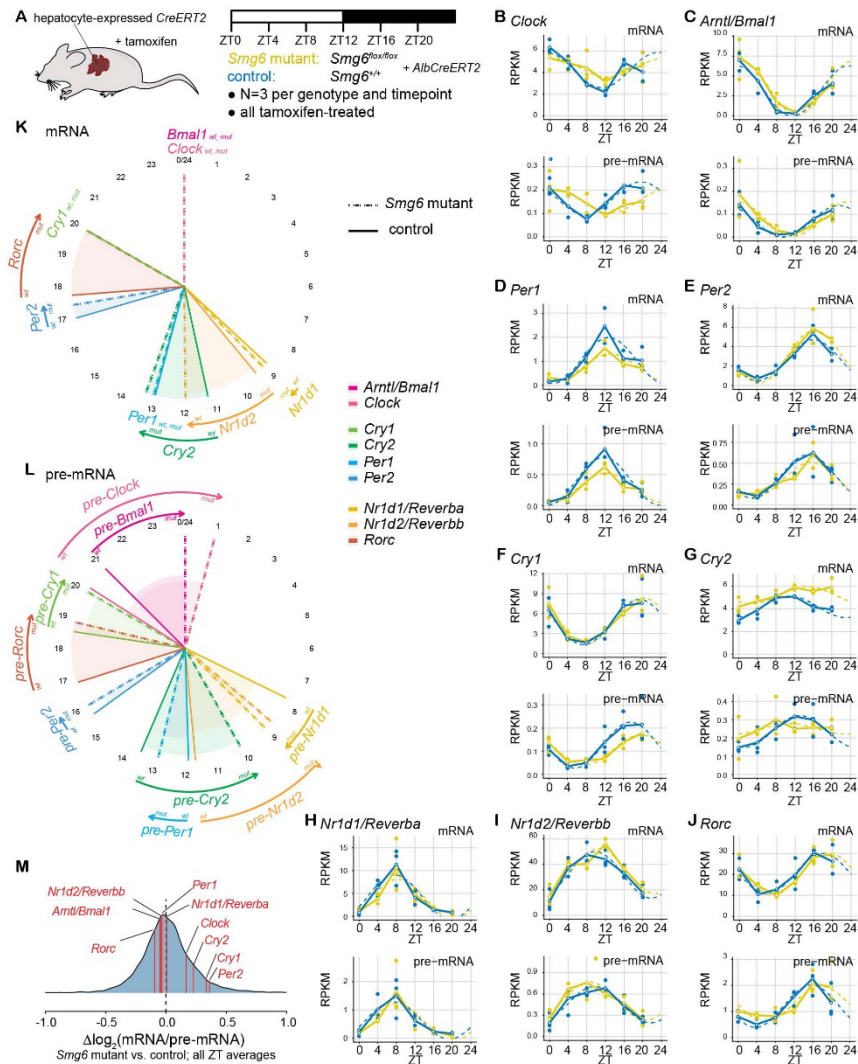
210 *In vivo*, and according to oscillator theory^{27,28}, a difference in period lengths between the
 211 entraining clock (here: wild-type period SCN) and the entrained clock (here: long period *Smg6*
 212 mutant hepatocytes) will typically translate to a phase shift of the entrained oscillator. Thus,
 213 we expected that the long period mPER2-Luc rhythms seen in liver explants *ex vivo* would
 214 lead to a change in phase *in vivo*. To evaluate this prediction, we used a method for the real-
 215 time recording of daily liver gene expression in freely moving mice^{29,30} that relies on luciferase
 216 reporters, luciferin delivery via an osmotic minipump, and highly sensitive bioluminescence
 217 photon counting (**Fig. 2F**). Using the same *mPer2::Luc* reporter knock-in animals (NMD-
 218 deficient vs. controls) as for the above tissue explant experiments, real-time recording was
 219 carried out under conditions that ensured light-entrainment of the SCN clock to an external
 220 24-hour light-dark cycle by means of a skeleton photoperiod, i.e. two 30 min light pulses
 221 applied at times corresponding to the beginning and to the end of the light phase in a 12h-
 222 light-12h-dark (LD12:12) cycle. We observed high-amplitude rhythmic bioluminescence
 223 rhythms in both genotypes (**Fig. 2G**) with phases that were, however, indistinguishable (**Fig.**
 224 **2H**). Next, we also investigated the effect of the *Smg6* mutation on the central clock in the
 225 SCN. We stereotactically injected an adeno-associated virus (AAV) expressing Cre::eGFP to
 226 induce recombination (**Fig. S1A, B**) and scored circadian clock parameters by two different
 227 assays: *in vivo*, we measured behavioral locomotor rhythms under constant conditions (free-
 228 running clock) by running wheel assays (**Fig. S1C, D**) and *ex vivo*, we recorded mPER2::LUC
 229 rhythms from SCN explants (**Fig. S1E, F**). Neither assay revealed an effect of the *Smg6*
 230 mutation on free-running periods for the SCN clock; yet, as a caveat, we also noted overall
 231 less efficient recombination as compared to our liver experiments (**Fig. S1G**). We concluded
 232 that loss of NMD triggered by the *Smg6* mutant allele had a strong period lengthening effect,
 233 notably for peripheral clocks and in particular in liver explants.

234 **NMD inactivation differentially affects the phases of core clock gene expression in the**
 235 **entrained liver**

236 We next analyzed the apparent discrepancy between the long periods of liver rhythms *ex vivo*
 237 (**Fig. 2C, D**) and the lack of a phase phenotype *in vivo* (**Fig. 2G, H**). Briefly, other tissues than
 238 liver (e.g. kidney³¹) may have contributed to the overall bioluminescence signal detected in
 239 the *in vivo* recording experiments, thereby masking a hepatic phase phenotype. Moreover,
 240 systemic cues that are dependent on the SCN, yet do not require a functional hepatocyte
 241 clock, can drive rhythmic PER2 accumulation in liver^{32,33}; therefore, mPER2::LUC signal may
 242 not be representative of the intrinsic liver clock phase. In order to evaluate in a comprehensive
 243 fashion how rhythmic gene expression was altered *in vivo*, we collected livers at 4-hour
 244 intervals around-the-clock from LD12:12-entrained *Smg6* mutant and control mice, with
 245 timepoints ZT0 (*Zeitgeber* Time 0, corresponding to time of "lights-on"), ZT4, ZT8, ZT12

246 (“lights-off”), ZT16 and ZT20 (**Fig. 3A**). We carried out RNA-seq on all individual mouse liver
 247 samples (triplicates per genotype and timepoint) and assembled the data into two time series
 248 representing the diurnal liver transcriptome under conditions of an inactive vs. active NMD
 249 pathway. As a means of quality control, we first validated that known NMD targets were
 250 upregulated in *Smg6* mutant livers. Indeed, as in the fibroblasts (**Fig. 1H, I**), NMD-annotated
 251 isoform exons were increased in abundance (**Fig. S2A**). Other transcripts diagnostic for an
 252 inactive NMD pathway showed the expected post-transcriptional upregulation as well. For
 253 example, mRNAs encoding components of the NMD machinery itself were post-
 254 transcriptionally upregulated (**Fig. S2B**), as reported previously from cell lines ⁷. This
 255 phenomenon has been proposed to represent an autoregulatory mechanism that involves as
 256 NMD-activating features the long 3' UTRs that these mRNAs carry. Similarly, the uORF-
 257 regulated *Atf4* and *Atf5* transcripts, which are documented NMD substrates ^{5,34} and encode
 258 key transcription factors in the integrated stress response (ISR) ³⁵, showed the expected
 259 upregulation (**Fig. S2C**). Of note, higher ATF5 protein accumulation (**Fig. S2D, E**) occurred in
 260 the absence of general ISR activation (as judged by eIF2 α phosphorylation levels that were
 261 only weakly affected; **Fig. S2D**), pinpointing the lack of direct NMD regulation rather than
 262 proteotoxic stress as the likely trigger.

263 We then analyzed the daily dynamics of core clock gene expression at the mRNA and pre-
 264 mRNA levels (**Fig. 3B-J**). Consistent with the *in vivo* recording of *mPer2::Luc* animals, *Per2*
 265 mRNA and pre-mRNA rhythms were highly similar between the two genotypes (**Fig. 3E**). By
 266 contrast, several other core clock genes - notably those encoding the main transcriptional
 267 activators, *Clock* and *Arntl/Bmal1* (**Fig. 3B, C**), as well as *Cry1* (**Fig. 3F**) and *Rorc* (**Fig. 3J**) -
 268 showed phase-delayed pre-mRNAs indicative of transcription occurring several hours later.
 269 The complete analysis of core clock mRNA (**Fig. 3K**) and pre-mRNA (**Fig. 3L**) rhythms
 270 revealed that the considerable phase differences seen for many core clock genes at the
 271 transcriptional (pre-mRNA) level (**Fig. 3L**), only partially propagated to the mRNA level (**Fig.**
 272 **3K**). Of the core loop constituents, *Cry2* mRNA showed a substantial delay by ca. 2 hours
 273 (**Fig. 3G, K**). The later phase did not have its origins in the timing of transcription, which rather
 274 appeared to be advanced (**Fig. 3G, L**). Other delays in mRNA accumulation that we observed
 275 affected the two nuclear receptors and components of the stabilizing loop, *Nr1d2/Rev-erbb*
 276 and *Rorc* (**Fig. 3H, J, K**).

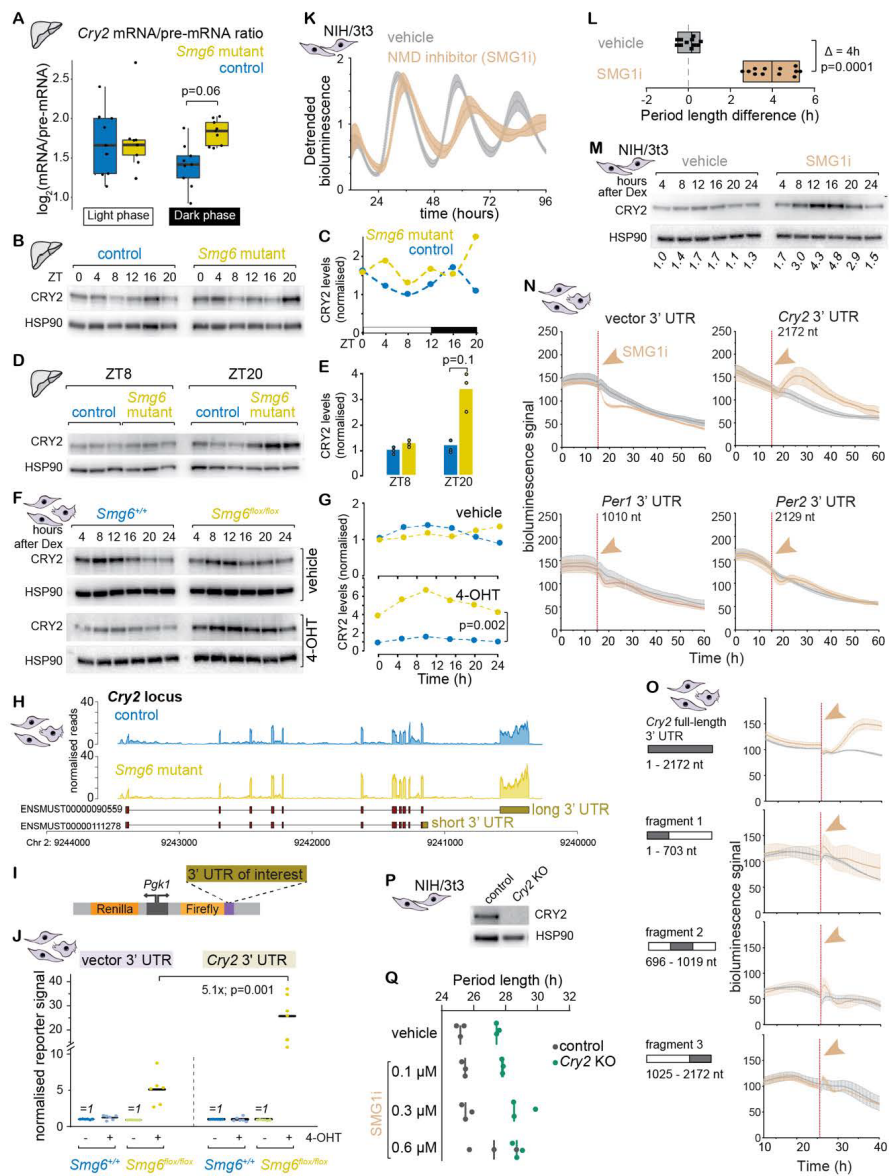


277

278 **Figure 3. *Smg6* mutation differentially affects hepatic core clock pre-mRNA and mRNA rhythms.** **A.** Schematic of the around-the-
 279 clock RNA-seq experiment, which was carried out on a time series of liver samples collected from LD12:12-entrained male *Smg6* mutant
 280 (*Smg6^{flax/flax}; AlbCreERT2*; tamoxifen-treated) and control (*Smg6^{+/+}; AlbCreERT2*; tamoxifen-treated) mice. **B–J.** RNA-seq data is plotted
 281 for indicated core clock genes for mRNA (upper panels; exonic reads) and pre-mRNA (lower panels; intronic reads) for *Smg6* mutants
 282 (yellow) and controls (blue). RPKM values (Reads Per Kilobase of transcript, per Million mapped reads) of individual mice are shown as
 283 dots with solid lines connecting the means for each timepoint. The dashed lines represent the rhythmic data fit using the parameters from
 284 Metacycle³⁶. **K.** Circular plot representing the phases of peak mRNA abundances according to the Metacycle fits for *Smg6* mutants (dashed)
 285 and controls (solid) for indicated core clock genes. *Cry2*, *Nr1d2* and *Rorc* accumulated several hours later in *Smg6* mutants, whereas minor
 286 effects were seen for the other genes. **L.** As in **K.** but for pre-mRNA rhythms. Several core clock pre-mRNAs showed later phases, indicative
 287 of transcriptional shifts; notable exceptions being *Per2* (almost invariable) and *Cry2* and *Nr1d2*, which both showed a phase advance. **M.**
 288 Similar to Fig. 1F, mRNA/pre-mRNA ratios were calculated for the liver RNA-seq data, briefly, average mRNA counts were first averaged
 289 over all samples per genotype, before dividing by average pre-mRNA counts. Three components of the negative limb, *Cry2*, *Cry1* and *Per2*,
 290 show higher mRNA/pre-mRNA ratios in *Smg6* mutants.

291 **NMD regulation of *Cry2* mRNA occurs through its 3' UTR and limits CRY2 protein**
292 **accumulation in the dark phase**

293 Among the core clock genes, the observed change in the daily *Cry2* expression profile (i.e. a
294 peak in *Cry2* mRNA levels at ZT8-12 with subsequent decrease in control animals; yet *Cry2*
295 mRNA abundances persisting on a high plateau until ZT20 in *Smg6* mutants; **Fig. 3G**) was
296 consistent with the hypothesis that the *Cry2* transcript became stabilized in the absence of
297 NMD. Indeed, the analysis of *Cry2* mRNA/pre-mRNA ratios across all liver samples suggested
298 elevated stability during the dark phase of the cycle (ZT12-20) (**Fig. 4A**). Western blot analysis
299 of total liver proteins revealed that the prolonged mRNA abundance under NMD-inactive
300 conditions led to corresponding changes in the levels of CRY2 protein, whose peak
301 accumulation was delayed by 4 hours in *Smg6* mutant animals (peak at ZT20) compared to
302 controls (peak at ZT16) (**Fig. 4B, C**). Moreover, the analysis of individual livers showed that
303 CRY2 reproducibly accumulated to >2x higher levels in *Smg6* mutant livers towards the end
304 of the dark phase, at ZT20 (**Fig. 4D, E**). Furthermore, increased CRY2 levels were also
305 apparent in *Smg6* mutant fibroblasts (**Fig. 4F, G**). These observations were consistent with a
306 direct regulation of *Cry2* mRNA stability through NMD. To explore this hypothesis, we
307 analyzed whether the *Cry2* mRNA contained any specific NMD-activating features. First, we
308 inspected RNA-seq coverage on the *Cry2* locus in our fibroblast data, which revealed the
309 expression of a single *Cry2* transcript isoform carrying a long 3' UTR of ~2.2 kb (**Fig. 4H**;
310 identical observations were made in the liver RNA-seq data; data not shown), i.e. well beyond
311 the ~1 kb cut-off that has been used as a benchmark for the definition of potential endogenous
312 NMD substrates^{2,6,7}. There was no evidence that a second annotated mRNA isoform with a
313 shorter 3' UTR (~0.4 kb; **Fig. 4H**) or any other, additional transcript variants were generated
314 from the locus. Finally, with a 5' UTR that is particularly short (20 nt) and no evidence for
315 translating ribosomes upstream of the annotated start codon according to previous ribosome
316 profiling data from liver²¹ or murine fibroblasts³⁷ (data not shown), we excluded the possibility
317 that the transcript contained NMD-activating uORFs. We thus assessed whether the ~2.2 kb
318 *Cry2* 3' UTR would confer NMD regulation to a luciferase reporter gene (**Fig. 4I**). Dual
319 luciferase assays revealed that inactivating NMD in fibroblasts led to a >5-fold activity increase
320 for the *Cry2* 3' UTR-carrying reporter as compared to the control reporter (**Fig. 4J**), providing
321 evidence that the *Cry2* 3' UTR acts to elicit NMD.



322

323 **Figure 4. NMD regulation of *Cry2* mRNA via its 3' UTR.** A. mRNA/pre-mRNA ratios across individual liver samples – grouped into light
 324 (ZT0, 4, 8) and dark phase (ZT12, 16, 20) samples – indicate *Cry2* mRNA stability increase in *Smg6* mutants, (which is visible in particular in
 325 the dark phase; p-value=0.06; ANOVA). B. Western blot analysis of total liver proteins, for CRY2 and HSP90 (loading control). Each sample
 326 is a pool of 3 individual mice. C. Quantification of Western blot shown in B; CRY2 intensity was normalized to the loading control, HSP90.
 327 D. Western blot as in panel B, but from individual animals at ZT8 and ZT20, indicating that CRY2 is reproducibly more abundant at ZT20 in
 328 *Smg6* mutants. E. Quantification of Western blot in D; p=0.1; Mann-Whitney non-parametric test. F. Western blot analysis of total protein
 329 extract from fibroblasts (cells as shown in Fig. 1C) reveals CRY2 upregulation specifically in 4-OHT-treated *Smg6^{lox/lox}* cells. G.
 330 Quantification of Western blot shown in F; p=0.002; Mann-Whitney non-parametric test. H. RNA-seq read coverage on the *Cry2* locus

331 (fibroblasts). Only one transcript isoform - carrying the 2.2 kb 3' UTR - is expressed; there is no evidence for expression of the short UTR
 332 isoform. I. Schematic of the lentiviral dual luciferase system used in assays to test 3' UTRs of interest for NMD regulation. J. Dual-luciferase
 333 assays reveal that the *Cry2* 3' UTR confers NMD regulation. Non-treated cells for each genotype/reporter were internally set to 1. Vector
 334 UTR alone shows ca. 5-fold upregulation under *Smg6^{lox/lox}* + 4-OHT conditions (an effect coming from both Firefly luciferase up- and Renilla
 335 luciferase downregulation). Against this background of the assay, the *Cry2* 3' UTR confers an additional >5-fold increase. Cells of each
 336 genotype/reporter condition without 4-OHT treatment were internally set to 1, and the signal of 4-OHT-treated cells relative to these untreated
 337 cells is reported; N=5 from 3 different experiments; p=0.001; Mann-Whitney non-parametric test. K. Bioluminescence traces of NIH/3T3 cells
 338 carrying the DBP-Luciferase reporter, with (orange) and without (grey) 0.6 μ M SMG1i treatment. Traces show average (mean) signal and
 339 standard deviation from 3 independent experiments. L. Quantification of experiments shown in K, showing reproducible period lengthening
 340 by ca. 4h in the presence of 0.6 μ M SMG1i (N=11-12; p<0.001; Mann-Whitney test). M. Western blot analysis of total protein extract from
 341 NIH/3T3 cells treated with vehicle or 0.6 μ M SMG1i; values of CRY2 abundance normalized to HSP90 (loading control) below the lanes. N.
 342 Primary fibroblast (genotype *Smg6^{+/+}*, no 4-OHT) were stably transduced with luciferase reporters carrying different 3' UTRs (as in panel I).
 343 Real-time recording of Firefly luciferase signal was carried until the signal reached stable state, before addition of 1 μ M SMG1i (orange) or
 344 vehicle (grey). The reporter carrying the *Cry2* 3' UTR was specifically upregulated, as compared to *Per1*, *Per2* or vector 3' UTRs. Traces
 345 show average (mean) signal and standard deviation; N=3. O. In assays as in N., only full-length *Cry2* 3' UTR showed upregulation upon
 346 SMG1i treatment, but not individual fragments (N=2). P. Western blot showing absence of CRY2 in Crispr/Cas9-generated *Cry2* knockout
 347 NIH/3T3 cells. Q. Period length of *Dbp*-luciferase reporter traces in NIH/3T3 cells - controls (grey) or *Cry2* knockouts (green) - treated with
 348 0.1 μ M, 0.3 μ M or 0.6 μ M of SMG1i or with vehicle (DMSO) corresponding to the volume used in highest SMG1i treatment.

349 We wished to further validate NMD regulation of the *Cry2* 3' UTR by an approach that would
 350 allow more rapid and direct readout of reporter activity after NMD inhibition, rather than having
 351 to rely on prolonged 4-OHT treatment of reporter-expressing cells to induce the *Smg6*
 352 mutation. To this end, we used a pharmacological inhibitor of the kinase SMG1, hSMG-1
 353 inhibitor 11e (SMG1i in the following)³⁸. Briefly, for this compound an IC50 in the sub-
 354 nanomolar range had originally been reported³⁸, yet subsequent studies *in vitro*³⁹ and in cells
 355 (e.g.⁴⁰) have applied SMG1i at considerable higher concentrations (0.2-1 μ M) to inhibit NMD;
 356 additional effects on other kinases (e.g. mTOR³⁸) cannot be excluded under these conditions.
 357 Indeed, we observed a strong effect of 0.6 μ M SMG1i on circadian period in two commonly
 358 used circadian model cell lines, murine NIH/3T3 fibroblasts (**Fig. 4K, L**) and human U2OS
 359 osteosarcoma cells (**Fig. S3**). Of note, the period lengthening phenotype caused by the
 360 compound (~4 hours; **Fig. 4L**) was considerably stronger than that seen in the genetic *Smg6*
 361 fibroblast model (~1.5 hours; **Fig. 2B**), in line with possibly broader activity of SMG1i.
 362 Moreover, cellular toxicity was observable after prolonged SMG1i treatment for several days
 363 (data not shown). We thus concluded that this compound would be most appropriate for short-
 364 term NMD inhibition up to 24 hours, which is also the timeframe in which it increased
 365 endogenous CRY2 protein abundance (**Fig. 4M**). We then assessed how acute SMG1i
 366 treatment affected the activity of lentivirally delivered luciferase reporters carrying various core
 367 clock gene 3' UTRs, using real-time bioluminescence recording in mouse fibroblasts. Upon
 368 addition of SMG1i, output from a reporter carrying the *Cry2* 3' UTR increased rapidly within a
 369 few hours (**Fig. 4N**). By contrast, neither the vector 3' UTR, nor the 3' UTRs of other core clock
 370 genes that were similar in length to the *Cry2* 3' UTR, namely that of *Per1* (~1 kb) and *Per2*
 371 (~2.1 kb), showed increased reporter output. Based on this outcome, we concluded that the
 372 *Cry2* 3' UTR was a specific target of the NMD pathway. We next reasoned that the *Cry2* 3'

373 UTR may be NMD-activating due to its length or, alternatively, that it could contain specific
374 *cis*-acting elements important for NMD activity, e.g. specific binding sites for RNA binding
375 proteins (RBPs). To distinguish between these two scenarios, we tested individual,
376 overlapping fragments of the full-length *Cry2* 3' UTR in the reporter assay. In contrast to full-
377 length *Cry2* 3' UTR, none of the fragments was associated with reporter upregulation upon
378 SMG1i treatment (**Fig. 4O**). We concluded that most likely the considerable length of the *Cry2*
379 3' UTR was responsible for downregulation via NMD.

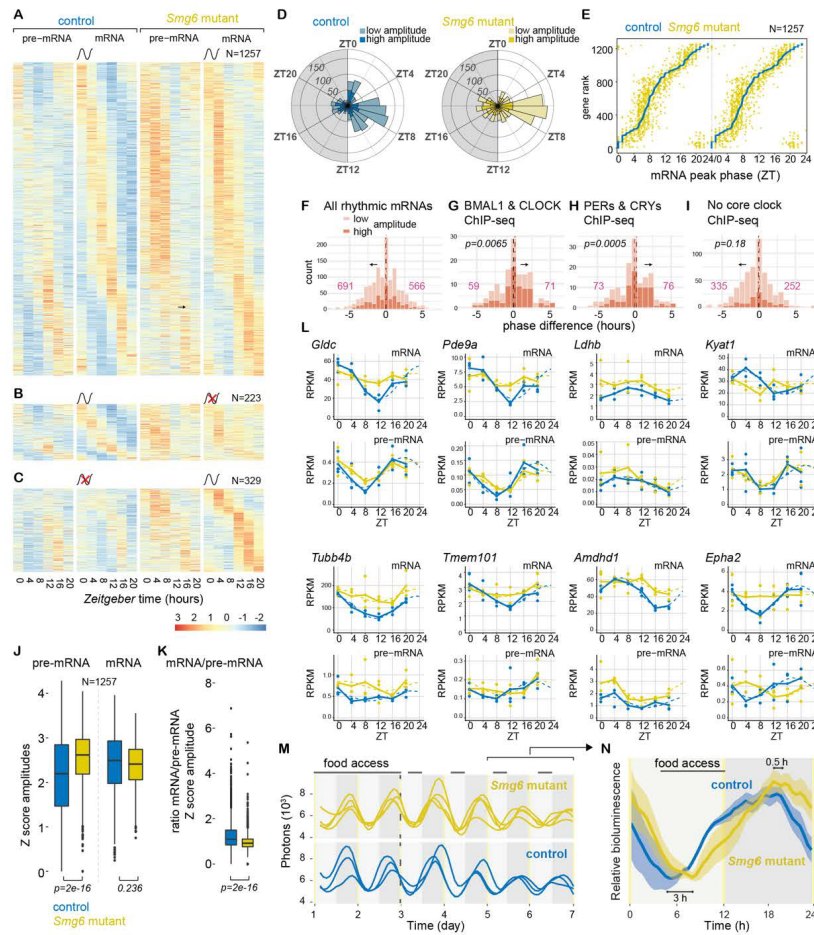
380 With NMD downregulation leading, on the one hand, to longer periods and, on the other hand,
381 to altered abundance and accumulation dynamics of CRY2, we next attempted to investigate
382 whether there was a causal link between both effects. To this end, we produced *Cry2*-deficient
383 NIH/3t3 cells (**Fig. 4P**). We treated these cells with SMG1i, based on the reasoning that NMD
384 inhibition may have a less severe phenotype in the absence of a functional *Cry2* gene.
385 However, in this setup we did not uncover an evident modulation of SMG1i-mediated period
386 lengthening by the absence of *Cry2* (**Fig. 4Q**). A similar outcome was obtained in *Cry2*-
387 deficient U2OS cells (**Fig. S3**). We concluded that the SMG1i-provoked period phenotype was
388 not dependent on *Cry2*. However, given the questions surrounding the specificity of SMG1i
389 detailed above, an interaction of the phenotype with *Cry2* may have been masked by other,
390 stronger effects of the compound. Dedicated experiments using *Smg6^{mut}* cells/livers will thus
391 be required in the future to evaluate to what extent NMD-mediated regulation of *Cry2*
392 contributes to period lengthening.

393 **Transcriptome-wide analyses uncover the extent of rhythmic gene expression** 394 **reprogramming in the entrained liver**

395 We next analyzed how, beyond the core clock genes (**Fig. 3**), the global rhythmic
396 transcriptome was affected in *Smg6* mutant livers *in vivo*. Our expectation was that we would
397 find a complex overlay of direct and indirect effects, due to (i) NMD directly controlling the
398 mRNA stability for some clock-controlled output genes, which would post-transcriptionally
399 impact on their amplitudes and phases; (ii) the altered phase of *Cry2* and other core clock
400 components (**Fig. 3K**) impacting on the transcriptional timing and dynamics at clock-controlled
401 loci; and (iii) additional secondary consequences that could be both transcriptional and post-
402 transcriptional in nature, as a result of the above effects. We first investigated whether there
403 were global changes in the populations of rhythmic transcripts between the two genotypes,
404 analyzing the RNA-seq datasets from the above cohort (**Fig. 3A**). Using established
405 rhythmicity detection algorithms (MetaCycle R package ³⁶), we found that the majority of
406 mRNAs classified as rhythmic in controls were also rhythmic in the *Smg6* mutant livers
407 (N=1257; **Fig. 5A**) and visual inspection of the pre-mRNA heatmaps further suggested that
408 most of these rhythms were of transcriptional origin. A lower number of transcripts passed the

409 rhythmicity criteria in only one of the genotypes, indicating possible loss (N=223; **Fig. 5B**) or
410 gain (N=323; **Fig. 5C**) of oscillations in the *Smg6* mutants. Inspection of the heatmaps,
411 however, indicated that in many cases, the alleged lack of rhythmicity in one or the other
412 genotype was probably the result of effects such as lower/noisier expression levels rather than
413 clear-cut loss of daily oscillations (a well-known phenomenon when comparing rhythmic gene
414 expression datasets, see ^{41,42}). We thus first focused our analyses on the common mRNA
415 rhythmic genes. Their peak phase distributions globally resembled each other in the two
416 genotypes (**Fig. 5D**). A large group of mRNAs showed maximal abundance around ZT6-12
417 (an interval that overlaps with the expected peak mRNA phase of direct BMAL1:CLOCK
418 targets containing E-box enhancers ⁴³), and this cluster appeared phase-advanced in *Smg6*
419 mutants. Moreover, several phases were underrepresented in mutants as compared to
420 controls, such as the distinct group of transcripts with maximal abundance at the beginning of
421 the light phase (ZT0-2) in controls that was absent in *Smg6* mutant livers (**Fig. 5D**). For a more
422 quantitative analysis of these effects, we calculated transcript-specific phase differences,
423 which indicated that mRNA phases in *Smg6* mutants globally followed those in controls, with
424 advances and delays spread out across the day (**Fig. 5E**). Overall, more transcripts were
425 phase advanced than delayed in *Smg6* mutant livers (**Fig. 5F**). This outcome was unexpected
426 given that the expression profiles for core clock transcripts (**Fig. 3B-J**), and specifically the
427 findings on *Cry2* (**Fig. 4**), had rather pointed towards a delay of the entrained liver clock in
428 *Smg6* mutants. To investigate these observations further, we overlaid our rhythmic transcript
429 set with data from a large circadian mouse liver ChIP-seq study ²⁰. Our analyses revealed that
430 mRNAs arising from loci with binding sites for BMAL1 and CLOCK (**Fig. 5G**) or PER and CRY
431 proteins (**Fig. 5H**) were indeed significantly skewed towards phase delays, in contrast to
432 rhythmic genes that were not direct targets of these core clock proteins (**Fig. 5I**). We
433 concluded that multiple factors engendered phase changes at the rhythmic transcriptome level
434 in *Smg6* mutants, manifesting in delays for many direct BMAL1:CLOCK targets, and overall
435 advanced phases for many other rhythmically expressed mRNAs. Next, we compared peak-
436 to-trough amplitudes between the genotypes, given that for rhythmic mRNAs that are direct
437 targets of NMD, increased transcript stability in *Smg6* mutants should lead to amplitude
438 reduction. To explore this possibility, we used the Z-scores (**Fig. 5A**) for the common rhythmic
439 transcripts to calculate the amplitudes (maximum-to-minimum fold-changes) for mRNAs and
440 for pre-mRNAs, which we compared between the two genotypes. In *Smg6* mutants, median
441 mRNA amplitudes were lower than in controls, but pre-mRNA amplitudes were higher (**Fig.**
442 **5J**); when normalizing mRNA amplitudes for pre-mRNA fold-changes – as a means to control
443 for differences in transcriptional rhythmicity at the locus – the decrease in rhythmic transcript
444 amplitudes in *Smg6* mutants became highly significant (**Fig. 5K**). This outcome indicated that
445 higher stability of rhythmic mRNAs in *Smg6* mutants was detectable at the global level. In the

446 extreme scenario, an mRNA that is rhythmic in control animals would lose its amplitude to the
 447 extent that it would not anymore be considered as rhythmic at all; it would then group within
 448 the N=223 genes shown in **Fig. 5B**. We inspected their individual gene expression profiles,
 449 which led to the identification of a sizeable number of transcripts that displayed severely
 450 blunted mRNA amplitudes in *Smg6* mutants, despite similar rhythmic pre-mRNAs (i.e.
 451 oscillations in transcription) (**Fig. 5L**). For several of the cases, we can speculate about
 452 possible NMD-eliciting features. For example, according to our previous mouse liver ribosome
 453 profiling data ²¹, *Glycine decarboxylase (Gldc)* contains translated uORFs (data not shown);
 454 in the case of *Lactate dehydrogenase B (Ldhb)*, a regulatory mechanism entailing stop codon
 455 readthrough has been demonstrated [31] and could potentially link *Ldhb* translation to NMD
 456 regulation. For the other transcripts shown in **Fig. 5L** (*Pde9a*, *Kyat1*, *Tubb4*, *Tmem101*,
 457 *Amdhd1*, *Epha2*), no obvious candidate NMD-eliciting features were found.



458

459 **Figure 5. Rhythmic RNA expression is altered in *Smg6* mutant livers under entrainment.** **A.** Heatmap of transcripts with significant
460 rhythms at the mRNA level in both genotypes. Expression levels are represented as Z-scores for mRNA or pre-mRNA with color code for
461 low (blue) to high (red) expression. Z-scores were calculated separately for mRNA and pre-mRNA data, but on a common scale for both
462 genotypes. Transcripts are phase-order for the control genotype. **B.** Heatmap as in A., but for transcripts with significant rhythms only in
463 control animals (N=223) and not in mutants. **C.** Heatmap as in A., but for transcripts with significant rhythms only in mutant animals (N=329)
464 and not in controls. **D.** Radial diagrams showing peak phase of rhythmic mRNAs in control (blue) and *Smg6* mutant (yellow) liver for the
465 common transcripts shown in A. Dark shaded: high amplitude rhythmic transcripts; light shaded: low amplitude rhythmic transcripts; high/low
466 cut-off on log₂ peak-trough amplitude of 1. **E.** Peak phase of mRNA in *Smg6* mutants (orange) relative to control phase (blue), ranked
467 according to the phase in the control (*Smg6* wt) for the transcripts shown in A (N=1257). **F.** Peak phase difference between mutant and
468 control mice for all common rhythmic mRNAs (N=1257). **G.** Peak phase difference of commonly rhythmic mRNAs as in F., but restricted to
469 loci with ChIP-seq binding sites for BMAL1 and CLOCK (N=130), according to ²⁰; p=0.0065; permutation test, calculated by 1000x
470 subsampling of N=130 transcripts from the "all rhythmic transcripts" (N=1257) of panel F, then comparing the means of these subsampling
471 groups with the observed mean (t-test). **H.** Peak phase difference of commonly rhythmic mRNAs as in F., but restricted to loci with ChIP-
472 seq binding sites for the ensemble of proteins PER1, PER2, CRY1 and CRY2 according to ²⁰; p=0.0005; permutation test as in panel G. **I.**
473 Peak phase difference of commonly rhythmic mRNAs as in F., but restricted to loci with no ChIP-seq binding sites for any of the proteins
474 BMAL1, CLOCK, PER1, PER2, CRY1 or CRY2 according to ²⁰; p=0.18; permutation test as in panel G. **J.** Z-score amplitudes – defined as
475 the difference between the maximum and minimum Z-score values, calculated independently for mRNAs and pre-mRNAs of commonly
476 rhythmic transcripts (N=1257) - show lower mean mRNA (p=0.236) and higher mean pre-mRNA amplitudes in mutants (p=2e-16);
477 significance calculations from a linear model (equivalent to t-test). **K.** Transcript mRNA/pre-mRNA Z-score amplitude ratios (from the N=1257
478 common rhythmic transcripts) stratified by genotype show decrease in mutants; p=2e-16; Student's t-test. **L.** RNA-seq data is plotted for
479 indicated genes for mRNA (upper panels; exonic reads) and pre-mRNA (lower panels; intronic reads) for *Smg6* mutants (yellow) and controls
480 (blue). Rhythmicity of mRNA levels observed in control (blue) is dampened or lost in *Smg6* mutant liver (yellow). RPKM values of individual
481 mice are shown as dots with solid lines connecting the means for each timepoint. The dashed lines represent the rhythmic data fit using the
482 parameters from Metacycle ³⁶. **M.** RT-Biolumicorder traces of individual mice in food shifting experiment. After 2 days under *ad libitum*
483 feeding, bioluminescence rhythms (photons) and activity (infrared signal) were recorded for 4 additional days under light-phase-restricted
484 feeding conditions (ZT10-20; horizontal black bar at top); skeleton photoperiod entrainment indicated by yellow vertical lines at ZT12 and
485 ZT0. Each line represents the signal from a control (blue) or a liver-specific *Smg6* mutant (yellow) animal **N.** Compiled data, averaged over
486 the last two days of the experiment. Mean signal (solid trace) and SEM (shaded). Indicated phase differences calculated from rhythmic fits
487 to the data.

488 Collectively, these analyses demonstrated that the stably entrained liver clock, under *ad*
489 *libitum* feeding and LD12:12 conditions, was subject to phase and amplitude alterations at the
490 level of clock-controlled gene expression. Our *in vivo* recording experiments (**Fig. 2F-H**) had
491 been insensitive to picking up such differences in liver rhythms due to the use of the
492 *mPer2::Luc* reporter allele, whose phase was unaffected by *Smg6* mutation under stable
493 entrainment conditions. We reasoned that under conditions where the stable entrainment was
494 challenged, a phenotype may be unmasked also for *mPer2::Luc*. To this end, we carried out
495 food shifting experiments i.e., switching from *ad libitum* to daytime feeding. Under these
496 conditions, the liver clock receives conflicting timing cues from the SCN and from
497 feeding/fasting cycles, which are not anymore aligned and will eventually lead to an inversion
498 of hepatic oscillator phase due to the dominance of feeding signals for peripheral oscillators
499 ⁴⁴. The kinetics and endpoint of phase adaptation can also be understood as a paradigm of
500 clock flexibility and can be recorded using the RT-Biolumicorder setup ³⁰. Our experiments
501 showed that in *Smg6* mutant animals, after 3 days of feeding during the light phase, daily
502 cycles in bioluminescence had readjusted to a new phase that substantially differed between
503 control and *Smg6* mutant animals (3 hours difference at trough/0.5 hours at peak; **Fig. 5M,**
504 **N**). We concluded that NMD contributes to the adaptation of circadian gene expression to food

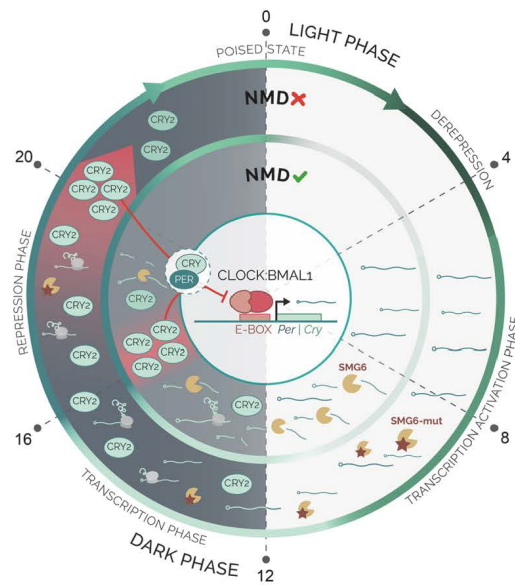
505 entrainment in mouse liver. More generally, the data point to notable differences between
506 *Smg6* mutant and control animals with regard to how different timing cues are integrated within
507 the core clock circuitry.

508 **Discussion**

509 Our novel conditional *Smg6* endonuclease-mutant allele provides unique possibilities to
510 explore *in vivo* activities of the NMD pathway and has allowed us to uncover an unexpected
511 role within the mammalian circadian system, which is a conserved, key mechanism for the
512 organization of daily rhythms in behavior, physiology and metabolism. We find that NMD loss-
513 of-function has a striking impact on free-running circadian periods in two peripheral clock
514 models, primary fibroblasts and liver. Moreover, we determine a specific core clock
515 component, *Cry2*, as NMD-regulated and attribute the NMD-eliciting activity to its long 3' UTR.
516 Although it is widely accepted that efficient mRNA decay is critical for the establishment of
517 gene expression oscillations, which specific pathways mediate the decay of transcripts
518 encoding core clock components has remained largely unknown. That NMD has been co-
519 opted for this purpose, as we find to be the case for *Cry2*, is surprising at first sight – yet it
520 may simply reflect that nature and evolution are opportunistic and employ the available
521 molecular pathways in the most efficient fashion. In line with this idea is the finding that a
522 sizeable number of other rhythmic transcripts appears to rely on NMD to ensure efficient
523 mRNA turnover as well (**Fig. 5L**). Our observations may change the way we should perceive
524 the evolutionary drives relating to NMD: for example, it has been speculated why many
525 mammalian mRNAs contain long 3' UTRs but evade NMD, and a model has been put forward
526 suggesting that such mRNAs have evolved to recruit NMD-inhibiting RBPs in spatial proximity
527 of the termination codon ⁶. However, an opposite drive to attract and retain NMD regulation
528 would be plausible as well – acting on endogenous transcripts, such as *Cry2*, whose intrinsic
529 instability is physiologically important. This idea is in line with findings that in the circadian
530 systems of *Neurospora* ¹⁵, *Arabidopsis* ¹³ and *Drosophila* ¹⁴, roles for NMD have emerged as
531 well.

532 In the absence of NMD, CRY2 protein in liver accumulates to higher levels and for an extended
533 time (**Figure 6**). Based on the experiments presented in our study, we are not yet fully in the
534 position to evaluate to what extent these effects are involved in the period lengthening
535 phenotype. Still, it would be plausible that the phase delay of CRY2 seen in the *Smg6* mutants
536 could be particularly critical. According to around-the-clock ChIP-Seq data from wild-type
537 mouse liver, CRY2 binds and represses its target genes at circadian time CT15-16 ²⁰, thus
538 closely matching the timing of maximal CRY2 abundance in our control mice (ZT16). The
539 ChIP-seq data from wild-type livers further indicates that by CT20, CRY2 is cleared and

540 replaced by CRY1, which binds to chromatin with a peak at around CT0 and is associated
 541 with a transcriptionally repressed, but poised state of BMAL1:CLOCK activity. Period
 542 lengthening through the prolonged availability of CRY2 may thus involve an extended CRY2-
 543 mediated repressive phase and/or CRY2 denying its homolog CRY1 access to its targets,
 544 causing a delay in the handover to CRY1. Of note, the period lengthening we observe is
 545 phenotypically comparable to that reported for a chemical, selective stabilizer of CRY2 protein,
 546 which also prolongs period in reporter assays across several cell types and species ⁴⁵.
 547 Moreover, period lengthening has also been reported upon CRY2 stabilisation (in a *Cry1*-
 548 deficient background) induced by genetic inactivation of the CRY-specific ubiquitin ligase
 549 *Fbxl3* ⁴⁶. For these reasons – and reminiscent of findings on CRY1 accumulation ⁴⁷ – the
 550 changed timing of CRY2 accumulation, rather than its generally higher levels, may be a critical
 551 feature for the period phenotype and for the phase effects seen in the entrained liver. We thus
 552 propose that limiting temporal *Cry2* mRNA availability, mediated through NMD, is an important
 553 mechanism within the core loop of the clock by which CRY2 protein biosynthesis is restricted
 554 to the beginning of the dark phase when it acts in sync with PER1 and PER2 to repress
 555 CLOCK:BMAL1-mediated transcription. Only after duly removal of this repressive complex
 556 can CRY1 join and advance the cycle through the late repressive and poised states, eventually
 557 leading to the next transcriptional cycle at CLOCK:BMAL1-bound E-box enhancers.



558

559 **Figure 6. Model of how the daily dynamics of CRY2 accumulation are regulated by NMD.** In the entrained liver clock, *Cry2* mRNA is
 560 translated and the protein accumulates with a peak in the dark phase (ZT16 in wild-type). In the absence of a functional NMD pathway, *Cry2*
 561 mRNA is stabilized, reaches higher levels, and its translation leads to increased CRY2 at later times (ZT20). The specific phases and states
 562 noted at the periphery of the circle (poised, derepression etc.) refer to the findings from Koike *et al.* ²⁰ on E-box binding of clock proteins.

563 Intriguingly, our findings suggest specificity of the phenotype for peripheral clocks. Thus, we
564 were unable to detect an impact on circadian period of the master clock in the SCN. Different
565 explanations may underlie this observation. First, we cannot exclude lack of phenotype due
566 to technical reasons, in particular the lower efficiency of Cre-mediated recombination in SCN
567 neurons, or slow replacement kinetics of wild-type SMG6 by its mutant version due to high
568 protein stability in neurons. For possible biological explanations, the decay of NMD substrates
569 may be less reliant on SMG6 in neuronal cells, or the strong intercellular coupling in the SCN
570 ⁴⁸ renders the clocks resilient against the genetic NMD perturbation and the resulting changes
571 in the critical NMD-regulated transcript. Finally, if the phenotype actually does involve CRY2,
572 it is interesting that it has been reported that the relative importance of the two homologs,
573 CRY1 and CRY2, in the negative feedback loop can be rather tissue-specific, with CRY1 being
574 the main transcriptional repressor in the SCN ⁴⁶, leading to another potential explanation for
575 the observed cell type-specificity. Future experiments will be required to distinguish between
576 these possibilities.

577 In summary, the unexpected role of NMD that we uncover within the circadian system
578 illustrates the ongoing shift in perception of NMD from surveillance to housekeeping functions.
579 We anticipate that our mouse model will provide valuable insights into so-far unidentified NMD
580 targets and functions in mammals *in vivo*, including in the context of pathologies such as
581 neurological diseases ⁴⁹ and cancer ^{50,51}, and in situations where NMD has been identified as
582 a promising therapeutic target ^{52,53}.

583 **Methods**

584 **Animals**

585 All animal experiments were performed according to the cantonal guidelines of the Canton of
586 Vaud, Switzerland, license VD3611. Healthy adult male mice of age 12 – 24 months were
587 used. All mouse lines were maintained on a C57BL/6J background. The alleles *AlbCre-ERT2^{ki}*
588 ²⁵ and *mPer2::Luc^{ki}* ²⁶ have been previously described. The novel *Smg6^{flox}* allele was
589 generated in collaboration with Taconic (official nomenclature of line:
590 *Smg6^{tm5498(D1352A,D1391A)Tac}*).

591 **Primary fibroblasts and immortalization**

592 Adult male *Smg6^{flox/flox}* and *Smg6^{+/+}* control littermate mice were euthanized and approximately
593 1 cm of tail tip was recovered and further sliced into thin pieces under sterile conditions. Tissue
594 fragments were overnight digested with 1 mg/ml collagenase type 1A (Sigma Aldrich) in
595 culture medium at 37°C. The culture medium consists of 15% of fetal calf serum (FCS), 1%
596 Penicillin-Streptomycin-Glutamine (Thermo Fisher Scientific, 10378016), 1% non-essential
597 amino acids (Thermo Fisher Scientific, 11140050), 1 mM sodium pyruvate (Thermo Fisher
598 Scientific, 11360070), 87 mM β-mercaptoethanol, 18 mM HEPES pH 7.0 (Thermo Fisher
599 Scientific, 15630080), 2.5 μg/ml Amphotericin B (Thermo Fisher Scientific, 15290018) and 2.5
600 μg/ml Plasmocin (InvivoGen).

601 Isolated fibroblasts became spontaneously immortal upon continuous culture, creating
602 *Smg6^{flox/flox}* or *Smg6^{+/+}* cell lines. Immortalized fibroblasts were transduced with a retrovirus
603 carrying a tamoxifen-inducible Cre and puromycin resistance (MSCV *CreERT2* puro, Addgene
604 plasmid #22776) ⁵⁴. Retrovirus production was performed using the pCL-eco (Addgene,
605 12371) ⁵⁵ and pCMV-VSV-G (Addgene, 8454) ⁵⁶ plasmids in 293FT HEK cells using the
606 CalPhos™ Mammalian Transfection Kit (Takara bio, 631312). Following 2 μM tamoxifen
607 treatment, renewed every 24h for 4 consecutive days, the cells were utilized for experiments
608 after 7-10 days from the treatment initiation.

609 **DNA genotyping**

610 DNA from cell cultures, liver or kidney tissue was extracted using the DNeasy® Blood & Tissue
611 Kit (Qiagen, 69504) according to the manufacturer's protocol. Genotyping PCR reaction was
612 performed using HotStar Taq DNA polymerase (Qiagen, 203207), 0.4 uM primers
613 (Microsynth), 0.2 uM dNTP mix (PROMEGA, U1511) and approximately 200-700 ng of DNA
614 template. The primer sequences are as follows (5'-3'): Forward: gaa ata cca ggg ccc ttg c ,
615 Reverse1: cat cac tac cca gct cag gaa c, Reverse2: gga ttg gct cct ctt tgc tg. The PCR program
616 is as follows : 15 sec at 95°C, 35 cycles : 1 min at 94°C, 1 min at 61°C, 1 min at 72°C and

617 final elongation at 72°C for 10 min. DNA extraction from dissected SCN tissue was done by
618 Arcturus® PicoPure® DNA Extraction Kit (Thermo Fisher Scientific, KIT0103). PCR reaction
619 was set up as above. The primer sequences are as follows (5'-3'): Forward gaa ata cca ggg
620 ccc ttg c, Reverse2: tct agc tcc ttt ctg cct ctt c. The PCR program is as follows : 15 sec at
621 95°C, 40 cycles : 1 min at 94°C, 1 min at 55°C, 1 min at 72°C and final elongation at 72°C for
622 10 min.

623 **Luciferase reporters and lentiviral production**

624 *CreERT2 Smg6^{flax/flax}* and *Smg6^{+/+}* immortalized fibroblasts were transduced with a lentivirus
625 carrying a dual luciferase (Firefly/Renilla) NMD reporter or a control vector. For the generation
626 of dual luciferase reporter plasmids, the prLV1 dual luciferase reporter plasmid ¹¹ was used,
627 with or without the introduction of an intron downstream of the *Firefly* stop codon. For the latter,
628 the chimeric intron of the pCI-neo vector (Promega, E1841) was cloned into the 3' UTR of the
629 prLV1 vector. The following primers were used for PCR amplification: forward:
630 aaagcggccGCTCGTTTAGTGAACCGTC (introducing a NotI restriction site) and reverse:
631 tTTCTCGAGCTGTAATTGAACTGGGAG (introducing a XhoI restriction site). *Dbp-Luciferase*
632 ²³ and the 3' UTR luciferase reporters ¹¹ have been described previously. Lentiviral particles
633 were produced in 293T cells using the envelope vector pMD2.G and the packaging plasmid
634 psPAX2 as previously described ⁵⁷. Filtered viral supernatant was spun 2h at 24,000 rpm, 4°C
635 using Optima L-90K Ultracentrifuge (SW32Ti rotor; Beckman, Brea, CA), then viral particles
636 were resuspended with normal growth medium and used for cell transduction.

637 **Circadian bioluminescence recording of cell cultures**

638 Fibroblasts cultured in 35 mm culture dishes (Falcon, 353001) were synchronized either with
639 serum shock (50% horse serum for 3h) or with temperature entrainment (cycles of 16h at 35°C
640 and 8h at 37°C for 5 days). During recording cells were cultured in phenol-free DMEM
641 (Gibco, Thermo Fisher Scientific, 11880028) containing 10% FBS, 1% PSG and 0.1 mM of
642 luciferin, sealed with parafilm to avoid evaporation, in the LumiCycler setup (Actimetrics) at
643 37°C and 5% CO₂. NIH/3T3 murine fibroblasts were cultured under the same conditions as
644 the immortalized fibroblasts but synchronized with 100 nM Dexamethasone treatment for 15
645 min. SMG1 inhibitor (hSMG-1 inhibitor 11e; Probecem Cat. No. PC-35788) ³⁸ was used as
646 10 mM stock (dissolved in DMSO) and, if not indicated otherwise, used at a concentration of
647 0.6 μM (NIH/3T3 experiments) to 1 μM (*Smg6^{flax}* fibroblasts).

648 **Dual Luciferase assay**

649 After lentiviral transduction cells were collected using 5x Passive Lysis Buffer (Promega) and
650 luciferase activity was measured using the Dual-Glo Luciferase Assay System (Promega,

651 E1910) according to the manufacturer's protocol. *Firefly*-Luciferase signal was normalized to
652 *Renilla*-Luciferase, and for each construct (3' UTR or NMD reporter) this signal was then
653 normalized to that of lentivector-control plasmid (only containing generic vector 3' UTR)
654 treated with vehicle (for each experiment).

655 **RNA sequencing and analysis**

656 Reads were mapped on the mouse genome GRCm38 (Ensembl version 91) using STAR⁵⁸
657 (v. 2.7.0f; options: --outFilterType BySJout --outFilterMultimapNmax 20 --
658 outMultimapperOrder Random --alignSJoverhangMin 8 --alignSJDBoverhangMin 1 --
659 outFilterMismatchNmax 999 --alignIntronMin 20 --alignIntronMax 1000000 --
660 alignMatesGapMax 1000000). Read counts in genes loci were evaluated with htseq-count⁵⁹
661 (v. 0.13.5) for transcript mapped reads (i.e. exons; options: --stranded=reverse --order=name
662 --type=exon --idattr=gene_id --mode=intersection-strict) and for whole locus mapped reads
663 (i.e. exons plus introns; options: --stranded=reverse --order=name --type=gene --
664 idattr=gene_id --mode=union). Read counting for exon analysis was not possible with htseq-
665 count (most reads spanned multiple exons and would have been discarded) so a new python
666 script was developed for this task. To avoid counting reads spanning different exons multiple
667 times, the script calculated average read depth for each exon. Read pileups for gene loci were
668 calculated using samtools depth⁶⁰ (v. 1.9) and plotted using R (v 4.1.1). Differential expression
669 analysis was done in R using DESeq2 package⁶¹. RNA stability analysis was performed using
670 RPKM normalised reads counts. Phase analysis was performed using RPKM normalised
671 reads counts and the MetaCycle R package³⁶.

672 **Induction of liver-specific *Smg6* mutation**

673 8-12 week old male *Smg6*^{flax/flax} mice, carrying the liver-specific Albumin-driven CreERT2
674 (allele *Alb*^{tm1(cre/ERT2)Mtz}²⁵), and their control littermates (*Smg6*^{+/+}) received 4 intraperitoneal
675 injections of 20 mg/ml tamoxifen (Sigma-Aldrich) in corn oil at a dosage of 75 mg tamoxifen/kg
676 of body weight. The mice were admitted for experiments 4 weeks later.

677 **Liver and kidney explants**

678 Male *Smg6*^{flax/flax} mice and their control littermates *Smg6*^{+/+} were euthanized following deep
679 anesthesia by isoflurane inhalation. Liver and kidney tissue were excised and put immediately
680 in ice-cold Hank's buffer (Thermo Fisher Scientific). The outermost edges of the tissues were
681 carefully excised in a sterile cabinet, and immediately placed on a 0.4 micron Millicell cell
682 culture inserts (PICMORG50) in a 35 mm dish with phenol-free DMEM (Thermo Fisher
683 Scientific, 11880028) containing 5% FBS, 2 mM glutamine, 100 U/ml penicillin, 100 µg/ml

684 streptomycin and 0.1 mM luciferin. The parafilm-sealed plates were placed for recording in the
685 LumiCycler (Actimetrics) at 37°C and 5% CO₂.

686 **RT-Biolumicorder experiments**

687 Adult male mice, 12-20 weeks of age, carrying the genetically encoded circadian reporter
688 allele *mPer2::Luc*²⁶ were used for the RT-Biolumicorder experiments. The experimental
689 procedure followed our recently published protocol²⁹. Briefly, Alzet mini-osmotic pumps
690 (model 100D5 or 2001) were filled with 90 mg/ml with D-Luciferin sodium salt, dissolved in
691 Phosphate Buffered Saline (PBS, pH 7.4) under sterile conditions. The pumps were closed
692 with blue-colored flow moderators (ALZET) and activated at 37°C according to the
693 manufacturer's instructions, followed by the subcutaneous, dorsal implantation. As analgesics
694 Carprofen (Rimadyl, 5 mg/kg subcutaneous), and paracetamol (2 mg/ml, via drinking water)
695 were administered. Prior implantation the dorsal area of the mouse at the site where the liver
696 is positioned was shaved using an electric razor. The RT-Biolumicorder (Lesa-Technology)
697 consists of a cylindrical cage for a single mouse with photon-reflecting walls, equipped with a
698 photomultiplier tube (PMT), water and food containers and a built-in infrared sensor that
699 records locomotor activity^(29,30). The RT-Biolumicorder records photon and activity levels in 1
700 min intervals. The data, which also contain light and food access information, were saved as
701 text files and later analyzed using the MatLab-based "Osiris" software according to²⁹ or a
702 custom-made R script.

703 **Running wheel experiments**

704 12-16 week old male mice were single-housed in cages equipped with a running wheel and
705 were placed in a light-tight cabinet. After approximately 10 days of habituation in 12h light-12h
706 dark the mice were released in constant darkness for approximately 14 days. For the running
707 wheel experiments with SCN-specific *Smg6* mutant recombination, the same protocol was
708 used, followed by 14 days of post-injection recovery under 12h-light-12h-dark conditions and
709 a second period of constant darkness for 14 days (adapted from⁶²).

710 **SCN-specific *Smg6* mutant mice**

711 Male adult *Smg6*^{flax/flax} mice and their control littermates (*Smg6*^{+/+}) received bilateral
712 stereotactic injections of CMV.HI-Cre::eGFP AAV5 particles (AddGene, 105545) into the SCN
713 (400 nl per site). Stereotactic coordinates: AP= - 0.34 ML= +/- 0.4, V=5.5. Ketamine/Xylazine
714 (80/12.5 mg/kg) by intraperitoneal injection was used as anesthetic and 5 mg/kg carprofen
715 was administered subcutaneously for analgesia. Additionally, paracetamol (2 mg/ml) was
716 administered via drinking water prior and 3 days following the procedure. Animal recovery was
717 monitored for ten days. Mice carrying *mPer2::Luc*²⁶ in addition to *Smg6*^{flax/flax} (experimental)

718 or *Smg6*^{+/+} (control) were used for the bioluminescence recording of SCN slices. For
719 evaluation of viral targeting, mice were transcardially perfused with phosphate-buffered saline
720 (PBS) followed by 4% paraformaldehyde (PFA). Brains were post fixed overnight in 4% PFA
721 at 4°C and then cryopreserved in 30% sucrose solution in PBS for at least 24 hours at 4°C
722 (until completely sunk to the bottom of the container). Cryopreserved brains were frozen and
723 sliced in 25 µm thick sections. Sections were mounted using DAPI-fluoromount. Fluorescent
724 images were acquired on a ZEISS Axio Imager.M2 microscope, equipped with ApoTome.2
725 and a Camera AxioCam 702 mono. Specific filter sets were used for the visualization of green
726 (Filter set 38 HE eGFP shift free [E] EX BP 470/40, BS FT 495, EM BP 525/50) and blue (Filter
727 set 49 DAPI shift free [E] EX G 365, BS FT 395, EM BP 445/50) fluorescence. For genomic
728 DNA extraction, fresh brain tissue was collected in RNAlater solution and kept at 4°C for 2
729 weeks. Then 250 µm thick sections containing the SCN were sliced using a microtome and
730 the SCN region was microdissected under a fluorescent equipped stereomicroscope (Nikon
731 SMZ-25).

732 **SCN slices and bioluminescence recording**

733 Approximately 14 days later, following bilateral stereotactic injections, the mice were sacrificed
734 and the SCN was dissected. Slices of 350 µm around the area of SCN were prepared with a
735 tissue chopper between ZT4.8 and ZT6.3; 2 slices per animal were used. Slicing and recovery
736 buffer contained of NMDG aCSF (85 mM NMDG, 9 mM MgSO₄, 2.3mM KCl, 1.1 mM
737 NaH₂PO₄, 0.5 mM CaCl₂, 23 mM D-Glucose, 28 mM NaHCO₃, 18 mM Hepes, 3 mM Na-
738 pyruvate, 5 mM Na-ascorbate and 2 mM thiourea; pH 7.3-7.4; 300-310 mOsm/Kg according
739 ⁶³. Each slice was cultured in a single well of a 24-well plate in 300 µl of culture medium (0.7
740 x MEM Eagle medium with 1.7 mM MgSO₄, 0.8 mM CaCl₂, 11 mM D-Glucose, 17 mM
741 NaHCO₃, 25 mM Hepes, 0.4 mM GlutaMAX, 17% Horse serum, 0.8 mg/L Insulin, 0.8495 mM
742 Ascorbic acid, 1% penicillin/streptomycin and 100 µM Luciferin; pH 7.3-7.4; 300-310
743 mOsm/Kg according ⁶³). Viral infection and accurate injection localization of the SCN was
744 evaluated with fluorescent imaging with THUNDER Imaging Systems widefield microscope
745 (Leica) on the 8th day in culture. Circadian bioluminescence was monitored by using
746 photomultiplier tubes (PMTs) for approximately one week at 34.5 °C with 5% CO₂ (in-house
747 built device).

748 **Protein extraction and Western Blot**

749 Total proteins from mouse liver were extracted in principle according to the NUN procedure
750 ⁶⁴. Freshly harvested liver extracts were homogenized in 2 tissue volume of Nuclear Lysis
751 Buffer (10 mM Hepes pH 7.6, 100 mM KCl, 0.1 mM EDTA, 10% Glycerol, 0.15 mM spermine,
752 0.5 mM spermidine) for 20 seconds using a Teflon homogenizer. 4 tissue volumes of 2x NUN

753 Buffer (2M Urea, 2% NP40, 0.6 M NaCl, 50 mM Hepes pH 7.6, 2 mM DTT, 0.1 mM PMSF and
754 supplemented with complete protease inhibitor tablets, Roche) were added dropwise and on
755 a vortex with constant low speed to ensure immediate mixing. The lysates were incubated on
756 ice for 30 min and then cleared through centrifugation at 10000 rpm, 4°C, for 20 min.
757 Supernatants were stored at -80°C. Aliquots of the lysates (20-30 µg of protein loaded per
758 lane, either from a pool from 3 mice or from individual mice, as indicated) were separated by
759 SDS-PAGE and transferred to PVDF membrane by dry transfer using an iBlot 2 gel transfer
760 device. After blocking (5% milk in TBST; for 1 hour at room temperature), the membrane was
761 incubated overnight at 4°C with appropriate dilutions of primary antibodies, including anti-
762 CRY2 (kind gift from Ueli Schibler, Geneva), anti-ATF5 (Abcam-ab184923), and anti-HSP90
763 (Cell signaling-4874), p-eif2alpha (Cell signaling-9721), eif2alpha (Cell signaling-9722).
764 Following TBST washing (3 x 5 minutes), the membranes were incubated with the appropriate
765 secondary antibody conjugated with HRP for 60 minutes at room temperature, followed by
766 washing as above. Chemiluminescence signal was detected with Supersignal West Femto
767 Maximum Sensitivity Substrate (Thermo Fisher Scientific, 34095), as described by the
768 manufacturer. The quantification of bands was performed using ImageJ software.

769 **Data and script availability**

770 Data has been deposited at GEO (reviewer token). Computational scripts are accessible at:

771 **Acknowledgements**

772 We thank Paul Franken and Yann Emmenegger for equipment and help with *in vivo*
773 experiments, and Oliver Mühlemann for generous gift of SMG1i compound. Work in DG's lab
774 was funded by the University of Lausanne and by the Swiss National Science Foundation
775 through the National Center of Competence in Research RNA & Disease (grant no. 141735)
776 and through individual grant 179190; work in AK's lab was funded by the Deutsche
777 Forschungsgemeinschaft (DFG, German Research Foundation) - Project Number 278001972
778 - TRR 186.

779 **References**

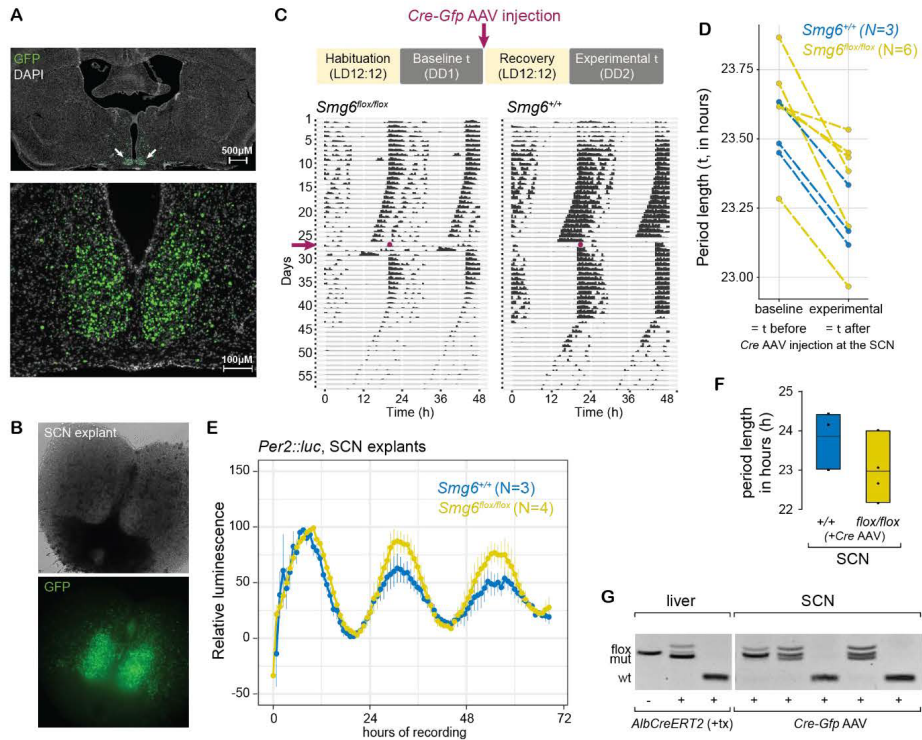
- 780 1. Karousis, E.D. & Muhlemann, O. Nonsense-Mediated mRNA Decay Begins Where Translation
781 Ends. *Cold Spring Harb Perspect Biol* **11**(2019).
- 782 2. Kurosaki, T., Popp, M.W. & Maquat, L.E. Quality and quantity control of gene expression by
783 nonsense-mediated mRNA decay. *Nat Rev Mol Cell Biol* **20**, 406-420 (2019).
- 784 3. Huth, M. *et al.* NMD is required for timely cell fate transitions by fine-tuning gene expression
785 and regulating translation. *Genes Dev* **36**, 348-367 (2022).
- 786 4. Boehm, V. *et al.* SMG5-SMG7 authorize nonsense-mediated mRNA decay by enabling SMG6
787 endonucleolytic activity. *Nat Commun* **12**, 3965 (2021).

- 788 5. Mendell, J.T., Sharifi, N.A., Meyers, J.L., Martinez-Murillo, F. & Dietz, H.C. Nonsense
789 surveillance regulates expression of diverse classes of mammalian transcripts and mutes
790 genomic noise. *Nat Genet* **36**, 1073-8 (2004).
- 791 6. Singh, G., Rebbapragada, I. & Lykke-Andersen, J. A competition between stimulators and
792 antagonists of Upf complex recruitment governs human nonsense-mediated mRNA decay.
793 *PLoS Biol* **6**, e111 (2008).
- 794 7. Yepiskoposyan, H., Aeschmann, F., Nilsson, D., Okoniewski, M. & Muhlemann, O.
795 Autoregulation of the nonsense-mediated mRNA decay pathway in human cells. *RNA* **17**,
796 2108-18 (2011).
- 797 8. Karousis, E.D., Gypas, F., Zavolan, M. & Muhlemann, O. Nanopore sequencing reveals
798 endogenous NMD-targeted isoforms in human cells. *Genome Biol* **22**, 223 (2021).
- 799 9. Cox, K.H. & Takahashi, J.S. Circadian clock genes and the transcriptional architecture of the
800 clock mechanism. *J Mol Endocrinol* **63**, R93-R102 (2019).
- 801 10. Partch, C.L., Green, C.B. & Takahashi, J.S. Molecular architecture of the mammalian circadian
802 clock. *Trends in cell biology* **24**, 90-99 (2014).
- 803 11. Du, N.H., Arpat, A.B., De Matos, M. & Gatfield, D. MicroRNAs shape circadian hepatic gene
804 expression on a transcriptome-wide scale. *Elife* **3**, e02510 (2014).
- 805 12. Kojima, S., Sher-Chen, E.L. & Green, C.B. Circadian control of mRNA polyadenylation dynamics
806 regulates rhythmic protein expression. *Genes Dev* **26**, 2724-2736 (2012).
- 807 13. Kwon, Y.J., Park, M.J., Kim, S.G., Baldwin, I.T. & Park, C.M. Alternative splicing and nonsense-
808 mediated decay of circadian clock genes under environmental stress conditions in
809 *Arabidopsis*. *BMC Plant Biol* **14**, 136 (2014).
- 810 14. Ri, H. *et al.* *Drosophila* CrebB is a Substrate of the Nonsense-Mediated mRNA Decay Pathway
811 that Sustains Circadian Behaviors. *Mol Cells* **42**, 301-312 (2019).
- 812 15. Wu, Y. *et al.* Up-Frameshift Protein UPF1 Regulates *Neurospora crassa* Circadian and Diurnal
813 Growth Rhythms. *Genetics* **206**, 1881-1893 (2017).
- 814 16. Glavan, F., Behm-Ansmant, I., Izaurralde, E. & Conti, E. Structures of the PIN domains of SMG6
815 and SMG5 reveal a nuclease within the mRNA surveillance complex. *EMBO J* **25**, 5117-25
816 (2006).
- 817 17. Azzalin, C.M. & Lingner, J. The double life of UPF1 in RNA and DNA stability pathways. *Cell*
818 *Cycle* **5**, 1496-8 (2006).
- 819 18. Li, T. *et al.* Smg6/Est1 licenses embryonic stem cell differentiation via nonsense-mediated
820 mRNA decay. *EMBO J* **34**, 1630-47 (2015).
- 821 19. Gaidatzis, D., Burger, L., Florescu, M. & Stadler, M.B. Analysis of intronic and exonic reads in
822 RNA-seq data characterizes transcriptional and post-transcriptional regulation. *Nat Biotechnol*
823 **33**, 722-9 (2015).
- 824 20. Koike, N. *et al.* Transcriptional architecture and chromatin landscape of the core circadian
825 clock in mammals. *Science* **338**, 349-54 (2012).
- 826 21. Janich, P., Arpat, A.B., Castelo-Szekely, V., Lopes, M. & Gatfield, D. Ribosome profiling reveals
827 the rhythmic liver transcriptome and circadian clock regulation by upstream open reading
828 frames. *Genome Res* **25**, 1848-59 (2015).
- 829 22. French, C.E. *et al.* Transcriptome analysis of alternative splicing-coupled nonsense-mediated
830 mRNA decay in human cells reveals broad regulatory potential. *bioRxiv*, 2020.07.01.183327
831 (2020).
- 832 23. Stratmann, M., Suter, D.M., Molina, N., Naef, F. & Schibler, U. Circadian Dbp transcription
833 relies on highly dynamic BMAL1-CLOCK interaction with E boxes and requires the proteasome.
834 *Mol Cell* **48**, 277-87 (2012).

- 835 24. Brown, S.A., Zumbrunn, G., Fleury-Olela, F., Preitner, N. & Schibler, U. Rhythms of mammalian
836 body temperature can sustain peripheral circadian clocks. *Curr Biol* **12**, 1574-83 (2002).
- 837 25. Schuler, M., Dierich, A., Chambon, P. & Metzger, D. Efficient temporally controlled targeted
838 somatic mutagenesis in hepatocytes of the mouse. *Genesis* **39**, 167-72 (2004).
- 839 26. Yoo, S.-H. *et al.* PERIOD2::LUCIFERASE real-time reporting of circadian dynamics reveals
840 persistent circadian oscillations in mouse peripheral tissues. *Proceedings of the National
841 Academy of Sciences* **101**, 5339-5346 (2004).
- 842 27. Aschoff, J. & Pohl, H. Phase relations between a circadian rhythm and its zeitgeber within the
843 range of entrainment. *Naturwissenschaften* **65**, 80-4 (1978).
- 844 28. Granada, A.E., Bordyugov, G., Kramer, A. & Herzog, H. Human chronotypes from a theoretical
845 perspective. *PLoS One* **8**, e59464 (2013).
- 846 29. Katsioudi, G. *et al.* Recording of Diurnal Gene Expression in Peripheral Organs of Mice Using
847 the RT-Biolumicorder. *Methods Mol Biol* **2482**, 217-242 (2022).
- 848 30. Saini, C. *et al.* Real-time recording of circadian liver gene expression in freely moving mice
849 reveals the phase-setting behavior of hepatocyte clocks. *Genes & development* **27**, 1526-1536
850 (2013).
- 851 31. Hoekstra, M.M., Jan, M., Katsioudi, G., Emmenegger, Y. & Franken, P. The sleep-wake
852 distribution contributes to the peripheral rhythms in PERIOD-2. *Elife* **10**(2021).
- 853 32. Debruyne, J.P. *et al.* A clock shock: mouse CLOCK is not required for circadian oscillator
854 function. *Neuron* **50**, 465-77 (2006).
- 855 33. Kornmann, B., Schaad, O., Bujard, H., Takahashi, J.S. & Schibler, U. System-driven and
856 oscillator-dependent circadian transcription in mice with a conditionally active liver clock.
857 *PLoS Biol* **5**, e34 (2007).
- 858 34. Hatano, M. *et al.* The 5'-untranslated region regulates ATF5 mRNA stability via nonsense-
859 mediated mRNA decay in response to environmental stress. *FEBS J* **280**, 4693-707 (2013).
- 860 35. Pakos-Zebrucka, K. *et al.* The integrated stress response. *EMBO Rep* **17**, 1374-1395 (2016).
- 861 36. Wu, G., Anafi, R.C., Hughes, M.E., Kornacker, K. & Hogenesch, J.B. MetaCycle: an integrated R
862 package to evaluate periodicity in large scale data. *Bioinformatics* **32**, 3351-3353 (2016).
- 863 37. Castelo-Szekely, V. *et al.* Charting DENR-dependent translation reinitiation uncovers
864 predictive uORF features and links to circadian timekeeping via Clock. *Nucleic Acids Res* **47**,
865 5193-5209 (2019).
- 866 38. Gopalsamy, A. *et al.* Identification of pyrimidine derivatives as hSMG-1 inhibitors. *Bioorg Med
867 Chem Lett* **22**, 6636-41 (2012).
- 868 39. Langer, L.M., Bonneau, F., Gat, Y. & Conti, E. Cryo-EM reconstructions of inhibitor-bound
869 SMG1 kinase reveal an autoinhibitory state dependent on SMG8. *Elife* **10**(2021).
- 870 40. Zinshteyn, B., Sinha, N.K., Enam, S.U., Koleske, B. & Green, R. Translational repression of NMD
871 targets by GIGYF2 and EIF4E2. *PLoS Genet* **17**, e1009813 (2021).
- 872 41. Luck, S. & Westermark, P.O. Circadian mRNA expression: insights from modeling and
873 transcriptomics. *Cell Mol Life Sci* **73**, 497-521 (2016).
- 874 42. Hughes, M.E. *et al.* Guidelines for Genome-Scale Analysis of Biological Rhythms. *J Biol Rhythms*
875 **32**, 380-393 (2017).
- 876 43. Rey, G. *et al.* Genome-wide and phase-specific DNA-binding rhythms of BMAL1 control
877 circadian output functions in mouse liver. *PLoS Biol* **9**, e1000595 (2011).
- 878 44. Damiola, F. *et al.* Restricted feeding uncouples circadian oscillators in peripheral tissues from
879 the central pacemaker in the suprachiasmatic nucleus. *Genes Dev* **14**, 2950-61 (2000).

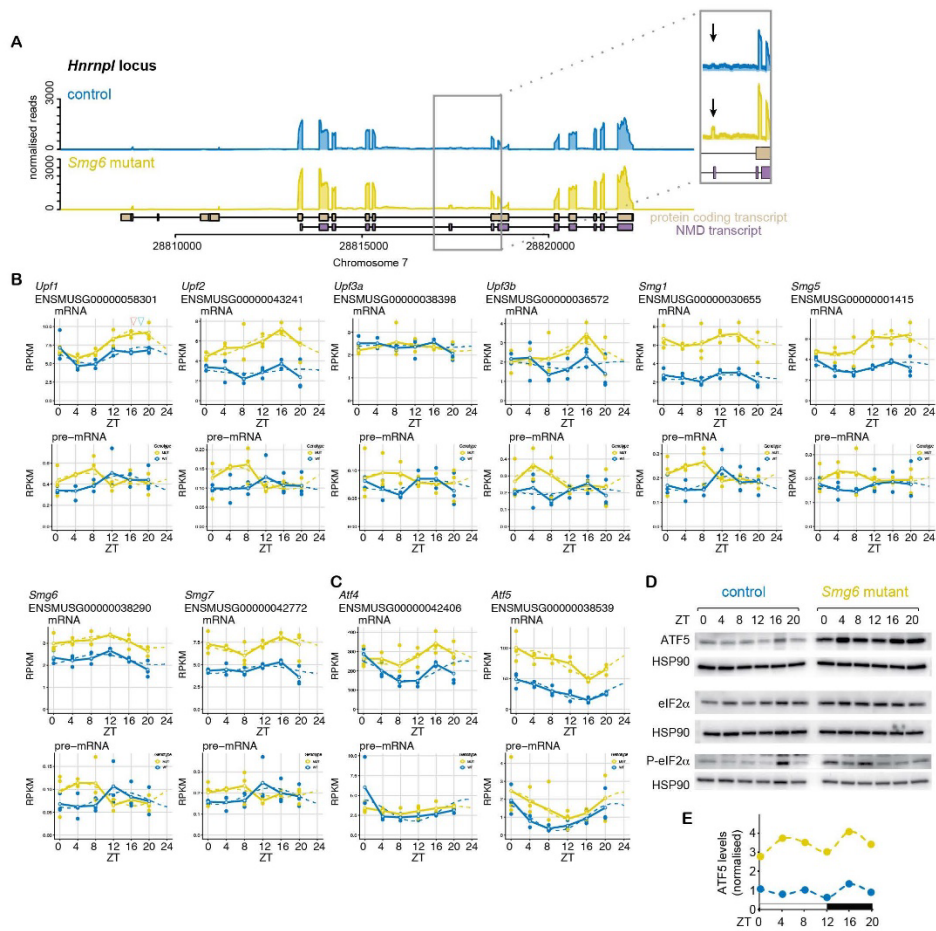
- 880 45. Miller, S. *et al.* Isoform-selective regulation of mammalian cryptochromes. *Nature chemical*
881 *biology* **16**, 676-685 (2020).
- 882 46. Anand, S.N. *et al.* Distinct and separable roles for endogenous CRY1 and CRY2 within the
883 circadian molecular clockwork of the suprachiasmatic nucleus, as revealed by the Fbxl3Afh
884 mutation. *Journal of Neuroscience* **33**, 7145-7153 (2013).
- 885 47. Ukai-Tadenuma, M. *et al.* Delay in feedback repression by cryptochrome 1 is required for
886 circadian clock function. *Cell* **144**, 268-81 (2011).
- 887 48. Liu, A.C. *et al.* Intercellular coupling confers robustness against mutations in the SCN circadian
888 clock network. *Cell* **129**, 605-616 (2007).
- 889 49. Jaffrey, S.R. & Wilkinson, M.F. Nonsense-mediated RNA decay in the brain: emerging
890 modulator of neural development and disease. *Nature Reviews Neuroscience* **19**, 715-728
891 (2018).
- 892 50. Popp, M.W. & Maquat, L.E. Nonsense-mediated mRNA decay and cancer. *Current opinion in*
893 *genetics & development* **48**, 44-50 (2018).
- 894 51. Lindeboom, R.G., Supek, F. & Lehner, B. The rules and impact of nonsense-mediated mRNA
895 decay in human cancers. *Nature genetics* **48**, 1112-1118 (2016).
- 896 52. Ivanov, I., Lo, K., Hawthorn, L., Cowell, J.K. & Ionov, Y. Identifying candidate colon cancer
897 tumor suppressor genes using inhibition of nonsense-mediated mRNA decay in colon cancer
898 cells. *Oncogene* **26**, 2873-2884 (2007).
- 899 53. Barmada, S.J. *et al.* Amelioration of toxicity in neuronal models of amyotrophic lateral sclerosis
900 by hUPF1. *Proceedings of the National Academy of Sciences* **112**, 7821-7826 (2015).
- 901 54. Kumar, M.S. *et al.* Dicer1 functions as a haploinsufficient tumor suppressor. *Genes &*
902 *development* **23**, 2700-2704 (2009).
- 903 55. Naviaux, R.K., Costanzi, E., Haas, M. & Verma, I.M. The pCL vector system: rapid production of
904 helper-free, high-titer, recombinant retroviruses. *Journal of virology* **70**, 5701-5705 (1996).
- 905 56. Stewart, S.A. *et al.* Lentivirus-delivered stable gene silencing by RNAi in primary cells. *Rna* **9**,
906 493-501 (2003).
- 907 57. Salmon, P. & Trono, D. Production and titration of lentiviral vectors. *Current protocols in*
908 *human genetics* **54**, 12.10. 1-12.10. 24 (2007).
- 909 58. Dobin, A. *et al.* STAR: ultrafast universal RNA-seq aligner. *Bioinformatics* **29**, 15-21 (2013).
- 910 59. Anders, S., Pyl, P.T. & Huber, W. HTSeq—a Python framework to work with high-throughput
911 sequencing data. *bioinformatics* **31**, 166-169 (2015).
- 912 60. Danecek, P. *et al.* Twelve years of SAMtools and BCFtools. *Gigascience* **10**, giab008 (2021).
- 913 61. Love, M.I., Huber, W. & Anders, S. Moderated estimation of fold change and dispersion for
914 RNA-seq data with DESeq2. *Genome biology* **15**, 1-21 (2014).
- 915 62. Brancaccio, M. *et al.* Cell-autonomous clock of astrocytes drives circadian behavior in
916 mammals. *Science* **363**, 187-192 (2019).
- 917 63. Ting, J.T. *et al.* Preparation of acute brain slices using an optimized N-methyl-D-glucamine
918 protective recovery method. *JoVE (Journal of Visualized Experiments)*, e53825 (2018).
- 919 64. Lavery, D.J. & Schibler, U. Circadian transcription of the cholesterol 7 alpha hydroxylase gene
920 may involve the liver-enriched bZIP protein DBP. *Genes & development* **7**, 1871-1884 (1993).
- 921

922 **Supplementary material**



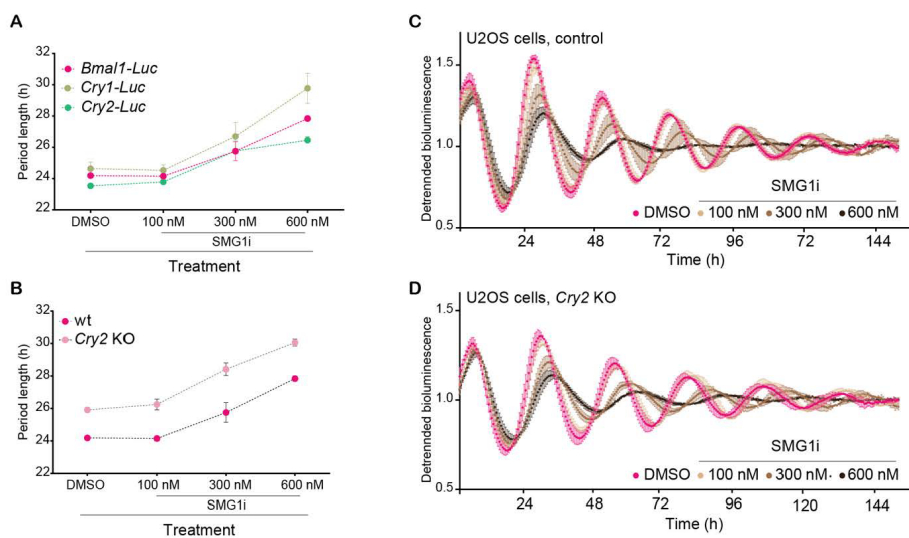
923

924 **Supplementary Figure S1. A.** Representative microphotographs of SCN sections to assess effective targeting of
 925 the SCN. Viral expression can be estimated from GFP signal, encoded with Cre on the same virus. **B.** Same as A,
 926 but image taken during bioluminescence recording of SCN slices. **C.** Upper diagram: Rhythms of voluntary
 927 locomotor activity were recorded prior to and after the SCN injection of the Cre- and GFP-expressing AAV. Lower:
 928 Representative actograms of a *Smg6^{flox/flox}* and *Smg6^{+/+}* mouse. The day of Cre:eGFP AAV injection is marked
 929 by an arrow and a dot. **D.** Period lengths of circadian locomotor activity rhythms of *Smg6^{flox/flox}* (in yellow) and *Smg6^{+/+}*
 930 (in blue) mice before (DD1) and after (DD2) stereotaxic surgery. **E.** Averaged traces of *mPer::Luc* rhythms of AAV-
 931 injected *Smg6^{flox/flox}* (yellow) and *Smg6^{+/+}* (blue) SCN explants. **F.** Period lengths of *mPer::Luc* expression in AAV-
 932 injected *Smg6^{flox/flox}* (yellow) and *Smg6^{+/+}* (blue) SCN explants. **G.** Recombination efficiency following Cre induction
 933 was evaluated by genotyping of genomic DNA extracted from SCN slices (liver-specific mutants served as controls
 934 for the genotyping).



935

936 **Supplementary Figure S2: A.** Read coverage on the *Hnrnp1* locus indicates the specific upregulation of transcript
 937 isoforms that are NMD-annotated and that can be identified by specific exons (see arrows in insets) in liver tissue.
 938 **B.** RNA-seq data is plotted for indicated genes – that all encode components of the NMD machinery itself – for
 939 mRNA (upper panels; exonic reads) and pre-mRNA (lower panels; intronic reads) for *Smg6* mutants (yellow) and
 940 controls (blue). RPKM values of individual animals are shown as dots with solid lines connecting the means for
 941 each timepoint. The dashed lines represent the rhythmic data fit using the parameters from Metacycle. **C.** RNA-
 942 seq data is plotted for *Atf4* and *Atf5* for mRNA (upper panels; exonic reads) and pre-mRNA (lower panels; intronic
 943 reads) for *Smg6* mutants (yellow) and controls (blue). RPKM values of individual animals are shown as dots with
 944 solid lines connecting the means for each timepoint. The dashed lines represent the rhythmic data fit using the
 945 parameters from Metacycle. **D.** Western blot analysis of liver tissue (as in Fig. 4D) for ATF5, eIF2 α and phospho-
 946 eIF2 α in *Smg6* mutant and control liver samples; HSP90 served as loading control. **E.** Quantification of ATF5 signal,
 947 normalized to HSP90 as loading control, from Western blot shown in D.



948

949 **Supplementary Figure S3: Pharmacological NMD inhibition prolongs circadian period in human**
 950 **osteosarcoma U2OS cells.** **A.** Period length of the circadian reporters *Bmal1-Luc* (fuchsia), *Cry1-Luc* (khaki) or
 951 *Cry2-Luc* (green) in the presence of increasing concentrations of SMG1i or vehicle (DMSO, equal volume as for
 952 the highest SMG1i dose). **B.** Period length of the circadian reporter *Bmal1-Luc* in wt (pink) or *Cry2* KO (fuchsia)
 953 U2OS cells **C.** Traces of *Bmal1-Luc* detrended bioluminescence signal in wild-type U2OS cells treated with
 954 increasing dosage of SMG1i or vehicle. Solid circles represent mean, error bars represent standard deviation. **D.**
 955 Average traces of *Bmal1-Luc* detrended bioluminescence signal in *Cry2* KO U2OS cells treated with increasing
 956 concentrations of SMG1i or vehicle. Solid circles represent mean, error bars represent standard deviation.

Recording of diurnal gene expression in peripheral organs of mice using the RT-Biolumicorder

G. Katsioudi, A. Osorio-Forero, F. Sinturel, C. Hagedorn, F. Kreppel,
U. Schibler & D. Gatfield

Circadian Regulation; Methods and Protocols

Methods in Molecular Biology, Springer

in press.

Recording of diurnal gene expression in peripheral organs of mice using the RT-Biolumicorder

Georgia Katsioudi ¹, Alejandro Osorio-Forero ², Flore Sinturel ^{3,4}, Claudia Hagedorn ⁵, Florian Kreppel ⁵, Ueli Schibler ⁶, David Gatfield ¹

1. Center for Integrative Genomics, University of Lausanne, Genopode, 1015 Lausanne, Switzerland
2. Department of Fundamental Neurosciences, University of Lausanne, Rue du Bugnon 9, 1005 Lausanne, Switzerland
3. Division of Endocrinology, Diabetes, Nutrition and Patient Education, Department of Medicine, University Hospital of Geneva, Geneva, Switzerland
4. Department of Cell Physiology and Metabolism, Faculty of Medicine, University of Geneva, Geneva, Switzerland
5. Chair for Biochemistry and Molecular Medicine, Center for Biomedical Education and Research (ZBAF), Faculty of Health, Witten/Herdecke University, Witten, Germany
6. Department of Molecular Biology, Faculty of Sciences, University of Geneva, Geneva, Switzerland

Running head: Recording of gene expression in peripheral organs *in vivo*.

Key words: Circadian rhythms, real-time bioluminescence recording, peripheral oscillators, feeding rhythms, luciferase, RT-Biolumicorder, mouse liver, gene expression regulation, transcription

Abstract

There is high interest in investigating the daily dynamics of gene expression in mammalian organs, for example in liver. Such studies help to elucidate how and with what kinetics peripheral clocks integrate circadian signals from the suprachiasmatic nucleus, which harbors the circadian master pacemaker, with other systemic and environmental cues, such as those associated with feeding and hormones. Organ sampling around the clock, followed by the analysis of RNA and/or proteins, is the most commonly used procedure in assessing rhythmic gene expression. However, this method requires large cohorts of animals and is only applicable to behaviorally rhythmic animals whose phases are known. Real-time recording of gene expression rhythms using luciferase reporters has emerged as a powerful method to acquire continuous, high resolution datasets from freely moving individual mice. Here, we share our experience and protocols with this technique, using the RT-Biolumicorder setup.

1. Introduction

Circadian clocks are pervasive in most light-sensitive organisms and serve to synchronize a variety of cellular, physiological and behavioral processes with the 24h solar day. Organisms possessing such biological timekeepers can actively anticipate daily recurring events, such as light-dark cycles, temperature rhythms, and nutrient availability, and thereby adapt their physiology in a proactive manner. Molecularly, the mammalian clock relies on negative

feedback loops in transcription that generate oscillations in gene expression. It is composed of about a dozen core clock genes whose daily oscillations drive the cyclic expression of hundreds to thousands of clock-controlled genes (that drive clock output) (see [1] for a comprehensive review of the mammalian circadian system). Anatomically, the circadian system is organized as a hierarchical network of self-sustained cell-autonomous clocks. These are capable of measuring time autonomously in the absence of external timing cues. However, they also integrate a variety of signaling cues and, in some cases, interact with the clocks of neighboring cells (coupling). At the top of the hierarchy, the master pacemaker in the suprachiasmatic nucleus (SCN) receives photic inputs from the retina. This allows the SCN to track external time and to relay internal time to the clocks found throughout virtually all peripheral organs. The synchronization of peripheral clocks by the SCN occurs via several, partially redundant, direct and indirect phase entrainment signals. While feeding-fasting rhythms, depending on rest-activity cycles, are the dominant synchronization cues for many if not most organs, rhythmic hormones and body temperature oscillations also participate in the phase adjustments of peripheral clocks [2–6]. In the liver, the best studied peripheral organ in the field, several studies have shown that feeding rhythms can even control the rhythmic expression of certain genes independently of local liver clocks [7, 8]. These findings reflect the necessity of this metabolically highly active organ to operate in synchrony with nutrient availability and to temporally coordinate the energy demands of the organism accordingly.

Continuous recording of oscillations in gene expression from peripheral cell types is readily achieved with *in vitro* cultured cells. Thus, many protocols are available for circadian reporter assays using cell lines and primary cells. These include a recent methods article in this journal for the real-time recording of bioluminescence rhythms in human primary cells expressing a firefly luciferase reporter gene [9]. Moreover, many peripheral tissues display circadian oscillations for several cycles when cultured as organ explants [10]. Such *in vitro* and *ex vivo* approaches are instrumental in studying the clock in isolation, but fail to recapitulate the complex interactions occurring *in vivo*. Moreover, explant and culture conditions likely inflict artefactual signals onto the clock, such as those elicited by medium and temperature changes. Rhythmic gene expression studies in animals have mostly relied on the analysis of tissues collected around-the-clock. Yet, even at a dense sampling rate (e.g. every 2 or 4 hours) the temporal resolution can be unsatisfactory for some purposes [11]. Moreover, the resulting data are non-continuous, providing a sequence of static snap-shots of circadian states from independent animals. This renders it virtually impossible to study kinetic properties or cause consequence relationships of the intrinsically dynamic clockwork. Moreover, biochemical time series are not feasible with behaviourally arrhythmic animals whose phase is not known. Another drawback is the need for large cohorts of animals. Real-time recording of peripheral circadian rhythms in intact animals can solve these issues. Initial approaches using the commercially available In Vivo Imaging System (IVIS) still relies on snap-shots taken at different time points from anesthetized mice that express rhythmically regulated luciferase reporter genes (*Per2::Luc* or *Bmal1-ELuc*) [12, 13]. The general anesthesia and the limited time resolution are major shortcomings of this system.

The RT-Biolumicorder (Figure 1A-B), a setup first described in 2013, allows for the long-term monitoring of bioluminescence in real time at a high temporal resolution in freely moving mice [6]. It is particularly suited for the recording of bioluminescence rhythms generated by large

organs, such as the liver, or entire animals (see also Note 1). Circadian reporter genes can be delivered either genetically (e.g. *Per2::Luc* [14]) or through adenoviral vectors. Here, we describe a protocol that we have established for RT-Biolumicorder experiments. It starts with the choice and administration of reporter genes and covers the animal operation procedures. It ends with considerations about the RT-Biolumicorder strategy and the description of settings used for recording and data analysis.

2. Materials

2.1 Mice and reporter gene

Mice carrying a genetically encoded reporter allele, for example the circadian *Per2::Luc* knockin (ki) reporter, can be used for RT-Biolumicorder studies [14]. Alternatively, the reporter can be introduced using an adenoviral vector. If none of the available reporter gene vectors (see Note 1) is suitable for the envisioned experiment, it is possible to custom-design, clone and prepare alternative adenoviral reporter constructs. Adenoviral vectors injected into the tail vein of animals predominantly accumulate in the liver [15], a well characterized process often applied for gene therapy [16]. In our experiments we use adult male mice at the age of 10 - 14 weeks, but female animals or animals of different ages may be used as well, depending on the addressed research question.

2.2 Adenovirus vector production and purification

Adenovirus (Ad) genome transfection

1. Restriction enzyme for Ad vector genome linearization
2. Polyethylenimine (PEI) solution: 7.5 mM linear 22 kDa PEI, pH 7.0 (adjust pH with NaOH). Sterile filtrate. Store at 4°C.
3. Adenovirus producer cells: E1-complementing cell line for production of first generation Δ E1 Ad vectors, e.g. HEK293 (ATCC, CRL-1573)

Adenovirus harvest, rescue and amplification

1. buffer: 50 mM HEPES, 150 mM NaCl, pH 7.8 (adjust pH with NaOH). Sterile filtrate. Prepare fresh, protect from light and store at 4°C.
2. Culture plates, 6 cm and 15 cm diameter
3. Cell scrapers
4. Conical centrifugation tubes
5. Liquid nitrogen
6. Water bath at 37°C

Adenovirus purification

1. Liquid nitrogen
2. Water bath at 37°C
3. Adenovirus buffer (Ad-buffer): 50 mM HEPES, 150 mM NaCl, pH 7.8; sterile filtrate. Prepare fresh, protect from light and store at 4°C.
4. CsCl step gradient buffer: CsCl=1.27 g/cm³ in Ad buffer, pH 7.8; sterile filtrate. Prepare fresh, protect from light and store at 4°C.
5. CsCl step gradient buffer: CsCl: 1.41 g/cm³ in Ad buffer, pH 7.8; sterile filtrate. Prepare fresh, protect from light and store at 4°C.
6. Glycerol (autoclaved)
7. 200 ml centrifugation tubes

8. 13.2 ml ultracentrifugation tubes, e.g. 13.2 ml UltraClear, Beckman Coulter
9. Ultracentrifuge with swing-out rotor, e.g. Beckman SW41
10. Syringes and needles
11. PD-10 size exclusion chromatography column (GE Healthcare)

Adenovirus titration by measurement of OD260

1. Sodium dodecyl sulfate (SDS) solution: 10% SDS in autoclaved ddH₂O
2. Blank sample: Adenovirus buffer, 10% glycerol

2.3 Adenovirus administration

If a viral vector is the approach of choice, an additional experimental step is required for its delivery. Our method of choice is tail vein injection. The materials required for tail vein injections of virus are:

1. Adenoviral reporter (stored at -80° C or below)
2. Restrainer for tail injection (commercially available or homemade). We use “The Mouse Tail Illuminator” from Braintree Scientific, Inc (Braintree, MA, USA) that restrains the mouse while at the same time warming up and illuminating the tail.
3. 70% ethanol
4. Heating box or a heating lamp for preheating the animals prior to the injection (recommended)
5. Single-use 1 ml plastic syringe and 30G needles; alternatively, insulin syringes or others can be used.

2.4 Pump implantation

Luciferin can be administered both via drinking water (see Note 2) or with the use of a micro-osmotic pump for constant supply. When delivery by pump is preferred, it must first be filled with luciferin, activated at 37°C, followed by the subcutaneous, dorsal implantation. The required material is:

1. Mini-osmotic pumps. Different pumps are commercially available (ALZET, <https://www.alzet.com>), differing in size/reservoir volume, flow rate, and duration of delivery. The choice will be mainly dictated by the experimental design and the age/weight of the animal. We use the 1007D ALZET pump with a reservoir volume of 100 µl and a diffusion rate of 0,5 µl/h, which has a duration of about one week with the *Per2::Luc* ki mouse. With viral vectors we use the 2001 ALZET pump with a reservoir volume of 200 µl and a diffusion rate of 1 µl/h, lasting approximately 7 days. For experiments in which the feeding schedule is modified during recording (recording of clock resetting kinetics), the use of pumps with longer duration is recommended (i.e., models with 200 µl reservoir).
2. Blue or teal coloured flow moderators (ALZET) (see Note 3)
3. D-Luciferin sodium salt, lyophilized powder - dissolved 90 mg/ml in Phosphate Buffered Saline (PBS, pH 7.4) For luciferin supply via drinking water, D-luciferin is diluted in tap water with 0.8 mM NaOH to a final concentration of 1.56 mg/ml.
4. Single-use 1 ml plastic syringe for filling the pump
5. Needle for filling the pump (filling tube provided by the pump supplier, or any sterile needle with appropriate diameter)
6. Sterile 0.9% NaCl for pump activation (at 37°C)
7. Shaver or epilation cream (see Note 4), unless genetically hairless animals – such as the immunocompetent SKH1 mouse strain – are used [6].

2.5 Animal care and room disinfection

1. 70% ethanol, deconex or other disinfectant for disinfecting the surfaces
2. Bepanthen® Plus creme and Povidone-iodine ointment for disinfection and care of the site of invasive procedure (sutures after pump implantation)
3. Anesthetics (isoflurane, ketamine/xylazine or others, according to the approved animal experimentation authorisation)
4. Painkillers (water soluble paracetamol, carprofen or others, according to the approved animal experimentation authorisation)
5. Topical ophthalmic ointment for eye protection during anesthesia
6. Heating pad for keeping animal temperature stable during anesthesia
7. Sterile scissors, hemostatic forceps, straight and curved forceps and surgical suture (all tools that are used for invasive procedures, such as in pump implantation, must be meticulously cleaned and sterilized)
8. Appropriate scoresheets for the monitoring of animal well-being according to the approved animal experimentation authorisation (see Supplemental attachment).

All animal procedures must ensure animal welfare and follow the regulations of your research institution and local legislation for animal experimentation. In most countries a detailed form describing the procedures must be submitted for approval to local authorities prior to starting experiments.

2.5 Recording

Hardware:

1. RT-Biolumicorder (Lesa-Technology), including air pumps and power supply, feeders and water bottles for each of the RT-Biolumicorder setups (see Notes 5, 6,7 & 8)

A computer with the relevant software (Biolumicounter, Lesa-Technology) (Notes 6 & 9)

Consumables:

1. Polyethylene-coated paper that allows infrared transmission in the 7-14 μm range (used to cover the infrared sensor at the center of the recording cage; Lesa-Technology)
2. Highly absorbent bedding (Lesa-Technology)
3. Sodium hydrogen carbonate (NaHCO_3) to apply to the bedding for neutralization of urine smell during recording (optional)
4. Chow (or any other) diet pellets with a diameter of approximately 12 mm, which are loaded into the feeder of the RT-Biolumicorder (see Note 10).

3. Methods

3.1 Choice of reporter gene

Since the experimental readout relies on bioluminescence signals, the first decision to take concerns the selection of the appropriate firefly luciferase reporter and the mode of its delivery. The two main possibilities are, (i) to use a mouse strain genetically carrying a suitable reporter allele, or (ii) to use a reporter gene delivered through viral transduction. Both methods need preparation (weeks/months) before the start of the actual recording experiments, e.g. to breed the reporter allele into the desired mouse strain, or to clone and prepare the adenoviral vectors (Figure 1C). Please see Note 1 for a detailed account of advantages and weaknesses of the two approaches.

3.2 Adenoviral preparation

Adenovirus is a non-enveloped virus harbouring a double-stranded DNA genome of 36-40 kb. Human adenoviruses, such as adenovirus type 5 (hAd5, Ad5), have been extensively studied and their cell entry and replication processes have been characterized in great detail. The virus genome can easily be cloned into a plasmid or bacmid backbone, and the virus is rendered replication-defective by removal of the early adenoviral gene region E1 from its genome. Plasmid/bacmid systems based on human Ad5, which allow for the insertion of heterologous transgene expression cassettes into the replication-defective vector genomes, are commercially available. Due to its high genome stability, its ability to transduce a wide variety of proliferating and post-mitotic cells, and the possibility to produce infectious virions to high titers with relative ease, replication-deficient Ad5 can serve as an attractive tool for transient gene transfer in various animal models. The amplification of Ad5-based vectors requires producer cells which complement the lack of the early viral gene region E1 in trans. HEK293 cells are the most commonly used cell line that constitutively expresses Ad5 E1 and that is thus able to support the production of replication-deficient adenoviral vectors after transient transfection of Δ E1 vector genomes. Although the efficiency with which vector particles are produced from transfected genomes is poor, the number of produced virions is still sufficient to re-infect fresh HEK-293 cells. Prior transfection, Ad5 Δ E1 genomes have to be released from the respective bacmid/plasmid backbone by using a suitable restriction enzyme.

For vector production and purification, the following steps should be performed:

1. Seed HEK-293 cells in 24-well plates with 2×10^5 cells/well and transfect the next day with 500 ng/well of the E1-deleted, linearized vector genome using Polyethylenimine (PEI).
2. A full cytopathic-effect (CPE), reflecting successful vector amplification, should be visible 7-12 days after PEI transfection. A full CPE is characterized by a morphological shift from an adherent to globular appearance and aciniform cell detachment. At this time point, most vector particles are retained intracellularly. We advise to perform multiple transfections in parallel since the efficiency of virus vector rescue from plasmid/bacmid can be low.
3. Release cells from the dishes by scraping and harvest by centrifugation for 10 min at 400 x g. Next, the pellet is resuspended in 1 ml Ad-buffer and subjected to three freeze/thaw cycles, using liquid nitrogen for freezing and a water bath at 37°C for thawing.
4. The lysate, now containing rescued Ad vector particles, can be used for reinfection of 1×10^6 cells seeded the day before in a 6-cm dish. Now, cells should exhibit a full CPE 48-72 h post-infection.

This serial amplification procedure should be repeated as described by Kratzer and Kreppel (17) up to a final reinfection of $1-2 \times 10^8$ cells (10 to 15 15-cm dishes). To obtain highly purified Ad vector particles, cells from final reinfection are harvested, lysed and subjected to two consecutive discontinuous CsCl gradients. It is very important to perform the purification with two subsequent discontinuous gradients in order to remove impurities which might interfere with vector performance in vivo.

5. Harvest cells from final reinfection into 200 ml centrifugation tubes and pellet as described above.
6. After centrifugation, resuspend the pellet in 3 ml Ad-buffer and rescue vector particles by three freezing/thawing cycles.

7. Subsequently, load the lysate onto a discontinuous CsCl density gradient (lower phase: 3 ml of ρ_{CsCl} : 1.41 g/cm³; upper phase: 5 ml of ρ_{CsCl} : 1.27 g/cm³) and centrifuge for 2 h at 176.000 x g and 4°C using an ultracentrifuge.
8. After centrifugation, the white-blue vector band is visible at the border of the two different CsCl solutions. Collect the vector band by puncturing the ultracentrifugation tube using a syringe.
9. Dilute aspirated Ad vector particles with Ad-buffer to a final volume of 3 ml, load onto the second discontinuous CsCl density gradient and centrifuge as described above.
10. Collect the vector band with a syringe as described above and dilute with Ad-buffer to a final volume of 2.5 ml.
11. To remove CsCl, disposable PD-10 columns are equilibrated with Ad-buffer (5 x 5 ml) before being loaded with Ad vector particle dilution.
12. The virus is eluted with a volume of 3 ml Ad-buffer and subsequently supplemented with glycerol to a final concentration of 10%.
13. Suitably sized aliquots (50 – 200 μ l) can be stored at -80°C.

To maintain the integrity and infectivity of Ad vector preparations, the vectors should always be stored at -80°C in the presence of 10% glycerol. Note that repeated freezing/thawing cycles can significantly reduce vector infectivity. Therefore, it is recommended to store appropriately sized aliquots.

To assess the quality of purified Ad vectors, the physical and infectious titers, and the purity of the preparation are evaluated.

3.2.1 Titer quantification

Physical titers are quantified by either quantitative PCR or the determination of the optical density at 260 nm.

1. For measuring OD₂₆₀, mix 20 μ l purified vector solution with 79 μ l deionized water and 1 μ l of 10% sodium dodecyl sulfate (SDS) and incubate for 10 min at 56°C for capsid denaturation.
2. Physical particle titers can be calculated from measured OD₂₆₀, with one OD₂₆₀ unit corresponding to 1.1 x 10⁹ vector particles per μ l (18, 19).

Infectious titers:

1. To determine the infectious titer, infect 2x10⁵ HEK-293 cells with a serial dilution (1:10,000 - 1:10) of purified vector and incubate at 37°C, 5% CO₂.
2. After 48 h cells are visually screened for a full CPE.

Since the ratio of infectious to non-infectious particles usually varies between 1:10 and 1:30 [20] a full CPE 48 h post-infection represents a multiplicity of infection (MOI) of 300 and can therefore be used to calculate the infectious titer.

Purity of vector preparation

Purity of Adenovirus vector preparation is verified by polyacrylamide gel electrophoresis (SDS-PAGE).

1. According to physical particle titers, incubate 1-2 x 10¹⁰ vector particles for 10 min at 75°C for denaturation.
2. Load on a 8% SDS-PAGE gel.

3. After electrophoresis, develop the gel by silver-staining [21]. This highly sensitive staining procedure allows the detection of even weak protein bands and contaminant traces (i.e. non-viral proteins).

3.3 Tail vein injection

Tail vein injection of viral vectors is a rapid procedure and allows for a quick recovery of the animal; please also refer to Figure 2A-B for a schematic drawing relating to this procedure.

1. Recommended: warm up the animals prior to the intervention. We place the mice in thin-walled plastic cages on a heated metal surface at 37°C for 1-2 hours before the injections. Similarly, the restrainer for tail vein injection and 70% ethanol for disinfecting the tail should be pre-warmed to 37°C.

2. Thaw the adenoviruses on ice or at room temperature for the time period of an experiment that involves injecting several animals. Avoid multiple freezing/thawing cycles of viral preparations.

3. Anesthetize the mouse by inhalation (constant supply of 2% isoflurane) or injectable anesthesia (80/12.5 mg/kg ketamine/xylazine intraperitoneally, which results in ~50 min anesthesia). Tail vein injection in non-anesthetized animals is also possible, if allowed by the local animal experimentation legislation. In our lab we have been using anesthesia by inhalation (2% isoflurane) as it allows for quicker recovery and is considered more animal-friendly (see Note 11).

4. Once the mouse is restrained apply topical ophthalmic ointment and disinfect the tail.

5. Draw the virus with the syringe (be sure to avoid any air/bubbles), place the needle on the syringe and remove any residual bubbles.

6. With the applied heat from the restrainer, the veins of the animal become visible; the mouse tail has two caudal veins laterally to the artery (Figure 2B). Locate one of them, place the animal on its side, and insert the needle into the vein, almost parallel to the tail (the angle should be no greater than 15 degrees to the vein). In most cases, we have found injections within the middle third of the tail most convenient (closer to the tail base, the vein is larger; closer to the tip, it can be more visible). A sign for correct placement in the vein is entry of a small amount of blood into the syringe, either spontaneously or after slowly drawing back the syringe.

7. Once proper localisation of the needle is ensured by this strategy, slowly inject the virus (ca. 5 seconds for the 100 µl). In case of resistance during injection, slightly readjust the needle or try with the other vein to avoid further irritation on the same side of the tail.

8. At the end of the injection carefully remove the needle and apply slight pressure to the puncture with a clean piece of cotton until the bleeding has stopped (blood at the end of the injection is a good indication of a successful injection).

9. Monitor the animal until the anesthesia has passed. About 24-48 hours after viral injection, the animal can proceed to pump implantation. We would like to point out that several videos showing correct tail vein injection practice are also available on YouTube.

3.4 Luciferin solution preparation, pump filling & activation

There are two ways of luciferin administration during recording, either via drinking water or via constant diffusion using a mini-osmotic pump. There are several pros and cons to both approaches.

For *in vivo* imaging, luciferin can be administered via drinking water, as it is not significantly degraded in the digestive tract [22]. Luciferin supply in drinking water has no toxic sideeffects.

This method is more animal-friendly and shortens the overall protocol. Even though this route of administration has been used in circadian studies using the RT-Biolumicorder before [6], other observations indicate that daily changes in liquid uptake (drinking) by the mice can lead to rhythmic fluctuations in *in vivo* luciferin availability (see Note 2) [23].

However, the drinking rhythms do not markedly confound the results when high-amplitude circadian bioluminescence rhythms are recorded [5].

By contrast, mini-osmotic pumps provide constant diffusion of luciferin for several days. Pumps furthermore allow to choose the appropriate diffusion rate and duration according to the study design. Lastly, mice tolerate the implanted pumps well, especially the smaller models with a 100 μ l reservoir volume. However, the pump implantation requires an extra round of anesthesia and painkiller administration and it prolongs the overall protocol for at least two more days. In addition there is a possibility that daily locomotor activity might influence the diffusion rate of the luciferin via the pump and thus create low-amplitude activity-related rhythms [23]. Animal experimentation approval is required prior to the pump implantation procedure.

Pump filling and activation are performed under sterile conditions, according to the following protocol:

1. Dissolve the D-Luciferin sodium salt at 90 mg/ml in sterile PBS, pass it through a 0.45 μ m filter and aliquot it. Dissolved luciferin is stored at -20°C. Luciferin is light sensitive, so keep the aliquot tubes wrapped in foil.
2. Filling the pump with luciferin solution is performed using a single-use 1 ml syringe, either with the needle provided together with the pump, or with a needle of your choice. If not using the needle provided with the pumps, be sure to use a needle that has a blunt tip in order to avoid damaging the inner wall of the pump.
3. Draw the luciferin without the needle to avoid any small bubbles, place the needle and remove excess air.
4. Place the needle carefully inside the opening of the pump and slowly inject the luciferin until the pump is completely full. Carefully, release the needle and place the flow moderator, always ensuring that there are no air bubbles (see Note 12). Air bubbles can potentially block the pump and affect its function.
5. Place the pump in a 15 ml tube containing ~5 ml sterile NaCl 0.9% covered with foil and leave for activation at 37°C. The pump activation duration varies depending on the pump type (we typically activate in the range of a few minutes to a few hours).

3.5 Pump implantation

Before the pump implantation, the animals are anesthetized. In addition, some of the dorsal fur coat is shaved or removed with epilation cream (see Note 4), in particular around the area of interest for recording, notably the liver (Figure 2A). Depending on the mouse strain, the dark fur can strongly reduce the signal intensity of emitted bioluminescence. For this procedure, injectable anesthetics are preferred, in order to shave the mice more easily and quickly. However, inhalational anesthetics are tolerated better by some mice strains and in general allow quicker recovery (see Note 11). All surfaces and surgical instruments must be disinfected, and animal body temperature must constantly remain at ~37°C by the use of a heating pad.

1. Place the anesthetized and shaved mouse on the head pad, apply ophthalmic ointment and inject painkiller (if an injectable painkiller is used). We inject 4-5 mg/kg of Carprofen

subcutaneously at the beginning of the pump implantation procedure. Check the animal reflexes to evaluate the status of anesthesia.

2. Using sterile forceps and surgical scissors, cut a small incision into the skin of the right upper back of the animal. The incision must be long enough to slip in the pump (pumps with 200 μ l of reservoir require larger incisions compared to those with 100 μ l of reservoir).
3. With a pair of straight forceps, carefully lift the skin and insert a pair of hemostatic forceps. Opening and closing the hemostatic forceps inside the incision will create a “pocket” in the skin that will accommodate the pump.
4. Remove the pump from the NaCl solution, slowly take out the hemostatic forceps, and insert the pump with the flow moderator facing downwards.
5. Once the whole pump is inserted under the skin (be careful not to implant the pump intraperitoneally), apply iodine, suture the wound using surgical suture, and administer Bepanthen® Plus creme at the back of the mouse.
6. Place the anesthetized animal in a heat-controlled environment (a dedicated recovery cage or, alternatively, a heating lamp) and monitor until it fully recovers from anesthesia.

3.6 Monitoring of animal welfare

The wellbeing of animals must be evaluated all along the experiment, especially after the invasive procedures, i.e. following the tail vein injection (if applicable) and the pump implantation (if applicable). The researchers should look for signs of discomfort or pain, such as altered grooming behavior, posture, or locomotor dysfunction. Body weight must also be monitored. Painkillers and antibiotics can be administered if required. In the case of severe signs of pain or infection the animal has to be sacrificed. We have created two dedicated scoresheets, according to the Swiss animal experimentation legislation. A carefully processed datasheet helps in the evaluation of animal health and in making the choice of the most appropriate action (medication, sacrifice) (see Supplemental attachment).

3.7 Recording

Figure 1A shows a schematic representation of the RT-Biolumicorder that was developed at the University of Geneva [6] and is now commercially available from Lesa-Technology. One single-housed mouse can be recorded in each RT-Biolumicorder setup at a time. The RTBiolumicorder consists of a cylindrical cage with photon-reflecting walls, equipped with a photomultiplier tube (PMT) centrally at the top of the cage, a food container (right side) and a water container (left side). In addition, the device contains a large reflecting cone on top of the cage (external cone) that projects photons to the photomultiplier tube and a small reflecting cone in the center of the cage floor (central cone) that projects photons to the reflecting walls. An infrared sensor built into the small cone records the locomotor activity of the mouse.

1. Use highly absorbent bedding in order to reduce the background light in the recording cage. The bedding must cover the entire surface at the cage bottom.
2. Apply sodium hydrogen carbonate on the bedding to neutralize the urine smell that can otherwise accumulate during the recording period (a small amount ~20 g equally dispersed on the bedding; optional).
3. Cover the small central cone at the center of the recording cage with special polyethylene-coated paper.
4. Lastly, after the bedding and the central cone, place the round metal grid on the cage floor.

5. Provide a small amount of bedding on top of the grid, as nesting material for the animals. It is important to not provide too much bedding material, as this might interfere with signal detection (in particular during the sleep phase).

6. Carefully fill the food and water containers. The food pellets must have a specific size in order to fit in the feeding tube (pellets of maximum 12 mm diameter). Take special care to ensure that there is no leakage from the water containers. We recommend manually tracking food and water consumption over the course of the experiment as a means to ensure that there are no issues with access to food/water and/or with animal wellbeing.

It is recommended not to open the recording cages during the experiment (see Note 10).

7. Place the animals in the recording cages and turn on the power supply of the RTBiolumicorders (multiple RT-Biolumicorders can be attached to one supply) and the air pumps for each recording cage (see Notes 5 & 8).

8. Constant air pressure in the cages is very important during the recording, as the air exchange is required for oxygen supply and removal of urine odors (see Note 8).

9. Using the ‘‘Biolumicounter’’ software, select the desired recording parameters (timing of lights-on, lights-off and food access) for each of the recording cages and initiate. During the recording period it is possible to change recording parameters and to evaluate photon levels and animal activity in real-time.

3.8 Recording parameters: habituation period, feeding schedules, skeleton photoperiods

Depending on the experimental design and the research questions, various parameters during the recording period are adjusted. An initial habituation period with 12h lights-on and 12h light-off (in phase with the previous timing experienced by the animal) of approximately 2448 hours is recommended before releasing the animals into constant darkness or other experimental conditions (see Note 13).

After the first 24h of the habituation period, the experimenter may potentially open the cages (during lights-on phase) and visually check the animals, which can inform on whether they have become accustomed to the new environment (in particular to the feeder/water supply). Prolonged habituation periods may be considered according to the scientific questions of the experiment. However, it is important to keep in mind that there is no recording during the lights-on period and that mini-osmotic pumps have a limited delivery duration (by contrast, the duration of adenoviral vector expression has rarely been a limiting factor in our experiments, as it persists for several weeks).

After habituation, animals are typically released into constant darkness, if data collection under free-running conditions is desired. Alternatively, a skeleton photoperiod is applied, if the experiment requires measurements under phase-entrained conditions. In our hands, a simple skeleton photoperiod consisting of two 30 min light pulses at the beginning and end of the ‘‘light’’ phase (ZT0-ZT0.5 and ZT11-ZT11.5) is sufficient to ensure a stable phase entrainment, while causing minimal disruptions to the recordings (that are, of course, suspended during illumination).

Through the programmable feeder, food availability can be set as desired. Typical settings used in many studies in the chronobiology literature are *ad libitum* feeding or time-restricted feeding. The activity cycles, entrained by skeletal photoperiods through the synchronisation of the SCN, can be deduced from locomotor activity records. High and low mobility periods

correspond to subjective nights and days, respectively, for nocturnal animals like mice (see Note 7).

3.9 Termination of experiments

1. At the end of the recording period, stop the recording and open the RT-Biolumicorder devices.
2. Evaluate the health status of the animal (body weight, grooming) and proceed with sacrificing the mice and, if applicable, collecting their tissues.
3. Total food consumption may also be evaluated at the end of the experiment.
4. Mini-osmotic pumps are designed for single usage, so discard them at the end of the recording (depending on the local biological waste regulation, removal of the pumps from the animal body and separate disposal might be required).

3.10 Data analysis

Data are obtained as numeric values of photon number and activity levels per minute in text files (*.txt*). Time, light and feeder information are also included in the data files. Data can be analyzed using the computational program of choice. In the past, we have used the commercially available software Igor Plus (Wavemetrics) [6]. In addition, we have recently programmed a software that enables easy visualisation and analysis of RT-Biolumicorder recording data, both for individual mice and by experimental groups (see Note 9).

We have developed a custom-made application that runs under the MATLAB environment (The Mathworks, Inc). The application, that we named Osiris, allows the user to easily load, visualize and analyse the *.txt* format data generated by the RT-Biolumicorder. Briefly, the signals obtained for locomotor activity and the bioluminescence data from an individual animal can be displayed as a smoothing average across the recording period (the raw data are displayed on demand, Figure 3A-B). Tracks for food access and illumination are available for display as well. Osiris also allows selecting different smoothing parameters (in particular moving average window size) for the rather spiky bioluminescence raw data.

In addition, with Osiris, the user can create a database that includes multiple animals within one or more groups. Within a group, it uses the information provided by the user to align the data across the individual animals and to visualize their signals (mean and dispersion, with options: standard error of the mean, standard deviation, 95% confidence interval) for the selected animals in each group (Figure 4A). The database of multiple animals can be saved in *.mat* format, and the output images in both *.tiff* and *.eps* formats.

Finally, for the current (first) version of Osiris, relevant (albeit still basic) rhythmicity analyses on the bioluminescence and activity signals can be executed. Thus, it is possible to collapse an animal's multi-day recording into a mean cycle across the 24 hour period (Figure 4B). Measures of peak-trough amplitude, peak phase (ZT values) and the steepness/rate of change from trough to peak values in the 24 hour period of the mean cycle can be exported in *.csv* format, and graphics outputs in both *.tiff* and *.eps* formats. In summary, all these features aim at making analyses and conclusions easier and more user friendly. Moreover, they greatly improve traceability and objectivity of the analyses. The Osiris application is publicly available at <https://github.com/aosorioforero/Osiris.git>.

4. Notes

1. Different considerations come into play when deciding on which reporter gene to use, and whether to rely on adenoviral delivery or a genetically encoded allele. A genetically encoded

reporter allele has multiple advantages, such as the high reproducibility of its expression that occurs from a defined genetic locus and that is not limited in time. As no viral injection is required, the experimental procedure is shorter and the setup considerably simpler and with less stress for the animal. By contrast, the genetic alleles will typically be expressed across tissues and cell types, which can have implications for the interpretability of the signal that is recorded from the whole animal. In published work [6] and additional experiments in our laboratories, the genetic reporter allele that has been successfully used is the *Per2::Luc* allele (official nomenclature: *Per2^{tm1Jr}*) developed by the Takahashi laboratory [14]. It is a knock-in of the coding sequence (cds) of firefly luciferase into the endogenous *Per2* locus, in frame with the *Per2* cds (lacking its termination codon) such that a fusion protein PER2-Luciferase is produced. This fusion protein fully replaces the function of PER2 within the circadian clockwork circuitry. Hence, the allele is more than a simple reporter of circadian transcriptional oscillations, but luciferase activity quantifies the abundance of the core clock protein Period 2. We have used the *Per2::Luc* allele in RT-Biolumicorder experiments in both heterozygous (*Per2::Luc* / +) and homozygous settings (*Per2::Luc* / *Per2::Luc*). The former already gives sufficiently robust signals for most purposes. Finally, it has been observed that the *Per2::Luc* reporter reacts relatively sensitively to changes in feeding rhythm [6], making it a suitable tool to study phase readjustment kinetics mediated by food-derived signals. Beyond the popular *Per2::Luc* allele, a number of other circadian luciferase alleles are available. Yet testing their performance and properties in RT-Biolumicorder experiments is, to the best of our knowledge, still pending. Thus, *mPer1-Luc* transgenic mice have been constructed independently by different labs. In these mice the luciferase expression is driven by mouse *Per1* promoter/5' UTR elements (e.g. *Tg(Per1-luc)025Jt* [24] or *Tg(Per1-luc)Chron* [25]). We expect these alleles to be suitable real-time reporters of *Per1* expression rhythms in RT-Biolumicorder experiments. Mice carrying the *Bmal1-ELuc* transgene [26] express enhanced green-emitting luciferase (ELuc) from the 5'-flanking region of the *Bmal1* promoter and would be suitable in RT-Biolumicorder experiments to track the rhythmic transcriptional activity at the *Bmal1* promoter.

Nevertheless, the number of available rhythmically expressed genetic luciferase alleles remains rather limited (and crossing them into a specific mouse model/genetic background can be time-consuming). Transduction with viral reporters is an alternative way of delivery. Moreover, this method allows testing reporter variants, as well as the co-delivery of additional genes. In our experiments, we use E1/E3-deleted replication-incompetent first generation adenovirus vectors based on human adenovirus serotype 5 (plasmid pCV100, a variant of pGS66 [27] with an additional deletion of Ad5 nt 28133-30818) purified to high titres (>10E9 infectious particles/ μ l) that are safe (replication-incompetent; no wild-type virus contamination; depending on your local biosafety regulations, they can be considered non-biohazardous) and do not elicit a severe immune response in the mice. Upon tail vein injection, adenoviral vectors transduce primarily liver cells. We typically inject 10E11 infectious particles through the tail vein, which results in robustly detectable signals for several weeks. Two reporter constructs have been particularly useful in our hands. The *Reverba-Luc* reporter (recapitulating the rhythmic transcription at the *Rev-erba/Nr1d1* locus) is fast-reacting to changes in feeding rhythm, whereas the *Bmal1-Luc* reporter (*Luciferase* cloned with *Bmal1/Arntl* promoter and 5' UTR sequences) has slower readjustment kinetics to food-derived signals and may thus be

more dependent on SCN signalling cues [6]. Moreover, the *Bmal1-Luc* construct also contains an expression cassette for Cre recombinase (driven from hCMV promoter) [28], which allows the recombination of floxed alleles and recording of transcriptional rhythms from the same cells. Other reporter constructs are in the making in our group, and possibly other laboratories as well, which should extend the repertoire of useful reporter viruses in the future.

In principle, every organ/tissue emitting sufficient amounts of photons would be suitable for RT-Biolumicorder recording experiments. We anticipate that lungs, heart and skeletal muscles, kidney, pancreas, whole brain, stomach, parts of the gut and skin would fall into this category of organs/tissues. Transgenic mice, whose genomes carry luciferase reporter genes with flox-stop signals, could probably be engineered for all of these tissues. In such animals, the tissue-specific expression of the reporter could be achieved by expressing a Cre recombinase transgene from cell type-specific transcriptional regulatory elements, such as locus control regions, enhancers, or promoters.

2. When administering luciferin via drinking water, it is important to exclude the possibility that drinking rhythms interfere with the rhythm of the reporter of interest. In this case it is recommended to measure temporal drinking profiles during the recording in order to control for potential bias due to rhythmic drinking of the animals. A way of doing so is by using an ultrasonic detector to record water consumption throughout the experiment (prototype at Lesa-Technology). A recent study detected rhythmic expression of an otherwise constitutively expressed reporter when luciferin was administered via drinking water and the observed rhythm resembled the expected rhythm of the drinking behaviour [23]. We speculate that environmental conditions of the experimental room, such as the humidity levels, or the reporter in use (genetic, viral, expression levels) could potentially determine whether bioluminescence levels are affected by the drinking behaviour. We would like to emphasize, however, that the bioluminescence cycles engendered by drinking rhythms are of much lower amplitude than bioluminescence cycles driven by circadian reporter genes. Indeed, Sinturel *et al.* [5] and Martin-Burgos *et al.* [29] have recently shown that drinking rhythms do not markedly confound the results obtained with circadian luciferase reporter genes.

3. We use blue flow moderators from ALZET, which are recommended for bioluminescence imaging applications. These were specifically developed to avoid background luminescence caused by the standard (white) flow moderators, which may interfere with the real signal from the reporter gene.

4. By shaving/depilation of a dorsal patch of the fur coat (corresponding to the position of the liver), it is possible to limit detected signal mostly to that emitted from hepatic tissue. Nevertheless, possible contributions from other organs must be kept in mind

5. Hardware problems: It is important to check that all parts of the equipment function properly before initiating experiments. Potential problems with hardware can include: power supply and computer problems, infrared sensor problems (often accidentally blocked by bedding), the indicator lights at the RT-Biolumicorder panel (for activity, PMT, shutter) might be out of order or burnt (and need replacement), or the shutter might be blocked.

6. Light settings: when setting the lights-on and lights-off timing in each of the RTBiolumicorders, always remove all pre-existing settings and set up the desired new settings. Often the software has a particular default setting assigned when starting the program and it can cause confusion if not removed.

7. Feeder opening/closing: When placing an animal for recording, always check that the feeder is placed in the correct position and the animal can access the food. Especially in cases when altered feeding schedules are applied, it is very important to evaluate the proper opening and closure of the feeder. During cleaning of the feeders between experiments it has happened to us that the position got slightly altered, which resulted in the mechanics of food access not closing properly. This will have repercussions on the obtained data and their interpretation. Of note, we found that *Bmall* knockout mice require a longer period of adaptation before recording can be started.

8. Air pump control: It is important to daily check the proper function of the air pump by evaluating the pressure at the recording cage (there is an air pressure indicator outside of each RT-Biolumicorder setup). Air pumps can be out of function over time or accidentally detach from the power supply, causing severe problems to the recorded mouse and eventually its death.

9. Data files and storage: it is recommended to securely save the data on an external disk at multiple time points during the recording period. Potential problems of the computer or the software might lead to loss of data. Moreover, it is important that there are no empty spaces at the end of the *.txt* file to be properly loaded by Osiris. This can happen in a small percentage of files created by the RT-Biolumicorder, in which case the empty spaces should be manually modified before loading for the current version. No further modifications of the files are needed.

10. Food/water consumption: When refilling the feeding tube, remove the metal weight, place the food pellets and then put the metal weight back. Always use a specific type of food granule that fits into the food supplier of the RT-Biolumicorder (as mentioned above we use a diet consisting of 12 mm pellets). Avoid using too small/broken pellets as they might block the tube and restrict food supply. The feeder cover should be well closed in order to avoid any potential light introduction from the external environment to the recording cage. When evaluating the water consumption, the floater/indicator might be stuck and show no changes in the water levels in the tube.

When filling up the water supplier always ensure that there is no leakage. To do so, assemble carefully all the parts of the supplier, fill in the water and let it stand for a few minutes or hours. If there are no drops coming out of the bottle, it can be placed in the recording cage. When placed in the cage, proper position and water access must be evaluated (water needs to be able to drip out when the animals touch it with their tongues. Check manually that the water is freely coming out of the reservoir and there is no blockage by air bubbles). Make sure that the indicator can freely move and is floating on the water, before concluding that the mouse is not drinking any water.

11. Anesthesia troubleshooting: In our experiments we have occasionally faced problems with mice recovering poorly from injectable anesthesia with ketamine/xylazine after mini-osmotic pump implantation. Please also note that some circadian knockout mice are particularly sensitive to xenobiotics, as detoxification by the liver is under clock control. We have thus changed to anesthesia by inhalation using isoflurane. Briefly, animals are placed in a plexiglass chamber, anesthetized and quickly shaved with an electric razor. We perform the pump implantation in a laminar hood using a homemade nose mask (which can be easily constructed using a small plastic funnel or the conical base of a 50 ml tube) for isoflurane administration

that adapts to the animal head. Mice recover much more quickly and with no signs of pain or discomfort.

12. While filling the mini-osmotic pump, let the luciferin slightly overflow and create a small liquid bubble at the opening of the pump. Place the metal flange of the flow moderator at the overflowed luciferin and gently press the moderator to close the pump. This avoids the introduction of any air bubbles in the internal part of the pump reservoir. A tiny amount of luciferin is expected to come out of the flow moderator cap while closing the pump. This is an indication that there are no air bubbles blocking the flow.

13. Food/water supply habituation: We have observed that mice relatively frequently fail to become habituated to the food and water supply in the recording cage, even with a prolonged habituation under 12h light/12h dark conditions. This may critically confound the obtained data, in addition to the undesired effects on animal health. In such cases it is recommended to add, early in the experimental period, during the lights-on phase a pad of water gel or food gel. This will ensure enough food/water supply during the recording without disturbing the experiment (naturally, this intervention is only compatible with *ad libitum* feeding experiments). At the beginning of the experiment, when placing the food and water suppliers, ensure their proper installation for unperturbed access.

Acknowledgements

We would like to express our gratitude to the following colleagues: Yann Emmenegger for his dedication in organising the sleep lab and its equipment at the University of Lausanne, Center for Integrative Genomics; Marieke Hoekstra for sharing her knowledge at the beginning of this work; Pascal Gos for sharing his expertise in tail vein injections and pump implantations; André Liani for his continuous availability for all technical questions regarding the RT-Biolumicorder setup; Paul Franken for advice and a critical comments throughout our experiments; and Bulak Arpat for ideas and advice on the analysis. Research in the laboratory of D.G. is funded by the University of Lausanne and by the Swiss National Science Foundation through the National Center of Competence in Research RNA & Disease (grant no. 141735) and through individual grant 179190. Work in the laboratory of U.S. was supported by the Canton of Geneva, the Swiss National Science Foundation (SNF 31-113565 and SNF 31-128656/1), the European Research Council (ERC-2009-AdG-TIMESIGNAL-250117), and the Louis Jeantet Foundation of Medicine. F.S. was supported by a SGED/SSSED Young Investigator grant.

Bibliography

1. Takahashi JS (2017) Transcriptional architecture of the mammalian circadian clock. *Nat Rev Genet* 18:164–179. doi: 10.1038/nrg.2016.150
2. Damiola F, Le Minh N, Preitner N, Kornmann B, Fleury-Olela F, Schibler U (2000) Restricted feeding uncouples circadian oscillators in peripheral tissues from the central pacemaker in the suprachiasmatic nucleus. *Genes Dev* 14:2950–2961. doi: 10.1101/gad.183500
3. Crosby P, Hamnett R, Putker M, Hoyle NP, Reed M, Karam CJ, Maywood ES, Stangherlin A, Chesham JE, Hayter EA, Rosenbrier-Ribeiro L, Newham P, Clevers H, Bechtold DA,

- O'Neill JS (2019) Insulin/IGF-1 Drives PERIOD Synthesis to Entrain Circadian Rhythms with Feeding Time. *Cell* 177:896-909.e20. doi: 10.1016/j.cell.2019.02.017
4. Stokkan KA, Yamazaki S, Tei H, Sakaki Y, Menaker M (2001) Entrainment of the circadian clock in the liver by feeding. *Science* 291:490–493. doi: 10.1126/science.291.5503.490
 5. Sinturel F, Gos P, Petrenko V, Hagedorn C, Kreppel F, Storch K-F, Knutti D, Liani A, Weitz CJ, Emmenegger Y, Franken P, Bonacina L, Dibner C, Schibler U (2021) Circadian hepatocyte clocks keep synchrony in the absence of a master pacemaker in the suprachiasmatic nucleus or other extrahepatic clocks. *Genes Dev* *in press*.
 6. Saini C, Liani A, Curie T, Gos P, Kreppel F, Emmenegger Y, Bonacina L, Wolf J-P, Poget Y-A, Franken P, Schibler U (2013) Real-time recording of circadian liver gene expression in freely moving mice reveals the phase-setting behavior of hepatocyte clocks. *Genes Dev* 27:1526–1536. doi: 10.1101/gad.221374.113
 7. Vollmers C, Gill S, DiTacchio L, Pulivarthy SR, Le HD, Panda S (2009) Time of feeding and the intrinsic circadian clock drive rhythms in hepatic gene expression. *Proc Natl Acad Sci USA* 106:21453–21458. doi: 10.1073/pnas.0909591106
 8. Greenwell BJ, Trott AJ, Beytebiere JR, Pao S, Bosley A, Beach E, Finegan P, Hernandez C, Menet JS (2019) Rhythmic Food Intake Drives Rhythmic Gene Expression More Potently than the Hepatic Circadian Clock in Mice. *Cell Rep* 27:649-657.e5. doi: 10.1016/j.celrep.2019.03.064
 9. Du N-H, Brown SA (2021) Measuring circadian rhythms in human cells. *Methods Mol Biol* 2130:53–67. doi: 10.1007/978-1-0716-0381-9_4
 10. Yamazaki S, Numano R, Abe M, Hida A, Takahashi R, Ueda M, Block GD, Sakaki Y, Menaker M, Tei H (2000) Resetting central and peripheral circadian oscillators in transgenic rats. *Science* 288:682–685. doi: 10.1126/science.288.5466.682
 11. Hughes ME, Abruzzi KC, Allada R, Anafi R, Arpat AB, Asher G, Baldi P, de Bekker C, BellPedersen D, Blau J, Brown S, Ceriani MF, Chen Z, Chiu JC, Cox J, Crowell AM, DeBruyne JP, Dijk D-J, DiTacchio L, Doyle FJ, Hogenesch JB (2017) Guidelines for Genome-Scale Analysis of Biological Rhythms. *J Biol Rhythms* 32:380–393. doi: 10.1177/0748730417728663
 12. Tahara Y, Kuroda H, Saito K, Nakajima Y, Kubo Y, Ohnishi N, Seo Y, Otsuka M, Fuse Y, Ohura Y, Komatsu T, Moriya Y, Okada S, Furutani N, Hirao A, Horikawa K, Kudo T, Shibata S (2012) In vivo monitoring of peripheral circadian clocks in the mouse. *Curr Biol* 22:1029–1034. doi: 10.1016/j.cub.2012.04.009
 13. Curie T, Maret S, Emmenegger Y, Franken P (2015) In Vivo Imaging of the Central and Peripheral Effects of Sleep Deprivation and Suprachiasmatic Nuclei Lesion on PERIOD-2 Protein in Mice. *Sleep* 38:1381–1394. doi: 10.5665/sleep.4974
 14. Yoo S-H, Yamazaki S, Lowrey PL, Shimomura K, Ko CH, Buhr ED, Siepkas SM, Hong H-K, Oh WJ, Yoo OJ, Menaker M, Takahashi JS (2004) PERIOD2::LUCIFERASE real-time reporting of circadian dynamics reveals persistent circadian oscillations in mouse peripheral tissues. *Proc Natl Acad Sci USA* 101:5339–5346. doi: 10.1073/pnas.0308709101
 15. Shayakhmetov DM, Li Z-Y, Ni S, Lieber A (2004) Analysis of adenovirus sequestration in the liver, transduction of hepatic cells, and innate toxicity after injection of fiber-modified vectors. *J Virol* 78:5368–5381. doi: 10.1128/jvi.78.10.5368-5381.2004

16. Peltola M, Kyttälä A, Heinonen O, Rapola J, Paunio T, Revah F, Peltonen L, Jalanko A (1998) Adenovirus-mediated gene transfer results in decreased lysosomal storage in brain and total correction in liver of aspartylglucosaminuria (AGU) mouse. *Gene Ther* 5:1314–1321. doi: 10.1038/sj.gt.3300740
17. Kratzer RF, Kreppel F (2017) Production, Purification, and Titration of First-Generation Adenovirus Vectors. *Methods Mol Biol* 1654:377–388. doi: 10.1007/978-1-4939-7231-9_28
- Mittereder N, March KL, Trapnell BC (1996) Evaluation of the concentration and bioactivity of adenovirus vectors for gene therapy. *J Virol* 70:7498–7509. doi: 10.1128/JVI.70.11.7498-7509.1996
19. Maizel JV, White DO, Scharff MD (1968) The polypeptides of adenovirus. I. Evidence for multiple protein components in the virion and a comparison of types 2, 7A, and 12. *Virology* 36:115–125.
20. Kreppel F, Biermann V, Kochanek S, Schiedner G (2002) A DNA-based method to assay total and infectious particle contents and helper virus contamination in high-capacity adenoviral vector preparations. *Hum Gene Ther* 13:1151–1156. doi: 10.1089/104303402320138934
21. Blum H, Beier H, Gross HJ (1987) Improved silver staining of plant proteins, RNA and DNA in polyacrylamide gels. *Electrophoresis* 8:93–99. doi: 10.1002/elps.1150080203
22. Hiler DJ, Greenwald ML, Geusz ME (2006) Imaging gene expression in live transgenic mice after providing luciferin in drinking water. *Photochem Photobiol Sci* 5:1082–1085. doi: 10.1039/b608360a
23. Hoekstra MMB, Jan M, Emmenegger Y, Franken P (2020) The sleep-wake distribution contributes to the peripheral rhythms in PERIOD-2. *BioRxiv*. doi: 10.1101/2020.07.25.221101
24. Wilsbacher LD, Yamazaki S, Herzog ED, Song E-J, Radcliffe LA, Abe M, Block G, Spitznagel E, Menaker M, Takahashi JS (2002) Photic and circadian expression of luciferase in mPeriod1-luc transgenic mice *in vivo*. *Proc Natl Acad Sci USA* 99:489–494. doi: 10.1073/pnas.012248599
25. Inagaki N, Honma S, Ono D, Tanahashi Y, Honma K (2007) Separate oscillating cell groups in mouse suprachiasmatic nucleus couple photoperiodically to the onset and end of daily activity. *Proc Natl Acad Sci USA* 104:7664–7669. doi: 10.1073/pnas.0607713104
26. Nakajima Y, Yamazaki T, Nishii S, Noguchi T, Hoshino H, Niwa K, Viviani VR, Ohmiya Y (2010) Enhanced beetle luciferase for high-resolution bioluminescence imaging. *PLoS ONE* 5:e10011. doi: 10.1371/journal.pone.0010011
27. Schiedner G, Hertel S, Kochanek S (2000) Efficient transformation of primary human amniocytes by E1 functions of Ad5: generation of new cell lines for adenoviral vector production. *Hum Gene Ther* 11:2105–2116. doi: 10.1089/104303400750001417
28. Asher G, Gatfield D, Stratmann M, Reinke H, Dibner C, Kreppel F, Mostoslavsky R, Alt FW, Schibler U (2008) SIRT1 regulates circadian clock gene expression through PER2 deacetylation. *Cell* 134:317–328. doi: 10.1016/j.cell.2008.06.050
29. Martin-Burgos B, Wang W, William I, Tir S, Mohammad I, Javed R, Smith S, Cui Y, Smith C, van der Vinne V, Molyneux PC, Miller SC, Weaver DR, Leise TL, Harrington M (2020) Methods for detecting PER2::LUCIFERASE bioluminescence rhythms in freely moving mice. *BioRxiv*. doi: 10.1101/2020.08.24.264531

Figures

Figure 1

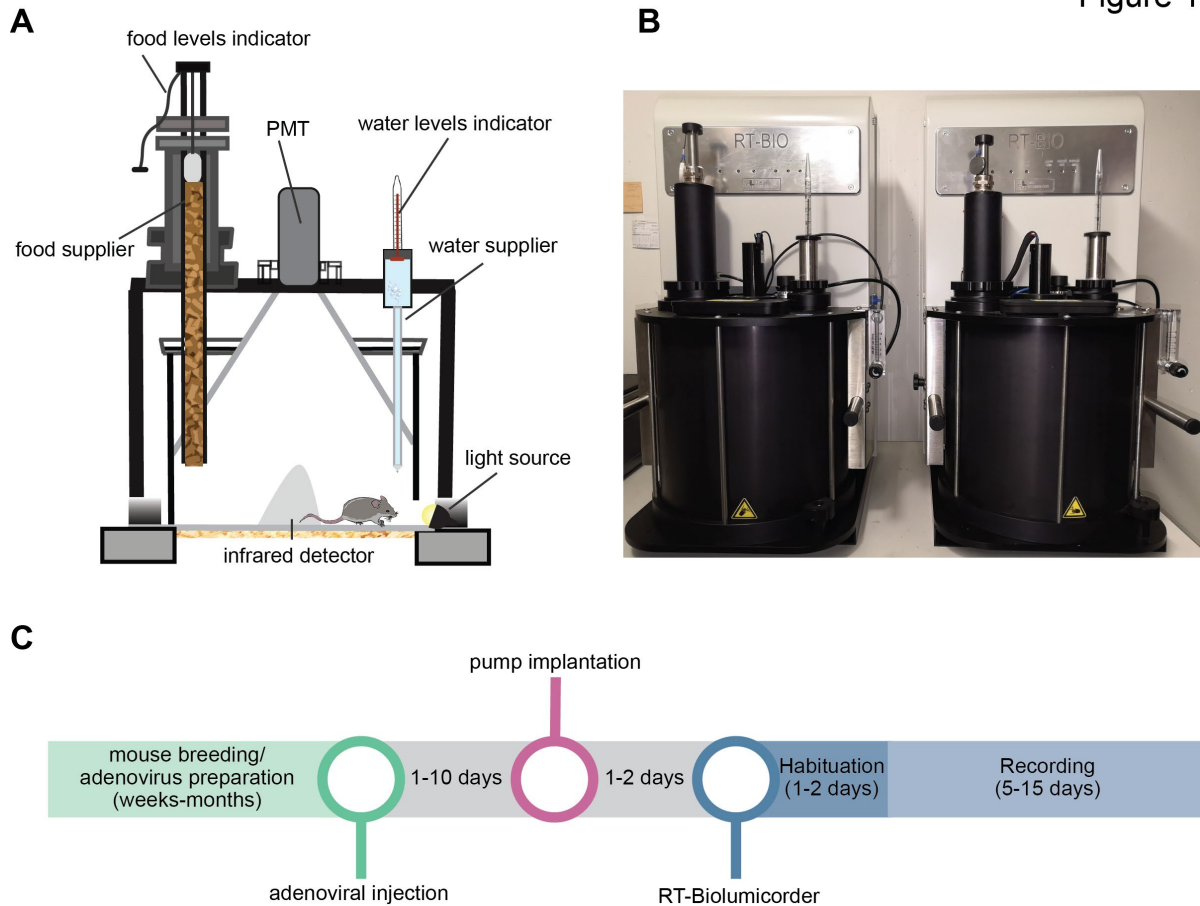


Figure 1. View of the RT-Biolumicorder setup. **A.** Schematic representation of the RT-Biolumicorder (Lesa-Technology) that allows for simultaneous real-time recording of bioluminescence and locomotor activity in freely moving mice. The RT-Biolumicorder consists of a cylindrical cage with reflective walls equipped with a photomultiplier tube (PMT) that is centrally placed above the recording cage and records bioluminescence levels. An infrared detector that records locomotor activity is built into a small cone in the middle of the cage floor. Water and food suppliers with their corresponding consumption indicators are depicted. **B.** A picture of two RT-Biolumicorders at the animal facility of our department. The medium-size black cylinder at the left side of each machine is the food supplier and the smaller metallic cylinder at the right is the water supplier with the water level indicator. Each RT-Biolumicorder has a control panel (silver metal panel labelled “RT-BIO”), which indicates: (a) activity, (b) food access off, (c) light on, (d) shutter on, (e) PMT on. **C.** Overview of the typical experimental workflow. After mouse breeding (to introduce luciferase reporter allele) or adenoviral reporter preparation, the whole experiment typically takes 2-3 weeks. After adenoviral injection, micro-osmotic pump implantation should occur within the following 1-10 days. Because the availability of luciferin limits the length of the recording, the animals should then be transferred rapidly (1-2 days) to the RT-Biolumicorder. After short habituation

(1-2 days), the actual recording takes place for approximately 5-15 days (i.e. until signal becomes too weak due to exhaustion of luciferin reservoir). Note that when the reporter gene is genetically encoded (e.g. *Per2::Luc* mice), the adenoviral injection is omitted. This makes the protocol significantly shorter and less stressful for the animal. Likewise, if luciferin is delivered through the drinking water, no operation for the micro-osmotic pump is required, thus eliminating the main invasive operational procedure. While in principle this would represent the ideal protocol, we would like to point out that delivery via drinking water may not be possible when low-amplitude rhythms are recorded (see note No. 2).

Figure 2

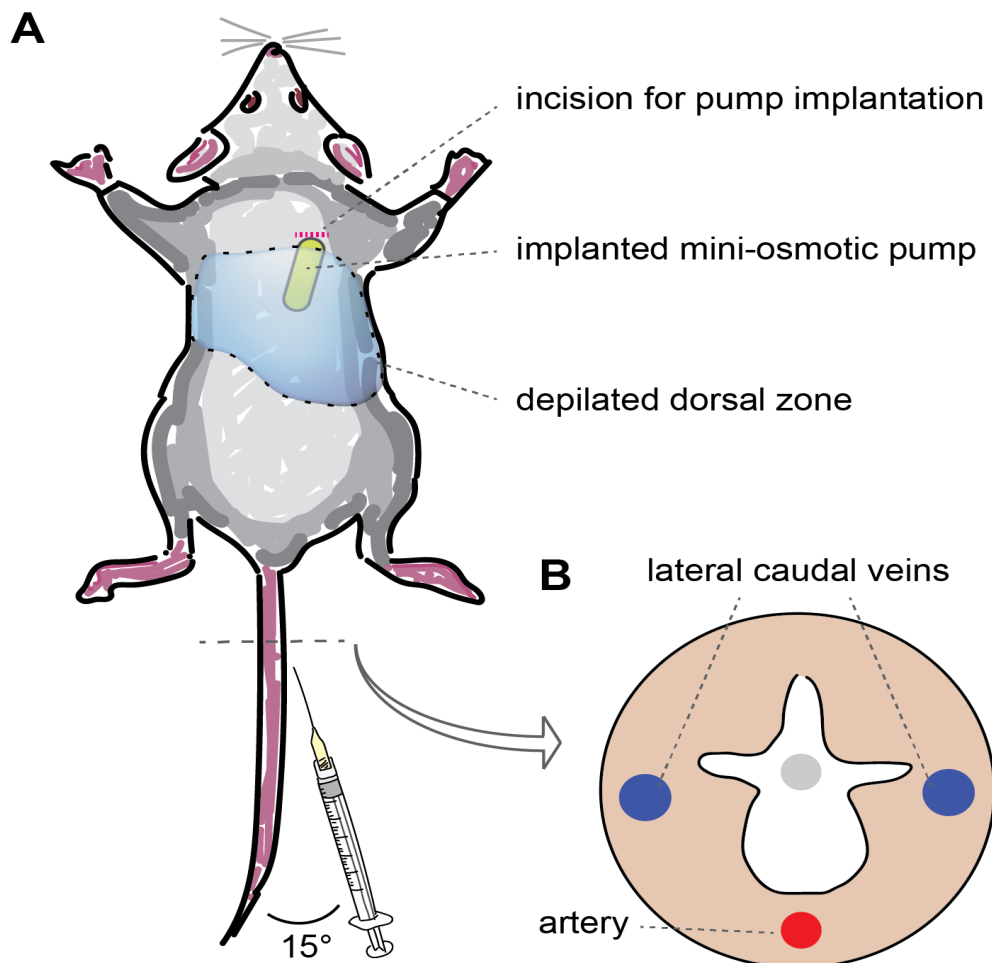


Figure 2. Schematic representation of main sites of animal handling. **A.** Dorsal view of an experimental animal. Blue shading depicts the dorsal zone that is depilated/shaved. The site of the incision made in the skin between the scapulae is shown as a red dotted line. Using a hemostat, a small pocket is formed by spreading the subcutaneous connective tissues apart, and the pump is inserted (depicted in yellow). The skin incision is then closed with sutures, and the area is disinfected. Adenoviral delivery (prior to the pump implantation) occurs through tail vein injection that is best performed at a very shallow angle ($<15^\circ$). **B.** Diagram of a sectional view of a mouse tail, with the two lateral caudal veins and the ventral artery. With the applied heat from the restrainer, the veins become more visible. After locating one of the veins, the animal is placed in a lateral position, the needle is inserted and the virus is carefully injected. Typically, we have had high-quality outcomes with injection sites located in the middle third of the tail. The vertebrae is shown in white.

Figure 3

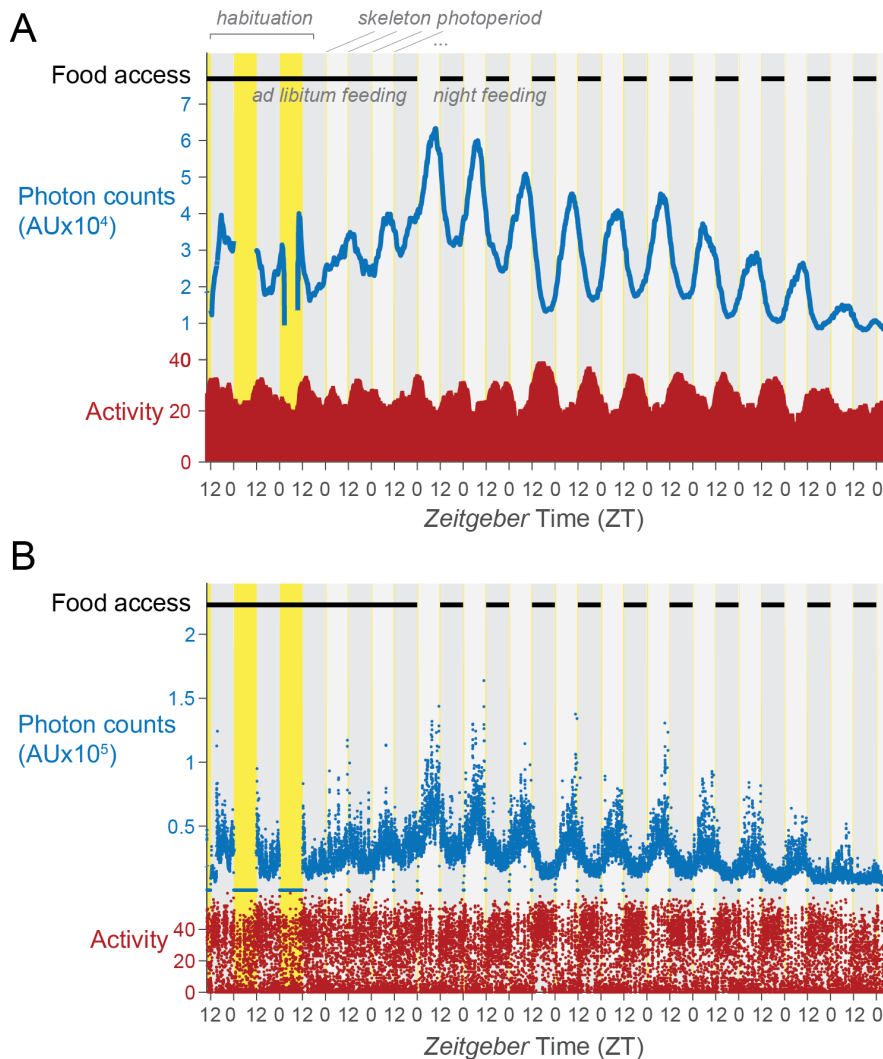


Figure 3. The Osiris software allows for straightforward display of RT-Biolumicorder data. A. Example of bioluminescence (blue) and activity (red) dynamics of a single animal, after detrending and smoothing (with a 5 min sliding window). Lights on, subjective days and subjective nights are depicted by yellow, light grey and dark grey shadings, respectively. Food access is indicated at the top of the graph. **B.** Corresponding raw data for tracks shown in (A), with photon counts in blue and activity in red. Data are from a C57BL/6 mouse that was injected with an adenoviral reporter, expressing luciferase (with the 5' UTR of the mouse *Rpl30* gene) from the human *Pgk1* promoter (to be reported elsewhere).

Figure 4

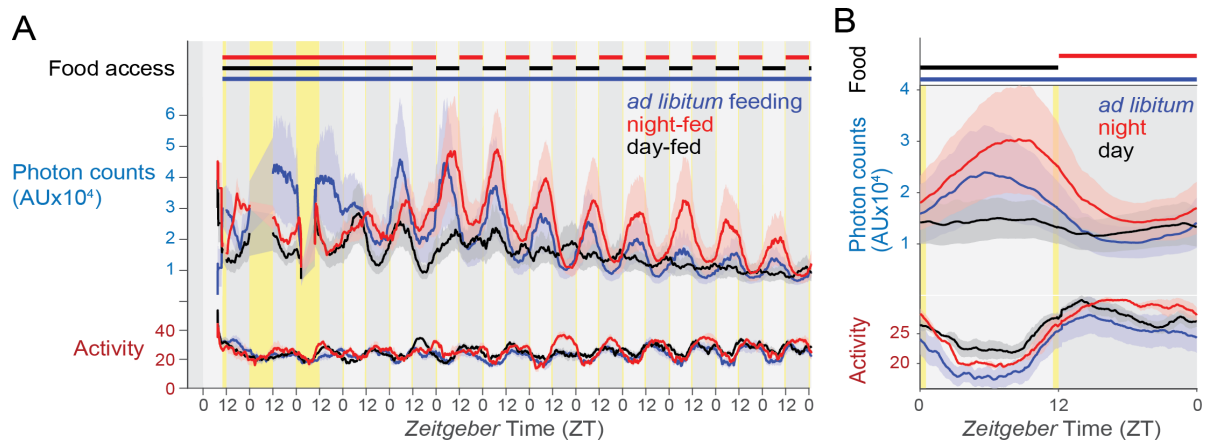


Figure 4. Data analysis for groups of animals and for rhythmicity parameters using the Osiris software. **A.** Luminescence and activity dynamics for three groups of animals with different timing of food access, *ad libitum* (blue, N=4), night-fed (red, N=3) and day-fed (black, N=4). The shaded areas represent the standard error of mean (SEM) of the data. The same reporter as in Figure 3 was used. **B.** Comparison of the mean cycle across the 24 hour period between three groups of animals with different timing of food access shown in (A). Yellow, light grey and dark grey backgrounds represent the skeleton photoperiod, subjective day, and subjective night, respectively.

**The sleep-wake distribution contributes to the peripheral
rhythms in PERIOD-2**

M.M.B. Hoekstra, M. Jan, G. Katsioudi, Y. Emmenegger & P. Franken

Elife, 2021

The sleep-wake distribution contributes to the peripheral rhythms in PERIOD-2

Marieke MB Hoekstra^{1‡}, Maxime Jan¹, Georgia Katsioudi, Yann Emmenegger, Paul Franken^{*}

Center for Integrative Genomics, University of Lausanne, Lausanne, Switzerland

Abstract In the mouse, *Period-2* (*Per2*) expression in tissues peripheral to the suprachiasmatic nuclei (SCN) increases during sleep deprivation and at times of the day when animals are predominantly awake spontaneously, suggesting that the circadian sleep-wake distribution directly contributes to the daily rhythms in *Per2*. We found support for this hypothesis by recording sleep-wake state alongside PER2 bioluminescence in freely behaving mice, demonstrating that PER2 bioluminescence increases during spontaneous waking and decreases during sleep. The temporary reinstatement of PER2-bioluminescence rhythmicity in behaviorally arrhythmic SCN-lesioned mice submitted to daily recurring sleep deprivations substantiates our hypothesis. Mathematical modeling revealed that PER2 dynamics can be described by a damped harmonic oscillator driven by two forces: a sleep-wake-dependent force and an SCN-independent circadian force. Our work underscores the notion that in peripheral tissues the clock gene circuitry integrates sleep-wake information and could thereby contribute to behavioral adaptability to respond to homeostatic requirements.

*For correspondence:
paul.franken@unil.ch

[‡]These authors contributed equally to this work

Present address: ¹UK Dementia Research Institute at Imperial College London, Division of Brain Sciences, London, United Kingdom

Competing interest: The authors declare that no competing interests exist.

Funding: See page 24

Preprinted: 26 July 2020

Received: 25 April 2021

Accepted: 12 December 2021

Published: 13 December 2021

Reviewing Editor: Luis F Larrondo, Pontificia Universidad Católica de Chile, Chile

© Copyright Hoekstra et al. This article is distributed under the terms of the [Creative Commons Attribution License](https://creativecommons.org/licenses/by/4.0/), which permits unrestricted use and redistribution provided that the original author and source are credited.

Editor's evaluation

This work contributes interesting data to both the circadian and sleep fields as it presents evidence that clock gene expression in peripheral tissues can be regulated in sleep-wake-state- and peripheral-circadian-dependent manners. To support this idea, the authors monitor sleep-wake state, as well as PER2 expression (utilizing a PER2-luciferase system), in both intact or SCN-lesioned freely behaving mice. Analysis of central and peripheral PER2LUC levels, under diverse sleep protocols, and aided by mathematical models allows them to support the idea that in peripheral tissues the clock gene circuitry integrates sleep-wake information, potentially contributing to behavioral adaptability to homeostatically respond to different challenges.

Introduction

The sleep-wake distribution is coordinated by the interaction of a circadian and a homeostatic process (Daan et al., 1984). The biological substrates underlying the circadian process are relatively well understood: circadian rhythms in overt behavior of mammals are generated by the suprachiasmatic nuclei (SCN) located in the hypothalamus (Hastings et al., 2018). At the molecular level, so-called 'clock genes' interact through negative transcriptional/translational feedback loops (TTFLs), where the CLOCK/NPAS2:ARNTL (BMAL1) heterodimers drive the transcription of their target genes, among them the *Period* (*Per1,2*) and *Cryptochrome* (*Cry1,2*) genes. Subsequently, PER and CRY proteins assemble into repressor complexes that inhibit CLOCK/NPAS2:ARNTL-mediated transcription, including their own. The resulting reduction of the repressor complex allows a new cycle to start. This feedback loop, present in almost each cell of the mammalian body, interacts with other molecular pathways, together ensuring a period of ~24 hr (Hastings et al., 2018). The SCN synchronizes

eLife digest Circadian rhythms are daily cycles in behavior and physiology which repeat approximately every 24 hours. The master regulator of these rhythms is located in a small part of the brain called the supra-chiasmatic nucleus. This brain structure regulates the timing of sleep and wakefulness and is also thought to control the daily rhythms of cells throughout the body on a molecular level. It does this by synchronizing the activity of a set of genes called clock genes.

Under normal conditions, the levels of proteins coded for by clock genes change throughout the day following a rhythm that matches sleep-wake patterns. However, keeping animals and humans awake at their preferred sleeping times affects the protein levels of clock genes in many tissues of the body. This suggests that, in addition to the supra-chiasmatic nucleus, sleep-wake cycles may also influence clock-gene rhythms throughout the body.

To test this theory, Hoekstra, Jan et al. measured the levels of PERIOD-2, a protein coded for by the clock gene *Period-2*, while tracking sleep-wake states in mice. They did this by imaging a bioluminescent version of the PERIOD-2 protein in the brain and the kidneys, at the same time as they recorded the brain activity, movement and muscle response of animals. Results showed that PERIOD-2 increased on waking and decreased when mice fell asleep. Additionally, in mice lacking a circadian rhythm in sleep-wake behavior – whose changes in PERIOD-2 levels with respect to time were greatly reduced – imposing a regular sleep-wake cycle restored normal PERIOD-2 rhythmicity.

Next, Hoekstra, Jan et al. developed a mathematical model to understand how sleep-wake cycles together with circadian rhythms affect clock-gene activity in the brain and kidneys. Computer simulations suggested that sleep-wake cycles and circadian factors act as forces of comparable strength driving clock-gene dynamics. Both need to act in concert to keep clock-genes rhythmic. The model also predicted the large and immediate effects of sleep deprivation on PERIOD-2 levels, giving further credence to the idea that waking accelerated clock-gene rhythms while sleeping slowed them down. Modelling also suggested that having regular clock-gene rhythms protects against sleep disturbances.

In summary, this work shows how sleep patterns contribute to the daily rhythms in clock genes in the brain and body. The findings support the idea that well-timed sleep-wake schedules could help people to adjust to new time zones. It might also be useful to inform other strategies to reduce the health impacts of shift work.

peripheral clock gene expression rhythms through its rhythmic behavioral, electrical, and humoral output generated across the day (Schibler et al., 2015).

Accumulating evidence suggests that, perhaps surprisingly, clock genes are also involved in the homeostatic aspect of sleep regulation (Franken, 2013). This is illustrated by the sleep deprivation (SD)-induced increase in the expression of the clock gene *Per2* in tissues peripheral to the SCN, including the cerebral cortex, liver, and kidney (Curie et al., 2013; Curie et al., 2015; Franken et al., 2007; Maret et al., 2007). Moreover, the highest level of peripheral *Per2* expression is reached after the time of day mice were awake most, suggesting that also during spontaneous periods of waking *Per2* expression accumulates. Accordingly, lesioning of the SCN, which eliminates the circadian sleep-wake distribution, attenuates the circadian amplitude of clock gene transcripts and proteins in peripheral tissues (Akhtar et al., 2002; Curie et al., 2015; Tahara et al., 2012; Saini et al., 2013; Sinturel et al., 2021). Together, these studies suggest that sleeping and waking are important contributors to clock gene expression, but dissecting the contribution of the sleep-wake distribution and circadian time is challenging because the two change in parallel.

By simultaneously recording electroencephalogram (EEG), electromyogram (EMG), locomotor activity (LMA), and PER2-dependent bioluminescence signals from cortex and kidney in freely behaving mice, we established that the circadian sleep-wake distribution importantly contributes to the daily rhythmic changes in central and peripheral PER2 levels. To further test this hypothesis, we predicted that (i) in behaviorally arrhythmic SCN-lesioned (SCNx) mice, daily recurring SDs mimicking a circadian sleep-wake distribution will temporarily reinstate high-amplitude PER2 bioluminescence rhythms, and (ii) in intact rhythmic animals, reducing the amplitude of the circadian sleep-wake distribution will result in a reduced amplitude of PER2 rhythms. While daily SDs indeed enhanced the amplitude of peripheral PER2 rhythms in SCNx mice, the protocol used to reduce the amplitude of

the sleep-wake distribution did not reduce PER2 amplitude in all mice. To reconcile the sleep-wake-driven and circadian aspects of PER2 dynamics, we implemented a mathematical model in which waking represents a force that sets in motion a harmonic oscillator describing PER2 dynamics and found that the sleep-wake distribution, also under undisturbed conditions, is an important contributor to the daily changes in PER2 bioluminescence. Moreover, we discovered a second, SCN and sleep-wake independent force with a circadian period that underlay the residual circadian PER2 rhythms in SCNx mice, and that the phase relationship between these two forces is important for predicting the amplitude response in PER2 rhythms to sleep-wake perturbations.

Results

To quantify PER2 levels, we used mice expressing a knock-in (KI) construct encoding a fused PER2::LUCIFERASE (PER2::LUC) protein and in which changes in emitted bioluminescence can be used as proxy for changes in PER2 protein levels (Yoo et al., 2004). *Per2^{Luc}* KI mice have been used to follow clock gene expression in vivo (Curie et al., 2015; Ohnishi et al., 2014; Tahara et al., 2012; van der Vinne et al., 2018). However, in these studies, mice had to be anesthetized for each measurement, while in the set-up used in our study (RT-Biolumicorder; Saini et al., 2013), we assessed PER2 bioluminescence continuously in freely moving mice, in central and peripheral tissues. For the central quantification of bioluminescence, we used mice in which the *Per2^{Luc}* construct was back-crossed onto a C57BL/6J (B6) background (see Materials and methods). For the experiments that quantified bioluminescence in the periphery, we used hairless SKH1 mice carrying the *Per2^{Luc}* KI construct because lack of fur allows for the unobstructed measurement of emitted photons (see also Figure 1—figure supplement 1 for experimental design and Figure 1—figure supplement 2A for imaging of bioluminescence in SKH1 mice). Under standard LD12:12 conditions, SKH1 mice exhibited sleep-wake patterns characteristic of mice, that is, during the light phase they spent more time in both non-rapid eye movement (NREM) sleep and REM sleep relative to the dark phase, the latter being their habitual active phase. Moreover, they showed the typical sleep homeostatic response to a 6 hr SD during the first 18 hr of recovery, both in sleep time and EEG delta power, although the increase in REM sleep did not reach significance levels (Figure 1—figure supplement 3).

In three pilot experiments, we optimized our experimental set-up. We established that the most important source contributing to the peripheral bioluminescence signals in the SKH1 mice are the kidneys (Figure 1—figure supplement 2A). We have previously shown that the central bioluminescence signal obtained in B6 mice is of cortical origin (Curie et al., 2015). To accomplish this, luciferin was infused directly into the brain, the skull locally thinned and equipped with a glass cone, and animals were not shaved, thereby preventing passage of photons from the periphery (see Materials and methods). We confirmed that in B6 mice thus prepared only photons emitted by the brain could be detected (Figure 1—figure supplement 2A). Finally, by using mice expressing luciferase under the control of synthetic CAG promoter (CAG-Luc mice; Cao et al., 2004), we determined that its substrate luciferin is best delivered through implantable osmotic mini-pumps compared to administration through the drinking water. Under the latter condition, strong daily rhythms in bioluminescence were observed, likely as a result of rhythms in drinking behavior, thereby driving luciferin availability (Figure 1—figure supplement 2B).

Sleep-wake state affects PER2 bioluminescence

It now has been well documented that enforced wakefulness affects *Per2* mRNA and protein levels in various tissues and mammalian species (Franken, 2013; Hoekstra et al., 2019; Möller-Levet et al., 2013; Vassalli and Franken, 2017), but it is not known whether circadian rhythms in spontaneous sleep-wake behavior contribute to the daily changes in PER2 levels. To address this question, we equipped *Per2^{Luc}* KI B6 and SKH1 mice ($n = 6$ and 5 , respectively) with wireless EEG/EMG recorders (i.e., NeuroLoggers) and monitored simultaneously sleep-wake state, PER2 bioluminescence, and LMA under constant darkness (DD; see Figure 1—figure supplement 1). Time asleep in mice kept in the RT-Biolumicorder quantified with the NeuroLoggers under DD was similar to that quantified under LD conditions using a tethered EEG acquisition system (48 hr baseline in DD vs. LD in C57BL/6J mice: NREM sleep: $42.2\% \pm 1.6\%$, REM sleep $6.1\% \pm 0.3\%$ of total recording time; $n = 6$; compared to 41.3 ± 1.1 and $5.2\% \pm 0.2\%$, respectively; $n = 12$, data taken from Diessler et al., 2018). Sleep

and EEG have not been recorded in SKH1 mice previously. Also in these mice, similar sleep durations were obtained under the two conditions (48 hr baseline in DD vs. LD: NREM sleep: $40.4\% \pm 2.1\%$, REM sleep $5.8\% \pm 0.9\%$; $n = 5$; compared to $40.0\% \pm 1.0\%$ and $6.9\% \pm 0.2\%$, respectively; $n = 8$; see *Figure 1—figure supplement 3*).

Next, we reproduced the circadian changes in PER2 bioluminescence as well as the response to a 6 hr SD (*Figure 1A*) as described previously (*Curie et al., 2015*) in both peripheral bioluminescence, mainly of renal origin, and central bioluminescence, emitted by the cortex (see Materials and methods for explanation of the SD procedure). Similar to what was observed in that publication, SD elicited a tissue-specific response, with an immediate increase in central PER2 bioluminescence after SD, while in the periphery the response was delayed and PER2-bioluminescence increases were observed in the second and fifth hour of recovery (*Figure 1A*). In addition to these direct effects on PER2 bioluminescence within the first 6 hr of recovery, the SD also caused a long-term reduction of rhythm amplitude during both recovery days; that is, the first (REC1) and last (REC2) 24 hr period of recovery. In the periphery, this decrease amounted to ca. 30% on both days (REC1: 17.5–41.1%; REC2: 18.7–42.4%, 95% confidence intervals [95% CI]). In the central recordings, PER2-bioluminescence amplitude decreased significantly during REC1 (32% [10.2–54.5%]), whereas the decrease during REC2 (22% [0.06–44.8%]) no longer reached significance levels (linear mixed model with fixed conditional effect ['BSL,' 'REC1,' 'REC2'] and random intercept effect ['Mouse']; periphery: BSL vs. REC1 $p=0.0014$; vs. REC2 $p=0.0011$; central: BSL vs. REC1 $p=0.022$; vs. REC2 $p=0.082$; sinewave-fitted baseline amplitudes: periphery 0.258 [0.15–0.36]; central 0.193 [0.08–0.31 a.u.]). This long-term reduction of PER2-bioluminescence is reminiscent of the long-term SD effects on rhythm amplitude we observed for *Per2* expression and for other clock genes in the cortex (*Hor et al., 2019*).

Although a circadian modulation of PER2 bioluminescence of both peripheral and central origin is evident (see *Figure 1B* and *Figure 1—figure supplement 4*), we observed additional changes in bioluminescence that occurred simultaneously with changes in sleep-wake state, indicating that PER2 bioluminescence increases during wake-dominated periods and decreases during sleep-dominated periods in both tissues. To quantify this observation, transitions from sleep (irrespective of sleep state) to wake and from wake to sleep were selected (see Materials and methods for selection criteria). Examples of the selected transitions are indicated in *Figure 1B* as a hypnogram. A similar number of sleep-to-wake and wake-to-sleep transitions passed selection criteria during the two-and-a-half baseline days (periphery: 31.2 ± 3.9 and 29.0 ± 3.9 ; central: 25.6 ± 1.4 and 24.6 ± 1.4 , respectively; mean \pm SEM). Transitions obtained in mice in which central bioluminescence was recorded were shorter (longest common wake period after sleep-to-wake transitions: 39 vs. 57 min; longest common sleep period after wake-to-sleep transitions: 63 vs. 75 min, for central and periphery, respectively). Although PER2 bioluminescence increased during wakefulness and decreased during sleep in both tissues, tissue-specific differences were observed (*Figure 1C*). At sleep-to-wake transitions, tissue differences concerned an initial decrease in peripheral PER2 bioluminescence after wake onset, followed by a steep increase saturating at 125%. In contrast, central levels of PER2 bioluminescence increased from the start and followed a linear time course throughout the waking period. Despite these different dynamics, similar bioluminescence levels were reached in both tissues. After wake-to-sleep transitions, peripheral PER2 bioluminescence initially increased before quickly decreasing and then leveling out at around 84% (*Figure 1C*). In contrast, the central signal decreased linearly throughout the sleep period reaching levels of 91% at the end.

Changes in sleep-wake state are accompanied by physiological alterations, such as changes in body and brain temperature (*Sela et al., 2020*; *Vishwakarma et al., 2021*), which could influence bioluminescence by changing substrate levels and/or the rate of the enzymatic reaction. Although the circadian rhythms of subcutaneous temperature and PER2 bioluminescence are ca. 4 hr out of phase (*Figure 1—figure supplement 6*), this does not exclude the possibility that fast changes in physiology associated with sleep-wake transitions contribute to luciferin availability. Therefore, we assessed sleep-wake-related changes in mice carrying two other luciferase reporter constructs. Besides the CAG-Luc mice we used to decide on the route of luciferin administration (*Figure 1—figure supplement 2B*), we also had access to *Pkg1-Luc* mice in which bioluminescence is under the control of the promoter of the housekeeping gene *Pkg1* (see Materials and methods). As expected from a housekeeping gene, bioluminescence in *Pkg1-Luc* mice was relatively constant and did not increase at sleep-wake transitions (*Figure 1—figure supplement 5*). In contrast, in CAG-Luc mice increases at

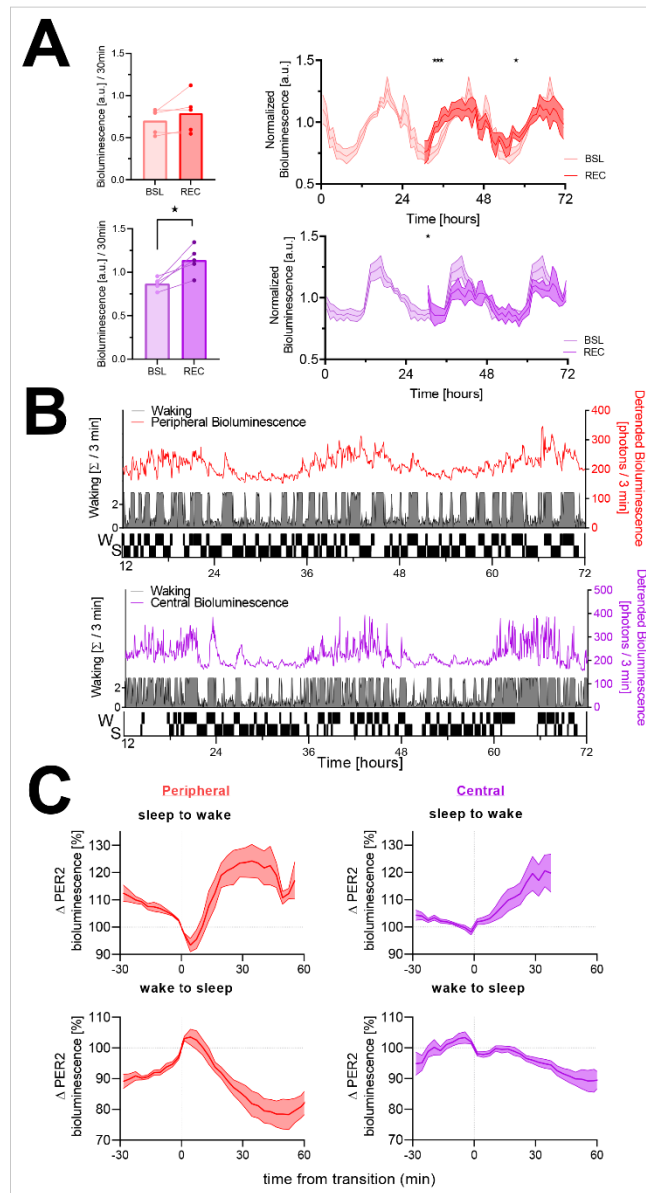


Figure 1. The sleep-wake distribution contributes to changes in PER2 bioluminescence. Red, peripheral (kidney) bioluminescence; purple, central (cortical) bioluminescence. **(A)** Left panels: PER2 bioluminescence measured in the first 30 min of recovery (REC) after sleep deprivation compared to levels reached at this circadian time during baseline (BSL). Sleep deprivation elicited an acute response in central PER2 (lower bar graph; $t(4) = 4.4$, $p=0.012$). *Figure 1 continued on next page*

Figure 1 continued

but not in the periphery (upper bar graph; $t(4) = 1.5$, $p=0.21$). Right panels: under baseline conditions (lighter graphs, time 0–24 hr repeated three times, average of 48 hr baseline), PER2 bioluminescence showed a circadian rhythm both in the periphery (left) and central (right). Sleep deprivation from ZT0 to –6 (times under preceding LD conditions) affected PER2 bioluminescence during recovery (two-way rANOVA w/ Condition \times Time, periphery: $F(41, 164) = 2.1$, $p=0.0007$; central: $F(41, 164) = 1.8$, $p=0.004$). Asterisks indicate significant differences assessed by post-hoc paired t-tests. Bioluminescence is expressed as a fraction of the individual average bioluminescence during the experiment and depicted in 1 hr intervals as mean \pm SEM for five mice (peripheral and central). **(B)** A sleep-wake state recording (gray area plot represents wakefulness in consecutive 3 min intervals) combined with peripheral (red line, upper graph) and central PER2 bioluminescence (purple line, lower graph) in two mice during baseline. Note that besides the circadian oscillation in PER2 bioluminescence, there are marked increases and decreases in PER2 bioluminescence. The ‘hypnogram’ (lower part of the graph) illustrates that the rapidly evoked changes in PER2 bioluminescence are related to periods of sleeping (S) and waking (W). This hypnogram is discontinuous as it depicts only the SW transitions selected in this mouse for the analysis in **(C)**. **(C)** Changes in PER2 bioluminescence associated with transitions from sleep to wake (top) and wake to sleep (bottom) of peripheral (left, $n = 5$) and cortical (right, $n = 6$) origin. Data underlying figures can be found in **Figure 1—source data 1**.

The online version of this article includes the following source data and figure supplement(s) for figure 1:

Source data 1. This file contains the numerical values on which the graphs in **Figure 1A–C** are based.

Figure supplement 1. Experimental protocol for the three experiments.

Figure supplement 2—source data 1. Sources of bioluminescence and different luciferin administration routes.

Figure supplement 2—source data 1. This file contains the numerical values on which the graphs in **Figure 1—figure supplement 2B** are based.

Figure supplement 3. Sleep phenotyping of SKH1 mice.

Figure supplement 3—source data 1. This file contains the numerical values on which the graphs in **Figure 1—figure supplement 3A–C** are based.

Figure supplement 4. PER2 bioluminescence co-detected with EEG-based sleep-wake state in the other mice.

Figure supplement 4—source data 1. This file contains the numerical values on which the nine graphs in **Figure 1—figure supplement 4** are based.

Figure supplement 5. The effect of activity on bioluminescence in three different bioluminescence reporters.

Figure supplement 5—source data 1. This file contains the numerical values on which the graphs in **Figure 1—figure supplement 5A and B** are based.

Figure supplement 6. Subcutaneous temperature is phase advanced relative to PER2 kidney bioluminescence.

Figure supplement 6—source data 1. This file contains the numerical values on which the graphs in **Figure 1—figure supplement 6A and B** are based.

Figure supplement 7. Locomotor activity (LMA) as proxy for wakefulness.

Figure supplement 7—source data 1. This file contains the numerical values on which the graphs in **Figure 1—figure supplement 7A and B** are based.

transitions were larger than in *Per2^{Luc}* mice, consistent with the rapidly activated CMV-immediate-early enhancer contained within the CAG synthetic promoter (*Brightwell et al., 1997; Collaco and Geusz, 2003*). These results show that the bioluminescence changes at sleep-wake transitions are specific to the luciferase reporter construct and therefore not an artifact of sleep-wake-related changes in physiology.

Taken together, three observations indicate that the sleep-wake distribution importantly contributes to both central and peripheral PER2-bioluminescence dynamics: (1) enforced wakefulness has both acute and long-term effects on PER2 bioluminescence; (2) the changes in PER2 bioluminescence at sleep-wake transitions demonstrate that also spontaneous waking is associated with an increase, and sleep with a decrease, in PER2 bioluminescence; and (3) that PER2 bioluminescence is high when mice are spontaneously awake more.

The central PER bioluminescence signals tended to be noisier than peripheral signals (signal-to-noise ratio: -1.15 ± 1.0 and 0.37 ± 1.0 dB, respectively; estimated on 3 min values in baseline of the 6 hr SD experiments according to *Leise et al., 2012*). Moreover, the peripheral signal was easier to obtain and minimally invasive to the animal. We therefore decided for the next experiments to focus

on peripheral PER2 bioluminescence using the *Per2^{uc}* SKH1 mice. Because waking correlates highly with LMA (Figure 1—figure supplement 7), we recorded LMA as proxy for wakefulness to avoid invasive EEG/EMG surgery and mice having to adapt to a ca. 2.7 g recorder mounted on the head.

Modulating the amplitude of the sleep-wake distribution and its influence on PER2 bioluminescence

The SCN is the main driver of the circadian sleep-wake distribution because animals in which the SCN is lesioned (SCNx) lack a circadian organization of sleep-wake behavior under constant conditions (Baker et al., 2005; Edgar et al., 1993). Under these conditions, the amplitude of clock gene expression in peripheral organs is significantly reduced, but not eliminated (Akhtar et al., 2002; Curie et al., 2015; Tahara et al., 2012; Sinturel et al., 2021). Given our results in freely behaving mice, we expect that imposing a rhythmic sleep-wake distribution in SCNx mice will reinstate high-amplitude rhythmicity in PER2 bioluminescence. Conversely, reducing the amplitude of the circadian sleep-wake distribution in SCN-intact mice is expected to reduce the amplitude of PER2 bioluminescence. We tested these predictions in two complementary experiments (see experimental design in Figure 1—figure supplement 1). In the first experiment, we enforced a daily sleep-wake rhythm in arrhythmic SCNx mice by sleep depriving them for 4 hr at 24 hr intervals during four subsequent days. In the second experiment, we aimed to acutely reduce the circadian distribution of sleeping and waking in intact mice according to a '2hOnOff' protocol, comprising 12 2-h SDs each followed by a 2 h sleep opportunity 'window' (SOW), previously utilized in the rat (Yasenkov and Deboer, 2010).

Repeated sleep deprivations in SCNx mice temporarily reinstate a circadian rhythm in PER2 bioluminescence

Lesioning the SCN rendered LMA arrhythmic under DD conditions (Figure 2—figure supplement 1). In arrhythmic SCNx mice, we confirmed that rhythms in PER2 bioluminescence were strongly reduced, but not completely abolished (Figure 2A–C). During the second baseline measurement after SCNx (BSL2 in Figure 2B), we observed in two of the four mice erratic high values (see also Figure 1—figure supplement 2) that we cannot readily explain especially because in the subsequent four SD days the variance in the PER2 bioluminescence signal among mice was again as small as in the earlier recordings (Figure 2A vs. B). The erratic values in these two mice led to a >10-fold increase in the residual sum of squares (RSS), indicating a poorer fit, and to a higher amplitude of the fitted sinewaves in the second compared to the first baseline recording (Figure 2C, BSL1 vs. BSL2). The repeated SDs induced a robust oscillation in the PER2-bioluminescence signal, restoring amplitude to the levels observed prior to SCN lesioning and higher than those observed in the baseline recordings (Figure 2C). The latter observation shows that the increased amplitude during the SD did not result from an SD-mediated alignment of different individual phases in baseline. Importantly, the oscillation continued after the end of the SDs while decreasing in amplitude (Figure 2C).

The 2hOnOff protocol reduces the circadian sleep-wake amplitude without consistently modulating PER2 dynamics

In the next experiment, we aimed at reducing the amplitude of the circadian sleep-wake distribution in intact mice using the 2-day 2hOnOff protocol. We measured sleep-wake state and PER2 bioluminescence during baseline conditions, the 2hOnOff procedure, and the two recovery days in two cohorts of mice. In the first cohort, PER2 bioluminescence was monitored, and mice were taken out of the RT-Biolumicorder for the 2 hr SDs. Bioluminescence was therefore quantified only during the SOWs, thus biasing the read-out of PER2 bioluminescence during the 2hOnOff protocol towards levels reached during sleep. A second cohort was implanted with tethered EEG/EMG electrodes to determine the efficacy of the 2hOnOff protocol in reducing the sleep-wake distribution amplitude.

As expected, mice exhibited a circadian PER2-bioluminescence rhythm under baseline conditions (Figure 3A). Contrary to expectation, the 2hOnOff protocol did not significantly decrease the ongoing circadian PER2 oscillation when analyzed at the group level (Figure 3B). When inspecting the individual responses, four out of the six mice did show a consistent 27% reduction (range 23–31%) in PER2-bioluminescence amplitude during the 2-day 2hOnOff protocol, while in the remaining two mice amplitude increased by 40% (Figure 3C). In all six mice, PER2-bioluminescence amplitude reverted to baseline values during recovery, irrespective of whether it was increased or decreased

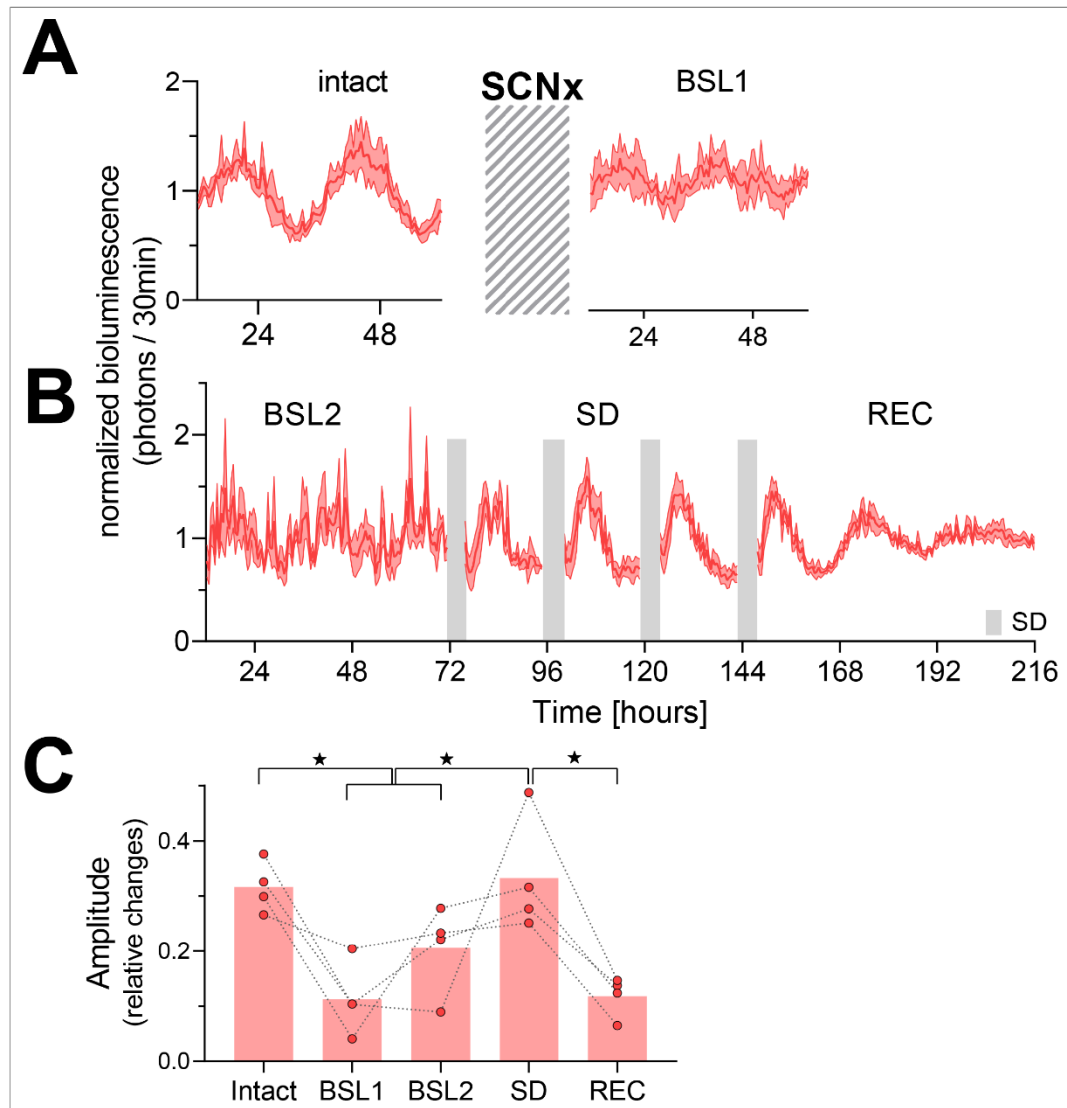


Figure 2. Temporary reinstatement of circadian PER2 oscillations in SCN lesion (SCNx) mice by repeated sleep deprivations (SDs). **(A)** Time course of PER2 bioluminescence across 2.5 days under baseline conditions (left) and after the SCNx (right). Cross-hatched area represents an approximately 5-week interval separating the two recordings during which the success of SCNx on locomotor activity was verified under DD (**Figure 2—figure supplement 1**). **(B)** Four 4 h SDs (gray bars) repeated daily at the beginning of the light phase under the preceding LD conditions reinstate rhythmic PER2 bioluminescence (n = 4). Abbreviations of experimental conditions: intact, baseline prior to SCNx; BSL1, baseline after DD locomotor activity recordings; BSL2, baseline immediately preceding the SDs; SD, 20 hr recordings between the four 4 hr SDs; REC, recovery after the four SDs. Data are depicted as mean \pm SEM (n = 4). **(C)** Effect of SCNx and SD on PER2-bioluminescence amplitude estimated by sinewave fitting (linear mixed model with fixed conditional effects ['Intact,' 'BSL1,' 'SD,' and 'REC'] and random intercept effect ['Mouse']) followed by Tukey's post-hoc tests; intact vs. BSL1 [BSL1

Figure 2 continued on next page

Figure 2 continued

and BSL2], $p=0.0045$; intact vs. REC, $p=0.0015$; SD vs. BSL: $p=0.0013$; SD vs. REC: $p<0.001$; ★ $p<0.05$). See **Figure 2—figure supplement 2** for individual time courses and amplitude estimates of the separate recovery days. Data underlying figures can be found in **Figure 2—source data 1**.

The online version of this article includes the following source data and figure supplement(s) for figure 2:

Source data 1. This file contains the numerical values on which the graphs in **Figure 2A–C** are based.

Figure supplement 1. Suprachiasmatic nuclei (SCN) lesion eliminates circadian organization of locomotor activity.

Figure supplement 1—source data 1. This file contains the numerical values on which the graphs in **Figure 2—figure supplement 1A and B** are based.

Figure supplement 2. Individual traces of PER2 kidney bioluminescence.

Figure supplement 2—source data 1. This file contains the numerical values on which the graphs in **Figure 2—figure supplement 2A–C** are based.

during the 2hOnOff protocol. The distinct bimodal, opposing response in amplitude observed among individual mice and the subsequent reverting back to baseline suggest that the 2hOnOff protocol did affect the ongoing PER2-bioluminescence rhythm. This phenomenon might relate to factors not accounted for in our experimental design. In the modeling section at the end of the Results section, we explore this observation further and find that variation in circadian phase could underlie the individual differential response (for details, see ‘Modeling PER2 dynamics’).

We used the second cohort of mice to determine the efficacy with which the 2hOnOff protocol reduced the circadian sleep-wake distribution. In contrast to bioluminescence, the amplitude of the circadian sleep-wake distribution did decrease consistently in all mice (**Figure 3D and E**). The circadian rhythm in the sleep-wake distribution was, however, not eliminated because the sleep obtained during the 2 hr SDs as well as during the 2 hr SOWs both varied as a function of time of day (sleep during SDs: average: 12.4%, min-max: 4.9–23.0%; during SOWs: average: 54.3%, min-max: 35.7–76.4%). This was especially evident at the beginning of the subjective light phase of day 2 when the average time spent asleep during the SD reached 23%. The sleep obtained during the SDs at this time could be due to a substantial sleep pressure because of lost sleep during day 1 of the 2hOnOff protocol (total time spent asleep/day, mean \pm SEM; baseline: 11.1 ± 0.1 hr; 2hOnOff: day 1: 7.3 ± 0.3 hr, day 2: 8.6 ± 0.7 hr, paired two-tailed t-test, BSL vs. 2hOnOff-day 1: $t(7) = 8.86$, $p<0.001$; BSL vs. 2hOnOff-day 2: $t(7) = 4.18$, $p=0.004$; 2hOnOff-day 1 vs. -day 2, $t(7) = 1.97$, $p=0.09$), combined with the difficulty for the experimenters to visually detect and prevent sleep in pinkish hairless mice under dim-red light conditions. During recovery from the 2hOnOff protocol, baseline amplitudes were re-established (**Figure 3E**).

Modeling circadian PER2 dynamics

The results above demonstrate that both circadian and sleep-wake-dependent factors need to be considered when studying PER2 dynamics. To understand how these two factors collectively generate the variance in PER2 bioluminescence, we put our experimental data into a theoretical framework and modeled changes in peripheral PER2 bioluminescence according to a driven harmonic oscillator (Curie et al., 2013). This type of oscillator is not self-sustained but depends on rhythmic forces to set in motion and maintain the oscillation. In the model, we assume the sleep-wake distribution to represent one such force. In the absence of rhythmic forces, the oscillator loses energy, resulting in a gradual reduction of its amplitude according to the rate set by its damping constant (γ). Besides amplitude and timing (i.e., phase) of the recurring forces and the damping constant, the oscillatory system is further defined by a string constant (ω_0^2) with the natural angular frequency (ω_0) defining the intrinsic period. Because waking was not quantified alongside bioluminescence in the SCNx and the 2hOnOff experiments, we used LMA as a proxy for the driving force provided by wakefulness (\vec{F}_{WAKE}). The 6 hr SD experiment showed that LMA and time spent awake are strongly correlated and that their hourly dynamics closely changed in parallel (**Figure 1—figure supplement 7**). Moreover, applying the model to this data set (see below) using either wakefulness or LMA as \vec{F}_{WAKE} yielded similar fits (**Figure 4—figure supplement 1**), demonstrating that LMA is an appropriate proxy for wakefulness for the purpose of our model. We performed the analyses at the group level; that is, the mean LMA level of all mice was used to reflect \vec{F}_{WAKE} , and the free parameters in the model were

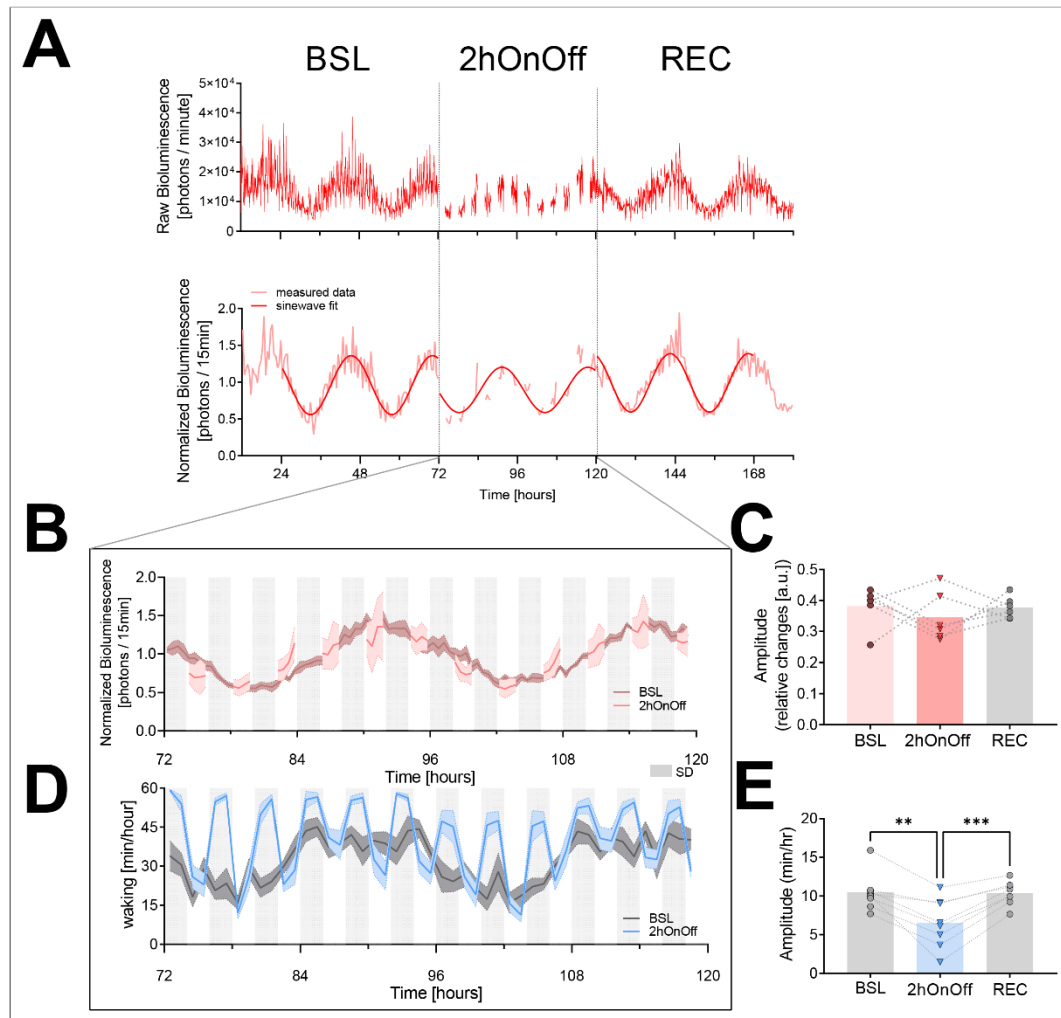


Figure 3. The 2hOnOff protocol reduced the circadian sleep-wake amplitude but did not consistently affect PER2 bioluminescence. **(A)** An example of a PER2-bioluminescence recording under baseline, 2hOnOff, and recovery conditions. Upper graph shows bioluminescence data as collected, whereas in the lower graph, the same data are linearly detrended, normalized (relative to the individual overall mean), and averaged over 30 min intervals. A sine wave was fit to the data of the two baseline days, the two 2hOnOff days, and the two recovery days separately (see Materials and methods). **(B)** The time course of PER2 bioluminescence under baseline conditions and during the 2hOnOff protocol ($n = 6$, data depicted as mean \pm SEM). Light gray squares below the graph mark the 2 hr sleep deprivations (SDs). **(C)** The amplitude of the PER2-bioluminescence rhythm decreased in four but increased in two mice, resulting in an overall lack of an effect of the 2hOnOff protocol (paired t-test, $t(5) = 0.74$, $p = 0.50$; mean \pm SEM; BSL: 0.38 ± 0.03 ; 2hOnOff: 0.35 ± 0.03 ; REC: 0.38 ± 0.01). For all six animals, the amplitude reverted to baseline during recovery. **(D)** The distribution of waking across the two baseline days (dark gray) and during the 2hOnOff protocol (blue) in EEG-implemented SKH1 mice ($n = 8$, hourly values depicted as mean \pm SEM) and a sine wave fit through the hourly average for visual comparison of BSL to SD. **(E)** Individual estimates of the amplitude of circadian changes in wakefulness during the 2hOnOff protocol were obtained by fitting a sine wave function to the wakefulness present in consecutive 4 hr intervals (i.e., SD + SOW). This amplitude was smaller compared to the amplitude obtained in baseline using the same approach (one-way ANOVA, $F(1.8, 12.3) = 21.9$, $p = 0.0001$; post-*Figure 3 continued on next page*

Figure 3 continued

hoc paired t-test, BSL vs. 2hOnOff: $t(7) = 4.9$, $p=0.002$; 2hOnOff vs. REC: $t(7) = 6.3$, $p=0.0004$; mean \pm SEM; BSL: 10.4 ± 0.9 ; 2hOnOff: 6.5 ± 1.1 ; REC: 10.4 ± 0.6 . However, a circadian modulation was still present under the 2hOnOff protocol (amplitude > 0 , one-sample t-test, $t(7) = 5.8$, $p=0.0007$). Note the overall higher levels of wakefulness during 2hOnOff compared to baseline. Data underlying figures can be found in **Figure 3—source data 1**. BSL, baseline; REC, recovery; SOW, sleep opportunity window.

The online version of this article includes the following source data for figure 3:

Source data 1. This file contains the numerical values on which the graphs in **Figure 3A–E** are based.

optimized by fitting the motion of the oscillator to the mean PER2-bioluminescence levels (see Materials and methods). Besides \vec{F}_{WAKE} , we implemented a circadian force to account for the residual PER2-bioluminescence rhythm observed in the SCNx mice (**Figure 2**). We assumed that this additional SCN and sleep-wake-independent force reflects a peripheral circadian process (\vec{F}_{PERI}) present in both intact and SCNx mice (*Sinturel et al., 2021*). This force was modeled as a sinewave with amplitude and phase as free parameters in both experiments while period was set to the period estimated from the baseline PER2-bioluminescence rhythm observed in the SCNx mice (23.7 ± 0.6 hr; $n = 4$). A schematic overview of the influence of \vec{F}_{PERI} and \vec{F}_{WAKE} on PER2 bioluminescence is presented in **Figure 4A**.

We first optimized the parameters of the model describing PER2-bioluminescence dynamics in the SCNx experiment (data from **Figure 2**), and then predicted PER2 bioluminescence under the 2hOnOff experiment. \vec{F}_{PERI} 's amplitude and phase again required optimization as both differed between the two experiments (nonoverlapping 95% CI for both in **Table 1**). With the parameters listed in **Table 1**, the model captured the dynamic changes in PER2 bioluminescence in the SCNx experiment with high precision including the residual rhythmicity in baseline, the reinstated pronounced rhythmicity during the four SDs, and its subsequent dampening thereafter (**Figure 4B**, black line, **Table 2**). The model also accurately captured average bioluminescence dynamics in the 2hOnOff experiment (**Figure 4C**, black line, **Table 2**). It furthermore predicted an 18% reduction of PER2-bioluminescence amplitude during the 2hOnOff protocol compared to baseline (relative amplitudes estimated by the model: 0.31 vs. 0.38 [a.u.]; **Figure 4C**), consistent with our hypotheses and the 27% reduction in PER2-bioluminescence amplitude observed in the four mice in which amplitude did decrease (see **Figure 3C**). To further test the performance of the model, we predicted the peripheral PER2-bioluminescence data obtained in the 6 hr SD experiment using the parameters optimized for the 2hOnOff experiment (**Figure 1A**, **Table 1**). Also, the results of this experiment could be accurately predicted with the model, including the higher PER2-bioluminescence levels reached over the initial recovery hours after SD and the subsequent longer-term reduction in amplitude (**Figures 1A and 4D**, **Table 2**). The model could not reliably predict the central PER2-bioluminescence dynamics mainly due to an earlier phase of the central compared to the peripheral signal (**Figure 4—figure supplement 2D**). Moreover, the increase in PER2 levels immediately following the SD (**Figure 1A**) was missed by the model, further underscoring the tissue-specific relationship between time-spent-awake and PER2 requiring the model to be optimized according to the tissue under study.

The model accurately captured peripheral PER2-bioluminescence dynamics under three different experimental conditions. The model's robust performance prompted us to assess *in silico* whether (1) both forces are required to predict PER2-bioluminescence dynamics, (2) lesioning the SCN affects the forces exerted on PER2 bioluminescence under undisturbed, DD conditions, and (3) differences in the circadian phase could predict the opposing response in PER2-bioluminescence amplitude among mice in the 2hOnOff experiment.

To evaluate if \vec{F}_{PERI} and \vec{F}_{WAKE} combined are required to predict PER2 dynamics, we compared the performance of the model by dropping these two modeling terms; that is, removing either \vec{F}_{PERI} or \vec{F}_{WAKE} . Removing \vec{F}_{PERI} from the model did not change the coefficient obtained for \vec{F}_{WAKE} ($8.25e-5$, which is still within the 95% CI estimated in the full model; see **Table 1**). However, this simpler model (only four free parameters to estimate compared to six in the full model) could not reliably predict the bioluminescence data of the SCNx and 2hOnOff experiments (**Figure 4B and C**, blue lines) and fit statistics indicated a poorer fit (i.e., a higher Bayesian information criterion [BIC]

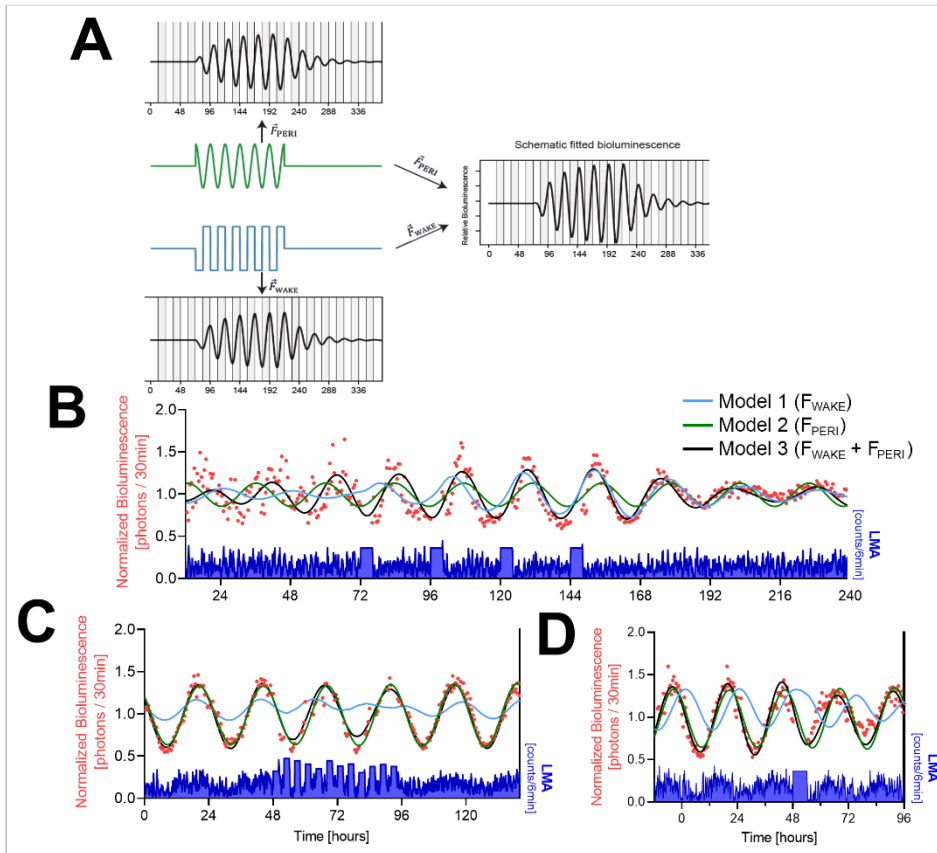


Figure 4. Mathematical modeling of PER2-bioluminescence dynamics. **(A)** Schematic view of a driven damped harmonic oscillator. The oscillation (black) is assumed to be driven by two forces: \vec{F}_{WAKE} (blue) and \vec{F}_{PERI} (green). In our model, \vec{F}_{WAKE} is based on locomotor activity (LMA) (here simplified as a square wave) and \vec{F}_{PERI} on a sinewave. Left panels show the individual effect of each force on the oscillator. Both forces start at $t = 72$ hr and end at $t = 216$ hr, illustrating the waxing and waning of the resulting rhythm amplitude. Right panel shows the resulting changes in PER2 bioluminescence when combining both forces. Note that combining the two forces increased amplitude and changed the phase of the oscillation. In this example, the amplitude of the peripheral circadian force is flat at beginning and end to illustrate that the oscillation is not self-sustained.

(B) Modeling of the SCNx experiment with the full model (model 3; black line) driving oscillations in PER2 bioluminescence or with either \vec{F}_{WAKE} (model 1; blue line) or \vec{F}_{PERI} (model 2; green line) as the only driving force. Red symbols, 30 min PER2-bioluminescence averages. Lower graph in blue: 6 min LMA values. **(C)** Simulation of the PER2-bioluminescence in the 2hOnOff experiment using parameter estimates listed in Table 1. Details and legend as in **(B)**. **(D)** Simulation of peripheral PER2-bioluminescence in the 6 hr SD experiment using parameter estimates obtained in **(C)** (see Table 1). Legend as in **(B)**. Data underlying figures can be found in Figure 4—source data 1.

The online version of this article includes the following source data and figure supplement(s) for figure 4:

Source data 1. This file contains the numerical values on which the graphs in Figure 4B–D are based.

Figure supplement 1. Locomotor activity (LMA) as proxy for wakefulness.

Figure supplement 1—source data 1. This file contains the numerical values on which the graph in Figure 4—figure supplement 1 is based.

Figure supplement 2. Predicting PER2 bioluminescence considering \vec{F}_{PERI} 's phase (A–C) and bioluminescence emitted by cortical regions (D).

Figure 4 continued on next page

Figure 4 continued

Figure supplement 2—source data 1. This file contains the numerical values on which the graphs in **Figure 4—figure supplement 2C and D** are based.

score, see **Table 2**). For instance, without \vec{F}_{PERI} the model is unable to capture the residual PER2 rhythmicity in the baseline of the SCNx experiment (**Figure 4B**, 'model 1' until 72 hr), and it took longer for the PER2 bioluminescence to reach high-amplitude levels compared to the full model because of \vec{F}_{PERI} being in phase with the timing of the SDs in the full model. With the same strategy, we evaluated the model's performance when dropping \vec{F}_{WAKE} (**Figure 4B and C**, green lines). As the sleep-wake distribution no longer affects the model, \vec{F}_{PERI} dynamics are unperturbed throughout the experiment and can therefore be solved as a sinewave in the differential equation. Fit statistics for the SCNx experiment were poor compared to the full model as the effects of SDs on PER2 amplitude could not be captured (**Figure 4B**, **Table 2**). Removing \vec{F}_{WAKE} when modeling the 2hOnOff experiment resulted in BIC scores similar to those obtained with the full model (**Table 2**), although the amplitude reduction during the 2hOnOff protocol could not be captured (**Figure 4C**). Also, the PER2-bioluminescence dynamics in the 6 hr SD experiment were captured best when using both \vec{F}_{WAKE} and \vec{F}_{PERI} (**Figure 4D**, **Table 2**). Together, these results demonstrate that both forces are required to accurately predict PER2 dynamics under the tested experimental conditions.

To answer the second question, we compared the forces driving PER2 bioluminescence in the baseline recordings of the 2hOnOff (intact mice) and the SCNx experiments. The model estimated that the average absolute force (\vec{F}_{WAKE} , \vec{F}_{PERI} , \vec{F}_{γ} , and $\vec{F}_{\omega_0^2}$ combined) exerted on the relative PER2-bioluminescence levels was more than twice as high in intact mice compared to SCNx mice ($2.11e-2$ vs. $0.90e-2$ h⁻²). This large difference was not due to a difference in \vec{F}_{WAKE} , which was somewhat lower in intact mice (2hOnOff vs. SCNx; $2.01e-3$ vs. $2.22e-3$ h⁻²). Although \vec{F}_{PERI} was higher by 32% ($2.45e-3$ vs. $1.85e-3$ h⁻²), this difference did not substantially contribute to the higher amplitude of the PER2 rhythm in intact mice. To illustrate this, we substituted the value of \vec{F}_{PERI} obtained in the 2hOnOff baseline with the lower value obtained in the SCNx baseline, which resulted in a 17% amplitude reduction of the PER2 rhythm. The presence of a circadian sleep-wake distribution impacted

Table 1. Parameter estimates obtained in the model optimization for the suprachiasmatic nuclei lesion (SCNx) and 2hOnOff experiments.

Damping constant, natural angular frequency, and the \vec{F}_{WAKE} coefficient were optimized in the SCNx experiment and then used to predict the results of the 2hOnOff experiment. Amplitude and phase of \vec{F}_{PERI} were optimized for both experiments separately. The natural angular frequency defines the intrinsic period of the harmonic oscillation with $0.288 \text{ rad} \cdot \text{hr}^{-1}$ corresponding to a period of 21.8 hr and its square, ω_0^2 , is referred to as the string constant. Phase of the sine function describing \vec{F}_{PERI} is expressed as radians and corresponds to maximum values reached at time 11.8 and 19.4 hr for the SCNx and 2hOnOff experiment, respectively. Values in parenthesis represent the 95% CI.

Parameters	SCNx	2hOnOff
γ (damping constant)	0.0155 (0.0103–0.0223) (hr ⁻¹)	
ω_0 (natural angular frequency)	0.288 (0.285–0.291) (rad * hr ⁻¹)	
β (coefficient \vec{F}_{WAKE})	6.81e-5 (4.48e-5–9.01e-5)	
Model intercept	0.92 (0.90–0.95)	0.91 (0.89–0.92)
A (amplitude \vec{F}_{PERI})	2.92e-3 (2.58e-3–3.32e-3)	3.87e-3 (3.80e-3–4.00e-3)
φ (phase \vec{F}_{PERI})	4.73 (4.6–4.85)	2.78 (2.78–2.82)

Table 2. Fit statistics for the suprachiasmatic nuclei lesion (SCNx), 2hOnOff, and 6 hr sleep deprivation (SD) experiments using a single force (\vec{F}_{WAKE} or \vec{F}_{PERI}) or two forces combined (\vec{F}_{WAKE} and \vec{F}_{PERI}).

Bayesian information criterion (BIC) for each model (lower is better; a BIC difference between two competing models larger than 10 is considered strong support for the model with the lower value). Residual sum of squares (RSS) minimized by the model (lower values reflect a better fit). Support of the driven harmonic model compared to a flat model using Bayes factor (>100 is considered a 'decisive' support for the driven harmonic model). Values should be compared only within the same experiment because variance and sample size differed among the experiments.

		BIC	RSS	Bayes factor (model vs. flat)
SCNx	$\vec{F} = \vec{F}_{WAKE}$	-287.0	11.94	2.47e32
	$\vec{F} = \vec{F}_{PERI}$	-224.5	13.60	6.48e18
	$\vec{F} = \vec{F}_{WAKE} + \vec{F}_{PERI}$	-427.5	8.36	7.87e62
2hOnOff	$\vec{F} = \vec{F}_{WAKE}$	-28.5	11.96	1.82e24
	$\vec{F} = \vec{F}_{PERI}$	-536.8	1.29	4.41e86
	$\vec{F} = \vec{F}_{WAKE} + \vec{F}_{PERI}$	-540.1	1.27	2.27e87
6 hr SD	$\vec{F} = \vec{F}_{WAKE}$	18.2	92.50	9.15e-17
	$\vec{F} = \vec{F}_{PERI}$	-205.9	4.16	5.80e48
	$\vec{F} = \vec{F}_{WAKE} + \vec{F}_{PERI}$	-311.9	2.46	6.23e71

PER2 amplitude to a larger extent: running the simulation with the parameters estimated for the 2hOnOff experiment but with the sleep-wake distribution of the SCNx mice resulted in a 32% reduction. Therefore, the circadian sleep-wake organization is an important contributor to high-amplitude oscillations in PER2. In the 2hOnOff experiment, the larger PER2 momentum resulted in a four times higher string and damping forces (2hOnOff vs. SCNx; $\vec{F}\omega_0^2$: 19.9e-3 vs. 4.4e-3 h⁻²; $\vec{F}\gamma$: 9.74e-4 vs. 2.52e-4 h⁻²) that together with the larger \vec{F}_{PERI} underlie the larger average absolute force. Moreover, this analysis demonstrated that the direct effects of \vec{F}_{WAKE} and \vec{F}_{PERI} on PER2 bioluminescence do not depend on an intact SCN and that the magnitude of the two forces is comparable.

Although the model predicted the expected decrease in PER2-bioluminescence rhythm amplitude in the 2hOnOff experiment, this decrease was not observed in the mean bioluminescence data. The individual data showed, however, that in four mice this intervention did decrease PER2-bioluminescence amplitude, while in the remaining two amplitude increased (Figure 3C). With the model, we addressed the third question: Do circadian phase differences predict the opposite effects of the 2hOnOff intervention on amplitude? Surprisingly, when systematically varying the phase of \vec{F}_{PERI} during the baseline prior to the 2hOnOff intervention (Figure 4—figure supplement 2C), we found that at phase advances larger than 2.5 hr, the model predicted an increase of PER2 amplitude during the subsequent 2hOnOff protocol instead of a decrease (illustrated in Figure 4—figure supplement 2A for a 6 hr phase advance). Circadian phase differences among animals might relate to individual differences in period length of their free-running rhythms that accumulate over time. We did not find evidence for a difference in PER2 bioluminescence or LMA phase at the end of the baseline recording (2.5 days under DD) between animals that showed a decrease in PER2-bioluminescence amplitude compared to animals that showed an increase. However, during the first day of recovery following the 2hOnOff protocol (5.5 days under DD), we observed a ca. 2 hr phase advance in bioluminescence

and 1 hr phase advance in LMA in the two mice that increased their amplitude during the preceding 2hOnOff protocol (Figure 4—figure supplement 2B, left) compared to the four mice for which we observed the anticipated decrease in PER2 amplitude (Figure 4—figure supplement 2B, right). Whether these differences in phase contributed to the opposite response cannot be answered with the current data set. Nevertheless, the model yielded a perhaps counterintuitive but testable hypothesis by demonstrating that phase angle between the sleep-wake distribution and peripheral circadian clock-gene rhythms is an important variable in predicting outcome and emphasizes the importance of carefully controlling the initial conditions.

Discussion

In this study, we assessed the contribution of the sleep-wake distribution to circadian peripheral PER2 rhythmicity. We presented four key findings, supporting the notion that sleep-wake state is indeed an important factor in determining the circadian amplitude of peripheral changes in PER2: (1) spontaneous sustained bouts of waking and sleep were associated with increased and decreased PER2 bioluminescence, respectively; (2) a single SD acutely increased PER2 bioluminescence and during subsequent recovery dampened its circadian amplitude; (3) repeated SDs temporarily reinstated robust rhythmicity in PER2 bioluminescence in behaviorally arrhythmic mice; and (4) mathematical modeling suggests that PER2 dynamics is best understood as a harmonic oscillator driven by two forces: a sleep-waking-dependent force (\vec{F}_{WAKE}) and an SCN-independent and sleep-wake-independent, circadian peripheral force (\vec{F}_{PERI}).

How does wakefulness increase PER2?

Per2 transcription can be initiated from its cognate E-boxes by CLOCK/NPAS2:ARNTL. This transcriptional activation is at the core of the TTFL and drives the circadian changes in PER2. Enforced wakefulness not only affects *Per2* levels but also modulates the expression of other components of the TTFL (Mang and Franken, 2015; Hor et al., 2019). The SD-evoked increase in *Per2* expression could therefore be mediated through other clock genes in the circuitry, as was demonstrated by the differential SD-evoked response in *Per2* levels in mice lacking the core clock genes *Npas2* and both *Cry1* and *-2* genes (Franken et al., 2006; Wisor et al., 2002).

Apart from a TTFL-mediated activation, *Per2* transcription can be induced by other signaling molecules directly acting on elements within the *Per2* promoter (Schibler et al., 2015). For example, ligand-bound glucocorticoid receptors can induce *Per2* transcription by binding to their glucocorticoid response elements (Cheon et al., 2013; So et al., 2009). Similarly, cAMP response element (CRE)-binding protein (CREB), heat-shock factor 1 (HSF1), and serum-response factor (SRF) can directly activate *Per2* transcription through CREs, heat-shock elements, and CArG-boxes, respectively, present in the *Per2* gene (Gerber et al., 2013; Saini et al., 2012; Tamaru et al., 2011; Travnickova-Bendova et al., 2002). Through these pathways, *Per2* responds to stress, light, temperature, blood-borne systemic cues, and cellular activation as an immediate early gene (IEG). Because of this, *Per2* can appear rhythmic even in the absence of a functional TTFL, provided these signaling pathways fluctuate cyclically (Kornmann et al., 2007). In behaviorally arrhythmic SCNx animals, the residual PER2 rhythms we observed might similarly result from SCN-independent corticosterone (Andrews, 1968) or body temperature (Satinoff and Prosser, 1988) rhythms, or, alternatively, might be TTFL-driven locally (Sinturel et al., 2021).

Important for the current study is that several of the pathways known to directly influence *Per2* expression are activated by either spontaneous and/or enforced waking (e.g., corticosterone [Mongrain et al., 2010], temperature [Hoekstra et al., 2019], *Hsf1* and *Srf* [Hor et al., 2019], pCREB [Cirelli and Tononi, 2000]) and are therefore good candidates linking sleep-wake state to changes in PER2. The observed changes in PER2 bioluminescence were rapid and suggest that increases in protein can occur within an hour of spontaneous wakefulness. Other studies document that PER genes can indeed be rapidly transcribed and translated. For instance, a light pulse given at CT14 leads within an hour to a significant increase in *Per2* transcript in the SCN (Yan and Silver, 2002). One study reported a large increase in hepatic *Per2* transcript levels within 1 hr after food presentation in fasted rats (Wu et al., 2010), underscoring the ability of this transcript to rapidly adapt to homeostatic need. *Per2* translation is not solely dependent on de novo transcription and, for example, in the SCN, light

was shown to promote *Per2* translation (Cao et al., 2015), suggesting that transcription would not be necessary to increase PER2 protein levels. Such mechanism could also underlie the very fast (<30 min) 1.5-fold increase in PER2 protein observed in fibroblasts after serum shock (Cao et al., 2015).

Finally, as the PER2 protein levels measured are the net result of translation and degradation, also sleep-wake-dependent changes in PER2-degradation rate may contribute both to its increase during wakefulness and its decrease during sleep. PER2 degradation is crucial in setting TTFL period and the timing and stability of the circadian sleep-wake distribution (Chong et al., 2012; D'Alessandro et al., 2017). One established pathway leading to PER2 degradation involves Casein kinase 1 (*Csnk1*)-mediated phosphorylation (Eide et al., 2005) followed by the recruitment of the ubiquitin ligase β -transducin repeat-containing proteins (*Btrc*) (Masuda et al., 2020; Ohsaki et al., 2008; Reischl et al., 2007). Other kinases, such as Salt-inducible kinase 3 (*Sik3*) (Hayasaka et al., 2017), and phosphorylation-independent ubiquitin ligases, such as *Transformed mouse 3T3 cell double minute 2* (*Mdm2*) (Liu et al., 2018, p. 2), also target PER2 for degradation. Using a modeling approach to estimate the role of *Btrc* in circadian period length, Reischl et al., 2007 estimated a linear decay rate of 0.18/hr for PER2 degradation, which is not inconsistent with the approximately 0.10/hr net decay rate we observed for the PER2 bioluminescence during sleep. However, the dynamics of PER2 degradation have been assessed in a circadian context exclusively, and effects of sleep-wake state have not been quantified previously.

The obvious next step is to determine which pathway(s) contributes to the wake-driven changes in PER2 protein. We already established that the SD-incurred increase in *Per2* in the forebrain partly depended on glucocorticoids (Mongrain et al., 2010). Along those lines, restoration of daily glucocorticoid rhythms in adrenalectomized rats reinstates PER2 rhythms in several extra-SCN brain areas (Segall and Amir, 2010). To determine the contribution of the aforementioned wake-driven factors, a genetic screen could be deployed where one-by-one the regulatory elements in the *Per2* promoter are mutated, and the effect of sleep-wake driven *Per2* changes is assessed. This approach has already been taken for the GRE and CRE elements in the *Per2* promoter to test their respective roles in circadian phase resetting and integrating light information (Cheon et al., 2013; So et al., 2009; Travnickova-Bendova et al., 2002).

Insights from the model

The model accurately captured the main features of peripheral PER2 dynamics observed in all three experiments, thereby giving further credence to the notion that sleep-wake state importantly contributes to the changes in PER2 observed in the periphery. Moreover, it demonstrated that the large amplitude of the circadian PER2 rhythm in intact mice is likely the result of the momentum gained in the harmonic oscillator through the daily recurring sleep-wake distribution. This is conceptually different from a currently accepted scenario, in which direct and indirect outputs from the SCN assure phase coherence of locally generated self-sustained circadian rhythms (Schibler et al., 2015). According to this model, loss of amplitude observed at the tissue level in SCNx mice is caused by phase dispersion of the continuing rhythms in individual cells. Among the SCN outputs thought to convey phase coherence are feeding, LMA, and changes in temperature. Because these outputs all require or are associated with the animal being awake, it can be argued that in both models the circadian sleep-wake distribution is key in keeping peripheral organs rhythmic.

The harmonic oscillator model further showed that, although important, the sleep-wake force alone was not sufficient to predict PER2 dynamics. In addition to account for the residual PER2 rhythms observed in undisturbed SCNx mice, the SCN-independent and sleep-wake-independent circadian force greatly improved the performance of the model. The synergistic effect of both forces (\vec{F}_{PERI} and \vec{F}_{WAKE}) was needed to explain the rapid response to the SDs observed in the SCNx experiment and also in maintaining robust circadian rhythms during the SDs in the 2hOnOff experiment as illustrated in Figure 4B and C, respectively. Furthermore, this synergistic effect greatly depended on the relative phase of the two forces as we could illustrate in silico for the 2hOnOff experiment: a relative subtle change in the phase of \vec{F}_{PERI} might underlie the increase (instead of the predicted decrease) in PER2 amplitude in two of the six mice recorded.

Which pathways set the phase of \vec{F}_{PERI} and whether it is truly independent of \vec{F}_{WAKE} , as assumed in the model, our current results cannot answer. In an earlier modeling effort using a similar approach in SCN-intact, light-dark entrained mice, we also required a second force to correctly predict the

phase of the observed rhythm in brain *Per2* expression (Curie et al., 2013). In that publication, we based the second force on the pattern of corticosterone production sharply peaking at ZT11 just prior to the light-dark transition. The phase of \vec{F}_{PERI} in the 2hOnOff experiment, which followed a more gradual, sinewave function of which values became positive shortly after ZT11 (extrapolated from the preceding LD cycle), seems consistent with this. In the SCNx experiment, the phase of \vec{F}_{PERI} was positioned ~7 hr earlier with a positive driving force starting at the end of each of the SDs. As SD is accompanied by an increase in corticosterone (Mongrain et al., 2010), the phase of \vec{F}_{PERI} could be associated with corticosterone signaling also in the SCNx experiment. Thus in intact mice, the SCN output would dictate the phase of corticosterone production in the adrenals (and thus that of \vec{F}_{PERI}), while in SCNx mice the phase of the corticosterone rhythm can be reset by stressors such as SD. As *PER2* and *Per2* levels in the SCN seem insensitive to SD (Curie et al., 2015; Zhang et al., 2016), this could explain why the phase of \vec{F}_{PERI} is maintained in sleep-deprived SCN-intact mice. Moreover, ex vivo experiments demonstrated that the adrenal gland can generate bona fide circadian rhythms in corticosterone release independent of the SCN (Andrews, 1968; Engeland et al., 2018; Kofuji et al., 2016), even though SCNx is generally thought to abolish rhythms in circulating corticosterone levels (Moore and Eichler, 1972). While rhythmic corticosterone release represents a plausible candidate contributing to \vec{F}_{PERI} , especially considering its role in synchronizing peripheral clocks (Balsalobre et al., 2000; Cuesta et al., 2015; Dickmeis, 2009; Le Minh et al., 2001), our current results cannot rule out other sources underlying or contributing to \vec{F}_{PERI} . Above we argued that also wakefulness (i.e., \vec{F}_{WAKE} in the model) could influence peripheral PER2 through corticosterone signaling, further complicating the issue. Indeed, adrenalectomy was found to reduce (but not abolish) the SD-induced increase in *Per2* expression in the forebrain (Mongrain et al., 2010). However, enforced but not spontaneous wakefulness is accompanied by increases in corticosterone and the model could predict PER2 dynamics without having to distinguish between the two types of waking. Therefore, other candidate signals among those listed above must be considered to understand the biological basis of \vec{F}_{PERI} and \vec{F}_{WAKE} .

Model optimization yielded an unexpected short 21.8 hr period for the natural frequency of the PER2 oscillator, which, in addition, differed from the 23.7 hr period we set for \vec{F}_{PERI} . While in the intact mice of the 2hOnOff experiment it is difficult to independently determine \vec{F}_{PERI} 's period, we estimated a 23.7 hr period length for the residual PER2 rhythmicity observed during baseline in SCNx mice, which we assume is driven by \vec{F}_{PERI} . In intact mice kept under constant conditions, SCN output drives behavioral sleep-wake rhythms and synchronizes peripheral clock-gene rhythms forcing the entire system to oscillate at the intrinsic period of the SCN. Similarly, in behaviorally arrhythmic SCNx mice, we assume that the period of the observed residual PER2 rhythm reflects that of the only remaining driver, \vec{F}_{PERI} , as \vec{F}_{WAKE} is no longer rhythmic and direct effects of the SCN are absent. Ex vivo experiments showed that periods vary among tissues and do not depend on whether tissues were obtained from an intact or SCNx mouse (Cederroth et al., 2019; Yoo et al., 2004), pointing to tissue-specific TTFLs, which we assume to underlie the intrinsic rhythmicity of both \vec{F}_{PERI} and PER2 bioluminescence in our experiments. The difference in period length of \vec{F}_{PERI} and that of the intrinsic PER2 oscillator therefore suggests that \vec{F}_{PERI} is not of renal origin; that is, the tissue that contributed most to the bioluminescence signal we recorded.

Tissue specificity of the relationship between sleep-wake state and PER2

Our data demonstrated that both central and peripheral PER2-bioluminescence dynamics are affected by sleep-wake state, not only after SD but also after spontaneous periods of wakefulness. Despite this general observation, we found clear tissue-specific differences: the 6 hr SD elicited an immediate increase in the central PER2 signal, while in the periphery this increase occurred several hours later, confirming our earlier findings in brain versus liver and kidney (Curie et al., 2015). Tissue specificity was also observed after spontaneous bouts of wakefulness: in the brain, PER2 bioluminescence immediately increased after the animal woke up and continued to do so until the end of the waking bout, whereas in the kidney the increase in PER2 bioluminescence became apparent only 5–10 min

after the transition. Similar differences in PER2 dynamics were observed after falling asleep, albeit in opposite direction. Also, the model suggested a tissue specificity as central dynamics of the 6 hr SD experiment could not be accurately predicted with the parameters optimized on peripheral PER2-bioluminescence data. In its current form, the model describes the global effects of external forces (the sleep-wake distribution and the SCN-independent circadian force) on the behavior of the oscillator, but not their acute effects. Translated into molecular terms, the model only makes predictions on the TTFL aspect of PER2 regulation, not on PER2 as an IEG. Accordingly, the model cannot capture the fast changes at the transitions. Similarly, the short-lasting high levels of PER2 observed in the brain immediately after the 6 hr SD might reflect an IEG response rather than the state of the TTFL oscillator, which would explain why the model could not predict it. As sleep-wake states are brain states, it stands to reason that changes in brain PER2 levels capture more of the acute IEG effects than in the periphery. One could test this hypothesis by quantifying the PER2 response after activating a peripheral tissue, provided this can be achieved without affecting sleep-wake state as well.

Do changes in bioluminescence reflect changes in PER2 levels?

The method we implemented to quantify PER2 protein levels presents advantages over previous methods used. It enabled us to acquire data at a time resolution needed to link changes in PER2 to sleep-wake state transitions in individual mice. Moreover, because of the within-subject experimental design, there is a substantial reduction in data variability, and, as illustrated with the effects of individual phase on PER2 amplitude in the 2hOnOff experiment, we could assess the presence of individual differences in the initial conditions that might influence experimental outcome. Finally, the number of mice needed for these experiments has been greatly reduced while obtaining better quality data.

A limitation of this method is the assumption that changes in bioluminescence reflect changes in PER2 protein levels. Using western blot, we previously validated that changes in bioluminescence during baseline and after a 6 hr SD indeed reflect changes in PER2 protein (*Curie et al., 2015*). Nevertheless, substrate availability can importantly contribute to the signal as demonstrated in the experiment in which we delivered luciferin in the drinking water. Even the use of osmotic mini-pumps does not guarantee constant delivery as its release rate is temperature dependent (Alzet, manufacturer's notes) and bioluminescence's increase during wakefulness might therefore result from the accompanying increase in temperature during this state. Arguments against a possible temperature effect on bioluminescence changes come from a study in which, using the same osmotic mini-pumps, the expression of two clock genes known to oscillate in anti-phase could be confirmed (*Ono et al., 2015*), which would not be possible if temperature was the main determinant of bioluminescence. In the current data, the circadian rhythm in wakefulness in the CAG-Luc and *Pkg1-Luc* mice was not accompanied by changes in bioluminescence. Moreover, we observed that the circadian rhythms of subcutaneous temperature and PER2 bioluminescence are ca. 4 hr out of phase (*Figure 1—figure supplement 6*), supporting that the large circadian changes in bioluminescence are not driven by changes in luciferin availability. Moreover, the lack of an increase in bioluminescence during wake bouts in *Pkg1-Luc* mice demonstrates that changes in rate-limiting availability of luciferin did not contribute to the fast sleep-wake-evoked changes in PER2.

Conclusions

In this study, we used a unique combination of methods allowing us to collect high-resolution data of sleep-wake state in conjunction with PER2 levels and found that the sleep-wake distribution profoundly affects PER2 bioluminescence both short and long term. Such behavior-dependent plasticity of the time-keeping machinery in tissues peripheral to the SCN enables the organism to respond to challenges as time-restricted feeding experiments have demonstrated (*Damiola et al., 2000; Saini et al., 2013*). Besides its importance in regulating feeding and energy homeostasis (*Bass and Takahashi, 2010*), the clock circuitry also plays a prominent role in sleep homeostasis (*Franken, 2013*). PER2 seems perfectly suited as an integrator of sleep-wake state and circadian time because it is sensitive to a variety of sleep-wake-driven signals. Our model suggests that having a large amplitude rhythm protects from acute disturbances of sleep as observed in the 2hOnOff experiment, while sleep-depriving arrhythmic SCN_x mice had immediate and large effects on PER2. These rapid effects could only be achieved through the synergistic effect of a second force that we found to be independent of

the SCN and the sleep-wake distribution. The coordination of the sleep-wake force and this second force in the model was critical in predicting the effects of sleep-wake interventions on PER2. Research on the nature of this second force would therefore be important to facilitate phase resetting and normalize disrupted clock gene rhythms under conditions of jet lag and shift work, complementing strategies aimed at altering the timing of the central pacemaker.

Materials and methods

Mice and housing conditions

To measure peripheral PER2-bioluminescence levels, we made use of the *Per2^{Luc}* KI construct (Yoo *et al.*, 2004). The KI construct was originally generated on a C57BL/6J-129 mixed background and subsequently brought onto a C57BL/6J (B6) background by backcrossing for at least 11 generations. These mice were then crossed with outbred SKH1 mice (Crl:SKH1-Hrhr; Charles River) to create hairless *Per2^{Luc}* KI mice. We used male homozygous *Per2^{Luc}* KI B6 and hairless heterozygous *Per2^{Luc}* KI SKH1-B6 hybrid (here referred to as SKH1 mice) mice. Mice were kept under a 12 hr light/12 hr dark cycle with light- and dark onset referred to as Zeitgeber time (ZT)-0 and -12, respectively. Age at time of recording varied between 12 and 24 weeks. Food and water was available ad libitum, and after surgery mice were singly housed. All experiments were approved by the Ethical Committee of the State of Vaud Veterinary Office Switzerland under license VD2743, 3201, and 3402.

Source of bioluminescence and luciferin's route of administration

Because *Per2^{Luc}* KI mice express ubiquitously luciferase and the RT-Biolumicorder cannot discriminate between different sources of bioluminescence, we assessed which peripheral organ(s) was/were the major source of bioluminescence. Two male heterozygous *Per2^{Luc}* SKH1 mice were implanted with an osmotic mini-pump (model 1002; 35 mg/mL luciferin) and 5 days later lightly anesthetized with 2.5% isoflurane and imaged for 60 s (Xenogen IVIS Lumina II) around ZT6. The main source of dorsal bioluminescence overlapped with the expected location of the kidney, whereas ventrally almost no bioluminescence was detected (see *Figure 1—figure supplement 2A*). Most bioluminescence quantified during the experiment is of dorsal origin due to the orientation of the mouse relative to the PMT, suggesting that the kidneys are the main source of peripheral bioluminescence in *Per2^{Luc}* SKH1 mice. To confirm our previous report that the main source of central bioluminescence was the brain (Curie *et al.*, 2015), we imaged one male B6 PER2::LUC mouse at ZT3 again using the IVIS system (*Figure 1—figure supplement 2*). When luciferin is infused centrally and the skull is thinned and a glass cone mounted, all emitted bioluminescence originates from the head of the mouse, with no detectable signal from the periphery. For details on the surgery see 'Surgical procedures and experimental design.'

In a second pilot experiment, we investigated the optimal route of luciferin administration. Although luciferin administration via drinking water has been used before to measure bioluminescence (Saini *et al.*, 2013, Iwano *et al.*, 2018, Hall *et al.*, 2018, Sinturel *et al.*, 2021), we were concerned that this route could limit luciferin availability in a circadian fashion because drinking behavior has a strong circadian rhythm (Bainier *et al.*, 2017). To address these concerns, we made use of mice expressing constitutively luciferase under control of the synthetic CAG promoter (Cao *et al.*, 2004, Jackson catalog number 008450), thus allowing for testing of circadian fluctuating levels of luciferin. Mice received luciferin via the drinking water or via an osmotic mini-pump and served as their own control. Four male CAG-Luc mice were housed for two subsequent experiments in constant darkness in the RT-Biolumicorder. During the first experiment, 0.5 mg/mL luciferin was dissolved in the drinking water. At the end of this experiment, mice received subcutaneously an osmotic mini-pump (Alzet, model 1002) under light anesthesia (isoflurane; 2–4% mixed with O₂) containing 70 mg/mL of luciferin and could recover for 2 days before bioluminescence and activity was monitored for the second experiment in the RT-Biolumicorder.

Surgical procedures and experimental design

Experimental design of the three main experiments is depicted in *Figure 1—figure supplement 1* with the upper panel (Experiment 1) illustrating the central and peripheral recordings of PER2 bioluminescence alongside EEG/EMG and LMA before, during, and after a 6 hr SD, and the middle and

bottom panels (Experiment 2 and 3) the SCNx and the 2hOnOff experiments, respectively. In the latter two experiments, peripheral PER2 bioluminescence and LMA were recorded.

Sleep-wake state determination in parallel with PER2 bioluminescence

Mice were implanted with EEG and EMG electrodes under deep ketamine/xylazine anesthesia. Three gold-plated screws (frontal, parietal, and cerebellar) were screwed into the skull over the right cerebral hemisphere, where the cerebellar screw served as a reference for the other two electrodes. Two additional screws were used as anchor screws. For the EMG, a gold wire was inserted into the neck musculature along the back of the skull. For brain delivery of D-luciferin, a cannula (Brain Infusion Kit1, Alzet) was introduced stereotaxically into the right lateral ventricle (1 mm lateral, 0.3 mm posterior to bregma, and 2.2 mm deep) under deep anesthesia (ketamine/xylazine; intraperitoneally, 75 and 10 mg/kg, respectively), and connected to the mini-pump. A depression (diameter 2 mm) was made in (but not through) the skull in a region of the left frontal cortex (approximate coordinates 2 mm lateral to midline, 2 mm anterior to bregma), in which a glass cylinder (length 4.0 mm; diameter 2.0 mm) was positioned and fixed with dental cement. The EMG and three EEG electrodes were subsequently soldered to a connector and cemented to the skull. The cerebellar screw served as a reference for the parietal and frontal screw and the EMG. After the first recovery day, mice were habituated to the weight of the wireless EEG recording system by attaching a dummy of same size and weight to their connector. Two days before habituation to the RT-Biolumicorder, mice were implanted with the osmotic mini-pump (model 1002, Alzet; luciferin 35 mg/mL) under light anesthesia. 8–10 days post-surgery, mice were placed in the RT-Biolumicorder at the end of the light phase (~ZT10-ZT12) for 2 days in LD to habituate to the novel environment. At the end of the second habituation day, the dummy was replaced with a wireless EEG (NeuroLogger, TSE Systems GmbH). After two-and-a-half days of baseline recording in constant darkness, mice were sleep deprived for 6 hr at a time they were expected to rest (ZT0 under LD conditions) by gentle handling as described (*Mang and Franken, 2012*). In short, mice are left undisturbed as long as they do not show signs of sleep. Sleep is prevented by introducing and removing paper tissue, changing the litter, bringing a pipet in the animal's proximity, or gentle tapping of the cage. As opposed to what the term might suggest, mice are not handled. After SD, mice were placed back into the RT-Biolumicorder for the subsequent two recovery days.

SCNx experiment

Four SKH1 mice were recorded over the course of the experiment and served as their own control. Briefly, their PER2-bioluminescence rhythm was monitored before SCNx (once), under undisturbed conditions post-SCNx (twice), and after the second measure under SCNx conditions, the mice were subjected to the repeated 4 hr SDs.

Bilateral lesion of the two SCNs was performed stereotaxically (Kopf Instruments, 963LS, Miami Lakes, FL) under ketamine/xylazine anesthesia (intraperitoneal injection, 75 and 10 mg/kg, at a volume of 8 mL/kg). Two electrodes (0.3 mm in diameter) were introduced bilaterally at the following coordinates (position of the frontal electrode: anteroposterior using bregma as reference: ± 0.2 mm lateral, + 0.5 mm bregma, depth: -5.9 mm; the second electrode was positioned 0.7 mm posterior to the frontal one). Electrolytic lesions (1 mA, 5 s) were made using a direct current (DC) lesion device (3500, Ugo Basile, Comerio, Italy). After lesion, mice were housed in constant dark (DD) conditions for at least 10 days to verify absence of circadian organization of overt behavior. Activity was quantified using passive infrared sensors (Visonic SPY 4/RTEA, Riverside, CA). ClockLab software (Actimetrics, Wilmette, IL) was used for data acquisition and analyses.

Surgeries for tethered EEG/EMG recordings

SKH1 mice ($n = 8$) were implanted with EEG and EMG electrodes as described previously (*Mang and Franken, 2012*) to determine sleep-wake state. The surgery took place under deep xylazine/ketamine anesthesia. Briefly, six gold-plated screws (diameter 1.1 mm) were screwed bilaterally into the skull over the frontal and parietal cortices. Two screws served as EEG electrodes, and the remaining four screws anchored the electrode connector assembly. As EMG electrodes, two gold wires were inserted into the neck musculature. The EEG and EMG electrodes were soldered to a connector and cemented to the skull. Mice recovered from surgery during several days before they were connected to the

recording cables in their home cage for habituation to the cable and their environment, which was at least 6 days prior to the experiment. The habituation to the room and the recovery from the 2-day SD procedure took place under LD 12:12 conditions.

During the baseline recording and SD days, red light at very low intensity was present to allow the experimenters to observe the mice. Mice were sleep deprived for 2 hr according to the 'gentle handling' method.

Mice for bioluminescence data collection

SKH1 mice ($n = 6$) were implanted with an osmotic mini-pump (Alzet, 1002, luciferin concentration: 35 mg/mL; blue flow moderator) 2 days before the habituation. At the end of the light phase (~ZT10-ZT12), mice were moved from their cage to the RT-Biolumicorder for 2–3 days of habituation in LD. They were housed for 2.5 days in DD, after which the 2hOnOff protocol was initiated at light onset (ZT0) under the preceding LD conditions. At the start of each SD, mice were moved from the RT-Biolumicorder and placed into a novel cage that was in the same room as the EEG-implanted mice. Fifteen minutes before the end of each SD, mice were brought back to their RT-Biolumicorder cage.

Bioluminescence recordings in *Pkg1-Luc* mice

The adenoviral vector used in the experiment was constructed by cloning the cassette flanked by PacI sites from vector prLV1 (Du *et al.*, 2014) into vector pCV100, an E1/E3-deleted replication-incompetent first-generation adenovirus vector based on human adenovirus serotype 5 (a variant of pGS66 [Schiedner *et al.*, 2000] with an additional deletion of Ad5 nt 28133–30818). In this construct, firefly luciferase is expressed from a bidirectionally active, minimal *Pkg1* promoter (note: the other side of the promoter carries Renilla luciferase cDNA, which was not used/measured in the framework of this study). See *Supplementary file 1* for the construct sequence. Liver cells were transduced with the pCV100 vector (2.1×10^8 to 4.5×10^{11} adenoviral particles) via tail vein injection using an illuminated restrainer according to Saini *et al.*, 2013 and Sinturel *et al.*, 2021. Male C57BL/6J mice kept under LD 12:12 were injected 2–5 days prior to pump implantation, and pump was implanted 3 days prior to commencing experiment in DD in the RT-Biolumicorder. To allow passage of photons emitted from liver, mid-section of mice' backs was shaved.

Data collection of sleep-wake state

Simultaneous recording of sleep-wake state and PER2 bioluminescence
Batteries (hearing aid; Ansmann, 312 PR41, 1.45 V 180 mAh) were inserted into the NeuroLogger. This insertion was timed with the clock of the computer that controlled the RT-Biolumicorder to *post hoc* align the EEG/EMG signals with the bioluminescence signal. In addition, time stamps provided by the SyncBox (NeuroLogger, TSE) were used to verify the start and end time of the EEG/EMG recording. The cerebellar electrode was used as a reference for both EMG and EEG. Data were sampled at 256 Hz. The frontal signal was subtracted from the parietal signal (EDF Browser) to support sleep-wake state determination by enhancing the identification of slow waves and theta waves within the same trace. The data were subsequently loaded in Somnologica (Somnologica 3, MedCare) to determine offline the mouse's behavior as wakefulness, REM sleep, or NREM sleep per 4 s epochs based on the EEG and EMG signals. Wakefulness was characterized by EEG activity of mixed frequency and low amplitude, and present but variable muscle tone. NREM sleep (NREM) was defined by synchronous activity in the delta frequency (1–4 Hz) and low and stable muscle tone. REM sleep (REM) was characterized by regular theta oscillations (6–9 Hz) and EMG muscle atonia.

2hOnOff experiment

EEG and EMG signals were recorded continuously for 96 hr. The recording started at the beginning of the subjective rest phase, ZT0 of the preceding LD cycle. The analog EEG and EMG signals were amplified (2000 \times) and digitized at 2 kHz and subsequently down-sampled to 200 Hz and stored. Like the EEG and EMG traces obtained with the NeuroLogger, the data were imported in Somnologica and sleep-wake state was determined per 4 s epochs. LMA was monitored with passive infrared activity (Actimetrics) and recorded with ClockLab (Actimetrics).

Data analysis

Route of luciferin administration

Circadian time was determined to inspect the circadian changes in bioluminescence relative to LMA. To this end, the period length per mouse was determined based on activity measurements (1 min resolution) by chi-square analysis in ClockLab. Subsequently, the activity and bioluminescence data were folded according to the period. The activity data were binned per 10 min, and activity onset was visually determined for each mouse and set at CT12. The aligned activity and bioluminescence data were subsequently averaged per circadian hour across mice.

Spontaneous sleep-wake state and bioluminescence

Bioluminescence and activity were sampled at a resolution of 4 s, which is the same resolution of the epochs for sleep-wake state determination. Data processing was subsequently performed in MATLAB 2017b (The MathWorks, Inc, Natick, MA) and R (version 4.0.0). Linear trends were removed from the signal by the build-in function *detrend* in MATLAB and R (*pracma* package). Subsequently, the bioluminescence signal was expressed relative to the overall mean per mouse to account for inter-individual differences. Changes in PER2 would be expected to occur at a slower rate than 4 s. Therefore, sleep-wake and bioluminescence data are averaged per blocks of 3 min.

For the sleep-wake transition analysis, 3 min intervals in which the mouse was awake for more than 50% (i.e., 23 or more 4 s epochs) were deemed awake, otherwise as asleep. Based on this new 3 min sleep-wake sequence, clear sleep-to-wake and wake-to-sleep transitions were selected according to the following criteria: at least 9 min (three 3 min intervals) of the initial state had to be followed by at least 15 min (five 3 min intervals) of the other state. Transitions were followed both forward and backward in time as long as state did not change. Bioluminescence for all 3 min intervals of a transition was expressed as a percentage of the level reached at the transition; that is, the average between the level reached in the last 3 min prior to the transition and the first 3 min after the transition. Transitions were aligned according to time of the state transition (time 0) and then averaged first within and then across mice. Average time courses were reported for the longest time spent in state after the transition to which all mice contributed.

2hOnOff experiment

Bioluminescence data obtained 5 min before and 10 min after the SDs were excluded from analysis. Subsequent data normalization of the bioluminescence data was as above. To determine the influence of the 2hOnOff protocol on the strength of the ongoing circadian oscillation of the circadian distribution of sleep and wake, as well as on PER2 bioluminescence, an estimation of amplitude by sinewave fitting was done (MATLAB, $fit = Y_0 + a * \sin\left(\frac{2*\pi}{b} * t + c\right)$).

Modeling PER2 bioluminescence with a damped harmonic oscillator

The temporal dynamic of PER2 bioluminescence was modeled according to the equation of motion describing a driven damped harmonic oscillator:

$$\frac{d^2x}{dt^2} + \gamma \frac{dx}{dt} + \omega_0^2 x = F$$

where x is the displacement of the oscillator, γ is the damping constant of the model, and ω_0^2 is the string constant defining the natural frequency of the model. The driving forces used in this model are the LMA representing waking \vec{F}_{WAKE} , and a circadian force \vec{F}_{PERI} , represented as a sinewave. The momentary force exerted on the oscillator is represented as the sum of these two forces (see **Figure 4A**):

$$F(t) = \beta LMA_t + A \sin(\omega t + \varphi)$$

where β , A , and φ are respectively the coefficient applied on LMA amount, the amplitude of the circadian sinewave force, and the phase of the circadian sinewave force. These coefficients were the free parameters to be optimized in the model. ω is the angular velocity of the sinewave and was set to $2*\pi/23.7$, based on the residual PER2-bioluminescence rhythm present in the baseline of SCNx mice. To solve this equation and optimize for parameters that best describe the observed PER2

bioluminescence, we proceeded as follows: the relative bioluminescence data from both experiments were averaged across mice using 30 min bins. LMA was averaged across mice using 6 min bins. LMA could not be measured directly during SDs and was estimated by assessing the increase in LMA during SDs measured in EEG-implanted mice, which was found to be 2.4 times higher compared to average baseline levels. Thus, the SD effect was estimated using 2.4 times the mean activity observed during baseline (i.e., 181.9 and 180.2 for the SCNx and 2hOnOff, respectively).

To solve the second-order ordinary differential equation (ODE) of the driven harmonic oscillator, we transformed it into the following system of two first-order ODEs describing the change of position and speed of our oscillator:

$$\begin{aligned}x_1' &= x_2 \\x_2' &= F - \gamma x_2 - \omega_0^2 x_1\end{aligned}$$

We then used the fourth-order Runge–Kutta (RK4) numerical method to approximate the solution using a fixed time step of 0.1 hr. In the SCNx experiment, initial values of speed ($x_2(0)$) and position ($x_1(0)$) were set to 0. For the 2hOnOff experiment, the model was generated for 20 days prior experiment to reach a steady state using replication of LMA observed in baseline (T0–T24). The position and speed of the oscillator at the end of the 20 days were taken as initial values for the fitting. We optimized the model for the following parameters: intercept (equilibrium position of the oscillator), natural frequency, damping constant, and coefficient for the force exerted by LMA, amplitude of circadian force and phase of circadian force. We optimized the fitting by minimizing the RSS between predicted position of our model and the observed PER2-bioluminescence level. The box-constrained PORT routines method (nlminb) implemented in the optimx/R package (Nash and Varadhan, 2011) was used to minimize the RSS.

The goodness of fit of the model was assessed as follows. We assumed that the model errors follow a normal distribution and computed a BIC value for the model according to

$$BIC = n \ln \left(\frac{RSS}{n} \right) + k \ln(n)$$

where n is the number of observations, and k is the number of optimized parameters +1 of the model. We approximated the Bayes factor (BF) between our model and a flat model (linear model with intercept only) as follows:

$$BF \approx \exp \left(-\frac{1}{2} (BIC_{flat} - BIC_{model}) \right)$$

To compute confidence interval of our model parameters, we used 500 Monte Carlo simulations and calculated a confidence interval for our parameters based on 95% empirical quantiles (95% CI). The method was adapted from the code of Marc Lavielle (Inria Saclay [Xpop] and Ecole Polytechnique [CMAP], Université Paris-Saclay, France) for nonlinear models, available here: <http://sia.webpopix.org/nonlinearRegression.html>.

Statistics

Statistics were performed in R (version 4.0.0), SAS (version 9.4), and Prism (version 7.0), with the threshold of significance set at $\alpha = 0.05$. Performed statistical tests are mentioned in the text and figure legends.

Acknowledgements

We are greatly indebted to all who helped with the sleep deprivations: Lisa Häri, Charlotte Hor, and Jeffrey Hubbard, and especially to those who sacrificed their sleep during the graveyard shifts: Kostas Kompotis, Simone Mumbauer, Violeta Castelo-Szekely, and Sonia Jimenez. We also thank Sonia for her help with the sleep-wake annotation of EEG/EMG files. We thank David Gatfield for a great suggestion and David Gatfield and Florian Kreppel for designing, cloning, growing, and producing the adenoviral vector used for *Figure 1—figure supplement 5*. This study was performed at the University of Lausanne, Switzerland, and supported by the Swiss National Science Foundation (SNF

no. 146694 to PF supporting MMBH and SNF no. 179190 to David Gatfield supporting GK) and the State of Vaud (supporting MMBH, MJ, YE, and PF).

Additional information

Funding

Funder	Grant reference number	Author
Schweizerischer Nationalfonds zur Förderung der Wissenschaftlichen Forschung	146694	Marieke MB Hoekstra
Schweizerischer Nationalfonds zur Förderung der Wissenschaftlichen Forschung	179190	Georgia Katsioudi
State of Vaud		Marieke MB Hoekstra Maxime Jan Yann Emmenegger Paul Franken

The funders had no role in study design, data collection and interpretation, or the decision to submit the work for publication.

Author contributions

Marieke MB Hoekstra, Conceptualization, Data curation, Formal analysis, Investigation, Project administration, Visualization, Writing – original draft, Writing – review and editing; Maxime Jan, Conceptualization, Data curation, Formal analysis, Investigation, Methodology, Visualization, Writing – review and editing; Georgia Katsioudi, Investigation, Methodology, Writing – review and editing; Yann Emmenegger, Investigation, Methodology; Paul Franken, Conceptualization, Data curation, Formal analysis, Funding acquisition, Project administration, Supervision, Visualization, Writing – review and editing

Author ORCIDs

Marieke MB Hoekstra <http://orcid.org/0000-0003-0723-2026>

Maxime Jan <http://orcid.org/0000-0001-6483-7430>

Paul Franken <http://orcid.org/0000-0002-2500-2921>

Ethics

All experiments were approved by the Ethical Committee of the State of Vaud Veterinary Office Switzerland under license VD 2743, 3201 and 3402.

Decision letter and Author response

Decision letter <https://doi.org/10.7554/eLife.69773.sa1>

Author response <https://doi.org/10.7554/eLife.69773.sa2>

Additional files

Supplementary files

- Supplementary file 1. Sequence of the pCV100 viral vector construct containing *Pkg1-Luc*.
- Transparent reporting form

Data availability

Data underlying the experimental figures is available through the source files.

- blood transcriptome. *PNAS* **110**:E1132–E1141. DOI: <https://doi.org/10.1073/pnas.1217154110>, PMID: 23440187
- Mongrain V, Hernandez SA, Pradervand S, Dorsaz S, Curie T, Hagiwara G, Gip P, Heller HC, Franken P. 2010. Separating the contribution of glucocorticoids and wakefulness to the molecular and electrophysiological correlates of sleep homeostasis. *Sleep* **33**:1147–1157. DOI: <https://doi.org/10.1093/sleep/33.9.1147>, PMID: 20857860
- Moore RY, Eichler VB. 1972. Loss of a circadian adrenal corticosterone rhythm following suprachiasmatic lesions in the rat. *Brain Research* **42**:201–206. DOI: [https://doi.org/10.1016/0006-8993\(72\)90054-6](https://doi.org/10.1016/0006-8993(72)90054-6), PMID: 5047187
- Nash JC, Varadhan R. 2011. Unifying Optimization Algorithms to Aid Software System Users: optimx for R. *Journal of Statistical Software* **43**:i09. DOI: <https://doi.org/10.18637/jss.v043.i09>
- Ohnishi N, Tahara Y, Kuriki D, Haraguchi A, Shibata S, Ebihara S. 2014. Warm Water Bath Stimulates Phase-Shifts of the Peripheral Circadian Clocks in PER2::LUCIFERASE Mouse. *PLOS ONE* **9**:e100272. DOI: <https://doi.org/10.1371/journal.pone.0100272>
- Ohsaki K, Oishi K, Kozono Y, Nakayama K, Nakayama KI, Ishida N. 2008. The role of {beta}-TrCP1 and {beta}-TrCP2 in circadian rhythm generation by mediating degradation of clock protein PER2. *Journal of Biochemistry* **144**:609–618. DOI: <https://doi.org/10.1093/jb/mvn112>, PMID: 18782782
- Ono D, Honma K, Honma S. 2015. Circadian and ultradian rhythms of clock gene expression in the suprachiasmatic nucleus of freely moving mice. *Scientific Reports* **5**:12310. DOI: <https://doi.org/10.1038/srep12310>
- Reischl S, Vanselow K, Westermark PO, Thierfelder N, Maier B, Herzog H, Kramer A. 2007. Beta-TrCP1-mediated degradation of PERIOD2 is essential for circadian dynamics. *Journal of Biological Rhythms* **22**:375–386. DOI: <https://doi.org/10.1177/0748730407303926>, PMID: 17876059
- Saini C, Morf J, Stratmann M, Gos P, Schibler U. 2012. Simulated body temperature rhythms reveal the phase-shifting behavior and plasticity of mammalian circadian oscillators. *Genes & Development* **26**:567–580. DOI: <https://doi.org/10.1101/gad.183251.111>, PMID: 22379191
- Saini C, Liani A, Curie T, Gos P, Kreppel F, Emmenegger Y, Bonacina L, Wolf JP, Poget YA, Franken P, Schibler U. 2013. Real-time recording of circadian liver gene expression in freely moving mice reveals the phase-setting behavior of hepatocyte clocks. *Genes & Development* **27**:1526–1536. DOI: <https://doi.org/10.1101/gad.221374.113>, PMID: 23824542
- Satinoff E, Prosser RA. 1988. Suprachiasmatic nuclear lesions eliminate circadian rhythms of drinking and activity, but not of body temperature, in male rats. *Journal of Biological Rhythms* **3**:1–22. DOI: <https://doi.org/10.1177/074873048800300101>, PMID: 2979628
- Schibler U, Gotic I, Saini C, Gos P, Curie T, Emmenegger Y, Sinturel F, Gosselin P, Gerber A, Fleury-Olela F, Rando G, Demarque M, Franken P. 2015. Clock-Talk: Interactions between Central and Peripheral Circadian Oscillators in Mammals. *Cold Spring Harbor Symposia on Quantitative Biology*. 223–232. DOI: <https://doi.org/10.1101/sqb.2015.80.027490>
- Schiedner G, Hertel S, Kochanek S. 2000. Efficient transformation of primary human amniocytes by E1 functions of Ad5: Generation of new cell lines for adenoviral vector production. *Human Gene Therapy* **11**:2105–2116. DOI: <https://doi.org/10.1089/104303400750001417>
- Segall LA, Amir S. 2010. Exogenous corticosterone induces the expression of the clock protein, PERIOD2, in the oval nucleus of the bed nucleus of the stria terminalis and the central nucleus of the amygdala of adrenalectomized and intact rats. *Journal of Molecular Neuroscience* **42**:176–182. DOI: <https://doi.org/10.1007/s12031-010-9375-4>, PMID: 20422314
- Sela Y, Hoekstra MMB, Franken P. 2020. A Sub-Minute Resolution Prediction of Brain Temperature Based on Sleep-Wake State in the Mouse. [bioRxiv]. DOI: <https://doi.org/10.1101/2020.08.12.246405>
- Sinturel F, Gos P, Petrenko V, Hagedorn C, Kreppel F, Storch KF, Knutti D, Liani A, Weitz C, Emmenegger Y, Franken P, Bonacina L, Dibner C, Schibler U. 2021. Circadian hepatocyte clocks keep synchrony in the absence of a master pacemaker in the suprachiasmatic nucleus or other extrahepatic clocks. *Genes & Development* **35**:329–334. DOI: <https://doi.org/10.1101/gad.346460.120>
- So AYL, Bernal TU, Pillsbury ML, Yamamoto KR, Feldman BJ. 2009. Glucocorticoid regulation of the circadian clock modulates glucose homeostasis. *PNAS* **106**:17582–17587. DOI: <https://doi.org/10.1073/pnas.0909733106>, PMID: 19805059
- Tahara Y, Kuroda H, Saito K, Nakajima Y, Kubo Y, Ohnishi N, Seo Y, Otsuka M, Fuse Y, Ohura Y, Komatsu T, Moriya Y, Okada S, Furutani N, Hirao A, Horikawa K, Kudo T, Shibata S. 2012. In vivo monitoring of peripheral circadian clocks in the mouse. *Current Biology* **22**:1029–1034. DOI: <https://doi.org/10.1016/j.cub.2012.04.009>, PMID: 22578421
- Tamaru T, Hattori M, Honda K, Benjamin I, Ozawa T, Takamatsu K. 2011. Synchronization of circadian Per2 rhythms and HSF1-BMAL1-CLOCK interaction in mouse fibroblasts after short-term heat shock pulse. *PLOS ONE* **6**:e24521. DOI: <https://doi.org/10.1371/journal.pone.0024521>, PMID: 21915348
- Travnickova-Bendova Z, Cermakian N, Reppert SM, Sassone-Corsi P. 2002. Bimodal regulation of mPeriod promoters by CREB-dependent signaling and CLOCK/BMAL1 activity. *PNAS* **99**:7728–7733. DOI: <https://doi.org/10.1073/pnas.102075599>, PMID: 12032351
- van der Vinne V, Swoap SJ, Vajtay TJ, Weaver DR. 2018. Desynchrony between brain and peripheral clocks caused by CK1δ/ε disruption in GABA neurons does not lead to adverse metabolic outcomes. *PNAS* **115**:E2437–E2446. DOI: <https://doi.org/10.1073/pnas.1712324115>, PMID: 29463694
- Vassalli A, Franken P. 2017. Hypocretin (orexin) is critical in sustaining theta/gamma-rich waking behaviors that drive sleep need. *PNAS* **114**:E5464–E5473. DOI: <https://doi.org/10.1073/pnas.1700983114>, PMID: 28630298

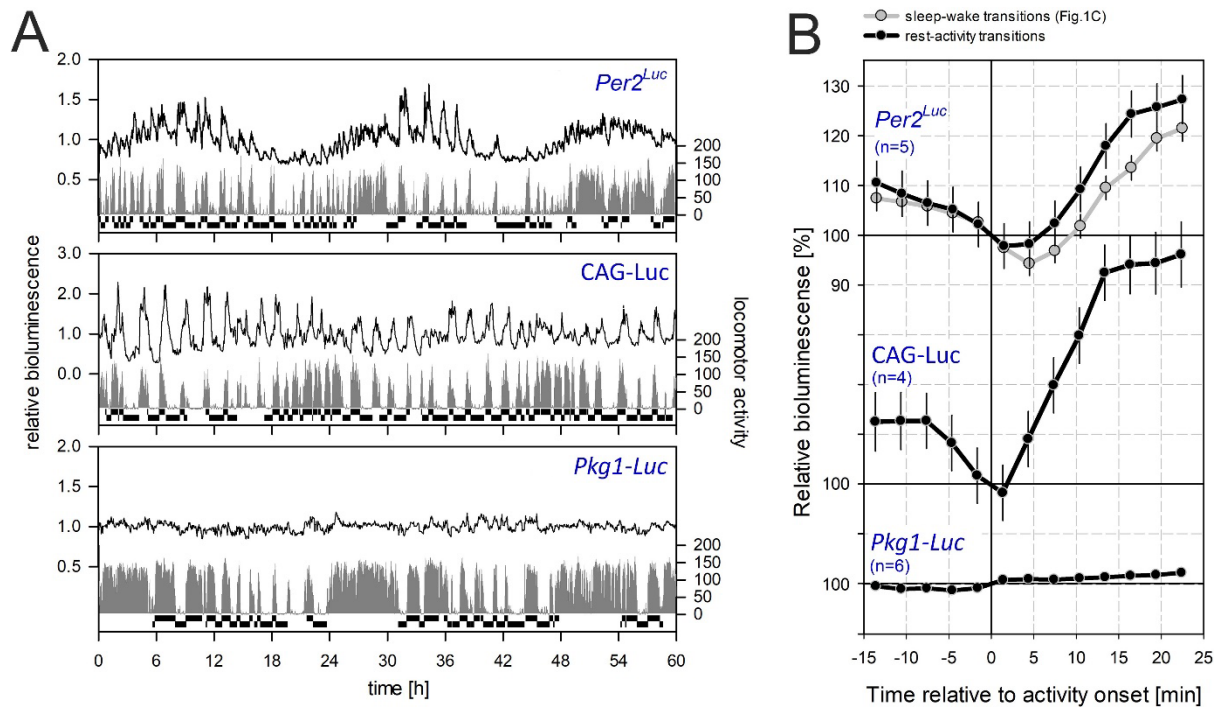
- Vishwakarma LC, Sharma B, Singh V, Jaryal AK, Mallick HN. 2021. Acute sleep deprivation elevates brain and body temperature in rats. *Journal of Sleep Research* **30**:e13030. DOI: <https://doi.org/10.1111/jsr.13030>
- Wisor JP, O'Hara BF, Terao A, Selby CP, Kilduff TS, Sancar A, Edgar DM, Franken P. 2002. A role for cryptochromes in sleep regulation. *BMC Neuroscience* **3**:20. DOI: <https://doi.org/10.1186/1471-2202-3-20>
- Wu T, Ni Y, Kato H, Fu Z. 2010. Feeding-induced rapid resetting of the hepatic circadian clock is associated with acute induction of Per2 and Dec1 transcription in rats. *Chronobiology International* **27**:1–18. DOI: <https://doi.org/10.3109/07420520903398625>, PMID: 20205554
- Yan L, Silver R. 2002. Differential induction and localization of mPer1 and mPer2 during advancing and delaying phase shifts. *The European Journal of Neuroscience* **16**:1531–1540. DOI: <https://doi.org/10.1046/j.1460-9568.2002.02224.x>, PMID: 12405967
- Yasenkov R, Deboer T. 2010. Circadian regulation of sleep and the sleep EEG under constant sleep pressure in the rat. *Sleep* **33**:631–641. DOI: <https://doi.org/10.1093/sleep/33.5.631>, PMID: 20469805
- Yoo SH, Yamazaki S, Lowrey PL, Shimomura K, Ko CH, Buhr ED, Slepka SM, Hong HK, Oh WJ, Yoo OJ, Menaker M, Takahashi JS. 2004. PERIOD2::LUCIFERASE real-time reporting of circadian dynamics reveals persistent circadian oscillations in mouse peripheral tissues. *PNAS* **101**:5339–5346. DOI: <https://doi.org/10.1073/pnas.0308709101>
- Zhang B, Gao Y, Li Y, Yang J, Zhao H. 2016. Sleep Deprivation Influences Circadian Gene Expression in the Lateral Habenula. *Behavioural Neurology* **2016**:7919534. DOI: <https://doi.org/10.1155/2016/7919534>

- Edgar DM, Dement WC, Fuller CA. 1993. Effect of SCN lesions on sleep in squirrel monkeys: evidence for opponent processes in sleep-wake regulation. *The Journal of Neuroscience* **13**:1065–1079. DOI: <https://doi.org/10.1523/JNEUROSCI.13-03-01065.1993>, PMID: 8441003
- Eide EJ, Woolf MF, Kang H, Woolf P, Hurst W, Camacho F, Vielhaber EL, Giovanni A, Virshup DM. 2005. Control of mammalian circadian rhythm by CKleptin-regulated proteasome-mediated PER2 degradation. *Molecular and Cellular Biology* **25**:2795–2807. DOI: <https://doi.org/10.1128/MCB.25.7.2795-2807.2005>, PMID: 15767683
- Engeland WC, Massman L, Mishra S, Yoder JM, Leng S, Pignatti E, Piper ME, Carlone DL, Breault DT, Kofuji P. 2018. The Adrenal Clock Prevents Aberrant Light-Induced Alterations in Circadian Glucocorticoid Rhythms. *Endocrinology* **159**:3950–3964. DOI: <https://doi.org/10.1210/en.2018-00769>, PMID: 30321360
- Franken P, Dudley CA, Estill SJ, Barakat M, Thomason R, O'Hara BF, McKnight SL. 2006. NPAS2 as a transcriptional regulator of non-rapid eye movement sleep: genotype and sex interactions. *PNAS* **103**:7118–7123. DOI: <https://doi.org/10.1073/pnas.0602006103>, PMID: 16636276
- Franken P, Thomason R, Heller HC, O'Hara BF. 2007. A non-circadian role for clock-genes in sleep homeostasis: a strain comparison. *BMC Neuroscience* **8**:87. DOI: <https://doi.org/10.1186/1471-2202-8-87>, PMID: 17945005
- Franken P. 2013. A role for clock genes in sleep homeostasis. *Current Opinion in Neurobiology* **23**:864–872. DOI: <https://doi.org/10.1016/j.conb.2013.05.002>, PMID: 23756047
- Gerber A, Esnault C, Aubert G, Treisman R, Pralong F, Schibler U. 2013. Blood-borne circadian signal stimulates daily oscillations in actin dynamics and SRF activity. *Cell* **152**:492–503. DOI: <https://doi.org/10.1016/j.cell.2012.12.027>, PMID: 23374345
- Hall MP, Woodroffe CC, Wood MG, Que I, Van't Root M, Ridwan Y, Shi C, Kirkland TA, Encell LP, Wood KV, Löwik C, Mezzanotte L. 2018. Click beetle luciferase mutant and near infrared naphthyl-luciferins for improved bioluminescence imaging. *Nature Communications* **9**:132. DOI: <https://doi.org/10.1038/s41467-017-02542-9>, PMID: 29317625
- Hastings MH, Maywood ES, Brancaccio M. 2018. Generation of circadian rhythms in the suprachiasmatic nucleus. *Nature Reviews. Neuroscience* **19**:453–469. DOI: <https://doi.org/10.1038/s41583-018-0026-z>, PMID: 29934559
- Hayasaka N, Hirano A, Miyoshi Y, Tokuda IT, Yoshitane H, Matsuda J, Fukada Y. 2017. Salt-inducible kinase 3 regulates the mammalian circadian clock by destabilizing PER2 protein. *eLife* **6**:e24779. DOI: <https://doi.org/10.7554/eLife.24779>, PMID: 29227248
- Hoekstra MM, Emmenegger Y, Hubbard J, Franken P. 2019. Cold-inducible RNA-binding protein (CIRBP) adjusts clock-gene expression and REM-sleep recovery following sleep deprivation. *eLife* **8**:e43400. DOI: <https://doi.org/10.7554/eLife.43400>, PMID: 30720431
- Hor CN, Yeung J, Jan M, Emmenegger Y, Hubbard J, Xenarios I, Naef F, Franken P. 2019. Sleep-wake-driven and circadian contributions to daily rhythms in gene expression and chromatin accessibility in the murine cortex. *PNAS* **116**:25773–25783. DOI: <https://doi.org/10.1073/pnas.1910590116>, PMID: 31776259
- Iwano S, Sugiyama M, Hama H, Watakabe A, Hasegawa N, Kuchimaru T, Tanaka KZ, Takahashi M, Ishida Y, Hata J, Shimozono S, Namiki K, Fukano T, Kiyama M, Okano H, Kizaka-Kondoh S, McHugh TJ, Yamamori T, Hioki H, Maki S, et al. 2018. Single-cell bioluminescence imaging of deep tissue in freely moving animals. *Science* **359**:935–939. DOI: <https://doi.org/10.1126/science.aag1067>, PMID: 29472486
- Kofuji P, Mure LS, Massman LJ, Purrier N, Panda S, Engeland WC. 2016. Intrinsically Photosensitive Retinal Ganglion Cells (ipRGCs) Are Necessary for Light Entrainment of Peripheral Clocks. *PLOS ONE* **11**:e0168651. DOI: <https://doi.org/10.1371/journal.pone.0168651>, PMID: 27992553
- Kornmann B, Schaad O, Bujard H, Takahashi JS, Schibler U. 2007. System-driven and oscillator-dependent circadian transcription in mice with a conditionally active liver clock. *PLOS Biology* **5**:e34. DOI: <https://doi.org/10.1371/journal.pbio.0050034>, PMID: 17298173
- Le Minh N, Damiola F, Tronche F, Schütz G, Schibler U. 2001. Glucocorticoid hormones inhibit food-induced phase-shifting of peripheral circadian oscillators. *The EMBO Journal* **20**:7128–7136. DOI: <https://doi.org/10.1093/emboj/20.24.7128>, PMID: 11742989
- Leise TL, Wang CW, Gitis PJ, Welsh DK. 2012. Persistent Cell-Autonomous Circadian Oscillations in Fibroblasts Revealed by Six-Week Single-Cell Imaging of PER2::LUC Bioluminescence. *PLOS ONE* **7**:e33334. DOI: <https://doi.org/10.1371/journal.pone.0033334>
- Liu J, Zou X, Gotoh T, Brown AM, Jiang L, Wisdom EL, Kim JK, Finkielstein CV. 2018. Distinct control of PERIOD2 degradation and circadian rhythms by the oncoprotein and ubiquitin ligase MDM2. *Science Signaling* **11**:eaau0715. DOI: <https://doi.org/10.1126/scisignal.aau0715>
- Mang GM, Franken P. 2012. Sleep and EEG Phenotyping in Mice. *Current Protocols in Mouse Biology* **2**:55–74. DOI: <https://doi.org/10.1002/9780470942390.mo110126>, PMID: 26069005
- Mang GM, Franken P. 2015. Genetic dissection of sleep homeostasis. *Current Topics in Behavioral Neurosciences* **25**:25–63. DOI: https://doi.org/10.1007/7854_2013_270, PMID: 24338665
- Maret S, Dorsaz S, Gurcel L, Pradervand S, Petit B, Pfister C, Hagenbuchle O, O'Hara BF, Franken P, Tafti M. 2007. Homer1a is a core brain molecular correlate of sleep loss. *PNAS* **104**:20090–20095. DOI: <https://doi.org/10.1073/pnas.0710131104>, PMID: 18077435
- Masuda S, Narasimamurthy R, Yoshitane H, Kim JK, Fukada Y, Virshup DM. 2020. Mutation of a PER2 phosphodegron perturbs the circadian phosphoswitch. *PNAS* **117**:10888–10896. DOI: <https://doi.org/10.1073/pnas.2000266117>, PMID: 32354999
- Möller-Levet CS, Archer SN, Bucca G, Laing EE, Slak A, Kabiljo R, Lo JCY, Santhi N, von Schantz M, Smith CP, Dijk DJ. 2013. Effects of insufficient sleep on circadian rhythmicity and expression amplitude of the human

References

- Akhtar RA, Reddy AB, Maywood ES, Clayton JD, King VM, Smith AG, Gant TW, Hastings MH, Kyriacou CP. 2002. Circadian cycling of the mouse liver transcriptome, as revealed by cDNA microarray, is driven by the suprachiasmatic nucleus. *Current Biology* **12**:540–550. DOI: [https://doi.org/10.1016/s0960-9822\(02\)00759-5](https://doi.org/10.1016/s0960-9822(02)00759-5), PMID: 11937022
- Andrews RV. 1968. Temporal secretory responses of cultured hamster adrenals. *Comparative Biochemistry and Physiology* **26**:179–193. DOI: [https://doi.org/10.1016/0010-406x\(68\)90324-1](https://doi.org/10.1016/0010-406x(68)90324-1), PMID: 4320134
- Bainier C, Mateo M, Felder-Schmittbuhl M-P, Mendoza J. 2017. Circadian rhythms of hedonic drinking behavior in mice. *Neuroscience* **349**:229–238. DOI: <https://doi.org/10.1016/j.neuroscience.2017.03.002>, PMID: 28286126
- Baker FC, Angara C, Szymusiak R, McGinty D. 2005. Persistence of sleep-temperature coupling after suprachiasmatic nuclei lesions in rats. *American Journal of Physiology. Regulatory, Integrative and Comparative Physiology* **289**:R827–R838. DOI: <https://doi.org/10.1152/ajpregu.00093.2005>, PMID: 15860650
- Balsalobre A, Brown SA, Marcacci L, Tronche F, Kellendonk C, Reichardt HM, Schütz G, Schibler U. 2000. Resetting of circadian time in peripheral tissues by glucocorticoid signaling. *Science* **289**:2344–2347. DOI: <https://doi.org/10.1126/science.289.5488.2344>, PMID: 11009419
- Bass J, Takahashi JS. 2010. Circadian integration of metabolism and energetics. *Science* **330**:1349–1354. DOI: <https://doi.org/10.1126/science.1195027>, PMID: 21127246
- Brightwell G, Poirier V, Cole E, Ivins S, Brown KW. 1997. Serum-dependent and cell cycle-dependent expression from a cytomegalovirus-based mammalian expression vector. *Gene* **194**:115–123. DOI: [https://doi.org/10.1016/s0378-1119\(97\)00178-9](https://doi.org/10.1016/s0378-1119(97)00178-9), PMID: 9266680
- Cao YA, Wagers AJ, Beilhack A, Dusich J, Bachmann MH, Negrin RS, Weissman IL, Contag CH. 2004. Shifting foci of hematopoiesis during reconstitution from single stem cells. *PNAS* **101**:221–226. DOI: <https://doi.org/10.1073/pnas.2637010100>, PMID: 14688412
- Cao R, Gkogkas CG, de Zavalía N, Blum ID, Yanagiya A, Tsukumo Y, Xu H, Lee C, Storch K-F, Liu AC, Amir S, Sonenberg N. 2015. Light-regulated translational control of circadian behavior by eIF4E phosphorylation. *Nature Neuroscience* **18**:855–862. DOI: <https://doi.org/10.1038/nn.4010>, PMID: 25915475
- Cederroth CR, Park JS, Basinou V, Weiger BD, Tserga E, Sarlus H, Magnusson AK, Kadri N, Gachon F, Canon B. 2019. Circadian Regulation of Cochlear Sensitivity to Noise by Circulating Glucocorticoids. *Current Biology* **29**:2477–2487. DOI: <https://doi.org/10.1016/j.cub.2019.06.057>, PMID: 31353184
- Cheon S, Park N, Cho S, Kim K. 2013. Glucocorticoid-mediated Period2 induction delays the phase of circadian rhythm. *Nucleic Acids Research* **41**:6161–6174. DOI: <https://doi.org/10.1093/nar/gkt307>, PMID: 23620290
- Chong SYC, Ptáček LJ, Fu YH. 2012. Genetic insights on sleep schedules: this time, it's PERsonal. *Trends in Genetics* **28**:598–605. DOI: <https://doi.org/10.1016/j.tig.2012.08.002>, PMID: 22939700
- Cirelli C, Tononi G. 2000. Differential expression of plasticity-related genes in waking and sleep and their regulation by the noradrenergic system. *The Journal of Neuroscience* **20**:9187–9194. DOI: <https://doi.org/10.1523/JNEUROSCI.20-24-09187.2000>, PMID: 11124996
- Collaco AM, Geusz ME. 2003. Monitoring immediate-early gene expression through firefly luciferase imaging of HRS/J hairless mice. *BMC Physiology* **3**:8. DOI: <https://doi.org/10.1186/1472-6793-3-8>
- Cuesta M, Cermakian N, Boivin DB. 2015. Glucocorticoids entrain molecular clock components in human peripheral cells. *FASEB Journal* **29**:1360–1370. DOI: <https://doi.org/10.1096/fj.14-265686>, PMID: 25500935
- Curie T, Mongrain V, Dorsaz S, Mang GM, Emmenegger Y, Franken P. 2013. Homeostatic and circadian contribution to EEG and molecular state variables of sleep regulation. *Sleep* **36**:311–323. DOI: <https://doi.org/10.5665/sleep.2440>, PMID: 23450268
- Curie T, Maret S, Emmenegger Y, Franken P. 2015. In Vivo Imaging of the Central and Peripheral Effects of Sleep Deprivation and Suprachiasmatic Nuclei Lesion on PERIOD-2 Protein in Mice. *Sleep* **38**:1381–1394. DOI: <https://doi.org/10.5665/sleep.4974>, PMID: 25581923
- Daan S, Beersma DG, Borbély AA. 1984. Timing of human sleep: recovery process gated by a circadian pacemaker. *The American Journal of Physiology* **246**:R161–R183. DOI: <https://doi.org/10.1152/ajpregu.1984.246.2.R161>, PMID: 6696142
- Damiola F, Le Minh N, Preitner N, Kornmann B, Fleury-Olela F, Schibler U. 2000. Restricted feeding uncouples circadian oscillators in peripheral tissues from the central pacemaker in the suprachiasmatic nucleus. *Genes & Development* **14**:2950–2961. DOI: <https://doi.org/10.1101/gad.183500>, PMID: 11114885
- Dickmeis T. 2009. Glucocorticoids and the circadian clock. *The Journal of Endocrinology* **200**:3–22. DOI: <https://doi.org/10.1677/JOE-08-0415>, PMID: 18971218
- Diebler S, Jan M, Emmenegger Y, Guex N, Middleton B, Skene DJ, Ibberson M, Burdet F, Götz L, Pagni M, Sankar M, Liechti R, Hor CN, Xenarios I, Franken P. 2018. A systems genetics resource and analysis of sleep regulation in the mouse. *PLOS Biology* **16**:e2005750. DOI: <https://doi.org/10.1371/journal.pbio.2005750>, PMID: 30091978
- Du NH, Arpat AB, De Matos M, Gatfield D. 2014. MicroRNAs shape circadian hepatic gene expression on a transcriptome-wide scale. *eLife* **3**:e02510. DOI: <https://doi.org/10.7554/eLife.02510>
- D'Alessandro M, Beesley S, Kim JK, Jones Z, Chen R, Wi J, Kyle K, Vera D, Pagano M, Nowakowski R, Lee C. 2017. Stability of Wake-Sleep Cycles Requires Robust Degradation of the PERIOD Protein. *Current Biology* **27**:3454–3467. DOI: <https://doi.org/10.1016/j.cub.2017.10.014>, PMID: 29103939

Figure 1—figure supplement 5*



The effect of activity on bioluminescence in three different bioluminescence reporters. (A) Three representative recordings of activity co-detected with bioluminescence in *Per2^{Luc}* mice (top), reflecting both circadian and sleep-wake/activity-evoked changes, *CAG-Luc* mice (middle), representing activity-evoked changes, and *Pkg1-Luc* mice (bottom), not affected by changes in activity. The selected transitions are annotated on the bottom of each individual recording. Bioluminescence data are plotted relative to the mean bioluminescence of the individual's recording. **(B)** Quantification of changes in bioluminescence around rest-activity transitions. For comparison, gray symbols and lines depict sleep-to-wake transition dynamics for PER2::LUC mice (same data as in Figure 1C). Note that the same scaling is used for all three constructs and that only the 100% level is indicated for the *CAG-Luc* and *Pkg1-Luc* mice. Data underlying this figure can be found in Figure 1—figure supplement 5—source data 1.

*Here only the Figure 1—figure supplement 5 is shown, as I performed the *Pkg1-Luc* (there is a typographic mistake at the article figure *Pkg1* instead *Pgk1*) experiments. There rest of the supplementary material can be found at the online version of the article (<https://elifesciences.org/articles/69773/figures#fig1>).

« ... ἐγὼ δέ, ὥσπερ οὖν οὐκ οἶδα, οὐδὲ οἶομαι· ἔοικα γοῦν τούτου γε σμικρῷ τινι αὐτῷ τούτῳ σοφώτερος εἶναι, ὅτι ἂ μὴ οἶδα οὐδὲ οἶομαι εἰδέναί.».

(Socrates' statement in *Apology*, Plato)